# ICRR ANNUAL REPORT 2018

**INSTITUTE**

FOR

**COSMIC RAY RESEARCH**

THE UNIVERSITY OF TOKYO

# ANNUAL REPORT
# (APRIL 2018 – MARCH 2019)

5-1-5, Kashiwanoha, Kashiwa, Chiba 277-8582, Japan

Telephone: (81) 4-7136-3102
Facsimile: (81) 4-7136-3115
WWW URL: http://www.icrr.u-tokyo.ac.jp/

# TABLE OF CONTENTS

# PREFACE

This report summarizes the scientific activities of the Institute for Cosmic Ray Research (ICRR) of The University of Tokyo in the Japanese FY 2018.

ICRR is an inter-university research institute for studies of cosmic rays. The headquarters of ICRR is located in Kashiwa, Chiba prefecture, Japan. In order to promote various cosmic-ray-related studies efficiently, ICRR has three research divisions; Neutrino and Astroparticle division, High Energy Cosmic Ray division, and Astrophysics and Gravity division. ICRR have four observatories in Japan; Kamioka and KAGRA Observatories (Kamioka underground, Gifu prefecture), Norikura Observatory (2770 meters above sea level, Mt. Norikura, Gifu prefecture), and Akeno Observatory (Yamanashi prefecture), together with 1 research center; Research Center for Cosmic Neutrinos (Kashiwa, Chiba prefecture). In addition, there are two major experimental facilities outside of Japan. They are located in Utah in USA, and Yangbajing in Tibet, China. The La Palma island in Spain is also recognized as an important site for the ICRR activities.

Many researchers from various Japanese institutions as well as those from overseas are involved in the research programs of ICRR. It should be noted that most of the scientific outputs from this institute are the results of the collaborative efforts by many researchers from various institutions. In order to produce outstanding results, it is very important to carry out an experiment by an international collaboration composed of top-level researchers all over the world. Hence, all of the experimental collaborations that ICRR is involved are international ones. With these activities, ICRR has been selected as one of the international inter-university research institute by Ministry of Education, Culture, Sports, Science and Technology -Japan (MEXT) in November 2018.

Many exciting scientific activities of ICRR are described in this report. For example, the Super-Kamiokande and T2K (which uses Super-Kamiokande as the far detector) experiments have been continuously producing impressive results on neutrino oscillation physics. The discovery of neutrino oscillations by the Super-Kamiokande experiment was recognized by the 2015 Nobel Prize in Physics.

Some of the other recent highlights are mentioned here: the KAGRA gravitational wave project is going to begin the observation run in early 2020. TA (Telescope Array) has been producing impressive data on highest energy cosmic rays, including the indication that these cosmic rays arrive from a particular direction of the sky. ICRR is playing a major role in CTA, which is a global TeV gamma ray astronomy project. ICRR is contributing substantially to the construction of Large-Sized Telescopes (LST) of the CTA-North observatory. The construction of the first LST has been completed in October 2018.

As an inter-university research institute, ICRR is reviewed by the top-level researchers in the field. In particular, future projects of ICRR are evaluated by a committee composed of top-level researchers from various nearby fields. The ICRR Future Project Evaluation Committee released its report in October 2017. Several projects have been recommended highly. Among them, Hyper-Kamiokande, which is the next generation neutrino detector, has been recommended as the top priority ICRR future project. ICRR is working hard toward the realization of Hyper-Kamiokande.

We hope that this report is useful for the understanding of the current research activities of ICRR. Finally, we appreciate the strong support of our colleagues in this research field, The University of Tokyo and MEXT. They are indispensable for the continuing, and exciting scientific outcome of ICRR.

Takaaki Kajita,
Director,
Institute for Cosmic Ray Research,
The University of Tokyo

The ICRR building at Kashiwa, Chiba, Japan.

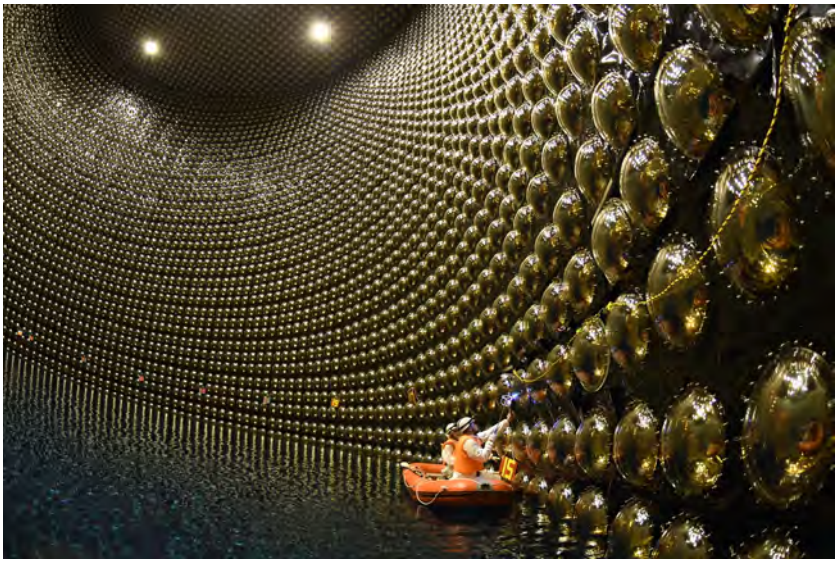

The Super-Kamiokande detector (the photo was taken during refurbishment work in 2018).

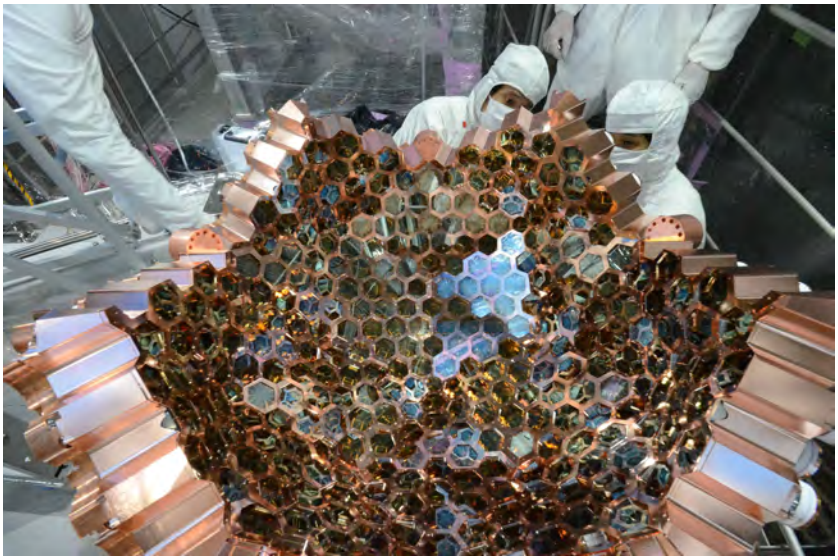

The XMASS detector (the photo was taken during the refurbishment work in 2013).

The first Large Size Telescope of CTA installed at Observatory Roque de los Muchachos inaugurated on October 10 2018.

Tibet-III air shower array (37000 $m^2$) at Yangbajing, Tibet (4300 m in altitude).

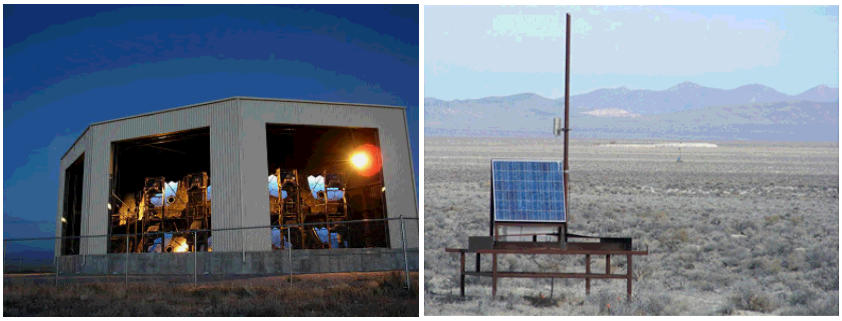

Air fluorescence telescopes (left) and a scintillator surface detector (right) of the Telescope Array experiment in Utah, USA to explore the origin of extremely high energy cosmic rays.

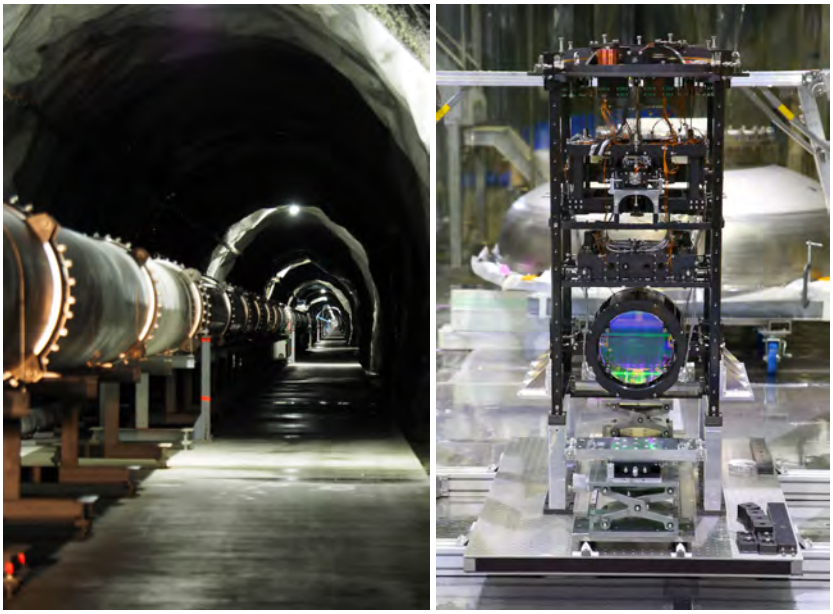

KAGRA's (left) 3km-long arm tunnel and (right) a sapphire mirror installed in a cryogenic suspension system.


A public lecture co-organized with the Institute for the Physics and Mathematics of the Universe (Kavli IPMU).

## Organization

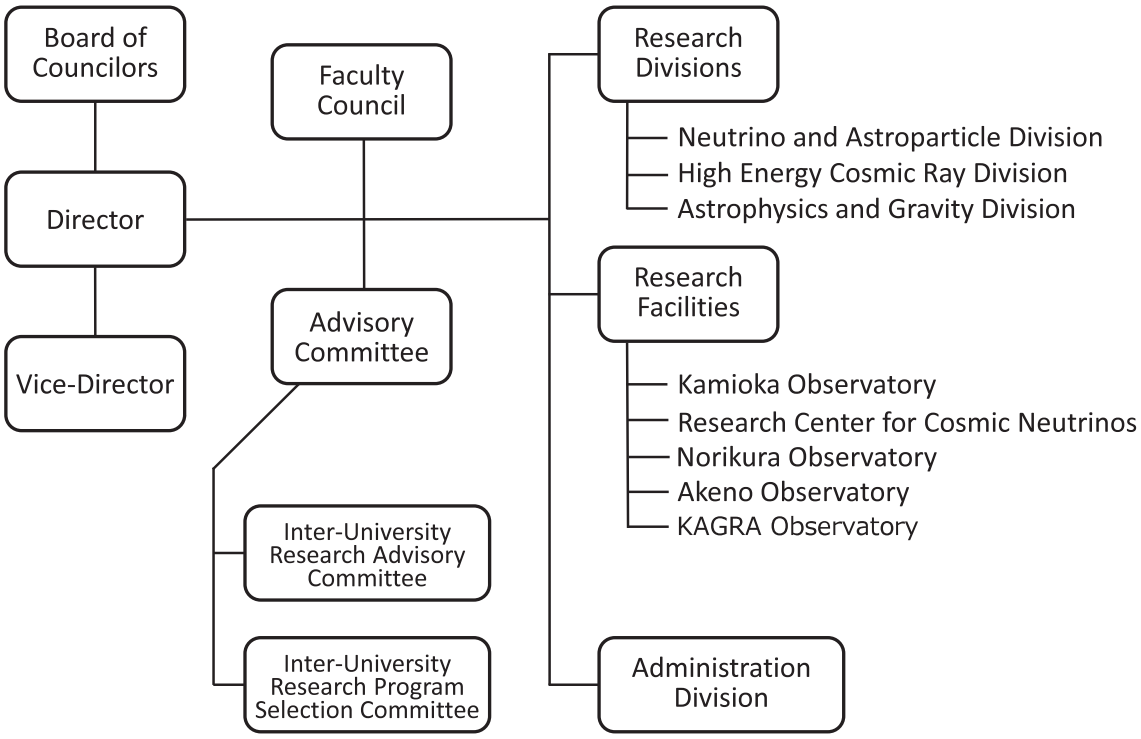


## Number of Staff Members (As of May 1, 2018)

| | Scientific Staff | Technical Staff | Research Fellows | Administrators and Secretaries | Total |
|---|---|---|---|---|---|
| Neutrino and Astroparticle Div. | 26 | 5 | 3 | 17 | 51 |
| High Energy Cosmic Ray Div. | 17 | 13 | 1 | 2 | 33 |
| Astrophysics and Gravity Div. | 16 | 7 | 6 | 11 | 40 |
| Administration | 0 | 0 | 0 | 16 | 16 |
| Total | 59 | 25 | 10 | 46 | 140 |

## FY 2012-2018 Budget

| | 2012 | 2013 | 2014 | 2015 | 2016 | 2017 | 2018 |
|---|---|---|---|---|---|---|---|
| Personnel expenses | 658 000 | 687 000 | 706 000 | 684 000 | 683 000 | 779 000 | 823 000 |
| Non-personnel expenses | 1 172 000 | 1 095 000 | 1 282 000 | 1 595 000 | 1 288 000 | 1 514 000 | 1 729 000 |
| Total | 1 830 000 | 1 782 000 | 1 988 000 | 2 279 000 | 1 971 000 | 2 293 000 | 2 552 000 |

(in 1 000 yen)

# RESEARCH DIVISIONS

## Neutrino and Astroparticle Division



## High Energy Cosmic Ray Division



## Astrophysics and Gravity Division

# NEUTRINO AND ASTROPARTICLE DIVISION

## Overview

This division aims to study particle physics with prime interests in physics of neutrinos and proton decay, and astroparticle physics with the use of underground experimental facilities.

The Super-Kamiokande (SK) detector is a 50 kton water Cherenkov detector using 11,129 50 cm-diameter photomultipliers (PMTs) for its inner detector and 1,885 20 cm-diameter PMTs for its outer detector. The data taking of SK started in April 1996 and 20th anniversary was celebrated in 2016. The neutrino oscillations in atmospheric neutrinos were discovered in 1998 and thereby it was demonstrated that neutrinos have a finite mass. In 2001, the accurate measurements of the $^8$B solar neutrino flux by SK and SNO discovered that neutrino oscillations are the solution of the solar neutrino problem beyond doubt. These findings became the research achievement for which the Nobel Prize in Physics was awarded in 2015. After the epoch-making discoveries, precise measurements of atmospheric neutrinos and solar neutrinos have been performed and they unraveled various phenomena of neutrino oscillations. The evidence of tau neutrino appearance in atmospheric neutrinos was confirmed in 2013 and atmospheric neutrino anomaly has been finally concluded. The indication of day-night asymmetry of the solar neutrino flux, which is expected from the matter effect of neutrino oscillations, was reported in 2014. At present, the most interesting subjects in those observations are the determination of neutrino mass hierarchy using atmospheric neutrinos and the consistency check of solar($\nu_e$) and reactor($\bar{\nu}_e$) oscillations.

A high intensity neutrino beam experiment using the J-PARC accelerator (T2K) was started in 2009. The T2K experiment uses the SK detector as the far detector. Search for leptonic *CP* violation and the high precision measurement of oscillation parameters are main physics subjects in T2K. An indication of electron neutrino appearance was found in June 2011, and later the electron appearance has been established with greatly improved significance. Since 2014, anti-neutrino beam data also have been taken in order to search for *CP* violation.

The search for nucleon decay is another important subject at SK because it gives a direct evidence for the Grand Unified Theories (GUTs). SK gives the current best limit which strongly constrains various GUT models.

If a supernova happens in our galaxy, thousands of neutrino interactions are expected at SK and they will reveal detailed mechanism of the supernova explosion. SK is the only detector in the world which can identify the direction of the supernova neutrinos. So, SK has been operated almost all the time with small dead time and if a supernova is observed at SK, we will send burst information to astronomers as soon as it is detected. In addition, SK aims to observe supernova relic neutrinos, which is an accumulated supernova burst neutrinos from the beginning of the universe. For this purpose, it is planned to add 0.1% of gadolinium into the Super-K tank (called SK-Gd project) in order to tag neutrons for $\bar{\nu}_e$ detection. A feasibility study for the SK-Gd project is being performed using a 200 ton tank which mimics the Super-K detector. Refurbishment of the Super-K tank and upgrade of the water circulation system had been conducted in 2018 to become ready for Gd doping.

Another activity of the Neutrino and Astroparticle division is a multi-purpose experiment using liquid xenon aiming at the detection of cold dark matter, neutrino absolute mass using neutrinoless double beta decay, and low energy solar neutrinos. A 800 kg liquid xenon detector was constructed in an experimental hall near the SK site. Data taking continued for more than five years and finished in February 2019. Searches for dark matter interactions and rare phenomena in liquid xenon are being conducted.

The Hyper-Kamiokande (Hyper-K or HK) experiment is proposed as a joint project of the university of Tokyo and KEK by combining a next generation underground water Cherenkov detector and upgraded J-PARC neutrino beam. The Hyper-K detector is an order of magnitude larger in detector fiducial mass than Super-K and has discovery potential of leptonic *CP* violation and proton decays. The detector construction has been endorsed by the ICRR future project committee's report in March 2017. Hyper-K has been selected as one of the seven large scientific projects in the Roadmap of the Japanese Ministry of Education, Culture, Sports, Science and Technology (MEXT) in 2017. We are eagerly waiting for the approval by the Japanese government.

## SUPER-KAMIOKANDE

[Spokesperson : Masayuki Nakahata
(Kamioka Observatory, ICRR, The University of Tokyo)]

### *Search for nucleon decay*

Proton decays and bound neutron decays (nucleon decays in general) is the most dramatic prediction of Grand Unified Theories (GUTs) in which three fundamental forces of elementary particles are unified into a single force. Super-Kam iokande (SK) is the world's largest detector to search for nucleon decays. Various nucleon decay modes have been looked for, but we have found no significant signal excess so far.

A proton decay into one charged lepton and one neutral pion ($p \to e^+\pi^0,\ p \to \mu^+\pi^0$) is one of the popular decay modes which most of GUT models predict and have relatively large detection efficiency. On the other hand, a proton decay into $K^+$ and $\nu$ is suggested by GUTs collaborated with Supersymmetry theories (SUSY-GUTs). These bench mark decay

modes have been analyzed with 365 kton·year exposure. SK data was consistent with background estimation and obtained lower limit of proton lifetime were 2.0, 1.2, and $0.8\times10^{34}$ years for $p\to e^+\pi^0$, $p\to\mu^+\pi^0$, and $p\to K^+\nu$, respectively. These analysis has been done with 22.5 kton fiducial volume which is defined by 2 m inward from the inner tank wall. If we can expand the fiducial volume to 1 m from the inner wall, for example, we can gain 20% more data than the current analysis. To expand the fiducial volume, we need to understand background contamination from the wall and reconstruction performance close to the wall. The new attempt to expand fiducial volume has just started and it is important for the other neutrino oscillation analysis.

It was pointed out that observation of a proton decay into three charged leptons (e or $\mu$) would provide energy scale of order 100 TeV and explanation to recent $b\to s\mu\mu$ anomalies as the relevant effective operators arise at dimension 9 or 10 [1]. All possible decay modes with combination of e and $\mu$, p$\to e^+e^+e^-, e^+e^+\mu^-, e^+e^-\mu^+, e^+\mu^+\mu^-, e^-\mu^+\mu^+, \mu^+\mu^+\mu^-$ are started to investigate at the first time in SK. Typical proton lifetime for these modes is predicted as order of $10^{33}$ years which could be accessible with exposure of SK. Even though there are no significant signal observed for these modes, proton lifetime limits would be largely improved because the current world records for these modes were set by IMB about 20 years ago [2]. All final particles above Chrenkov threshold for these decay modes are detectable in SK and higher selection efficiencies are expected. There are no pions in the final particles and these decay modes are free from $\pi$ interactions in nucleus ($\pi$-FSI) which often provides the largest uncertainty in signal selection of nucleon decay searches.

To select signal, following cuts are required: (1) fully contained and event vertex locates more than 2 m apart from the inner tank, (2) three rings are reconstructed, (3) proper number of e-like and $\mu$-like rings (for example, three e-like rings are required for p$\to e^+e^+e^-$), (4) require the same number of Michel electron as number of $\mu$ in particles from proton decay, but accept two Michel electron case for p$\to\mu^+\mu^+\mu^-$, (5) no tagged neutron only for SK-IV, (6) reconstructed invariant mass should be in between 800 and 1050 MeV/$c^2$ and total momentum should be less than 250 MeV/c. Figure 1 shows number of ring distributions for each mode. Fraction of three ring events decreases if number of $\mu$ in final particles increases because there are some amount of $\mu$ below Cherenkov threshold. Figure 2 shows number of Michel electron distributions for p$\to e^+\mu^+\mu^-, e^-\mu^+\mu^+$. Less fraction of two Michel electrons is observed in p$\to e^+\mu^+\mu^-$ than p$\to e\mu^+\mu^+$ because Michel electron can not be emitted in case of $\mu^-$ capture in water.

Table 1 summarizes selection efficiencies and background estimations only for SK-IV period. Signal region is divided into lower ($P_{tot} < 100\ MeV/c$) and higher ($100 \le P_{tot} < 250\ MeV/c$) total momentum region as same as p$\to e^+\pi^0$ analysis [3]. Total efficiency for p$\to e^+e^+e^-$ exceeds 60% and expected background is well suppressed and there are no background events remained in lower momentum region. Number of expected background for $p\to\mu^+e^+e^-$ and $p\to\mu^-e^+e^+$, $p\to e^+\mu^+\mu^-$ $p\to e^-\mu^+\mu^+$ are common because the same selection criteria is applied to background MC for these two modes, while efficiency is different due to $\mu^-$ capture. The study will be expanded to all SK era and after systematic uncertainty estimation and side band check, data will be opened.

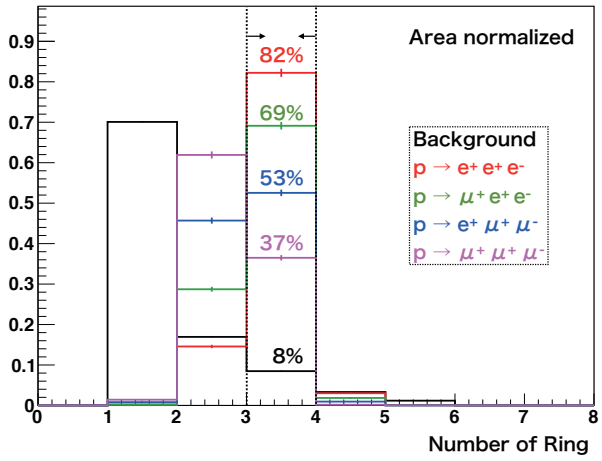


Fig. 1. Number of ring distribution after fiducial volume cut. Red green, blue, cyan corresponds to signal MC of p$\to e^+e^+e^-, \mu^+e^+e^-, e^+\mu^+\mu^-, \mu^+\mu^+\mu^-$, respectively. Black histogram shows atmospheric neutrino background. Only three ring events are selected.

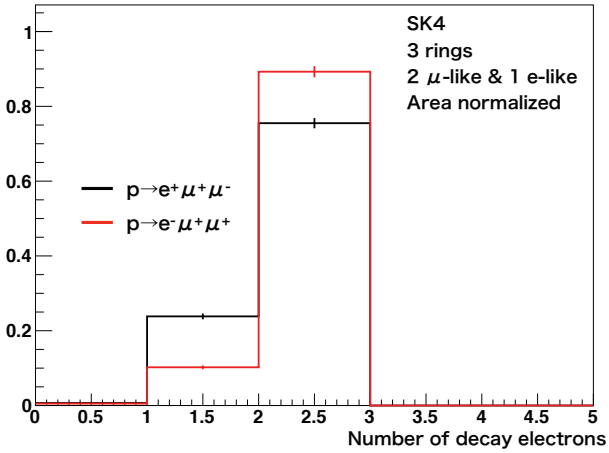


Fig. 2. Number of Michel electron distribution for signal MC. Black corresponds to p$\to e^+\mu^+\mu^-$ and red shows p$\to e^-\mu^+\mu^+$. Due to $\mu^-$ capture in water, p$\to e^+\mu^+\mu^-$ events have less Michel electron than p$\to e^-\mu^+\mu^+$.

## Bibliography


[1] T. Hambye and J. Heeck, PRL **120**, 171801 (2018).

[2] C. McGrew *et al.* [IMB Collaboration], Phys. Rev. D **59**, 052004 (1999).

[3] K. Abe *et al.* [Super-Kamiokande Collaboration], Phys. Rev. D **95**, 012004 (2017).

| | Efficiency (%) | | Background | |
|---|---|---|---|---|
| | low $P_{tot}$ | high $P_{tot}$ | low $P_{tot}$ | high $P_{tot}$ |
| $p \to e^+e^+e^-$ | 22.4 | 41.1 | <0.01 | 0.24±0.07 |
| $p \to \mu^+e^+e^-$ | 17.6 | 30.3 | <0.01 | 0.17±0.05 |
| $p \to \mu^-e^+e^+$ | 14.9 | 25.9 | <0.01 | 0.17±0.05 |
| $p \to e^+\mu^+\mu^-$ | 11.7 | 20.9 | <0.01 | 0.08±0.03 |
| $p \to e^-\mu^+\mu^+$ | 14.4 | 24.2 | <0.01 | 0.08±0.03 |
| $p \to \mu^-\mu^+\mu^+$ | 12.2 | 20.4 | <0.01 | 0.22±0.06 |

Table 1. Summary of efficiencies and backround for SK-IV. Low $P_{tot}$ and high $P_{tot}$ are defined as $P_{tot} < 100$MeV/$c$ and $100 \leq P_{tot} < 250$MeV/$c$, respectively.

### *Atmospheric neutrinos*

Atmospheric neutrinos are produced from the decays of secondary particles produced in the collision of primary cosmic rays with nuclei in the atmosphere. Atmospheric neutrinos have several remarkable features:

- The flavor ratio, $(\nu_\mu + \bar{\nu}_\mu)/(\nu_e + \bar{\nu}_e)$ is 2 ( $> 2$ for above few GeV)
- Zenith angle distribution is up/down symmetry above a few GeV

These features are realized without neutrino oscillations, and provide a useful constraint in the study of these neutrinos. Super-Kamiokande has been observing atmospheric neutrinos since 1996 and has accordingly made several important measurements, including the discovery of neutrino oscillations [1].

**Three flavor oscillations and the neutrino mass hierarchy**

The SK atmospheric neutrino data are described at leading order by two-flavor $\nu_\mu \to \nu_\tau$ oscillations with maximal mixing ($\theta_{23}$=$\pi$/4). However, sub-leading contributions via $\nu_\mu \to \nu_e$ oscillations induced by the mixing angle $\theta_{13}$ as well as the "solar" mixing parameters ($\Delta m^2_{12}, \theta_{12}$) provide the ability to probe currently unknown aspects of the standard neutrino oscillation paradigm, such as the existence of leptonic *CP* violation and the neutrino mass ordering (hierarchy). Understanding these open questions may bring important insight into larger questions, such as the origin and evolution of today's matter-dominated universe.

Several sub-leading oscillation effects are expected to appear in atmospheric neutrinos:

- Resonant enhancement of $\nu_\mu \to \nu_e$ oscillations due to the effects of matter is expected to occur at energies between 2 and 10 GeV and will manifest as an excess of upward-going electron-like events (e-like) in the atmospheric sample.
- This enhancement exists for either $\nu_e$ or $\bar{\nu}_e$ depending on the mass hierarchy. Therefore the mass hierarchy can be probed by understanding the relative amount of neutrino and antineutrino interactions in the detector.
- The combination of the solar oscillation parameters and the octant of $\sin^2\theta_{23}$, may enhance or suppress the event rate, and to some extent alter the spectral shape, of Sub-GeV electron-like data the due to the $\nu_\mu \leftrightarrow \nu_e$ oscillations they induce.
- The standard oscillation paradigm includes a *CP*-violating factor, $\delta_{cp}$, which is expected to induce several sub-dominant oscillation effects in many of the SK atmospheric neutrino samples, even if CP is conserved.

Super-Kamiokande has studied the effects of these oscillations on atmospheric neutrino data separated into fully-contained (FC) events, partially-contained (PC) events, and upward-going muon topologies. Fully-contained events are characterized by a primary interaction vertex that is located inside the fiducial volume of the detector and whose visible particles stop within the inner detector. On the other hand, though the primary vertex position of PC events is within the fiducial volume, they are characterized by having at least one charged particle escaping the inner detector and depositing light in the outer detector. In most cases the escaping particle is a muon. Upward-going muons originate from high energy muon-neutrino interactions in the rock surrounding the detector. Since all other particles are lost to interactions in the rock, only the muon is penetrating enough to reach the detector and be identified. The FC sample is separated into electron-like and muon-like ($\mu$-like) subsamples by applying a particle identification algorithm to the most energetic Cherenkov ring of each event. Since PC and upward-going events are predominantly produced by muon neutrinos, no particle identification is applied. Though SK cannot distinguish on an event-by-event basis neutrino and antineutrino interactions, statistical separation of multi-GeV electron-like subsamples is performed to improve sensitivity to the mass hierarchy. A likelihood method designed to enhance the kinematic differences between neutrino and antineutrino interactions is applied to separate events into $\nu_e$-like and $\bar{\nu}_e$-like subsamples.

A new reconstruction algorithm based on a maximum likelihood method has been developed for Super-K. Compared to the conventional reconstruction algorithm, the new algorithm shows improved performance in a variety of metrics including event vertex resolution, particle momentum resolution, and particle identification. Fig. 3 shows an improved ability to discriminate between electrons and muons with less than a 1% mis-identification rate for visible energies less than 1330 MeV. The new algorithm has further demonstrated reliable performance over a larger volume of the detector than the previous volume. Accordingly, in the present analysis the fiducial volume definition has been expanded to include all events reconstructed more than 50 cm from any ID wall. This represents a 32% increase in the number of events available for analysis relative to the 200 cm threshold used in previous SK analyses [3, 4]. Zenith angle distributions for each analysis sample using the expanded FV are shown in Fig. 4.

Using the new algorithm with its expanded fiducial volume definition an analysis of a 253.9 kton-year exposure of the SK-IV atmospheric data has yielded oscillation parameter estimates consistent with both previous Super-K measurements and results from other experiments [2]. Parame-

ter values and their 1 $\sigma$ errors are summarized in Table 2. Fig. 5shows the $\chi^2$ value as a function of the atmospheric neutrino mixing parameters and $\delta_{CP}$ in the $\theta_{13}$-constrained fit. The data show a weak preference for the normal mass hierarchy, disfavoring the inverted mass hierarchy at 74.0% assuming oscillation parameters at the analysis best-fit point. No strong preference for the $\theta_{23}$ octant is observed.

Fig. 6 shows the expected sensitivity to mass hierarchy as the function of livetime for both reconstruction algorithms and their fiducial volumes. The expected improvement in sensitivity with the new algorithm becomes more apparent as data is accumulated, even assuming the conventional FV. While the new reconstruction has only been applied to the 3118.5 day SK-IV fully contained data set, future efforts will expand this study to include other Super-K samples and run periods, which constitute an additional 2,800 days of livetime.

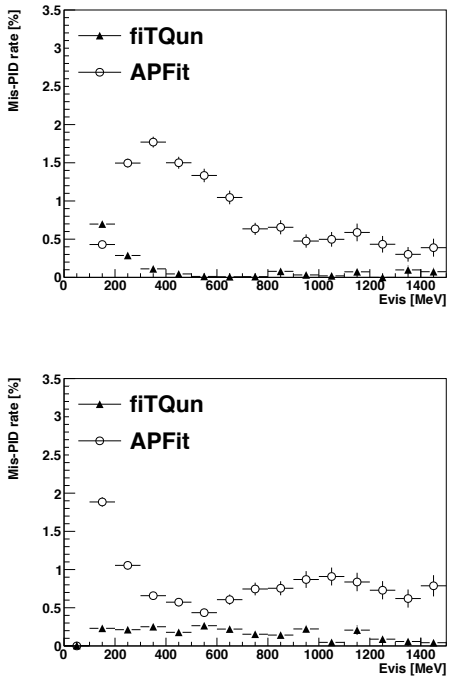


Fig. 3. Mis-identification rate of single-ring electron (top) and muon (bottom) events from FC CCQE atmospheric neutrino MC events plotted as a function of visible energy. The open circles indicate the performance of APFit and the triangles are for fiTQun. The reconstructed event vertex is required to be at least 200 cm away from the ID wall.

**Measurement of the tau neutrino cross section**

The deficit of the muon neutrinos observed in the Super-K data is predominantly explained by the oscillation of the original muon neutrinos into tau neutrinos. For this reason, the direct detection of tau neutrinos is important to confirm the standard three-flavor neutrino oscillation scheme. Super-Kamiokande collaboration previously published a measurement of atmospheric tau neutrino appearance consistent with three-flavor neutrino oscillation with data collected in SK-I through SK-III [5]. The analysis has been updated to use fitting technique and includes new data from the SK-IV period for a total livetime of 5,326 days [6].

| Hierarchy | Normal | Inverted |
|---|---|---|
| $\sin^2\theta_{23}$ (1st oct.) | $0.425^{+0.046}_{-0.037}$ | $0.425^{+0.055}_{-0.036}$ |
| $\sin^2\theta_{23}$ (2nd oct.) | $0.600^{+0.013}_{-0.030}$ | $0.588^{+0.022}_{-0.037}$ |
| $\lvert\Delta m^2_{32,31}\rvert$ ($\times 10^{-3}$ eV$^2$) | $2.53^{+0.22}_{-0.12}$ | $2.53^{+0.14}_{-0.31}$ |
| $\delta_{CP}$ | $3.14^{+2.67}_{-1.35}$ | $4.89^{+1.51}_{-3.46}$ |

Table 2. Parameter estimates for each analysis and hierarchy hypothesis considered. Here "Normal" ("Inverted") refers to the normal (inverted) hierarchy fit. The value of $\sin^2\theta_{13}$ is constrainted to be 0.0210±0.0011 according to reactor measurements. The terms " Unconstrained " and " Constrained " refer to fits without and with a constraint on sin2 $\theta$ 13, respectively. For $\sin^2\theta_{23}$ parameter ranges are shown for both octants, with the best-fit octant enclosed in a box.

The $\nu_\tau$ signal is characterized by an isotropic distribution of hadrons produced when the $\tau$ lepton emerging from the original neutrino interaction decays. Background events are mainly are result of charged current CC $\nu_\mu$ and $\nu_e$ and NC interactions which produce multiple hadrons. As shown in Fig. 7, CC $\nu_\tau$ events typically produce multiple rings in the detector. Multiple-ring events are relatively easy to separate from single-ring atmospheric neutrino events. However, the multiring background events, resulting from multipion/DIS atmospheric neutrino interactions, are difficult to distinguish from the tau signal. Simple selection criteria based on kinematic variables do not identify CC $\nu_\tau$ events efficiently. Therefore we employ a neural network (NN) technique to help distinguish CC $\nu_\tau$ events from background events. Seven kinematic variables are sampled from simulated signal and background events to build and train the NN before applying it to the data. When selecting tau-like events from the events after reduction by requiring the NN output be greater than 0.5, 76% of the signal events and only 28% of the background remain.

To search for atmospheric tau neutrino appearance, the data is fit to a combination of the expected tau signal resulting from neutrino oscillations and atmospheric neutrino background with neutrino oscillations. In order to extract maximum information from the sample, the analysis uses a two-dimensional unbinned maximum likelihood fit. Using two-dimensional histograms of the neural network output and the reconstructed zenith angle of the events, two-dimensional probability distribution functions (PDFs) are built for background and tau signal. The PDFs for each event is a combination of that for background and signal:

$$PDFs = PDFs_{bg} + \alpha \times PDFs_{tau} + \sum_i \varepsilon_i \cdot PDFs_{sys},$$

where the last term represents the change of the PDFs due to systematic error effects. The likelihood is calculated as the product of PDFs for each events and the parameters $\alpha$ and $\varepsilon_i$'s are adjusted to maximize the likelihood.

Figure 8 shows the zenith angle distribution of tau-like and non-tau-like samples after fitting. The NN output distributions for upward- and downward-going events are shown in the right panels. Relative to the expectation for standard three-

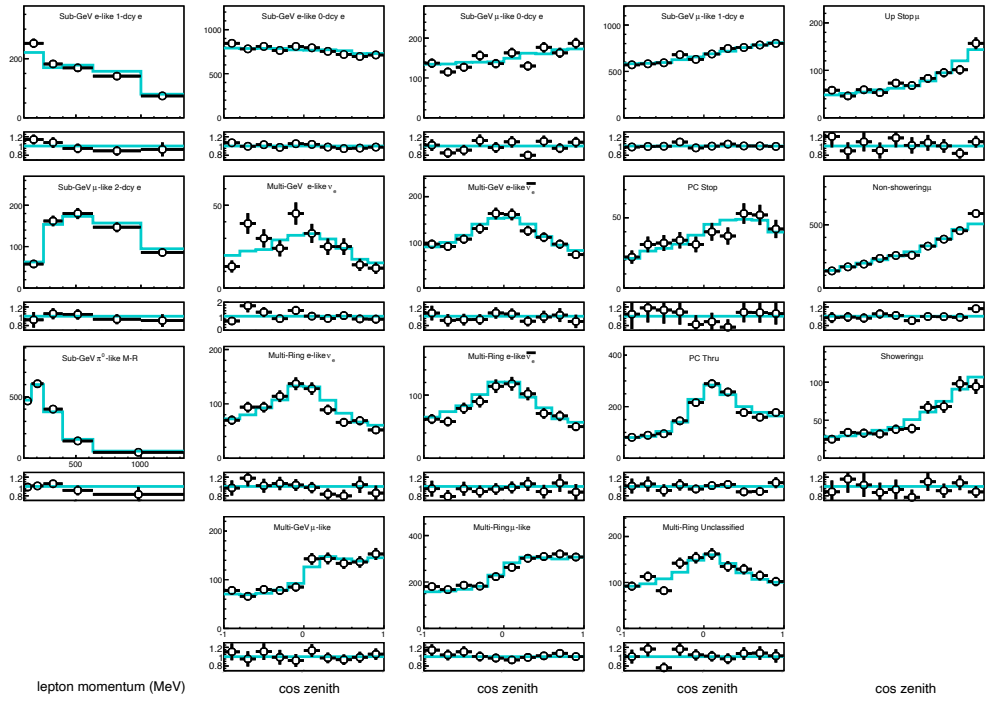


Fig. 4. Data and MC comparisons for the SK-IV data divided into 18 analysis samples. The expanded FV, where $dwall$>50 cm, is shown here. Samples with more than one zenith angle bin are shown as zenith angle distributions (second through fifth column) and other samples are shown as reconstructed momentum distributions (first column). Cyan lines denote the best−fit MC assuming the normal hierarchy. Narrow panels below each distribution show the ratio relative to the normal hierarchy MC. In all panels the error bars represent the statistical uncertainty.

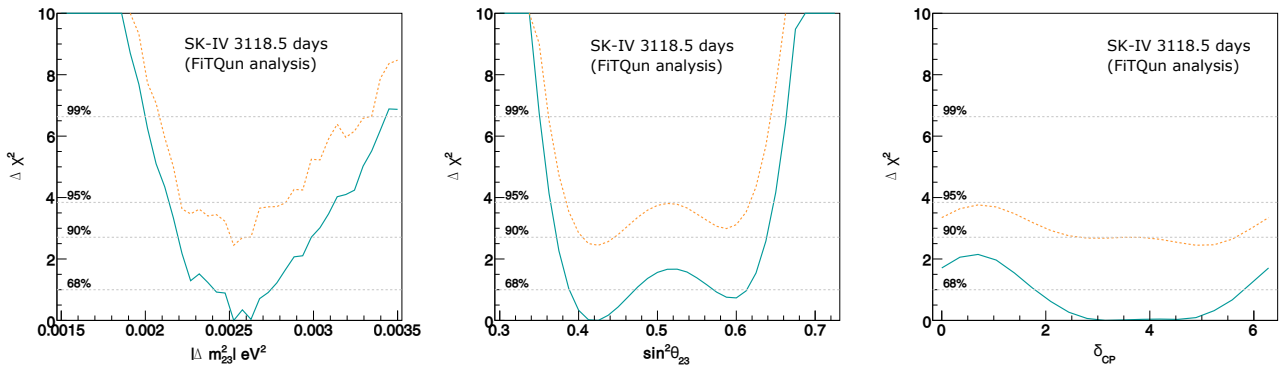


Fig. 5. Constraints on neutrino oscillation parameters from SK-IV atmospheric neutrino data using the expanded FV and assuming $\sin^2\theta_{13}$=0.0210±0.0011. The solid blue and dashed orange lines denote the normal and inverted hierarchy fit results, respectively. The latter has been offset from the former by the difference in their minimum $\chi^2$ values.

flavor neutrino oscillations the fitted number of tau events in the data is $\alpha = 1.47 \pm 0.32$ (stat+syst.). This corresponds to a statistical significance $4.6\sigma$ to reject the no-tau-appearance hypothesis.

Because of the difficulties in tau neutrino production and detection, charged-current tau neutrino cross sections have not been well measured. DONUT [7] is the only experiment that reported a measurement of the cross section. We wish to compare the $\nu_\tau$ cross section measured with atmospheric neutrinos by Super-K at relatively low energies to that measured by DONUT with a neutrino beam at higher energies. A flux-averaged charged current tau neutrino cross section is measured to be $(0.94\pm0.20)\times10^{-38}$ cm$^2$ for neutrino energy between 3.5 and 70 GeV in Super-K, to be compared with the flux-averaged theoretical cross section of $0.64\times10^{-38}$ cm$^2$, as shown in Fig. 9. Our result is consistent with the previous DONUT result, and is consistent with the Standard Model prediction to within $1.5\sigma$.

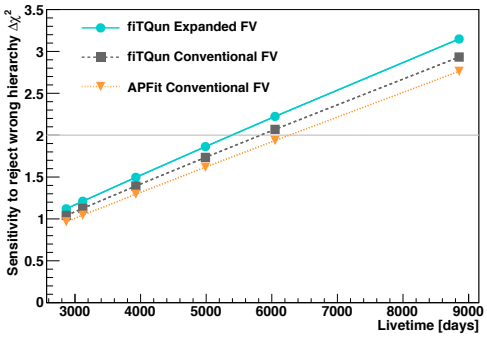


Fig. 6. Expected sensitivity to the normal mass hierarchy as a function of livetime assuming $\sin^2\theta_{23}$=0.5. Grey and blue bands show the sensitivity of the atmospheric neutrino sample reconstructed with fiTQun in the conventional FV and expanded FV, respectively. Orange lines denote the sensitivity when events are reconstructed with APFit in the conventional FV.

### *Search for boosted dark matter*

With the properties of dark matter so uncertain, various possibilities must be considered. One possibility is that some dark matter is, in fact, not cold but is highly relativistic and has been produced at late times, thus denoted "boosted" dark matter [8]. Boosted dark matter could exist as a subdominant dark matter component, with a dominant cold dark matter component accounting for most of the dark matter energy density of the Universe. In this way, boosted dark matter can remain consistent with ΛCDM. The sub-dominant boosted dark matter can be the same particle as the dominant cold dark matter, or it can be a different, lighter particle. Boosted dark matter can be produced from the dominant cold dark matter through a variety of processes, including annihilation, semiannihilation, number-changing 3→2 self-annihilation, and decay. Boosted dark matter can then be observed through its scattering off electrons or nuclei in large-volume terrestrial detectors. Current direct detection limits can be evaded in multicomponent models by having only the boosted dark matter species couple directly to standard model particles or in boosted dark matter single-component models by invoking a spin-dependent dark matter-nucleon cross section.

The results of a search for boosted dark matter coupling to electrons in Super-Kamiokande (SK) was reported [9], with the boosted dark matter originating in the Galactic center or the Sun and with scattered electron energies ranging from 100 MeV to 1 TeV. This is the first time that this class of high-energy "electron elastic scatter- like" events has been studied at SK. The search is performed on 2628.1 days of SK-IV data, which corresponds to 161.9 kt yr exposure. The analysis is designed to be independent of the particular model of the coupling between boosted dark matter and electrons. This way, the results can be applied to any model that predicts a source of particles from the Galactic center or Sun which would scatter electrons to energies greater than 100 MeV.

The search begins with the fully contained fiducial volume (FCFV) data set. This is a standard SK data set used to study atmospheric neutrinos. From this data set, we search for elastically scattered electrons by applying the following analysis

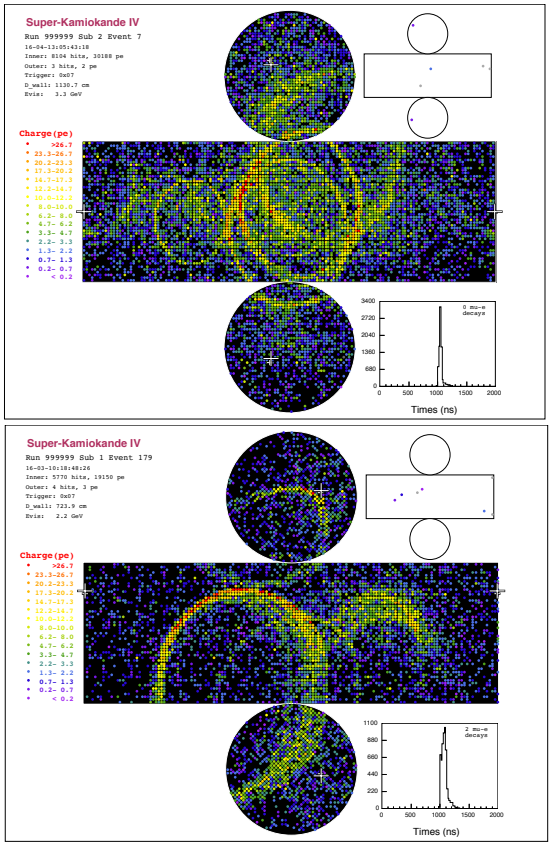


Fig. 7. Simulation of a CC $\nu_\tau$ event (upper) with 3.3 GeV visible energy in the ID and a multiring NC background event (lower) with 2.2 GeV visible energy in the ID. The tau signal event produces multiple rings, making it different from the single-ring background event. The background event with multirings has a similar pattern to the signal event, and requires more effort to statistically distinguish.

cuts: (i) one-ring (if Evis<100 GeV), (ii) e-like, (iii) zero decay electrons, and (iv) zero tagged neutrons. The first two cuts search for a single relativistic electron, while the final two cuts remove events with a signature of a nuclear interaction. Decay electrons in e-like events are the result of the $\pi\to\mu\to e$ decay chain with the $\pi$ coming from a neutrino-nucleus interaction. Tagged neutrons originate from neutrons being knocked out of the nucleus following a neutrino-nucleus interaction, thermalizing, and capturing on hydrogen. Neutron captures are particularly numerous following neutrino deep inelastic scattering. Neither decay electrons nor neutron captures should occur following the elastic scatter of an electron by a boosted dark matter particle.

Since boosted dark matter is expected to originate in regions of high dark matter density, this search looks for a signal coming from the Galactic center or the Sun. Cones are drawn around the signal source, and the number of events passing the analysis cuts in each cone is counted. When the source of the signal is the Galactic center, the optimal size of the search cone is dependent on both the distribution of the dominant dark matter species in the Galaxy and the production method of the boosted dark matter. Production of boosted dark matter through both dark matter annihilation and decay were consid-

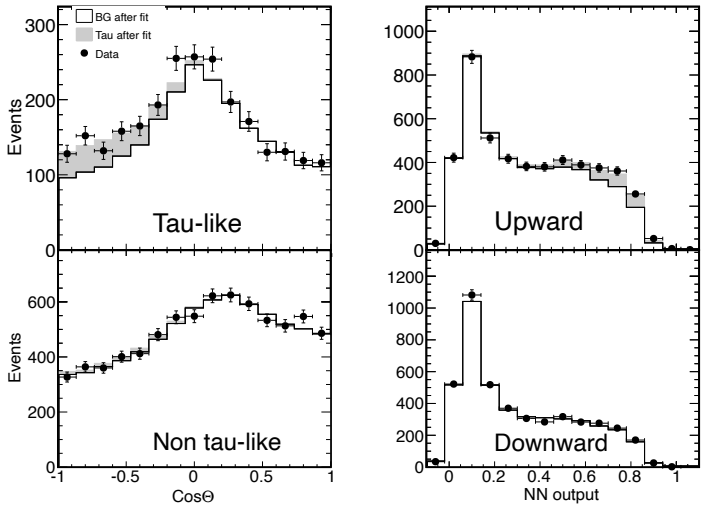


Fig. 8. Fit results, assuming the normal hierarchy, showing binned projections in the NN output and zenith angle distribution for tau-like (NN>0.5), upward-going [$\cos\theta < -0.2$], non-tau-like (NN<0.5) and downward-going [$\cos\theta > 0.2$] events for both the two-dimensional PDFs and data. The PDFs and data sets have been combined from SK-I through SK-IV. The fitted tau signal is shown in gray.

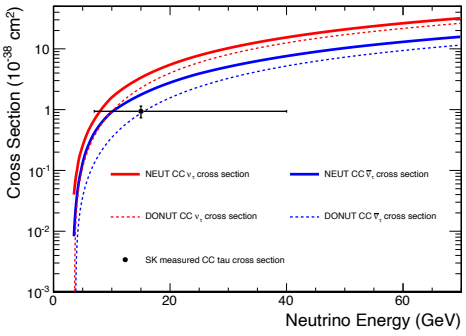


Fig. 9. Comparison of the Super-K measured (marker with error bars) and expected tau neutrino cross sections (solid lines) with $\sigma(E)$ inferred from DONUT (dashed lines).

ered for three dark matter halo models: Moore [10], Navarro-Frenk-White (NFW) [11], and Kravtsov [12]. The optimal half-opeining angle of the search cone was found to range from less than 5° to around 40°. We therefore used eight search cones around the Galactic center, ranging from 5° to 40° in steps of 5°. When the Sun is the signal source, the situation is much simpler, since it is effectively a point source. Therefore, a single search cone of 5° around the Sun was used for the solar search.

The results of the search are shown in Table 3. The observed data are consistent with expected background for both the Galactic center and Sun searches. In the highest energy sample, the search is essentially background-free, and no candidates were found in any of the search cones. Limits were calculated separately for the Moore, NFW, and Kravtsov galactic halo models, using the results from a different cone for each fit. For the annihilation scenario, the 5° cone was used for the Moore model, the 10° cone for the NFW model, and the 40° cone for the Kravtsov model. For the decay scenario, the 40° cone was used for all three galactic halo models. Ninety-percent confidence intervals were computed in the $\varepsilon$ vs $m_A$ plane for the annihilation scenario, and the $\varepsilon=\tau/\text{decay}$ vs $m_A$ plane for the decay scenario, with representative values of $m_B$=200 MeV, $m'_\gamma$=420 MeV,and $g'$=0.5, respectively. These limits are shown for the Moore, NFW, and Kravtsov halo models in Fig. 10.

## Bibliography


[1] Y. Fukuda *et al.* [Super-Kamiokande Collaboration], Phys. Rev. Lett. **81**, 1562 (1998).

[2] M. Jiang *et al.* [Super-Kamiokande Collaboration], arXiv:1901.03230 [hep-ex].

[3] R. Wendell *et al.* [Super-Kamiokande Collaboration], Phys. Rev. D **81**, 092004 (2010).

[4] K. Abe *et al.* [Super-Kamiokande Collaboration], Phys. Rev. D **97**, no. 7, 072001 (2018).

[5] K. Abe *et al.* [Super-Kamiokande Collaboration], Phys.Rev.Lett **110**, 181802 (2013).

[6] Z. Li *et al.* [Super-Kamiokande Collaboration], Phys. Rev. D **98**, no. 5, 052006 (2018).

[7] K. Kodama *et al.* [DONUT Collaboration], Phys. Lett. B **504**, 218 (2001).

[8] See references in [9]

[9] C. Kachulis *et al.* [Super-Kamiokande Collaboration], Phys. Rev. Lett. **120**, no. 22, 221301 (2018).

[10] B. Moore, T. R. Quinn, F. Governato, J. Stadel, and G. Lake, Mon. Not. R. Astron. Soc. **310**, 1147 (1999).

[11] J. F. Navarro, C. S. Frenk, and S. D. M. White, Astrophys. J. **462**, 563 (1996).

| Search Cone | 100 MeV$< E_{vis} <$ 1.33 GeV | | | 1.33 GeV $< E_{vis} <$ 20 GeV | | | $E_{vis} >$ 20 GeV | | |
|---|---|---|---|---|---|---|---|---|---|
| | Expected Bckg | Data | Sig Rate Limit (kT-y)$^{-1}$ | Expected Bckg | Data | Sig Rate Limit (kT-y)$^{-1}$ | Expected Bckg | Data | Sig Rate Limit (kT-y)$^{-1}$ |
| GC 5° | $8.4 \pm 0.7$ | 5 | 0.017 | $1.6 \pm 0.3$ | 1 | 0.018 | $0.016 \pm 0.005$ | 0 | 0.015 |
| GC 10° | $32.0 \pm 1.9$ | 24 | 0.023 | $6.3 \pm 0.84$ | 5 | 0.026 | $0.060 \pm 0.018$ | 0 | 0.015 |
| GC 15° | $72.5 \pm 3.5$ | 69 | 0.078 | $13.6 \pm 1.6$ | 11 | 0.032 | $0.14 \pm 0.04$ | 0 | 0.014 |
| GC 20° | $126.5 \pm 5.4$ | 125 | 0.123 | $23.3 \pm 2.3$ | 18 | 0.028 | $0.25 \pm 0.07$ | 0 | 0.014 |
| GC 25° | $196.8 \pm 7.6$ | 202 | 0.201 | $35.4 \pm 3.3$ | 31 | 0.049 | $0.37 \pm 0.11$ | 0 | 0.013 |
| GC 30° | $283.7 \pm 10.1$ | 285 | 0.214 | $49.3 \pm 4.3$ | 48 | 0.081 | $0.53 \pm 0.16$ | 0 | 0.012 |
| GC 35° | $384.8 \pm 12.8$ | 375 | 0.187 | $68.1 \pm 5.4$ | 67 | 0.101 | $0.70 \pm 0.21$ | 0 | 0.011 |
| GC 40° | $499.6 \pm 15.9$ | 494 | 0.249 | $90.2 \pm 6.9$ | 90 | 0.124 | $0.90 \pm 0.27$ | 0 | 0.011 |
| Sun 5° | $7.59 \pm 0.18$ | 5 | 0.017 | $1.25 \pm 0.07$ | 1 | 0.020 | $0.015 \pm 0.004$ | 0 | 0.015 |

Table 3. Estimated backgrounds,numbers of events in data, and signal event rate limits for each cone and each energy sample. The event rate limits are at the 90% confidence level.

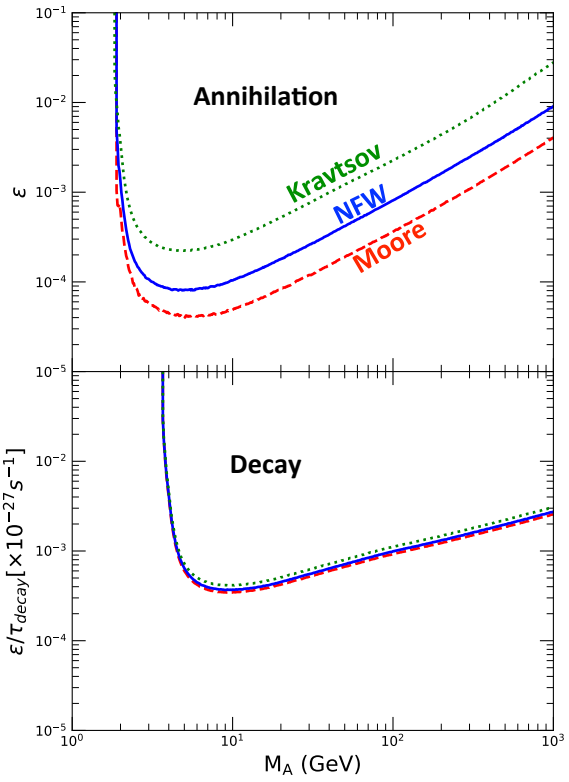


Fig. 10. 90% confidence interval upper limits for $m_B$=200 MeV, $m'_\gamma$=20 MeV, and $g'$=0.5, for boosted dark matter produced by annihilation (top) and decay (bottom).

[12] A. V. Kravtsov, A. A. Klypin, J. S. Bullock, and J. R. Primack, Astrophys. J. **502**, 48 (1998).

## *Solar Neutrinos*

### Introduction

Solar neutrinos constitute by far the largest component of neutrino flux on Earth among those produced from natural sources. Most of solar neutrinos are produced by proton-proton reaction, $p+p \rightarrow d+e^+ + \nu_e$, and its subsequent fusions and $\beta$-decays. They are categorized into so called *pp*, *pep*, $^7$Be, $^8$B and *hep* neutrinos[1], whose predicted fluxes by the standard solar model [1] are shown in the left panel of Figure 11. Among these, $^8$B solar neutrino can be detected relatively easily by many detectors due to its higher energy which extends up to ∼20 MeV.

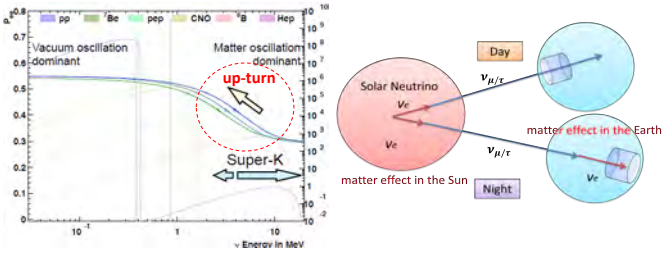


Fig. 11. Left: Several predictions of the survival probability of electron neutrinos emitted from the Sun as well as the fluxes of each solar neutrino; Right: The visual explanation of the day/night flux asymmetry.

Past observations of solar neutrino flux by Super-Kamiokande (SK) [2] and the Sudbury Neutrino Observatory (SNO) [3] led to the discovery of solar neutrino flavor conversion. Our current interest for solar neutrino measurement with the SK detector [4] is to make a precision test of the Mikheyev-Smirnov-Wolfenstein (MSW) effect [5, 6], so called the matter effect. The MSW effect leads to a resonant conversion of the solar neutrinos within the Sun and results in an about 30% level of the survival probability above ∼5 MeV as shown in the left panel of Figure 11. The survival probability of lower energy neutrinos are described by vacuum oscillation probability of ∼ 50%, and the transition region between the two lies at a few MeV region. This transition from the matter dominant oscillation to the vacuum dominant oscillation is often called as the "up-turn" of the solar neutrino spectrum. This "up-turn" have not been directory demonstrated by the past experimental data.

SK aims to directly test the "Spectrum up-turn" by precisely measuring energy spectrum of $^8$B solar neutrino in this transition region. This measurement is not only important to test the MSW effect but also to test several alternative theoretical models, such as sterile neutrinos [7, 8], mass-varying neutrinos [9], non-standard interactions [10, 11] and so on.

*[1] As well as CNO neutrinos

The matter effect can also be tested with the matter in interior of the Earth. Electron flavor neutrinos are regenerated due to the matter effect of the Earth as shown in the right panel of Figure 11, making the neutrino flux in night is larger than that in day by about a few % level depending on the neutrino oscillation parameters. In 2014, SK reported an indication of the terrestrial matter effects by about $2.7\sigma$ [12].

In 2016, the Super-Kamiokande collaboration released a paper reporting a solar neutrino analysis results using 1664 days of SK-IV data [13]. In this annual report, updated results using data taken through the end of January, 2018 (SK-IV 2,860 days data set) with improved energy reconstruction are presented. The total livetime throughout the different phases of SK [2, 14, 15] is 5,695 days.

In addition, we tested effects of non-standard interactions with the solar neutrino spectrum. These results are also shown in this report.

## $^8$B solar neutrino flux measurement

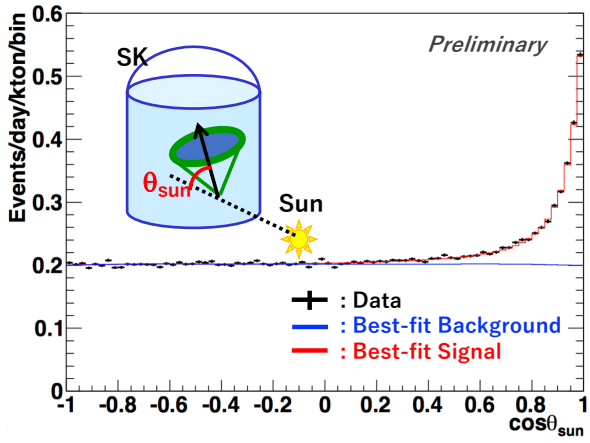


Fig. 12. The solar angle distribution in SK-IV. The horizontal axis shows the cosine of the solar angle $\cos\theta_{\rm Sun}$ and the vertical axis shows the number of the observed events. The red points shows the observed data, the black (blue) histogram shows the best-fit (background-shape).

The SK detector observes solar neutrinos via elastic scatterings with electrons in pure water. The direction of a recoiled electron is highly correlated with the direction of the incident neutrino. Figure 12 shows the distribution of cosine between the reconstructed direction of observed recoiled electrons and the direction of the Sun. With 2860 days of data in SK-IV, more than 55,000 events are observed over the background. Adding the solar neutrino events observed in other phases, the total number of the solar neutrino events is more than 93,000 events. Based on this data, the $^8$B solar neutrino flux is determined to be $(2.33 \pm 0.04) \times 10^6$ /cm$^2$/sec assuming a pure electron neutrino flavor content. The ratio between the SK result and the SNO NC current flux ($5.25 \times 10^6$ /cm$^2$/sec) [16] becomes $0.4432 \pm 0.0084$.

The solar activity cycle is the 11 years periodic change of sun spots releasing the magnetic flux at the surface of the Sun. The number of the sun spots strongly correlated with the solar activity cycle. SK has observed solar neutrinos for more than 21 years, which covers about two solar activity cycles. Figure 13 shows the SK yearly flux measured throughout the different phases of SK together with the corresponding sun spot number (Source: WDC–SILSO, Royal Observatory of Belgium, Brussels [17]). The $\chi^2$ between observed data and no time dependence hypothesis is calculated with the total experimental uncertainties as $\chi^2 = 21.57/21$ d.o.f., which corresponds to a probability of 41.4%. The SK solar rate measurements are fully consistent with a constant solar neutrino flux emitted by the Sun.

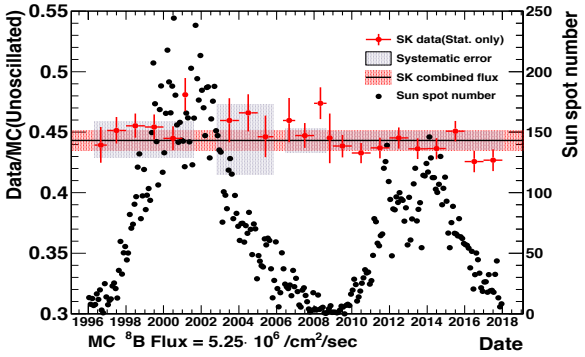


Fig. 13. The ratio of $^8$B solar neutrino flux in SK over the SNO's NC current flux from 1996 to 2018. The red points show the yearly flux measured by SK (statistical uncertainty only), the gray bands show the systematic uncertainties for each SK phase, the black-horizontal line shows the combined measured flux with the uncertainty drawn as the red horizontal band. The back points show the sun spot number provided by [17].

## Energy spectrum analysis

Because of the installation of new front-end electronics for SK-IV [18], the improvements of the water circulation system and the upgrade of calibration methods [19], solar neutrino interactions as well as the background event in multi-MeV regions has been well understood in SK-IV. Owing to these upgrades above, SK has achieved the lowest background (induced by radioisotopes in pure water, especially $^{214}$Bi) among all SK phases [20]. Finally, the energy threshold in SK-IV have been lowered at 3.5 MeV in recoil energy kinetic energy (SK-I: 4.5 MeV, SK-III: 4.0 MeV) and this enables SK to measure the solar neutrino energy spectrum with high sensitivity. In addition, on May 2015, the trigger threshold was changed from 34 observed PMT signals within 200 nsec to 31 hits [21, 22]. Because of this lower threshold, the detection efficiency between 3.5 MeV and 4.0 MeV was improved from $\sim$86% to $\sim$100%. This improvement leads the further reduction of the statistics uncertainty below 5 MeV in SK-IV.

In this analysis, we further improved energy reconstruction method with an improved correction for the detector time variation. For low-energy events in SK, their energy is reconstructed based on number of PMT hits. The gains of PMTs have been gradually increasing at a rate of 1-2%/year and causing time-dependent bias to the reconstructed energies. The new energy reconstruction method for low-energy events also corrects for this gain increase effect. Figure 14 shows the effective number of hits after gain correction for decay-electrons from stopped cosmic muons as a function of time.

The time variation of energy scale is well corrected with the new method and is within ±0.5%.

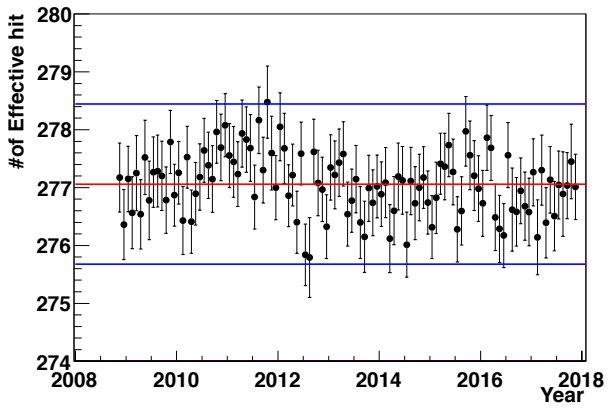


Fig. 14. Time variation of averaged effective number of hits after gain correction for decay-electrons from stopped cosmic muons. Black points show the data with statistical uncertainties. The horizontal red line shows the average for the entire SK-IV period and the blue lines show the ±0.5% range.

Figure 15 shows the energy spectrum obtained among all SK phases, its best-fits with polynomial functions and the prediction of the MSW up-turn assuming the current oscillation parameters described in the next section. Figure 16 shows the combined energy spectrum from SK-I to SK-IV with the predictions of the MSW effect assuming the current oscillation parameters described later. Note that all SK phases are combined without regard to energy resolution or systematic uncertainties in Figure 16, but those uncertainties are taken into account in the $\chi^2$ calculation between the data and the prediction. Comparing $\chi^2$ between the data (black) and the predictions (green or blue), the energy spectrum of SK is consistent within $\sim 1\sigma$ with the MSW up-turn for the solar best-fit parameters (green in Figure 18) and marginally consistent within $\sim 2\sigma$ with the MSW up-turn for KamLAND best-fit parameters (blue in Figure 18).

## Oscillation parameter extraction

The oscillation parameters were extracted using the results from SK [2, 14, 15, 13], SNO [16], radiochemical solar neutrino experiments [23, 24, 25] and Borexino [26, 27, 28] as well as the anti-neutrino measurement by KamLAND [29, 30]. Figure 17 shows the allowed parameter region from SK as well as KamLAND data. SK uniquely selects the large mixing angle MSW region by more than $3\sigma$ and SK significantly contributes to the measurement of the solar angle $\theta_{12}$. The SK energy spectrum and day/night data favors a lower $\Delta m^2_{21}$ value than KamLAND's by more than $2\sigma$.

When combining with results from the other solar neutrino experiments, the mixing angle is determined to be $\sin^2\theta_{12} = 0.310 \pm 0.014$ and the mass difference is determined to be $\Delta m^2_{21} = 4.82^{+1.20}_{-0.60} \times 10^{-5}$ eV$^{-2}$ as shown in Figure 18. Adding the KamLAND result, the oscillation parameters are determined as $\sin^2\theta_{12} = 0.310 \pm 0.012$, $\Delta m^2_{21} = 7.49^{+0.19}_{-0.17} \times 10^{-5}$ eV$^2$. These parameters are mostly determined by the solar neutrino oscillation fit and further precise measurements are required in future.

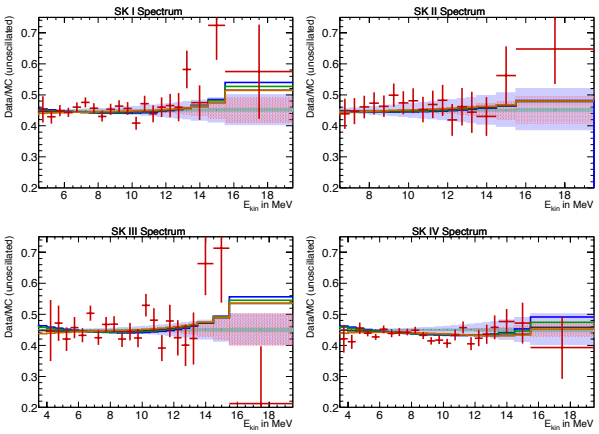


Fig. 15. SK-I, II, III and IV recoil electron spectra divided by the nonoscillated expectation. The green (blue) line represents the best-fit to SK data using the oscillation parameters from the fit to all solar (solar plus KamLAND) data. The orange (black) line is the best-fit to SK data of a general exponential or quadratic (cubic) $P_{ee}$ survival probability. Error bars on the data points give the statistical plus systematic energy-uncorrelated uncertainties while the shaded purple, red, and green histograms give the energy-correlated systematic uncertainties arising from energy scale, energy resolution, and neutrino energy spectrum shift.

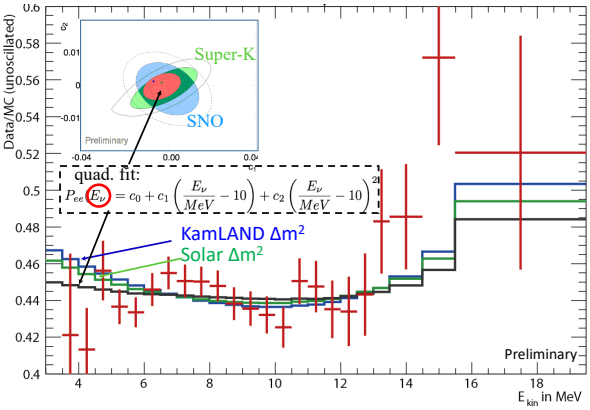


Fig. 16. The energy spectrum combining SK-I through SK-IV as a function of the recoil electron energy. The red points show the ratio of the data to the expected flux using a non-oscillated $^8$B solar neutrino spectrum. The green (blue) curve shows the expected energy spectrum assuming the MSW effect inputting oscillation parameters of solar global (solar plus KamLAND). The black curve is the result of a fit with the quadratic function shown in the inset.

## Search for non-standard interactions

If there are Non-Standard Interactions (NSI) between neutrinos and matter beyond the Standard Model of Particle Physics, they would alter the matter effect. The $^8$B solar neutrino data at Suker-Kamiokande have the potential to constrain the strength of NSI thanks to high matter density at the center of the sun and high data statistics at SK. Such NSI could also flatten or invert the "up-turn", and could provide a better agreement with the observed data.

The effective Hamiltonian for the matter potential for the 2-flavor mass basis can be expressed using effective parameters $\varepsilon_{11}$ and $\varepsilon_{12}$ as

$$H^{eff}_{mat} = \frac{G_F n_e}{\sqrt{2}} \begin{bmatrix} \cos^2\theta_{13} + \varepsilon_{11} & \varepsilon^*_{12} \\ \varepsilon_{12} & -\cos^2\theta_{13} - \varepsilon_{11} \end{bmatrix} \quad (1)$$

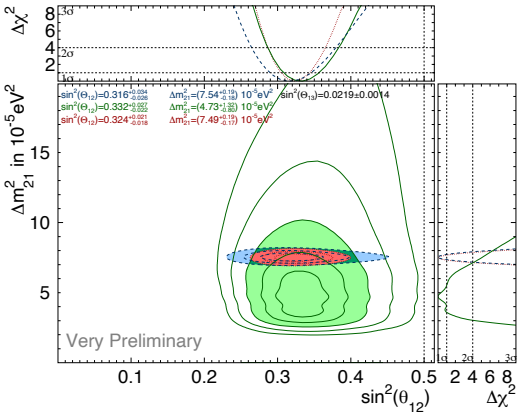


Fig. 17. The allowed contours for $\Delta m^2_{21}$ vs. $\sin^2\theta_{12}$ from the SK combined analysis (green) as well as the allowed region from KamLAND (blue). The combined allowed region is shown in red.

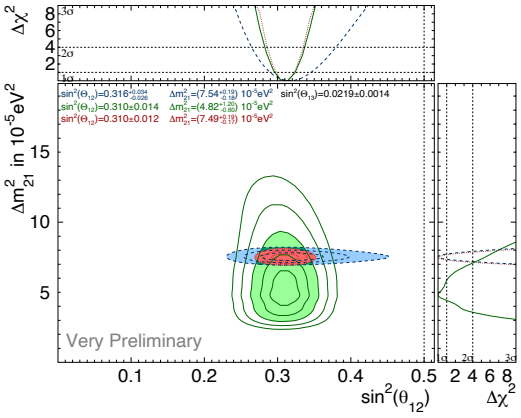


Fig. 18. The allowed contours for $\Delta m^2_{21}$ vs. $\sin^2\theta_{12}$ from all solar neutrino data (green solid line). The allowed contour from KamLAND is also shown in blue. The combined allowed region is shown in red.

where where $G_F$ is the Fermi coupling constant and $n_e$ is the number density of electrons [10].

We tested $\varepsilon_{11}$ and $\varepsilon_{12}$ for $\nu$-up quark interactions and $\nu$-down quark interactions using SK-I, II, III, and IV(1670 days) of data with Day/Night asymmetry and the SNO data. Figure 19 shows the observed spectra with the best fit curves with NSI. The obtained constraints to $\varepsilon_{11}$ and $\varepsilon_{12}$ are shown in Fig. 20.

### Summary

In summary, Super-Kamiokande has precisely measured the $^8$B solar neutrino flux, its time variation and recoil electron spectrum. Using 5,695 days data, more than 93,000 solar neutrino interactions are extracted over the background. SK has

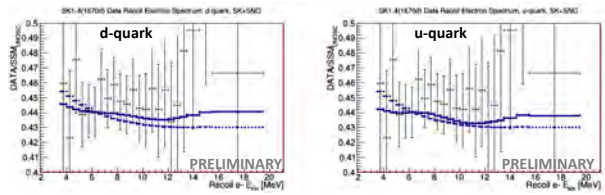


Fig. 19. Observed and best fit solar neutrino survival probabilities. The left panel show the result for $\nu$-down quark interactions while the right panel shows the result for $\nu$-up quark interactions. Solid blue curves shows the best fit with NSI, and the dashed curves show the fit without NSI.

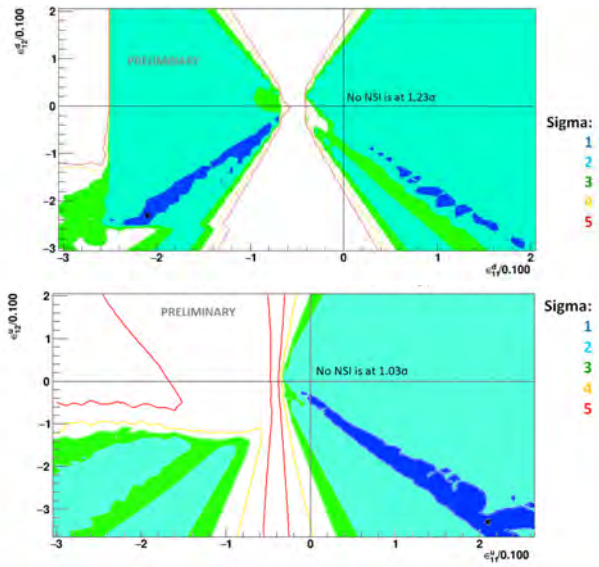


Fig. 20. The confidence intervals in the $\varepsilon_{12}$ vs. $\varepsilon_{11}$ planes for $\nu$-down quark (top panel) $\nu$-up quark (bottom panel) interactions. The best fit points are marked with black stars.

stably measured the solar neutrino flux for more than 21 years. No significant correlation between the observed solar neutrino flux and the sun spot number is found. The measured energy spectrum of $^8$B solar neutrino is consistent within $\sim 1\sigma$ with the MSW up-turn for the solar best-fit parameters and marginally consistent within $\sim 2\sigma$ with the MSW upturn for KamLAND best-fit parameters. In the solar neutrino oscillation analysis combined with the KamLAND result, the oscillation parameters are determined as $\Delta m^2_{21} = 7.49^{+0.19}_{-0.17} \times 10^{-5}$ eV$^2$, $\sin^2\theta_{12} = 0.310 \pm 0.012$. We also tested non-standard interactions with the observed solar neutrino energy spectrum, and obtained constraints to the effective parameters $\varepsilon_{11}$ and $\varepsilon_{12}$ for $\nu$-up quark and $\nu$-down quark interactions.

## Bibliography

[1] John N. Bahcall and Roger K. Ulrich, Rev. mod, Phys. **60**, 297 (1988).

[2] J. Hosaka *et al.*, Phys. Rev. D **73**, 112001 (2006).

[3] Q.R. Ahmad *et al.*, Phys. Rev. Lett. **87**, 071301 (2001).

[4] Y. Fukuda *et al.*, Nucl. Instrum. Meth. A **501**, 418 (2003).

[5] S.P. Mikheyev and A. Y. Smirnov, Sov. Jour. Nucl. Phys. **42**, 913 (1985).

[6] L. Wolfenstein, Phys. Rev. D **17**, 2369 (1978).

[7] P.C. de Holanda and Yu, Smirnov, Phys. Rev. D **69**, 113002 (2004).

[8] P.C. de Holanda and Yu, Smirnov, Phys. Rev. D **83**, 113011 (2011).

[9] V.Barger *et al*., Phys. Rev. Lett. **95**, 211802 (2005).

[10] A. Friedland *et al*., Phys. Rev. B **594**, 347 (2004).

[11] O.G. Miranda *et al*., J. High Energy Phys. **10** 008 (2006)

[12] A. Renshaw *et al*., Phys. Rev. Lett. **112**, 091805 (2014).

[13] K. Abe *et al.*, Phys. Rev. D **94**, 052010 (2016).

[14] J.P. Cravens *et al*., Phys. Rev. D **78**, 032002 (2008).

[15] K. Abe *et al*., Phys. Rev. D **83**, 052010 (2011).

[16] B. Aharmin *et al*., Phys. Rev. C **88**, 025501 (2013).

[17] WDC-SILSO, Royal Observatory of Belgium, Brussels. http://www.sidc.be/silso/datafiles

[18] H. Nishino *et al*., Nucl. Instrum. Meth. A **610**, 710 (2009).

[19] K. Abe *et al*., Nucl. Instrum. Meth. A **737**, 253 (2014).

[20] Y. Nakano, J. Phys. Conf. Ser. **888**, 012191 (2017).

[21] S. Yamada *et al*., IEEE Trans. Nucl. Sci. **57**, 428 (2010).

[22] Y. Nakano, PhD thesis, The Univ. of Tokyo (2016).

[23] R. Davis, Jr., D. S. Harmer, and K. C. Hoffman *et al*., Phys. Rev. Lett. **20**, 1205 (1968).

[24] J.N. Adburashitov *et al*., Phys. Rev. C **80**, 015807 (2009).

[25] M. Altmann *et al*., Phys. Lett. B **616**, 174 (2005).

[26] G. Bellini *et al*., Phys. Rev. Lett. **107**, 141302 (2011).

[27] G. Bellini *et al*., Phys. Rev. D **82**, 033006 (2010).

[28] G. Bellini *et al*., Phys. Rev. Lett. **707**, 051302 (2012).

[29] S. Abe *et al*., Phys. Rev. Lett **100**, 221803 (2008).

[30] A. Gando *et al*., Phys. Rev. D **88**, 033001 (2013).

### *Supernova neutrinos*

In 1987, the observation of supernova 1987a by Kamiokande and IMB etc, opened the neutrino astronomy. This observation confirmed that the energy released by neutrinos is about several$\times 10^{53}$ergs. However, the core collapse supernova (ccSN) mechanism is not yet fully understood. Super-Kamiokande (SK) would be able to detect several thousand neutrino events if a ccSN happened near the center of our galaxy. Such an observation would enable us to investigate in detail the mechanics of the ccSN explosion.

On average, 1-2 ccSNe per century are expected in our galaxy and therefore we must be prepared for these events. An online program called SNWATCH searches for time clustered events [1]. Events with total energy greater than 7 MeV and vertex position within the 22.5-kton fiducial volume in SK are selected. Cosmic ray muons and their subsequent decay electron events are removed. For each selected event, a 20-second time window is opened backwards in time, and the number of selected events in the window, $N_{clus}$, is counted. A variable $D$ that identifies the dimension of the vertex distribution is computed. It is an integer number from 0 to 3, corresponding to point-, line-, plane- and volume-like distributions, respectively.

When $N_{clus} \geq 60$ and $D = 3$ a prompt SN warning is generated including an automatic phone-calling and emails to experts. Then, the experts check whether it is a real supernova signal or not by looking at various plots which are uploaded to a secured site accessible from the Internet. These alarms are usually due to the accidental coincidence of two cosmic ray induced clusters. We have supernova drills several times per year. So far, no real supernova neutrino burst signal has been observed at SK.

In a drill, the SNWATCH conveners and the executive committee members meet via TV conference system, and discuss to make a decision for a prompt announcement (within 1 hour) to outside researchers and the press. We practice this drill as if a real supernova happened. We also have SK shift training by illuminating an LD in the SK detector a few times every month. SK shift members are notified by a dummy alarm that SNWATCH makes when the LD is illuminated. The shift members then cal l to the SNWATCH experts and give a report. The SK collaborators will be ready for the real supernovae through the drill and the training.

For a single SN far from our galaxy, the neutrino flux is not large enough to be detected at SK. However, there is about one ccSN in the universe every second which creates a copious and isotropic neutrino flux. Supernova Relic Neutrinos (SRN) are this diffuse supernova neutrino background from all the past ccSNe in the universe. This signal has never been detected, but it is expected to be detectable in the 16-30 MeV energy region, which is the gap between the energy ranges of solar neutrinos and atmospheric neutrinos. Our published result [2] utilizes SK-I, II and SK-III data with analysis energy threshold of 16 MeV. A maximum likelihood search was performed in multiple regions of the Cherenkov angle distribution to extract the most accurate flux limit. The obtained flux limit is between 2.7 and 3.0 $\bar{\nu} cm^{-2} s^{-1}$ (positron energy $>$ 16 MeV), which in fact depends on the shape of the neutrino spectrum assumed. This result currently provides the world's best limit

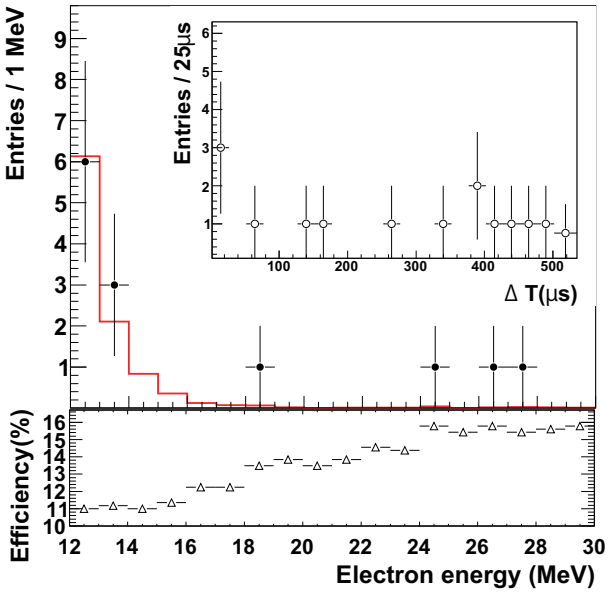


Fig. 21. Energy spectrum of prompt signals (points). The red histogram shows the expected accidental background. The plot embedded in the upper right shows the timing difference for the delayed candidates. The bottom figure shows the detection efficiency of SRN for each energy bin; the jumps at 18 MeV and 24 MeV are due to energy-dependent spallation cuts. Errors are statistical only.

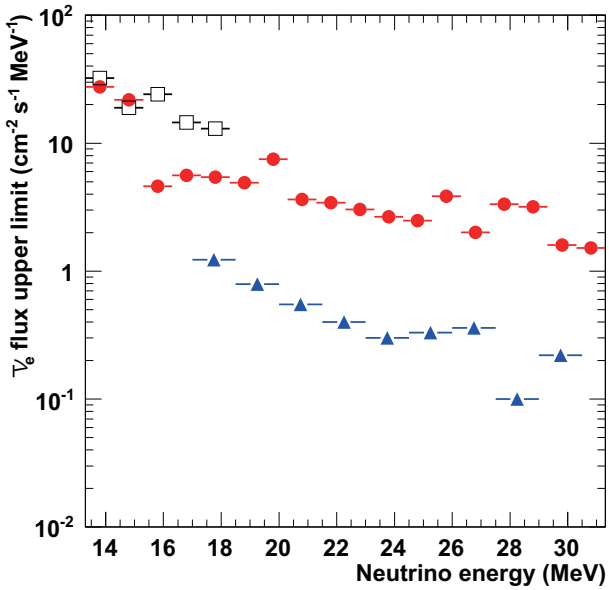


Fig. 22. Model-independent SRN 90% C.L. upper limits as a function of neutrino energy for SK-IV (solid circle). For comparison, both KamLAND result (open square) and previous SK result (solid triangle) are also shown.


Fig. 23. In the new cavern, the 200-ton tank (a) with currently 240 photomultipliers installed, the Gd pre-mixing and pre-treatment 15-ton tank (b), the selective filtration system (d), Gd removal resins (c) for test and a device to measure the water transparency (e) have been installed.

on SRN flux. (Figure 22).

In SK-IV, a new result of the SRN search using the neutron tagging technique was also published [3]. In this analysis, neutrons from inverse beta decay (IBD) reactions ($\bar{\nu}_e, p \rightarrow e^+, n$) are captured on hydrogen. After a neutron is captured, a single 2.2 MeV gamma is emitted. Thus, by detecting the prompt positron signal and the delayed 2.2 MeV gamma signal, we can reduce backgrounds, most of which are not accompanied by neutrons.

Figure 21 shows the energy spectrum of prompt signal, the time difference between a prompt signal and a delayed signal, and the detection efficiency of SRN for each energy bin. Figure 22 shows the obtained flux limit comparing with other results. The neutron detection efficiency is very low because of the low energy of the gamma from the neutron capture on hydrogen (to compare the 2.2 MeV gamma with the analysis kinetic energy threshold for solar neutrino of 3.5 MeV). However, we with this method we could obtain the world best limit below 16 MeV. This result shows a high potential of neutron tagging techniques, which can be a strong tool for SRN detection.

## Bibliography

[1] Abe, K. et al., Astropart. Phys. 81, 39 (2016)

[2] K.Bays et al., Phys. Rev. D 85, 052007 (2012)

[3] H.Zhang et al., Astropart. Phys. 60, 41 (2015)

### *EGADS: From R&D for the gadolinium project to standalone Supernova monitor*

As mentioned above, although at SK a few SRN events a year are expected, SRNs have not been detected yet because of the large backgrounds that constrain our search. The main goal of our research is to reduce these backgrounds and be able to detect SRNs. The observation of SRNs in general or neutrinos from distant supernovae in particular, would give us some information about the universe, for example the core collapse rate from SRNs, and about the neutrino itself too, for example its lifetime.

As shown in the previous section, the current SK detector can only detect positrons efficiently but not neutrons. In order to achieve a high detection efficiency for neutrons, it is proposed to add 0.2% of gadolinium (Gd) sulfate by mass into SK. Since Gd has a neutron capture cross section of 49.000 barns (about 5 orders of magnitude larger than that of protons) and emits a gamma cascade of 8 MeV, neutrons could be easily detected at SK (in space, vertices within tens of cm

and in time, with the neutron capture delayed about 20 $\mu$sec).

EGADS (Evaluating Gadolinium's Action on Detector Systems) project was funded in 2009. The main motivation of EGADS is to show that by adding Gd, SK will be able to detect anti-neutrinos using the delayed coincidence technique, while keeping all its capabilities in the other analyses like solar and atmospheric neutrinos. Since then, a new hall near the SK detector has been excavated and a 200-ton tank with its ancillary equipment has been installed, see Fig.23, to mimic the conditions at SK. The selective water filtration system filters out water impurities while keeping the Gd in the water.

From January 2010 to July 2011 we circulated pure water through the 200-ton tank and proved that our water system is stable and achieves a high water quality. In 2013, from February 6th to April 20th, the 200-ton tank has been stepwise loaded with Gd sulfate until the final 0.2% concentration was reached. Two values are monitored at three different depths: the Cherenkov light left after travelling 15 m (LL15) in water and the Gd concentration. Both values confirmed that we can achieve and maintain a good water quality and that Gd sulfate homogeneously and quickly dissolves in the 200-ton tank.

In summer 2013, we installed 240 photomultipliers and the data taking started from September without Gd and with a DAQ based on old SK ATM modules. In April 2015, the target concentration of 0.2% $Gd_2(SO_4)_3$ was achieved. Figure 24 shows the time variation of LL15. The blue band in the figure shows typical values for SK-III and SK-IV. As shown in the figure, the transparency of 0.2% $Gd_2(SO_4)_3$ water is within the SK range. In addition to the good water transparency, no Gd loss has been detected since the EGADS detector reached the final concentration until it was emptied again after about 2 years and 5 months, in October 2017

Detailed studies have evaluated the impact on current analyses at SK. These studies show that current analyses will be basically unharmed after adding Gd in SK and all other tests and studies conducted have shown no showstoppers. As a consequence, the SK collaboration decided in spring 2015 to approve the SuperK-Gd project. The SK tank has been opened for refurbishment work from last year (2018) April 1st.

In order to test the future Gd-loading in SK, forseen for 2020, the detector was refilled with pure-water in November 2017, and loaded with 0.02% $Gd_2(SO_4)_3$ in the end of March 2018. This loading was performed using only the pretreatment and the fast recirculation systems, with one pass, similar to what is expected for SK 0.02% loading.

Since then, different configurations of the water system have been tested in order to determine the water system needed to ensure high water transparency in SK in case the band-pass system could not be installed in time. Figure 25 shows the time variation of LL15 since this loading until the power cut of May 2019. With the fast recirculation system only, from March 2018 to June 2018 a slow but continous decreased of the water transparency has been observed. From June 2018 to August 2018 the use of the band-pass system allowed to recover high water transparency. There-after the fast-recirculation system only has been used.

A special cation exchange resin, developed to keep Gd in the water while removing other cations, has been installed, in addition to the usual anion exchange resin, in January-February 2019 (in January, the new cation exchange resin was used alone, leading a water transparency drop). Preliminary results indicate an improvement of the water transparency compared than with only anion exchange resin. This increase was enhanced following the replacement of the TOC and UV lamps in March 2019, which stressed the importance of the ionisation lamps for the water transparency. This study is still on-going.

In June 2017, EGADS electronics has been upgraded from the ATM electronics to SK's QBee electronics, the DAQ system was also upgraded to use these new electronics. Thanks to this upgrade, the stability of the DAQ has been greatly improved, specially at high rate. Several SN tests were performed, and demonstrated that EGADS is able to detect and process a 10 second long burst of more than 100k Hz without trouble. This is much more than what is expected from a very close galactic SN burst: in case of Betelgeuse, about 25k events are expected according to Nakazato's model.

We developed an online fitter, HEIMDALL, based on SK WIT. It is able to reconstruct all the events online during a SN burst and then provides an alarm within few seconds. HEIMDALL is looking for IBD candidates, therefore taking advantage of the delayed coincidence to reduce the background. Thanks to this, EGADS is able to look for SN in the far end of our galaxy. This enables us to instantly and autonomously detect a galactic SN and report to local experts and neutrino and astronomy community. This system was running during the SK refurbishment work last year.

### *Tank Open Work 2018-2019*

From May 31 to January 29, 2018, the tank open work to upgrade the Super-Kamiokande (SK) detector was performed after 12 years of continuous operations, Figure 26 shows a photo of the tank on August 18, 2018.

There were five main tasks:

1. Fix a small water leak in the Super-K tank.
2. Clean any rust and other dirt that has accumulated in the detector since its original completion in 1996.
3. Install additional water piping to increase the total water flow for increased water purification, and to enable better control of the flow direction in the tank.
4. Replace the photomultiplier tubes (PMTs) that have failed (a few hundred out of 13,000) since the previous in-tank refurbishment in 2006.
5. Maintenance of detector calibration devices.

### *Leak fixing in the SK tank*

A so-called "floating floor" was used to work at the walls of the detector. During this phase of the refurbishment effort we drained two meters of water from the tank every three days, and worked to seal potential water leakage points on the outer wall, as well as replace those failed PMTs that we could reach from the floor. The Super-K tank is 40 m in diameter and 42 m in height and contains 50,000 tons of pure water. Its sides form an icosagon comprised of 400 pieces of 4 mm thick

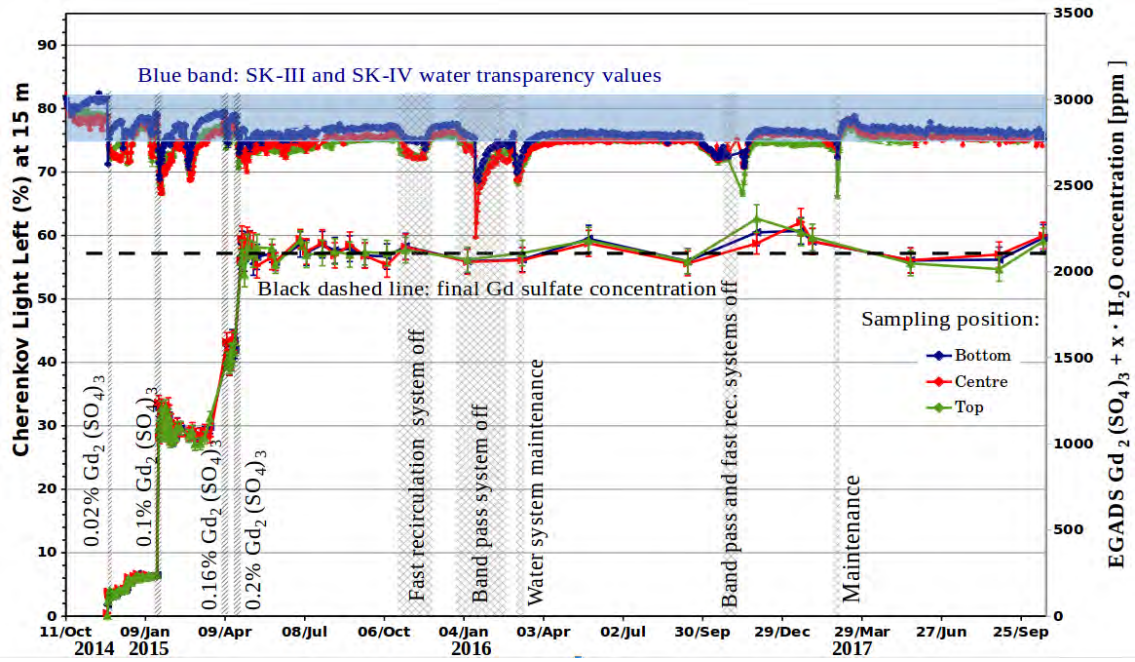


Fig. 24. Cherenkov light left at 15 m for Gd loaded water in EGADS until September 2017. The horizontal blue band are the typical values for SK-III and SK-IV. The vertical lines shows the injection dates where we also indicate the concentration (% in mass) in the 200-ton tank. The black dashed line shows the final expected concentration.

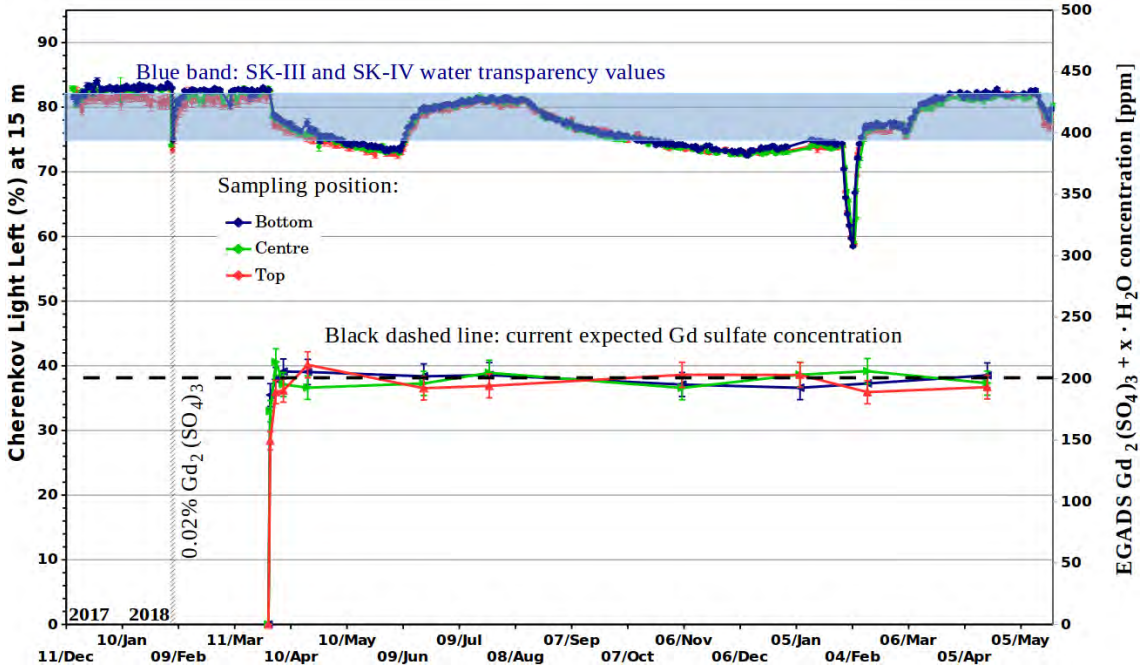


Fig. 25. Cherenkov light left at 15 m for Gd loaded water in EGADS since December 2017. The horizontal blue band are the typical values for SK-III and SK-IV. The vertical lines shows the injection dates where we also indicate the concentration (% in mass) in the 200-ton tank. The black dashed line shows the final expected concentration.

stainless steel plates, each 4 m wide and 2 m tall. The bottom also consists of an assembly of stainless steel plates. The total submerged surface area is more than 6,000 $m^2$ and the total length of welding lines is more than 6.2 km. More than 3,200 bolts penetrate the sides. Because of this complexity, a small amount of water leaked from the SK tank, which we could not fix for a long time. This is not serious as long as we use only pure water. Although there is no official regulation regarding Gd-loaded water, it is necessary to stop the SK water leak to avoid release even in the case of a large earthquake.

To achieve a reliable fix, Super-K colleagues have developed a special sealant material. It needed to be soft, flexible,

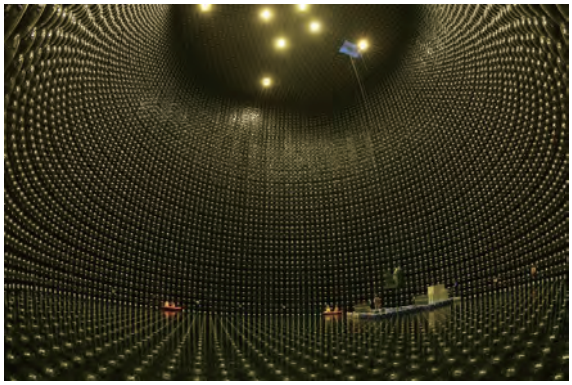

Fig. 26. Working inside the Super-Kamiokande tank on August 18, 2018.

Fig. 27. Sealant work on the SK tank wall being conducted from the floating floor.

and able to withstand external stretching forces. It had to meet requirements regarding small elution into water, low natural radioactivity, long-time stability during water exposure, and sufficient attachment strength to stainless steel plates.

Figure 27 shows the actual sealant work. Workers put thick tape along both sides of the welding line to hold the sealant material on the line. They used trowels and paintbrushes to spread the sealant material over the weld with the same thickness as the surrounding tape. A double layer of sealant was required to allow for unexpected gaps or pinholes in one of the two layers.

### *Cleaning and rust removal*

The dirty wall and structures inside the Super-K tank required a large amount of person power to clean up. In particular, the top and outermost structures were covered by a heavy residue of exhaust gas and dust left over from when we constructed the detector in 1991-1996. We also aimed to remove the most potential sources of rust during the cleaning work. As for tools, it was dangerous to choose arbitrary ones since most of them leave other types of dust which may then degrade the water after restarting operation of Super-K. The water team tried, investigated, combined, and developed many kinds of tools.

We maintained excellent quality of sealant attachment and removed a large amount of radioactivity; at least 100 Bq of radium was removed during the cleanup according to a measurement by a germanium detector. As the radon gas emitted from this radium is comparable to that arising from the PMTs themselves, the in-tank shiftworkers contributed to lowering the background for future solar neutrino observations.

### *Water system upgrade*

The SK water system, including in-tank piping, was upgraded during the tank open period. The water purification system was originally designed with a supply of 30 $m^3$/h and circulation of 60 $m^3$/h, and the piping inside the tank was made without separate lines for the inner detector (ID) and the outer detector (OD). This time, we decided to improve the water flow in the tank by separating not only the pipes of the inner volume and the outer volume, but also the pipes on the side, top, and bottom of the outer volume so that all the flow rates can be adjusted independently. Up until now the effective detector volume for the solar neutrino analysis has been limited by the inflow of radon background, but this plumbing improvement makes it possible to control and optimize the flow of water in the tank.

We started water filling on October 13, 2018. Previous water fills have taken place at a rate of 30 $m^3$/h using the original SK water purification system; this took 2.5 months to fill the tank. Since the water that had been fed to the tank was never circulated and repurified until after the tank became full, it took another two months or so after the tank was full before the water quality improved to the point that useful data could be collected. This time, as shown in Figure 28, the new SK-Gd water system is to be temporarily operated as an ordinary water purification/recirculation system by installing conventional ion exchange resins made for producing ultrapure water into the modules in the system. Water filling was stopped in the middle of December for the remaining work in the top region of the tank. After the final work, water filling was restarted in January, 2019 and completed on January 29. The water transparency was measured as soon as data taking started and confirmed that the transparency was actually good and similar to that of the end of SK-4.

### *PMT exchange and other work*

During this tank open period, in parallel with sealing work, the exchange of dead PMTs was also done. In total, 136 ID PMTs and 224 OD PMTs were exchanged.

For ID PMT replacement, new PMTs under development for Hyper-Kamiokande (HK) were used. In addition to the recovery of SK performance, another purpose of this exchange is to check the performance and long term stability of HK PMTs under the expected actual operating environment. Similarly to other SK ID PMTs, anti-implosion covers made of fibre-reinforced plastic (FRP) and acrylic were attached to these PMTs by shift workers. The exchange of ID and OD PMTs (Figure 29), including cable connections inside the tank

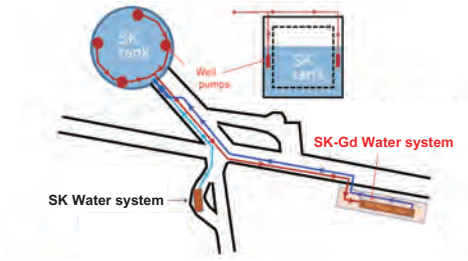


Fig. 28. New filling with circulation system using the SK-Gd system.

and the following signal checks, was also performed by shift workers with a well coordinated time schedule to avoid interference with the sealant work. Another important task carried out during the tank open work is related to the calibration system inside the tank and studies for more precise detector understanding, such as replacement of laser injectors and optical fibers, installation of a new light injection system, precise magnetic field mapping, and recording all PMTs' dynode directions. The installation work of the white Tyvek sheet that covers the OD region for high light detection efficiency was also a significant job. With much effort by many workers, all the sheets covering the tank wall were removed for the sealant work and re-installed afterwards (Figure 30).

Fig. 29. Exchange work of the ID (top two panels) and OD (bottom two panels) PMTs.

### *Water leak check*

After filling the tank completely with pure water, a water leakage measurement was conducted. The method monitors the water level to 0.1 mm precision while water circulation is stopped. The water circulation system was stopped between 11:30 on January 31, and 15:52 on February 7, 2019; the total measurement time was 7 days, 4 hours, 22 minutes. Over this period, we could not see any decrease of the water level.

Fig. 30. OD Tyvek installation work.

Therefore, we did not observe any water leakage from the SK tank within the precision of our measurement, which is less than 0.017 tonne per day. When the same measurement was performed one year ago, the water level decreased at a rate of $\sim$3 mm per day, corresponding to a leak rate of $\sim$4 tonne per day. As a result, we have concluded that the current SK water leakage has been reduced to less than 1/200 of the rate during the period before the tank upgrade work.

## T2K EXPERIMENT

[Spokesperson : Atsuko Ichikawa] Kyoto University

The Tokai to Kamioka (T2K) experiment [1] is a long baseline neutrino oscillation experiment: a man-made beam of neutrinos is used to do precise studies of the oscillations of neutrinos. Accelerated protons are used to produce the neutrinos in the J-PARC center in the Ibaraki prefecture, which then travel 295 km to reach the Super-Kamiokande (Super-K) detector in the Gifu prefecture where they can be detected after oscillations. A complex of near detectors located 280 meters away from the proton target is used to monitor the neutrino beam, and constrain systematic uncertainties on the neutrino fluxes and interactions. T2K was the first long baseline experiment to use the off-axis beam technique [2]: the beam is not aimed directly at Super-K, but in a direction making a 2.5° angle with the far detector direction. This gives increased sensitivity to neutrino oscillations while reducing the backgrounds by producing a narrow band neutrino beam centered on the energy corresponding to the first maximum of the $\nu_\mu \rightarrow \nu_e$ oscillation probability.

T2K realized the first observation of the appearance of a flavor of neutrinos through oscillation by detecting electron neutrinos in a beam of neutrinos produced in the muon flavor [3]. After achieving this milestone, the experiment has been using its ability to produce a beam of either neutrinos or anti-neutrinos to compare the oscillations of neutrinos and their antiparticles. This allows to study the main remaining open questions in neutrino oscillations (CP symmetry and or-

dering of the neutrino mass states) by looking at the differences between the oscillations $\nu_\mu \to \nu_e$ and $\bar{\nu}_\mu \to \bar{\nu}_e$. At the same time, T2K's physics goals include the precise measurement of the neutrino oscillation parameters $\theta_{23}$ and $\Delta m^2_{32}$ through a precise study of the pattern of disappearance of the muon neutrinos in conjunction with the data used to study the oscillation to the electron flavor. The experiment additionally performs searches for physics beyond the standard model, such as oscillations due to sterile neutrinos and CPT violation. Finally, the near detectors are used to perform a wide range of neutrino and anti-neutrino cross-section measurements.

In J-PARC, protons are accelerated to 30 GeV by a series of three accelerators, and hit a 1.9 interaction-length graphite target. The collisions produce hadrons, in particular charged pions and kaons, which are focused by three electromagnetic horns. The hadrons then go through a 96m long decay tunnel where they decay in flight into neutrinos. A beam dump at the end of the decay tunnel stops the remaining hadrons, while high energy muons (5 GeV/c or higher) can pass through this beam dump and are measured to provide a first, indirect monitoring of the neutrino beam. The horns can be used either with a positive current ($\nu$-mode), in which case the beam is mainly made of $\nu_\mu$, or with a negative current ($\bar{\nu}$-mode) which gives a mainly $\bar{\nu}_\mu$ beam.

The near detectors are separated into two groups. On the axis of the beam, the INGRID detector, made of fourteen identical modules is used to monitor the beam direction and rate stabilities. Each module is made of an succession of iron plates to provide large target mass ( 7.1 tons per module) alternating with scintillator planes for detection. Using the number of events reconstructed in each module, the beam direction can be measured daily with better than 0.4 mrad accuracy. Located in the direction of Super-K, the off-axis detector ND280 is made of several detectors located inside a 0.2T magnet. The higher precision of those off-axis detectors allow to do more detailed measurements of the unoscillated neutrino beam. In neutrino oscillation analyses, the ND280 is used to provide information on the $\nu_\mu$ and $\bar{\nu}_\mu$ unoscillated spectra directed at SK, constrain the dominant backgrounds, and constrain the combination of flux and interaction cross sections.

The far detector, Super-K, is a 50 kton water Cherenkov detector, shielded from atmospheric muons by 1000 m of rock, or 2700 meters-water-equivalent (m.w.e.) mean overburden. To select events corresponding to the T2K beam, Super-K is synchronized via GPS to the J-PARC beamline. Hit information within $\pm 500 \mu s$ from the beam arrival timing are used for T2K data analysis. Events where only one ring was reconstructed (corresponding to one charged particle above Cherenkov threshold) are used in oscillation analysis. Those events are separated into muon-like and electron-like events based on the light pattern of this ring, and additional selection cuts are applied to produce samples enriched in certain interaction modes.

To study neutrino oscillations, the data observed at the far detector are compared to the predictions of the three-flavor oscillation model for different values of the oscillation parameters. To this end, a model of the experiment is constructed: the fluxes of the different flavors of neutrinos reaching the detectors are predicted by a series of simulations, and the interactions of $\nu$ and $\bar{\nu}$ in the detectors are simulated using the NEUT Monte Carlo event generator [7]. First, the flux and properties of the proton beam reaching the target are measured by the proton beam line monitors. Interactions of the protons in the graphite target and production of secondary hadrons are then simulated using the FLUKA package [4]. Measurements from hadron production experiments, in particular NA61/SHINE [5], are used to tune this part of the simulation and the out-of-target interactions. The propagation and decay in flight of the hadrons in the decay tunnel are then simulated using the GEANT3 and GCALOR [6] packages. The predictions from this model are compared to the data observed in the near detectors to tune the predictions for the far detector by constraining the model parameters. The result of this near detector fit provides the initial values and uncertainties of the flux and interaction model parameters used in the far detector analysis to measure parameters describing neutrino oscillations.

Table 4. T2K data taking periods and integrated numbers of protons on target (POT) used in the far detector analysis.

| Run Period | Dates | $\times 10^{20}$ POT $\nu$ | $\bar{\nu}$ |
|---|---|---|---|
| Run 1 | Jan.2010 - Jun.2010 | 0.32 | – |
| Run 2 | Nov.2010 - Mar.2011 | 1.11 | – |
| Run 3 | Mar.2012 - Jun.2012 | 1.60 | – |
| Run 4 | Oct.2012 - May.2013 | 3.60 | – |
| Run 5 | May.2014 - Jun.2014 | 0.24 | 0.51 |
| Run 6 | Oct.2014 - Jun.2015 | 0.19 | 3.55 |
| Run 7 | Feb.2016 - May.2016 | 0.48 | 3.50 |
| Run 8 | Oct.2016 - Apr.2017 | 7.17 | – |
| Run 9 | Oct.2017 - May.2018 | 0.20 | 8.79 |
| **Total** | **Jan.2010 - May.2018** | **14.94** | **16.35** |

T2K started collecting physics data in January 2010, and has now completed its 9th run, accumulating a total of $1.51 \times 10^{21}$ protons on target (POT) in $\nu$-mode and $1.65 \times 10^{21}$ POT in $\bar{\nu}$-mode. The details of the data used in the far detector analysis (slightly lower due to data quality cuts) can be found in table 4. Over this period, the event rates and the beam direction were found to be consistent with the expectations and stable by the measurements of the muon monitor and the on-axis near detector. In particular, the beam direction remained stable well within the $\pm$1mrad target. During run 9, stable operation at 485 kW was achieved, and operation at more than 500 kW was successfully demonstrated.

### *Search for CP violation in Neutrino and Antineutrino Oscillations by the T2K experiment with 2.2$\times 10^{21}$ protons on target*

T2K published new neutrino oscillation results using data collected from January 2010 to May 2017 (corresponding to Run 1 to 8 on table 4) [10]. The data sets include a beam exposure of $14.7 \times 10^{20}$ POT in neutrino mode and $7.6 \times 10^{20}$ POT in antineutrino mode for the far-detector (SK) analysis and an exposure of $5.8 \times 10^{20}$ POT in neutrino mode and $3.9 \times 10^{20}$ POT in antineutrino mode for the near-detector (ND280) anal-

ysis. T2K has previously reported that the CP conservation hypothesis ($\delta_{CP} = 0, \pi$) is excluded at 90% C.L. using the data collected up to May 2016 [8, 9]. Since then, the neutrino mode data set has doubled, and the electron neutrino and antineutrino event selection efficiencies have increased by 30% and 20%, respectively, improving the ability of the experiment to study CP symmetry in neutrino oscillations. A significant improvement compared to previous T2K publications comes from the use of a new Cherenkov-ring reconstruction algorithm, previously used only for neutral current (NC) $\pi^0$ background suppression, and optimized event selection criteria. As a result, the acceptance for signal events in the muon-like samples (corresponding to charged current quasi-elastic (CCQE) interactions) increased by 15% with a 50% reduction of the main neutral current background (NC1$\pi^+$). The charged current events acceptance also increased by 20% for the nominal (CCQE-like) electron-like samples with similar purity to previous analyses. Finally, the acceptance of signal events increased by 33% with a 70% reduction in background caused by particle mis-identification for the electron-like sample enriched in resonant interactions (CC1$\pi^+$).

A particular effort was done to improve the neutrino interaction uncertainty model, and to understand the possible biases in the oscillation measurements coming from those uncertainties. The multi-nucleon contribution to CCQE-like events is of particular importance in T2K, as it leads to a bias in the neutrino reconstructed energy used to measure the parameters describing neutrino oscillations. Additional systematic parameters describing different uncertainties on those multi-nucleon processes, as well as parameters designed to cover the theoretical uncertainty in the transferred momentum dependence of the random phase approximation (RPA) corrections to the CCQE interaction model were added to the analysis. Some systematic uncertainties are not easily implemented by varying model parameters. A new procedure, "simulated data" studies, was used to study their impact on the oscillation measurements: data generated from a variant model are analyzed under the assumptions of the default model, and the results obtained with both models are compared to estimate the potential bias coming from this model uncertainty. Fits to these simulated data sets showed no significant biases in the parameter measuring CP asymmetry in neutrino oscillation , $\delta_{CP}$. However, biases in some of the other parameters describing the oscillations ($\Delta m^2_{32}$ and $\sin^2\theta_{23}$) were seen, and additional uncertainties were added in the fits to take those into account.

The fit of the run 1-8 data yielded best-fit values and $1\sigma$ errors for $\sin^2\theta_{23}$ and $\Delta m^2$ of $0.526^{+0.032}_{-0.036}$ $(0.530^{+0.030}_{-0.034})$ and $2.463^{+0.071}_{-0.070}\times10^{-3}(2.432\pm0.070\times10^{-3})$ eV$^2/c^4$ respectively for normal (inverted) ordering. The result is consistent with maximal disappearance and the posterior probability for $\theta_{23}$ to be in the second octant ($\sin^2\theta_{23} > 0.5$) is 78%. The $\Delta m^2$ value is consistent with the Daya Bay reactor measurement [11]. The measurement of $\sin^2 2\theta_{13}$ using only T2K data was found to agree well with the results of the reactor experiments.

Confidence intervals for $\delta_{CP}$ were calculated using the Feldman–Cousins method [12] from a fit using the result of the reactor measurement as a prior for $\sin^2 2\theta_{13}$. The best fit

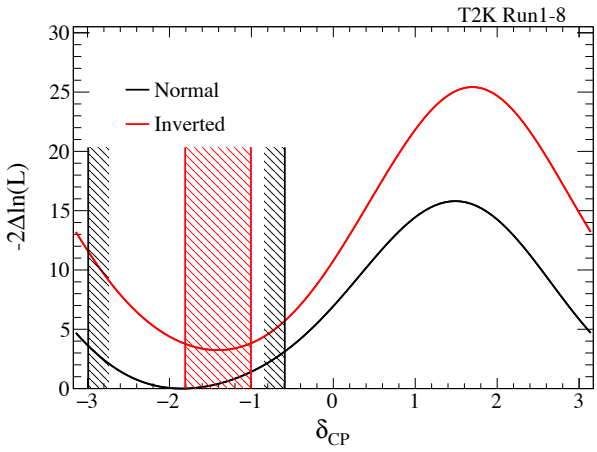


Fig. 31. Results of the fit of T2K run 1-8 data for $\delta_{CP}$ assuming normal (black) and inverted (red) mass ordering, using the reactor measurement prior on $\sin^2(2\theta_{13})$. The vertical lines show the corresponding allowed $2\sigma$ confidence intervals, calculated using the Feldman-Cousins method.

value is $\delta_{CP} = -1.87(-1.43)$ for the normal (inverted) ordering, which is close to maximal *CP* violation (Fig. 31). The $\delta_{CP}$ confidence intervals at $2\sigma$ (95.45%) are $(-2.99, -0.59)$ for normal ordering and $(-1.81, -1.01)$ for inverted ordering. Both intervals exclude the *CP*-conserving values of 0 and $\pi$, meaning that the significance of the exclusion of the conservation of CP symmetry in neutrino oscillations has increased from the 90% CL level previously reported to the $2\sigma$ level. Concerning the mass hierarchy, the normal ordering is preferred with a posterior probability of 87%.

### *Search for light sterile neutrinos with the T2K far detector Super-Kamiokande at a baseline of 295 km*

The data from most experiments studying neutrino oscillations are consistent with the three flavor paradigm where the three weakly interacting neutrino flavors are related to three neutrino mass states by the Pontecorvo-Maki-Nakagawa-Sakata mixing matrix. However, deviations from the three flavor scheme have been reported, and could be explained by a fourth neutrino state with a mass difference $\Delta m^2 \sim 1$ eV$^2$/c$^4$ with respect to the three Pontecorvo-Maki-Nakagawa-Sakata states [13, 14, 15]. While T2K is designed for studying standard three flavor oscillation at $\Delta m^2 \sim 10^{-3}$ eV$^2$/c$^4$, it also has the potential to search for oscillation signatures due to sterile neutrinos around this $\Delta m^2$ range. T2K performed a long-baseline search for sterile neutrinos in the "3 + 1" framework using the run 1 to 8 data [16].

Neutral-current (NC) neutrino interactions are also collected at the far detector. These events have previously only been used in publications for systematic uncertainties [10] and cross-section studies [17], but they can also be used to enhance the sensitivity to sterile mixing as the sterile neutrinos, unlike other active neutrinos, do not interact through CC or NC scattering. In this analysis, NC$\pi^0$ and NC $\gamma$-deexcitation samples are used in the oscillation fit to enhance the sensitivity to sterile mixing parameters. The NC$\pi^0$ samples select neutrino events with single $\pi^0$ production, where $\pi^0 \to 2\gamma$ decay produces two visible Cherenkov rings in the detector. The

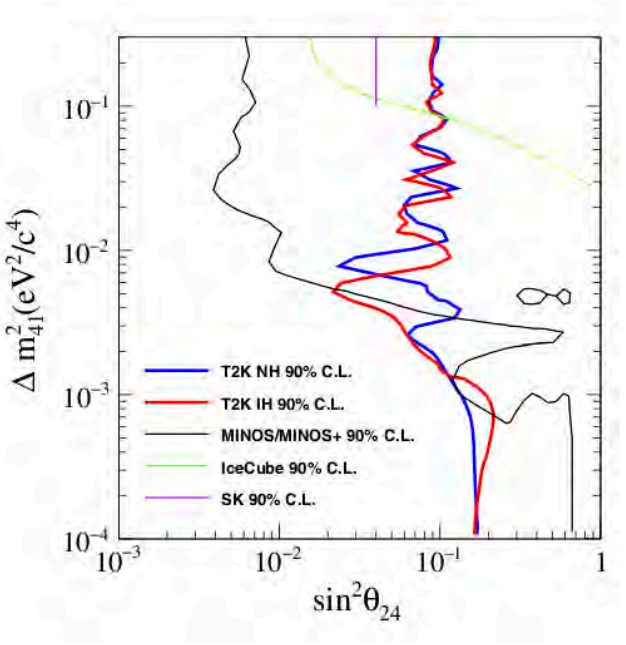


Fig. 32. The T2K 90% exclusion limits on $\sin^2\theta_{24}$ as a function of $\Delta m^2_{41}$, with results from other experiments [18, 19, 20]. The areas on the right are excluded.

NC $\gamma$-deexcitation sample targets NC quasi-elastic events in which $\gamma$ rays are emitted from residual nucleus deexcitation and when knocked-out nucleons interact with other nuclei in water. The overall analysis strategy is similar to that used in the standard T2K three flavor analysis, but with the addition of the three NC samples described previously to the 5 CC samples used in the standard analysis.

We considered the parameter space of $\Delta m^2_{41} > \Delta m^2_{21}$ which is most sensitive in T2K. The "3 + 1" best fit differs from the standard three flavor best fit by $\Delta\chi^2 = 1.0$ (4.7) assuming normal (inverted) mass hierarchy. From 2500 sets of MC studies with statistical fluctuations, this level of disagreement is expected with the standard three flavor hypothesis in 50% (30%) of the studies. Fig. 32 shows the T2K 90% exclusion limits in the ($\sin^2\theta_{24}$, $\Delta m^2_{41}$) plane together with results from other experiments, where we can see that T2K has set the most stringent limit on $\sin^2\theta_{24}$ for $\Delta m^2_{41} < 3\times10^{-3}$ eV$^2$/c$^4$. The NC samples allow us to constrain $\theta_{34}$ in conjunction with $\theta_{24}$. Because these samples have low statistics and large cross-section uncertainties, the sensitivity is limited, but our results are consistent with other measurements. We constrain $\sin^2\theta_{24} < 0.1$ and $|U_{\tau4}|^2 = \cos^2\theta_{24}\sin^2\theta_{34} < 0.5$ at 90% C.L if $\Delta m^2_{41} = 0.1$ eV$^2$/c$^4$ is assumed.

In summary, the data are consistent with the standard three flavor oscillation hypothesis. Limits have been set on the sterile mixing parameters, with the world's best constraint on $\sin^2\theta_{24}$ for $10^{-4}$ eV$^2$/c$^4$ $< \Delta m^2_{41} < 3\times10^{-3}$ eV$^2$/c$^4$. Our current precision is restricted by statistics and the uncertainty on the NC interaction cross section. Apart from future updates of the analysis as we take more data, dedicated systematic studies are required for further improvements to the precision. Another possible extension is to perform a joint analysis of near and far detector data that would expand the range of constraint to $\Delta m^2_{41} \gtrsim 1$ eV$^2$/c$^4$ with additional data at smaller L/E.

### *Measurement of inclusive double-differential $\nu_\mu$ charged-current cross section with improved acceptance in the T2K off-axis near detector*

In addition to the oscillation measurements, T2K has an ongoing program to study neutrino interactions using the near detector complex in order to improve the understanding and modeling of these interactions. Previously, T2K reported the measurement of the flux-integrated double-differential cross section for muon neutrino charged-current interactions on carbon as a function of the muon momentum and angle [21]. Since that time, many improvements have been made in the analysis. New results, obtained with more data, reduced neutrino flux uncertainties (thanks to new NA61/SHINE measurements [5]), increased angular acceptance, reduced background contamination, and a different unfolding method were presented this year [22].

This new analysis uses data collected in the near detector in neutrino running mode between November 2010 and May 2013. The total sample comes from 5.7 $\times10^{20}$ protons on target, which is a factor of 5 larger than that used in the similar previously published analysis from T2K [21]. Events containing muons emanating from interactions that occur in the fiducial volume of the first Fine Grained Detector (FGD1) are selected, and the cross section results are presented based on the kinematics of this outgoing muon. In previous T2K work on this topic, the analysis was optimized to select forward-going muons originating from FGD1 and making a long track. This new work aims to include the so-called high-angle tracks, as well as long backward-going tracks. The addition of backward-going muon candidates in the event selection only became possible with the introduction of timing information correlated between sub-detectors.

Two event generators, NEUT 5.3.2 [7] and GENIE 2.8.0 [23], are used to simulate the interaction of neutrinos in the near detector and the effect of the nuclear medium on the produced particles. The efficiency as calculated in NEUT and GENIE is generally in agreement. However, the predicted efficiency is different for low momentum muons going very forward with respect to the neutrino direction. The flux-integrated total cross section is computed by integrating both the number of signal events and the signal efficiency over the muon phase space,

$\sigma_{DATA\ FIT\ W/NEUT} = (6.950 \pm 0.049[\text{stat}] \pm 0.123[\text{syst}] \pm 0.608[\text{flux}]) \times 10^{-39}$ cm$^2$nucleon$^{-1}$

$\sigma_{DATA\ FIT\ W/GENIE} = (6.850 \pm 0.048[\text{stat}] \pm 0.121[\text{syst}] \pm 0.599[\text{flux}]) \times 10^{-39}$ cm$^2$nucleon$^{-1}$.

This is compatible with predictions from the two event generators: $\sigma_{NEUT} = 7.108\times10^{-39}$ cm$^2$nucleon$^{-1}$ and $\sigma_{GENIE} = 6.564\times10^{-39}$ cm$^2$nucleon$^{-1}$.

The flux-integrated, double-differential cross section is computed as a function of the outgoing muon kinematics and the result is compared to the NEUT and GENIE predictions (Fig. 33). In the new regions of phase space (high-angle and backward-going muons), there is good agreement, but uncertainties are still large. For forward-going muons, the binning is finer, and interesting structures are observed.

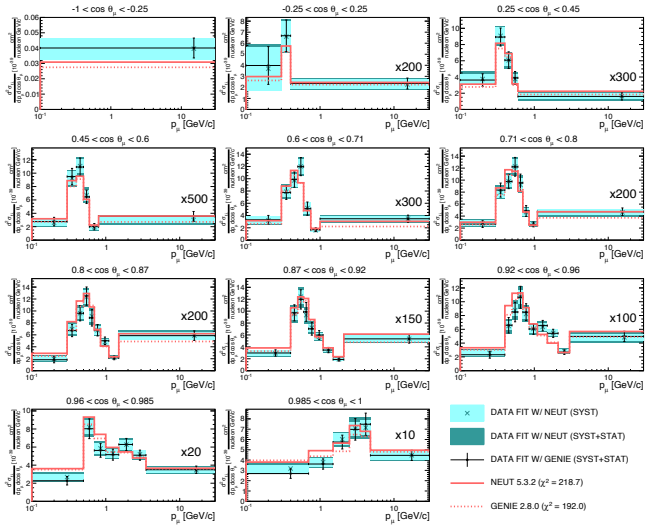


Fig. 33. The flux-integrated, double-differential cross section per nucleon for NEUT (continuous red line), for GENIE (dashed red line), and the unfolded-data result using as a prior either NEUT or GENIE. The bin of highest momentum is scaled by the factor shown in each plot to make it visible. $\chi^2$ values are computed with the unfolded-data result using NEUT as a prior.

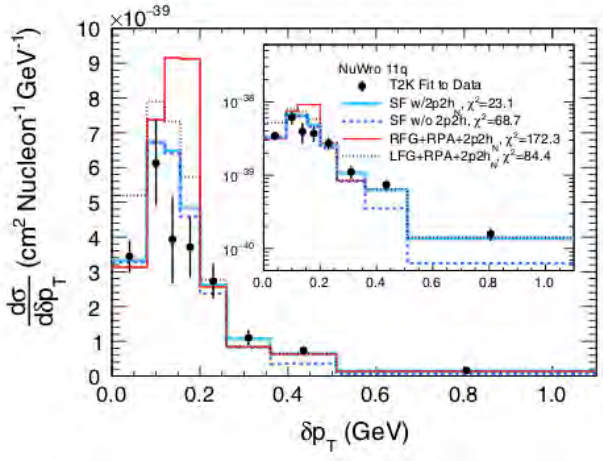


Fig. 34. The extracted differential cross section as a function of the STV $\delta p_T$ compared to different initial state models in the NuWro 11q simulation. The NuWro 11q RFG + RPA prediction shown is similar to the NEUT model used as a starting point for T2K's oscillation analyses. The inlays show the same comparisons on a logarithmic scale.

### *Characterization of nuclear effects in muon-neutrino scattering on hydrocarbon with a measurement of final-state kinematics and correlations in charged-current pionless interactions at T2K*

Experiments studying neutrino oscillations such as T2K use neutrino interactions on nuclei to provide evidence of neutrino oscillations and to search for leptonic CP-symmetry violation. The systematic uncertainties arising from neutrino-nucleus interactions, especially those related to nuclear effects, are currently one of the limiting factors for oscillation measurements in T2K and NOvA, and will become the dominant uncertainties for future long-baseline experiments, such as DUNE and Hyper-Kamiokande. T2K presented measurements of final-state proton multiplicity, muon and proton kinematics, and their correlations in charged-current pionless neutrino interactions, measured by the T2K ND280 near detector in its plastic scintillator target [24]. Thanks to their exploration of the proton kinematics and of imbalances between the proton and muon kinematics, the results offer a novel probe of the nuclear-medium effects most pertinent to the (sub-)GeV neutrino-nucleus interactions that are used in accelerator-based long-baseline neutrino oscillation measurements.

The measurements use data taken between years 2010 and 2013, corresponding to approximately $6\times10^{20}$ protons on target. Three different analyses were performed, each of them measuring differential cross sections as a function of different observables to study the kinematics of the outgoing muon and protons in charged-current events without pions in the final state (CC0$\pi$). In particular, one of them uses single transverse variables (STV) [25], which are built specifically to characterize, and minimize the degeneracy between, the nuclear effects most pertinent to long-baseline oscillation experiments. Each of the analyses take different approaches when extracting a cross section from the selected events. All of these methods involve an effective background subtraction; an efficiency correction; and the deconvolution of detector effects either by a binned likelihood fit for two of them, or an iterative unfolding procedure for the last one.

Many differential cross-sections are measured, and the results are compared to different neutrino-nucleus interaction models which all fail to describe at least part of the observed phase space. In particular the relativistic Fermi gas (RFG) model, widely used for the analysis of the data of neutrino oscillation experiments, is able to describe only a very limited region of phase space and is categorically disfavored when considering the results as a function of one of the STV, $\delta p_T$ (Fig. 34). In case of events without a proton above the detection threshold in the final state, a fully consistent implementation of the local Fermi gas (LFG) model with multinucleon interactions gives the best description of the data. In the case of at least one proton in the final state, the spectral function (SF) model agrees well with the data, most notably when measuring the kinematic imbalance between the muon and the proton in the plane transverse to the incoming neutrino. Within the models considered, only the existence of multinucleon interactions are able to describe the extracted cross section within regions of high transverse kinematic imbalance. The measurement of neutrino-nucleus interactions with a pionless final state with protons clearly shows the potential to provide an even more detailed characterization of nuclear effects in neutrino-nucleus scattering in the future. To this aim, larger statistics are needed, alongside more robust predictions of outgoing proton kinematics in multi-nucleon interactions (2p2h) and final state interaction models.

## Bibliography

[1] K. Abe *et al.* (T2K Collaboration), Nucl. Instrum. Meth. A **659**, 106 (2011)

[2] D. Beavis, A. Carroll, I. Chiang, *et al.*, Long Baseline

Neutrino Oscillation Experiment at the AGS (Proposal E889), 1995. Physics Design Report, BNL 52459.

[3] K. Abe *et al.* (T2K Collaboration), Phys. Rev. Lett. **112**, 061802 (2014)

[4] T. Bhlen *et al.*, Nucl. Data Sheets **120**, 211 (2014)

[5] N. Abgrall et al. (NA61/SHINE Collaboration), Eur. Phys. J. C **76**, 84 (2016).

[6] C. Zeitnitz and T. A. Gabriel, Proceedings of International Conference on Calorimetry in High Energy Physics (World Scientific, Corpus Christi, Texas, 1992), ISBN 9789810213039, pp. 394-404.

[7] Y. Hayato, Acta Phys. Pol. B **40**, 2477 (2009)

[8] K. Abe *et al.* (T2K Collaboration),Phys. Rev. Lett. **118**, 151801 (2017)

[9] K. Abe *et al.* (T2K Collaboration), Phys. Rev. D **96**, 092006 (2017)

[10] K. Abe *et al.* (T2K Collaboration), Phys. Rev. Lett. **121**, 171802 (2018)

[11] F. P. An et al. (Daya Bay Collaboration), Phys. Rev. D **95**,072006 (2017).

[12] G. J. Feldman and R. D. Cousins, Phys. Rev. D **57**, 3873 (1998).

[13] S. M. Bilenky, C. Giunti, and W. Grimus, Prog. Part. Nucl. Phys. **43**, 1 (1999)

[14] V. D. Barger, B. Kayser, J. Learned, T. J. Weiler, and K. Whisnant, Phys. Lett. B **489**, 345 (2000).

[15] J. Kopp, P. A. N. Machado, M. Maltoni, and T. Schwetz, J. High Energy Phys. **05** (2013) 050.

[16] K. Abe *et al.* (T2K Collaboration), Phys. Rev. D **99**, 071103 (2019)

[17] K. Abe et al. (T2K Collaboration) Phys. Rev. D **90**, 072012 (2014)

[18] P. Adamson et al. (MINOS+ Collaboration), Phys. Rev. Lett. **122**, 091803 (2019)

[19] K. Abe et al. (Super-Kamiokande Collaboration), Phys. Rev. D **91**, 052019 (2015).

[20] M. G. Aartsen et al. (IceCube Collaboration), Phys. Rev. Lett. **117**, 071801 (2016)

[21] K. Abe et al. (T2K Collaboration), Phys. Rev. D **87**, 092003 (2013)

[22] K. Abe et al. (T2K Collaboration) Phys. Rev. D **98**, 012004 (2018)

[23] C. Andreopoulos et al., Nucl. Instrum. Methods Phys. Res., Sect. A **614**, 87 (2010)

[24] K. Abe et al. (The T2K Collaboration) Phys. Rev. D **98**, 032003 (2018)

[25] X. G. Lu, L. Pickering, S. Dolan, G. Barr, D. Coplowe, Y. Uchida, D. Wark, M. O. Wascko, A. Weber, and T. Yuan, Phys. Rev. C **94**, 015503 (2016).

## XMASS EXPERIMENT

[Spokesperson : Shigetaka Moriyama]
Kamioka Observatory, ICRR, the University of Tokyo

### *Introduction*

The XMASS project is designed to detect dark matter, neutrinoless double beta decay, and $^{7}$Be/$pp$ solar neutrinos using highly-purified liquid xenon (LXe) scintillator in an ultra-low radioactivity environment [1]. The advantages of using LXe are a large amount of scintillation light yield, scalability of the size of the detector mass, an easy purification to reduce internal radioactive backgrounds (BGs), shielding ability against radiations from outside of the detector due to a high atomic number ($Z = 54$). The detector with $\sim$830 kg of LXe has been constructed in September 2010. After completion of the detector, commissioning data was taken from December 2010 to May 2012. We published results from searches for some dark matters [2] [3] [4], solar axions [5], and two-neutrino double electron capture on $^{124}$Xe [6]. We also studied a possibility to detect galactic supernova neutrinos via coherent elastic neutrino-nucleus scattering [7].

During the commissioning data-taking, we found that a majority of events at low energy originated from radioactive contamination in the aluminum seal of the photomultiplier tube (PMT) window. In order to minimize the BG contribution, detector refurbishment was conducted. The contaminated parts of PMTs were covered by copper rings and plates in order to stop scintillation lights and radiations caused by its contamination. PMT windows were cleaned by nitric acid and copper parts were electropolished in order to remove possible surface contamination. After a year of detector refurbishment, data-taking resumed in November 2013 and continued for more than five years. We then completed the data taking in February 2019. We have published results from the update of searches for annual modulation from dark matters [8] [9], for solar Kaluza-Klein axions [10], and for two-neutrino double electron capture on $^{124}$Xe [11].

In the following sections, we introduce the XMASS-I detector briefly and report the latest physics results from the XMASS data collected after the refurbishment.

### *The XMASS-I detector*

XMASS-I is a single phase LXe scintillator detector located underground (2700 m water equivalent) at the Kamioka Observatory [12]. Fig. 35 shows a schematic drawing of the XMASS-I detector. It contains $\sim$830 kg of LXe in an active region. The volume is viewed by 630 hexagonal and

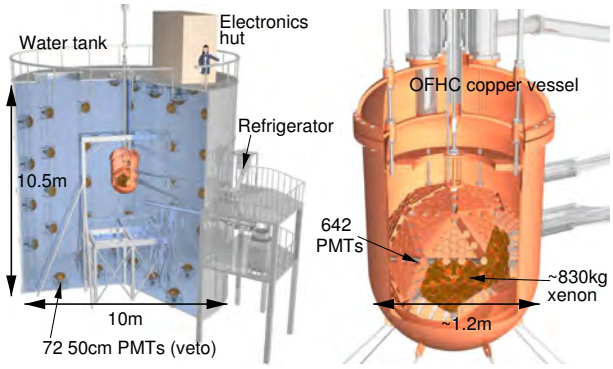


Fig. 35. Schematic drawing of the XMASS-I detector.

12 cylindrical Hamamatsu R10789 PMTs arranged on an 80 cm diameter pentakis-dodecahedron support structure. These PMTs were developed to achieve low background requirement [13]. The largest contributions to the reduction of radioactivity came from the stem and the dynode support. The glass stem was exchanged to the Kovar alloy one and the ceramic support were changed to the quartz one. R10789 is the first model of Hamamatsu Photonics K. K. that adopted these materials for low background purposes and provided a groundbreaking step for further reductions of radioactivity in PMTs. A total photocathode coverage of more than 62% is achieved. The spherical arrays of PMTs are arranged in a double wall vessel made of oxygen free high conductivity (OFHC) copper. The waveforms in each PMT are recorded with CAEN V1751 waveform digitizers with 1 GHz sampling rate and 10 bit resolution. The detector is calibrated regularly with a $^{57}$Co source inserted along the central vertical axis of the detector and external $^{60}$Co source. By the data taken with the $^{57}$Co source at the center of the detector volume, the photoelectron (PE) yield was determined to be $\sim$14 PE/keV. Two different energy scales were used: keV$_{ee}$ represents an electron equivalent energy, and keV$_{nr}$ denotes the nuclear recoil energy. Scintillation decay time constant was investigated in liquid xenon with the XMASS detector. These are summarized at [14] and [15].

In order to shield the LXe detector from external gammas, neutrons, and muon-induced BGs, the copper vessel was placed at the center of a $\phi$10 m$\times$ 10.5 m cylindrical tank filled with pure water. The water tank is equipped with 72 Hamamatsu R3600 20-inch PMTs to provide both an active muon veto and passive shielding against these BGs. XMASS-I is the first direct detection dark matter experiment equipped with such an active water Cherenkov shield. The LXe and water Cherenkov detectors are hence called an Inner Detector (ID) and an Outer Detector (OD), respectively.

### *Dark matter search in a fiducial volume [16]*

Weakly Interacting Massive Particles (WIMPs) are one of the well-motivated dark matter candidates and are thought to be observable through nuclear recoils in the target material. A number of experimental searches have been carried out, however, no indication of such a signature has been observed yet. Considering the latest experimental constraints on the WIMP-nucleon cross section, the detectors have to have a low energy threshold, ultra-low BG, and a large target mass.

We performed a search for WIMP dark matter in a fiducial volume using 705.9 live days of data collected between November 2013 and March 2016. The event vertex was reconstructed with two different methods: one based on hits' timing and the other based on the PE distribution. The reconstructed radial positions by these methods are referred to as $R(T)$ and $R(PE)$, respectively. The position resolution of $R(T)$ is worse than that of $R(PE)$ since traveling time of the scintillation light across the detector volume is not much larger than the scintillation time constant or PMT timing response. However, requiring $R(T) < 38$ cm eliminated some surface events that were often mis-reconstructed by the PE-based reconstruction. Then, a fiducial volume containing 97 kg of xenon was established by requiring $R(PE) < 20$ cm. The event rate after the selection was $(4.2 \pm 0.2) \times 10^{-3}$ event/day/kg/keV$_{ee}$ around 5 keV$_{ee}$ with the signal efficiency of 20%.

In order to extract the WIMP signals, the amount of BG and its systematic error were evaluated from a detailed detector simulation verified by various detector calibrations. The assumed radioactive BG was classified as either radioisotopes (RIs) dissolved in the LXe, $^{210}$Pb in the detector's inner surface, or RIs in other detector material.

For the RIs in the LXe, $^{222}$Rn, $^{85}$Kr, $^{39}$Ar, and $^{14}$C are considered. The $^{222}$Rn amount was measured to be $10.3 \pm 0.2$ $\mu$Bq/kg using the $^{214}$Bi-$^{214}$Po coincidence. The $^{85}$Kr contamination was found to be $0.30 \pm 0.05$ $\mu$Bq/kg by the $\beta$-$\gamma$ coincidence in its decay. The $^{39}$Ar and $^{14}$C concentrations were evaluated by the spectrum fitting in a larger fiducial volume of $R(PE) < 30$ cm in the 30–250 keV$_{ee}$ energy range where no contribution from possible WIMP-induced nuclear recoils appear. The $^{210}$Pb contamination at the detector surface was evaluated by $\alpha$-ray events extracted from the full volume of the LXe detector. The $\alpha$-ray events were selected based on their shorter scintillation decay time. Then, the ratio of the maximum number of PEs on a single PMT to the total number of PEs in the event was used to discriminate $\alpha$-ray events originating from the PMT's quartz window surface, the copper surface, or the bulk of the copper. The estimated concentration of $^{210}$Pb in the copper bulk was $25 \pm 5$ mBq/kg, which was consistent with the measured value of 17–40 mBq/kg with a low-BG $\alpha$-ray counter [17]. The RIs in other detector material were evaluated by the spectrum fitting using the full volume of the LXe detector. All the detector components except for the copper and the LXe were assayed with high-purity germanium (HPGe) detectors and the results of these measurements were used as initial values and their uncertainties as constraints for the full volume spectrum fit. The spectrum above $\sim$400 PE was fit to determine the activities of the RIs. Fig. 36 shows a comparison of the full volume spectrum and the expected BG spectrum corresponding to the best-fit. The $\gamma$-rays from the PMTs were the largest BG source in the full volume data.

Fig. 37 shows the expected BG spectrum in the fiducial volume. The dominant contribution comes from $^{210}$Pb in the bulk of the copper and the RIs in the PMTs. The size of the systematic uncertainty is also shown in the figure. The largest contribution comes from the uncertainty of the detector geometry such as gaps between the copper plates, the roughness of

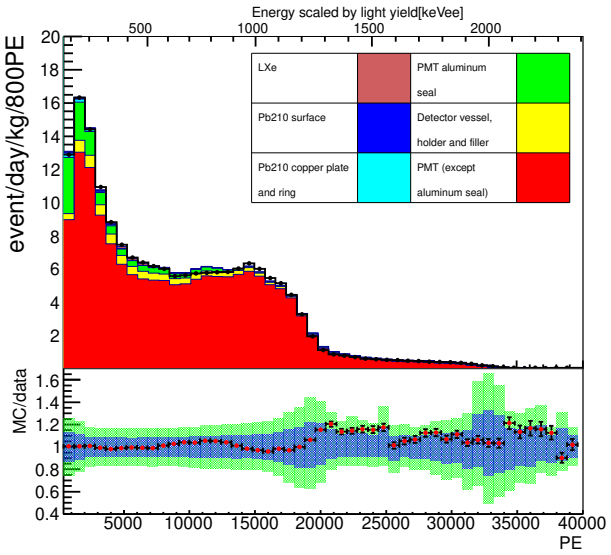


Fig. 36. Number of PE spectra in the full volume of data and the best–fit simulation. The black line represents the data and each colored histogram is a different BG RI. In the bottom plot, the ratio of the best-fit simulation to the data is shown as a red points. The blue and green bands indicate the $\pm1\sigma$ and $\pm2\sigma$ systematic uncertainties, respectively.

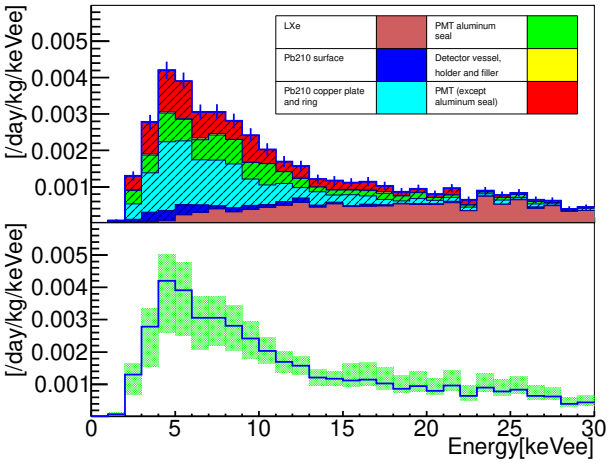


Fig. 37. Expected BG energy spectrum in the fiducial volume. The top figure illustrates a breakdown of the BG while the bottom figure shows the same energy spectrum with systematic error evaluation.

the copper rings, and the copper reflectivity.

To search for the WIMP dark matter signal in our fiducial volume data, we performed a chi-square fitting of the observed energy spectrum with the expected signal and BG spectra in the 2–15 keV$_{ee}$ energy range The best-fit result was obtained in the case of no existence of a WIMP signal, with $\chi^2$/NDF=8.1/12. Fig. 38 shows the energy spectrum of the data and the best-fit BG estimate with the $\pm1\sigma$ systematic error band. All the remaining events are consistent with our BG evaluation. Hence, the 90% confidence level (CL) upper limit on the spin-independent WIMP-nucleon cross section was derived as a function of mass between 20 GeV/$c^2$ and 10 TeV/$c^2$ as shown in Fig. 39. Our lowest limit is $2.2\times10^{-44}$ cm$^2$ for a 60 GeV/$c^2$ WIMP.

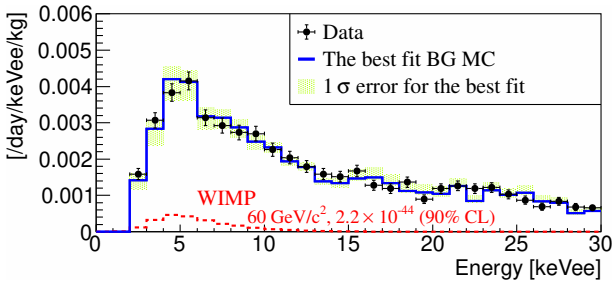


Fig. 38. Data spectrum (filled dots) overlaid with the best-fit BG estimate (blue) with the $\pm1\sigma$ error band (green). The expected 60 GeV/$c^2$ WIMP spectrum (red) at a WIMP-nucleon cross section of $2.2\times10^{-44}$ cm$^2$ is also shown.

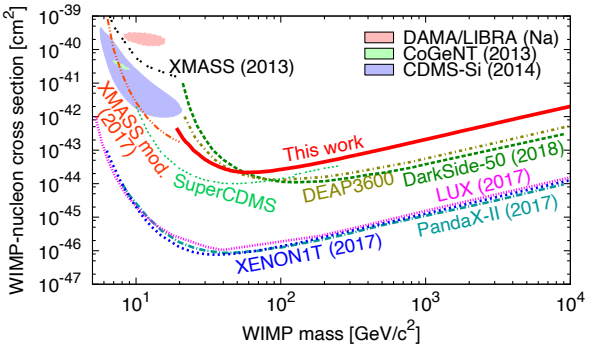


Fig. 39. Spin-independent WIMP-nucleon cross section as a function of the WIMP mass. The red solid curve represents the 90% CL limit obtained from the XMASS fiducial volume data.

### *Search for dark matter in the form of hidden photons and axion-like particles [18]*

Hidden Photons (HPs) and Axion-like Particles (ALPs), which are respectively vector and pseudo-scalar realizations of bosonic super-WIMPs, are alternative cold dark matter candidates with expected masses $<1$ MeV/$c^2$ if they were produced non-thermally in the early universe. XMASS already carried out searches around this mass region for HPs and ALPs using commissioning data taken in 2010–2012, and had given limits in the mass range of 40–120 keV/$c^2$ [4].

This time we conducted a improved search for both of these bosons using 800 live-days of data with 327 kg of liquid xenon in the fiducial volume. The $R(PE) < 30$ cm cut is applied in order to remove BG events originating from $\gamma$-rays or $\beta$-rays from RI in/on the detector's inner surfaces and bulk materials. We searched for a signal from the data by comparing the observed energy spectrum with the combined predictions of signal and BG simulation including their respective uncertainties. The energy spectrum after applying all the selections is shown in Fig. 40. The peak around corrected number of photoelectron (NPE$_{cor}$) = 2400 came from residual $^{131m}$Xe after calibration with $^{252}$Cf, which was useful as a reference for the global energy scale of the simulation. The energy range between NPE$_{cor}$=590–1760 (corresponding to $\gamma$-ray energies of 40–120 keV) was used for the signal search. In this region the spectrum is almost flat with an event rate of $5\times10^{-4}$ count/day/kg/keV. No significant signal was ob-

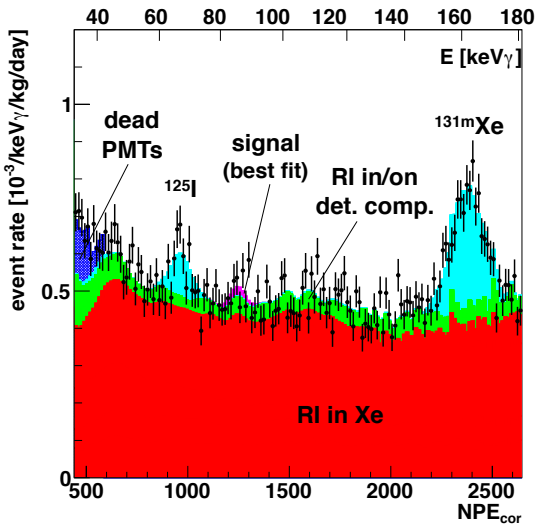


Fig. 40. Best fit $NPE_{cor}$ distributions. The upper scale is translated into the corresponding $\gamma$-ray energies. The black dots represent the data. The stacked histograms show the BG Monte Carlo simulation (MC) for RIs in/on the detector components (green), RIs in the liquid xenon (red), and xenon isotopes activated by neutrons (light blue). The dark hatched blue area shows the estimated contribution from dead PMTs. The magenta part of the histogram shows the best fit HP signal for a HP mass of $m_{HP}$ = 85 keV/$c^2$.

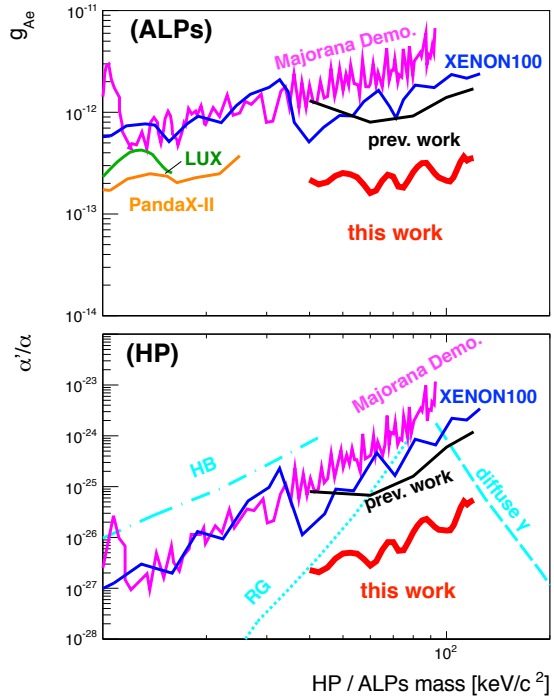


Fig. 41. Constraints on $g_{Ae}$ of the ALPs (top) and $\alpha'/\alpha$ of the HP (bottom). The red line shows the 90% CL constraint limit. The black line shows our previous result [4]. The blue, magenta, green, and orange lines are limits reported by the XENON100, the Majorana Demonstrator, the LUX, and the PandaX-II, respectively. The dotted, dashed, and dash-dotted lines in light blue color are constraints from indirect searches derived from red giant stars (RG), diffuse $\gamma$-ray flux, and horizontal branch stars (HB), respectively.

served, and thus we set constraints on the $\alpha'/\alpha$ parameter related to kinetic mixing of HPs and the coupling constant $g_{Ae}$ of ALPs in the mass range from 40 to 120 keV/$c^2$, resulting in $\alpha'/\alpha < 6\times10^{-26}$ and $g_{Ae} < 4\times10^{-13}$. These limits are the most stringent over this mass range derived from both direct and indirect searches to date as shown in Fig. 41.

### *Search for WIMP-$^{129}$Xe inelastic scattering with particle identification [19]*

A WIMP search was conducted through inelastic scattering in which $^{129}$Xe nuclei were excited. An observation of WIMP-nuclei inelastic scattering would be direct evidence of a spin dependent (SD) interaction mechanism as well as that WIMPs have spin since nuclear excitation in inelastic scattering can be led only by SD interaction. We have studied the inelastic scattering in 2014 [3]. This is the update of our previous study. The inelastic excitation sensitivity was improved by detailed evaluation of background, event classification based on scintillation timing that distinguished $\gamma$-rays and $\beta$-rays, and simultaneous fitting of the energy spectra of $\gamma$-like and $\beta$-like samples.

The data used for the analysis was collected from November 20, 2013 to July 20, 2016. The samples were separated into $\beta$-depleted and $\beta$-enriched samples. This separation was performed with a particle identification technique based on the different LXe scintillation time profiles. The time constant of scintillation from a $\beta$-ray becomes longer as the energy becomes larger [14]. Since a $\gamma$-ray is converted into lower energy electrons in LXe, its time constant is shorter than that of a $\beta$-ray. The scintillation light from the nuclear recoil (NR) has a shorter time constant than that of a $\beta$-ray and a $\gamma$-ray since its ionization density is higher and the ion-electron pairs recombine faster. Therefore, inelastic scattering, which has contributions from both NR and a $\gamma$-ray, has a shorter time constant than a pure $\beta$-ray event. This classification reduced the number of events by about one order of magnitude in the signal region. For a 200 GeV/$c^2$ WIMP, the signal efficiency in the fiducial volume region is approximately 51%. The $\beta$-ray events classified as $\beta$-depleted was typically about 10% for a 200 GeV/$c^2$ WIMP search. The data was divided into four periods, 1–4, because background condition is different. The energy spectra were fitted with WIMP + BG MC spectra in the energy range from 30 to 200 $keV_{ee}$. Fig. 42 shows the energy spectra for period 1. No evidence of a WIMP signal was found. Thus, we set the upper limits of the inelastic channel cross section at 90% CL. This result provides the most stringent limits on the SD WIMP-neutron interaction and is better by a factor of 7.7 at 200 GeV/$c^2$ than the existing experimental limit as shown in Fig. 43.

## Bibliography

[1] Y. Suzuki *et al.*, hep-ph/0008296.

[2] K. Abe *et al.* (XMASS Collaboration), Phys. Lett. B **719** (2013) 78.

[3] H. Uchida *et al.* (XMASS Collaboration), Prog. Theor.

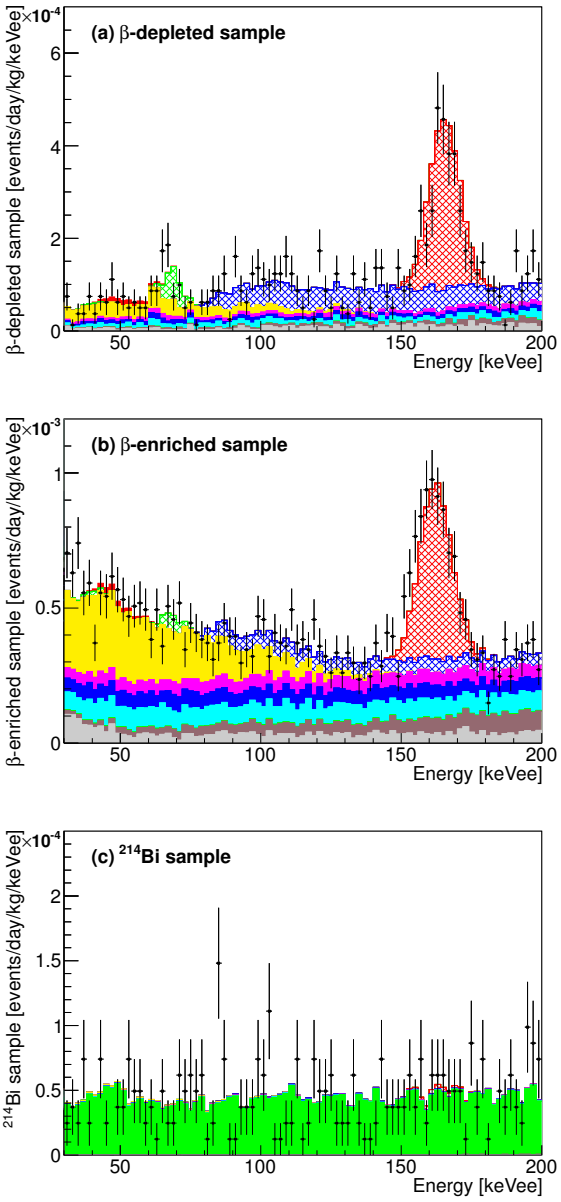


Fig. 42. Energy spectra for period 1 of 200 GeV/$c^2$ WIMP (90% CL upper limit). $\beta$-depleted, $\beta$-enriched, and $^{214}$Bi samples are shown in (a), (b), and (c), respectively. The observed data is shown as black points with error bars over the MC histograms. WIMP (red filled), $^{125}$I (green hatched), $^{14}$C (orange filled), $^{39}$Ar (magenta filled), $^{85}$Kr (blue filled), $^{214}$Pb (cyan filled), $^{136}$Xe (brown filled), external $\gamma$-rays (gray filled), $^{131m}$Xe (red hatched), $^{133}$Xe (blue hatched), and $^{214}$Bi (green filled) are shown as stacking histograms.

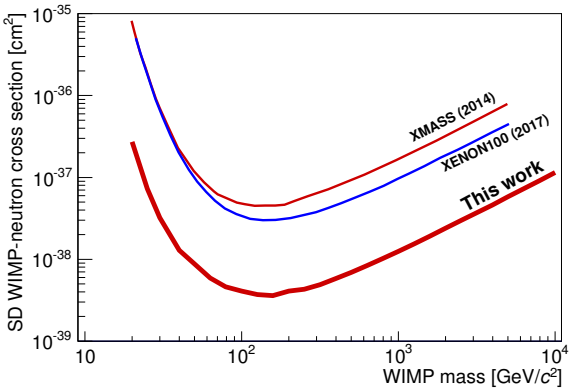


Fig. 43. 90% CL upper-limit for the WIMP-neutron cross section obtained by inelastic scattering searches. The result of this analysis is shown as a solid bold line. The results of other experimental SD inelastic scattering searches are shown with solid lines: XMASS (2014) [3], XENON100 (2017).

Exp. Phys. (2014) 063C01.

[4] K. Abe *et al.* (XMASS Collaboration), Phys. Rev. Lett. **113** (2014) 121301.

[5] K. Abe *et al.* (XMASS Collaboration), Phys. Lett. B **724** (2013) 46.

[6] K. Abe *et al.* (XMASS Collaboration), Phys. Lett. B **759** (2016) 64.

[7] K. Abe *et al.* (XMASS Collaboration), Astropart. Phys. **89** (2017) 51.

[8] K. Abe *et al.* (XMASS Collaboration), Phys. Lett. B **759** (2016) 272.

[9] K. Abe *et al.* (XMASS Collaboration), Phys. Rev. D **97** (2018) 102006.

[10] N. Oka *et al.* (XMASS Collaboration), Prog. Theor. Exp. Phys. **2017** (2017) 103C01.

[11] K. Abe *et al.* (XMASS Collaboration), Prog. Theor. Exp. Phys. **2018** (2018) 053D03.

[12] K. Abe *et al.* (XMASS Collaboration), Nucl. Instrum. Meth. A **716** (2013) 78.

[13] K. Abe *et al.* (XMASS Collaboration), Nucl. Instrum. Meth. A **922** (2019) 171.

[14] H. Takiya *et al.* (XMASS Collaboration), Nucl. Instrum. Meth. A **834** (2016) 192.

[15] K. Abe *et al.* (XMASS Collaboration), JINST **13** (2018) P12032.

[16] K. Abe *et al.* (XMASS Collaboration), Phys. Lett. B **789** (2019) 45.

[17] K. Abe *et al.* (XMASS Collaboration), Nucl. Instrum. Meth. A **884** (2018) 157.

[18] K. Abe *et al.* (XMASS Collaboration), Phys. Lett. B **787** (2018) 153.

[19] T. Suzuki *et al.* (XMASS Collaboration), Astropart. Phys. **110** (2019) 1.

## HYPER-KAMIOKANDE

[Project Leader: Masato Shiozawa
(Kamioka Observatory, ICRR, The University of Tokyo)]

### *Introduction*

The Hyper-Kamiokande (Hyper-K or HK) experiment is proposed as a joint project of the university of Tokyo and KEK by combining a next generation underground water Cherenkov detector and upgraded J-PARC (Japan Proton Accelerator Research Complex, Ibaraki, Japan) neutrino beam. In FY2016 ICRR and KEK have set first priority to the Hyper-K and upgrade of J-PARC for the project. The Hyper-K project has been chosen for inclusion in the Ministry of Education, Culture, Sports, Science and Technology (MEXT) Large Project Roadmap, "Roadmap 2017". A 'seed funding' towards the construction of Hyper-K has been allocated by MEXT within its budget request for the 2019 fiscal year.

Figure 44 shows a schematic drawing of the Hyper-K cylindrical detector. The detector is filled with 0.258 million metric tons of ultra pure water, which serves an order of magnitude larger fiducial mass of 0.187 million metric tons than Super-K. It provides an enormous potential to discover leptonic charge-parity (CP) violation by observing neutrino and anti-neutrino beams from J-PARC. A search for nucleon decays is an important subject to explore new paradigm beyond the standard model of particle physics. Hyper-K will also have far better capabilities to observe atmospheric neutrinos, solar neutrinos, and neutrinos from other astronomical sources than those of predecessor experiments.

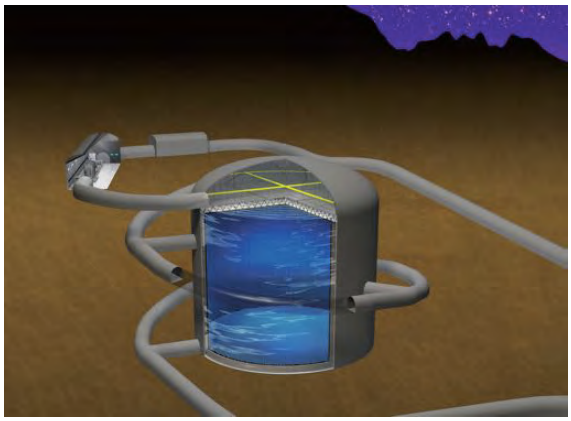

Fig. 44. Schematic view of the Hyper-K water tank.

The Hyper-K international proto-collaboration consists of about 300 researchers 17 countries. Technical details were published as a design report in May 2018 with various physics reaches [1]. The detector technology has been developed based upon the successful Super-K experiment. The candidate site has been pinned down by geological surveys. In conclusion the feasibility study has been completed and the project is technically ready to start construction. The international group aims to start the detector construction in 2020 and to start its operation in 2027.

### *Photosensors*

A Cherenkov light in a ultra pure water is detected by 40,000 newly developed photomultiplier tubes (PMTs), R12860 by Hamamatsu Photonics K.K., with 40% photocoverage. It was significantly upgraded from the R3600 PMT used in Super-K due to an improved dynode structure using a box-and-line type and optimized curvature glass as shown in Fig. 45.

Fig. 45. New 50 cm photomultiplier tube with a box-and-line dynode (R12860, Hamamatsu Photonics K.K.).

The peak quantum efficiency is about 30%, that is 1.4 times higher than that of the Super-K PMT. In total, the new PMT achieved twice higher single photon detection efficiency because the photoelectron collection efficiency was also greatly improved. The timing and charge resolutions at single photoelectron also becomes much better as 1.1 ns and 35% which can be compared with 2.1 ns and 53% of the Super-K PMT, respectively. These outstanding improvements enhance Hyper-K detector performance and its physics reaches.

Moreover, pressure tolerance of PMT was improved up to the 125 m water depth, so that new PMT can be used under about 70 m depth of the detector water. To prevent a chain reaction of imploding PMTs caused by the unlikely event of a single PMT implosion, every PMT in the Hyper-K water tank will be housed in the shockwave prevention cover. The first prototype cover consists of an acrylic front window and a stainless steel backside cover with conical shape. The prototype have been produced and tested in 2016 and 2018 using a long vertical shaft at Kamisunagawa town, Hokkaido, which is naturally filled with spring water. The first prototype testing was successful and confirmed the cover prevents the chain implosion at 80 m water depth. Alternative cover designs have also been studied to reduce production cost and its weight. One of the new designs employs back-side cover made of a resin, which largely reduce the total weight of the cover. A prototype of resin cover has been produced and tested in 2018 at the same testing site in Hokkaido.

More than 100 of R12860 PMTs with the protective covers were installed in Super-Kamiokande in 2018. Figure 46 shows photos of R12860 PMT installation in Super-K. Figure 47 shows photos of R12860 PMTs with new protective covers, which have been developed for Hyper-K and were installed in Super-K.


Fig. 46. Photos of box-and-line dynode PMT (R12860) installation in Super-K.

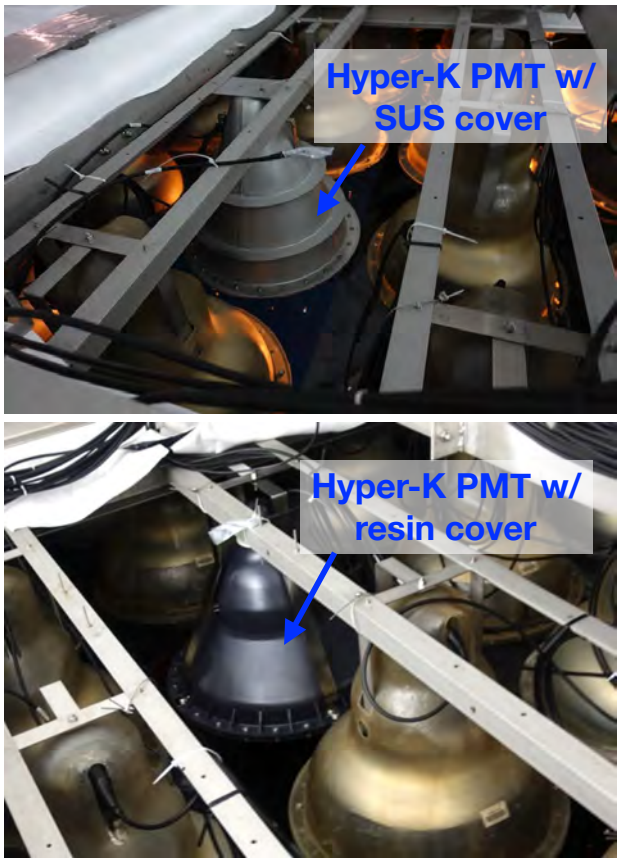


Fig. 47. Photos of R12860 PMT with Hyper-K PMT cover installation in Super-K.

Detailed *in-situ* calibrations of R12860 PMTs installed in Super-K have been done, and preliminary results of the calibration confirmed R12860 PMTs have approximately twice better photo-detection efficiency and twice better timing resolution than Super-K PMTs. The averaged dark rate of R12860 PMTs is evaluated to be about 6 kHz.

### *Physics*

Hyper-K will be able to measure the magnitude of the CP violation with high precision, which could explain the baryon asymmetry in the Universe. Figure 48 shows an expected significance of the CP violation discovery by ten years operation. Hyper-K covers the 76% of $\delta_{CP}$ parameter space with $3\sigma$ or more significance, and 57% of the parameter space with $5\sigma$ or more. Hyper-K will go beyond $7\sigma$ significance if $\delta_{CP} = -90^\circ$ as suggested by T2K [2] and NO$\nu$A [3] results.

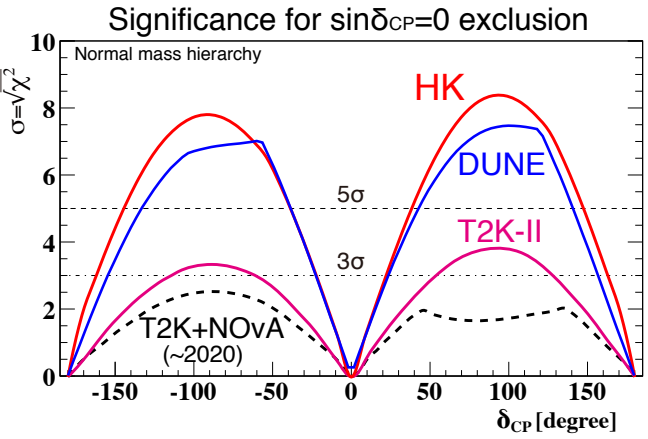


Fig. 48. Significance of the CP violation discovery in lepton sector with a 10-year observation in Hyper-K (HK) as a function of the unknown CP phase. The normal neutrino mass hierarchy is assumed. Ongoing and planned long baseline experiments are superimposed [4, 5].

A proton decay $p \to e^+\pi^0$ is an important signal favored by many Grand Unified Theory models with a prediction close to the current limit of the proton decay life time. Figure 49 shows reconstructed invariant mass distributions for $p \to e^+\pi^0$ search after applying the event selection cuts. Thanks to the high sensitive PMTs of Hyper-K, background events (atmospheric neutrinos) can be largely eliminated and $p \to e^+\pi^0$ search in Hyper-K is expected to be "background-free" particularly in the free-proton enhanced signal region. Figure 50 shows the $3\sigma$ discovery potential for the $p \to e^+\pi^0$ mode as a function of year. Hyper-K is an only realistic proposal which can go beyond the proton lifetime of $1 \times 10^{35}$ years.

As well as the supernova burst neutrino that was successfully observed in Kamiokande at once, undiscovered supernova relic neutrinos, accumulated by past all supernovae since the beginning of the universe, are interesting events to explore the history of heavy elements and the onset of stellar formation. Figure 51 shows the expected number of events as a function of year.

In January 2015, ICRR and the Institute of Particle and Nuclear Studies (IPNS) of KEK signed a memorandum of understanding (MoU) for cooperation on the Hyper-K project. In accordance of the MoU, the Hyper-K Advisory Committee (HKAC) has been formed under the directors of ICRR and KEK-IPNS. The HKAC is composed of international members outside the Hyper-K proto-collaboration, and its mandate is to advise on the scientific, technical and managerial strategy of the Hyper-K project with a view to further developing a highly effective neutrino programme based in Japan. Two rounds of the HKAC meetings were held so far, the first in winter 2015-2016 and the second in summer 2017. In the official report by the HKAC, the committee endorses Hyper-K

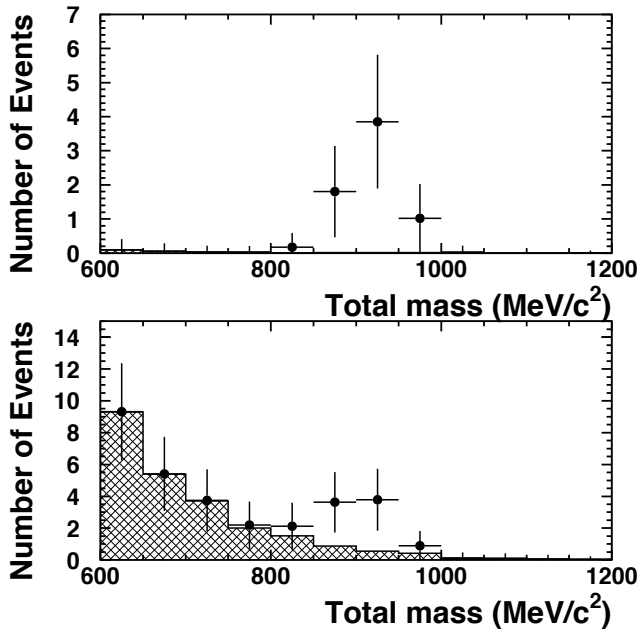


Fig. 49. Reconstructed invariant mass distribution of events passing all steps of the $p \to e^+\pi^0$ event selection except the invariant mass cut after a 10 year exposure of Hyper-K. The hatched histograms show the atmospheric neutrino background and the solid crosses denote the sum of the background and proton decay signal. Here the proton lifetime is assumed to be, $1.7\times10^{34}$ years, just beyond current Super-K limits. The free and bound proton-enhanced signal windows are the upper and lower panels of the plot. The figures are quoted from "Hyper-Kamiokande Design Report" [1].

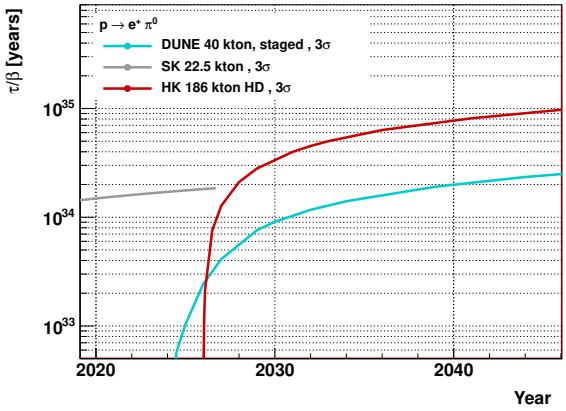


Fig. 50. The $p \to e^+\pi^0$ discovery reach in proton lifetime with $3\sigma$ significance as a function of year. It shows Hyper-K (HK) planing to start in 2026, superimposed with the ongoing Super-K (SK) and planned DUNE experiments. The DUNE project assumes 10 kton operation from 2024, toward full 40 kton by increasing 10 kton every year [6].

as a very important experiment for Japan and for the worldwide program of fundamental science, and encourages ICRR and IPNS to fully support it.

The Hyper-K project are strongly supported by research communities. The Japan Association of High Energy Physicists (JAHEP) and the Cosmic Ray Researchers Congress (CRC) in Japan endorse Hyper-K as the main future project.

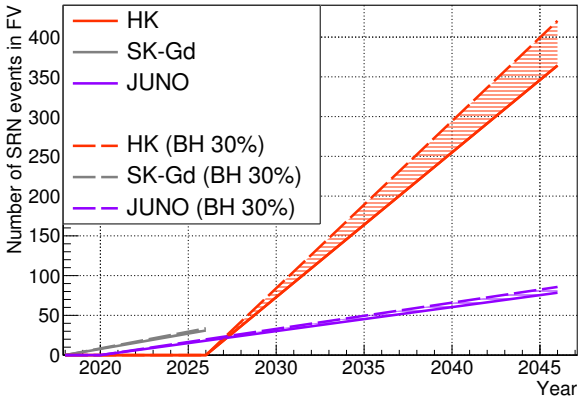


Fig. 51. The accumulated number of supernova relic neutrino events as a function of year. The JUNO experiment and SK-Gd are also plotted [7, 8, 9, 10]. Effective temperature of neutrinos inside supernova is assumed to be 6 MeV. The solid line assumes no black hole formation while the dashed line assumes that 30% of core–collapse stars form a black hole.

KEK Project Implementation Plan (KEK-PIP) released in June 2016 [11] has put the first priority to the upgrade of the J-PARC accelerator for the Hyper-K experiment. The ICRR Future Project Committee has concluded in March 2017 that Hyper-K should be the laboratory's next main project.

The Hyper-K project is listed in "Roadmap 2017" by Ministry of Education, Culture, Sports, Science and Technology (MEXT) as one of the seven highest-priority large-scale projects in Japan.

In October 2017, the University of Tokyo launched Next-Generation Neutrino Science Organization (NNSO), where ICRR, Kavli IPMU, and the School of Science cooperate for pioneering the future of neutrino physics through the development of neutrino research techniques and detector technologies. In particular, it aims to promote what will become its flagship facility, the Hyper-Kamiokande project. The development of the organization framework for the Hyper-K detector construction centered on NNSO is starting.

A 'seed funding' towards the construction of Hyper-K has been allocated by MEXT within its budget request for the 2019 fiscal year. A statement by the president of the University of Tokyo was released [12], which addresses that the University of Tokyo pledges to ensure construction of the Hyper-Kamiokande detector commences as scheduled in April 2020.

Hyper-Kamiokande Financial Forum (HKFF) has been established, in which foreign agency representatives and laboratory directors gathered to engage in discussion with Hyper-K host organizations and project members, and the first meeting was held on January 2019 [13]. Hyper-Kamiokande collaboration firmly makes all efforts towards the realization of the experiment.

## Bibliography

[1] "Hyper-Kamiokande Design Report," arXiv: 1805.04163.

[2] K. Abe *et al.* [T2K Collaboration], Phys. Rev. Lett. 118, 151801.

[3] P. Adamson *et al.* [NO$\nu$A Collaboration], Phys. Rev. Lett. 118, 231801.

[4] K. Abe *et al.* [The T2K Collaboration], arXiv:1609.04111 [physics.ins-det].

[5] K. Abe *et al.* [The T2K Collaboration], PTEP **2015**, no. 4, 043C01 (2015).

[6] R. Acciarri *et al.* [The DUNE Collaboration], arXiv:1601.05471 [physics.ins-det].

[7] H. Sekiya [Super-K Collaboration], PoS(ICHEP2016) 982 (2016).

[8] ICRR News (2016), http://www.icrr.u-tokyo.ac.jp/2016/06/30101400.html.

[9] F. An *et al.* [JUNO Collaboration], J. Phys. G **43**, no. 3, 030401 (2016).

[10] Yu-Feng LI, Presentation at "Workshop on Supernova at Hyper-Kamiokande" (2017).

[11] KEK Project Implementation Plan (2016), https://www.kek.jp/ja/About/OrganizationOverview/Assessment/Roadmap/KEK-PIP.pdf.

[12] "Statement from the President of The University of Tokyo Concerning the Start of Hyper-Kamiokande," http://www.hyper-k.org/doc/2018/Concerning%20the%20Start%20of%20Hyper-Kamiokande.pdf.

[13] "The First Meeting of the Hyper-Kamiokande Experiment Financial Forum," https://www.u-tokyo.ac.jp/focus/en/articles/z0208_00026.html.

# HIGH ENERGY COSMIC RAY DIVISION

## Overview

There are three major experimental research activities in the High Energy Cosmic Ray Division, the study of high energy gamma rays and the development of the next generation gamma-ray telescopes by the Cherenkov Cosmic Gamma Ray group, the study of extremely high energy cosmic rays by the Telescope Array (TA) group, and the study of very high energy cosmic rays and gamma rays by the Tibet AS$\gamma$ group.

Other activities, such as experiments utilizing the Akeno observatory, the Norikura observatory, the Mt. Chacaltaya observatory (jointly operated with Bolivia) are closely related to inter-university joint research programs. Also an all-sky high resolution air-shower detector (Ashra) is in partial operation on the Hawaii island. The High Energy Astrophysics group created in the fiscal year 2009 aims to explore various high energy astrophysical phenomena, through theoretical and observational approaches.

The CANGAROO telescopes had been in operation in South Australia since 1992, with a 3.8 m small telescope and then with four 10 m telescopes. The major scientific objective was the study of Very High Energy (VHE) gamma-ray sources in our galaxy in the southern hemisphere. The mission of these telescopes was completed and the CANGAROO observation site was closed in 2011.

For further development of VHE gamma-ray astronomy, the Cherenkov Cosmic Gamma Ray group is working on the design study and development and construction of the next generation international ground-based gamma-ray observatory CTA which will offer an order of magnitude better sensitivity than currently running Cherenkov telescopes, three times better angular resolution, and wider energy coverage from 20 GeV to 100 TeV or higher. The construction of the first Large-Sized Telescope (LST) was completed on the CTA-North site in La Palma in 2018.

At the Akeno observatory, a series of air shower arrays of increasing geometrical sizes were constructed and operated to observe extremely high energy cosmic rays (EHECRs). The Akeno Giant Air Shower Array (AGASA) was operated from 1991 to January 2004 and covered the ground area of 100 km$^2$ as the world largest air shower array. In 13 years of operation, AGASA observed a handful of cosmic rays exceeding the theoretical energy end of the extra-galactic cosmic rays (GZK cutoff) at around $10^{20}$ eV.

The Telescope Array (TA), a large plastic scintillator array with air fluorescence telescopes, has been constructed in Utah, USA, which succeeds AGASA and measures the EHECRs with an order of magnitude larger aperture than that of AGASA for the further study of EHECRs. The full-scale TA is accumulating data as the largest array viewing the northern sky and observed the energy spectrum with high statistics, which is in good agreement with the GZK suppression and found evidence for anisotropy of arrival directions of EHECRs. The TAx4, which is aimed at quadrupling TA, was partially constructed by March of 2018.

An air shower experiment aiming to search for celestial gamma-ray point sources started in 1990 with Chinese physicists at Yangbajing (Tibet, 4,300 m a.s.l.). This international collaboration is called the Tibet AS$\gamma$ Collaboration. An extension of the air shower array was completed in 1995 and an emulsion chamber has been combined with this air shower array since 1996 to study the primary cosmic rays around the knee energy region. After successive extensions carried out in 1999, 2002 and 2003, the total area of the air shower array amounts to 37,000 m$^2$. The sun's shadow in cosmic rays affected by the solar magnetic field was observed for the first time in 1992, utilizing its good angular resolution at multi-TeV energy region. The group added underground water Cherenkov muon detector to detect cosmic gamma rays above 100 TeV. The group is planning to construct a new air shower array, called ALPACA, to cover the sky in the Southern hemisphere, and started the construction of its partial array in Bolivia in 2019.

The High Energy Astrophysics group is conducting theoretical researches on fundamental processes responsible for non-thermal particle acceleration in various astrophysical environments, including first-order diffusive shock acceleration, second-order stochastic acceleration in shock downstream regions, modification of shock structure by pick-up interstellar neutrals, as well as injection processes of suprathermal particles. In addition to these theoretical works, R/D studies for radio observations of pulsars and cosmic ray air showers are also being made.

## Cherenkov Cosmic Gamma-Ray Group

### *CTA Project (Cherenkov Telescope Array)*

**CTA-Japan Consortium**
[Spokespersons : M.Teshima and H.Kubo]

Collaboration list:
Institute for Cosmic Ray Research, The University of Tokyo, Chiba, Japan; Department of Physics, Aoyama Gakuin University, Tokyo, Japan; Department of Physics, Hiroshima University, Hiroshima, Japan; Hiroshima Astrophysical Science Center, Hiroshima University, Hiroshima, Japan; Faculty of Science, Ibaraki University, Ibaraki, Japan; Institute of Particle and Nuclear Studies, High Energy Accelerator Research Organization (KEK), Ibaraki, Japan; Department of Physics, Konan University, Hyogo, Japan; Faculty of Medical Engineering and Technology, Kitasato University, Kanagawa, Japan; Graduate School of Science and Technology, Kumamoto University, Kumamoto, Japan; Department of Physics, Kyoto University, Kyoto, Japan; Department of

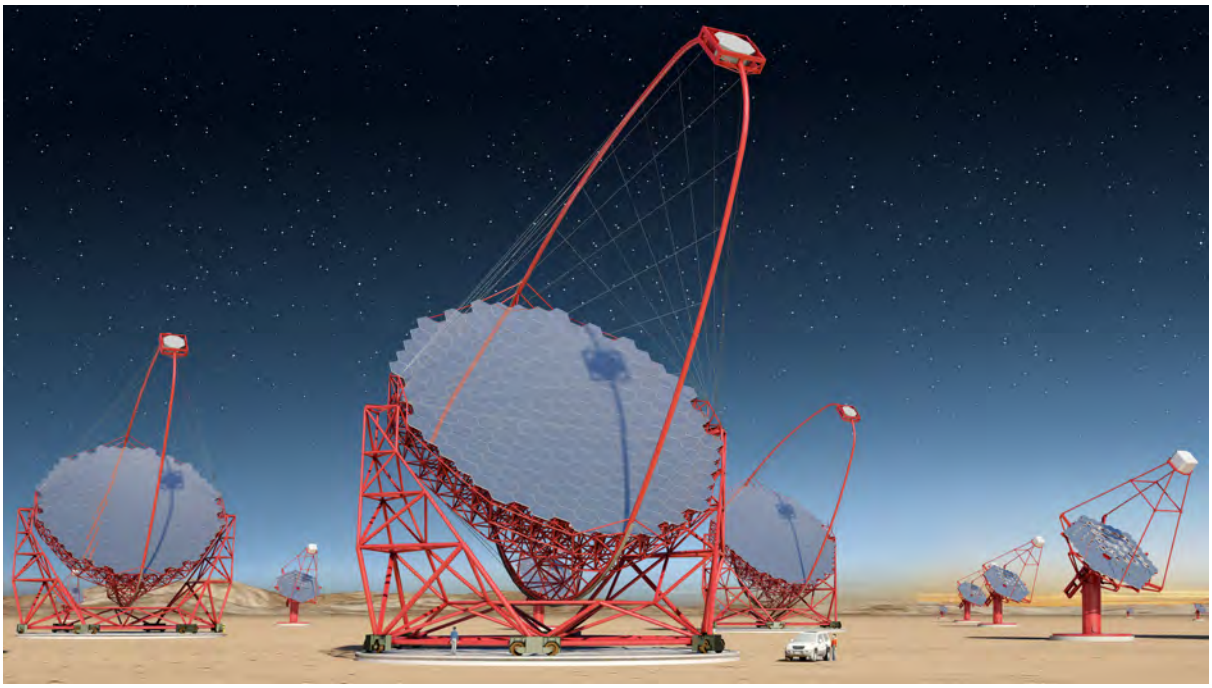

Fig. 1. Artist view of the CTA observatory. CTA consists of three types of telescopes, Large Size Telescopes (23m diameter), Mid Size Telescopes (12m) and Small Size Telescopes (4m), and covers the broad energy band from 20GeV to 100TeV.

Applied Physics, University of Miyazaki, Miyazaki, Japan; Department of Physics, Nagoya University, Aichi, Japan; Solar-Terrestrial Environment Laboratory, Nagoya University, Aichi, Japan; Kobayashi-Maskawa Institute, Nagoya University, Aichi, Japan; Department of Earth and Space Science, Osaka University, Japan; Department of Physics, Kinki University, Osaka, Japan; Astrophysical Big Bang laboratory, RIKEN, Wako, Japan; Department of Physics, Rikkyo University, Tokyo, Japan; Department of Physics, Saitama University, Saitama, Japan; Institute of Space and Astronautical Science, JAXA, Kanagawa, Japan; Department of Physics, Tokai University, Kanagawa, Japan; Faculty of Integrated Arts and Sciences, The University of Tokushima; Department of Astronomy, The University of Tokyo, Tokyo, Japan; Department of Physics, The University of Tokyo, Tokyo, Japan; Faculty of Science and Engineering, Waseda University, Tokyo, Japan; Department of Physics, Yamagata University, Yamagata, Japan; Faculty of Management Information, Yamanashi Gakuin University, Yamanashi, Japan; Center for Cosmology and AstroParticle Physics, Ohio State University, Ohio, USA; Max-Planck-Institute for Physics, Munich, Germany [1].

### *CTA Project*

During the past several years, Very High Energy (VHE) gamma-ray astronomy has made spectacular progress and has established itself as a vital branch of astrophysics. To advance this field even further, we are constructing the Cherenkov Telescope Array (CTA) [6], the next generation VHE gamma ray observatory, in the framework of a worldwide, international collaboration. CTA is the ultimate VHE gamma ray observatory, whose sensitivity and broad energy coverage will attain an order of magnitude improvement above those of current Imaging Atmospheric Cherenkov Telescopes (IACTs). By observing the highest energy photons known, CTA will clarify many aspects of the extreme Universe, including the origin of the highest energy cosmic rays in our Galaxy and beyond, the physics of energetic particle generation in neutron stars and black holes, as well as the star formation history of the Universe. CTA will also address critical issues in fundamental physics, such as the identity of dark matter particles and the nature of space and time.

VHE gamma rays from 100GeV to 10TeV can be observed with ground-based IACTs. The history of VHE gamma ray astronomy began with the discovery of VHE gamma rays from the Crab Nebula by the Whipple Observatory in 1989. To date, the current generation IACTs featuring new technologies, such as H.E.S.S., MAGIC, and VERITAS have discovered more than 200 Galactic and extragalactic sources of various types.

CTA is designed to achieve superior sensitivity and performance, utilizing established technologies and experience gained from the current IACTs. The project is presently in its pre-construction ( prototyping) phase, with international efforts from Japan, US, and EU countries. It will consist of several 10s of IACTs of three different sizes (Large Size Telescopes, Mid Size Telescopes, and Small Size Telescopes). With a factor of 10 increase in sensitivity (1m Crab $\sim 10^{-14} erg\ s^{-1}\ cm^{-2}$), together with a much broader energy coverage from 20GeV up to 300TeV, CTA will bring forth further dramatic advances for VHE gamma ray astronomy. The discovery of more than 1000 Galactic and extragalactic sources is anticipated with CTA.

CTA will allow us to explore numerous diverse topics in physics and astrophysics. The century-old question of the origin of cosmic rays is expected to be finally settled through detailed observations of supernova remnants and other Galactic

objects along with the diffuse Galactic gamma ray emission, which will also shed light on the physics of the interstellar medium. Observing pulsars and associated pulsar wind nebulae will clarify physical processes in the vicinity of neutron stars and extreme magnetic fields. The physics of accretion onto supermassive black holes, the long-standing puzzle of the origin of ultra-relativistic jets emanating from them, as well as their cosmological evolution, will be addressed by extensive studies of active galactic nuclei (AGN). Through dedicated observing strategies, CTA will also elucidate many aspects of the mysterious nature of gamma ray bursts (GRBs), the most energetic explosions in the Universe. Detailed studies of both AGNs and GRBs can also reveal the origin of the highest energy cosmic rays in the Universe, probe the cosmic history of star formation including the very first stars, as well as provide high precision tests of theories of quantum gravity. Finally, CTA will search for signatures from elementary particles constituting dark matter with the highest sensitivity yet. Realisation of the rich scientific potential of CTA is very much feasible, thanks to the positive experience gained from the current IACTs.

The CTA-Japan consortium [1] is contributing in particularly to the construction of the Large Size Telescopes (LSTs) and is involved in their development. The LST covers the low energy domain from 20GeV to 3000GeV and is especially important for studies of high redshift AGNs and GRBs. The diameter and area of the mirror are 23m and 400m$^2$, respectively, in order to achieve the lowest possible energy threshold of 20GeV. All optical elements/detectors require high specifications, for example, high reflectivity, high collection efficiency, high quantum efficiency and ultra fast digitisation of signal, etc. For this purpose, CTA-Japan is developing high quantum efficiency photomultipliers, ultrafast readout electronics and high precision segmented mirrors. On the strength of their experience gained from construction of the MAGIC telescope, the Max-Planck-Institute for Physics in Munich is responsible for the design of the 23m diameter telescope structure, based on a carbon fiber tube space frame. The LSTs require very fast rotation (180 degrees/20seconds) for promptly observing GRBs. The first LST has been built in the CTA North, La Palma, Spain in 2018 and now in the commissioning, and three more LSTs will be built until 2022, then four more LSTs in the CTA South are expected to built in the ESO site in Paranal, Chile. The location of the LST array in the CTA North will overlap with MAGIC telescopes, which will allow us to operate CTA-LSTs and MAGIC telescopes together in the early phase of the construction.

The Cherenkov Cosmic Gamma Ray group is also operating the MAGIC Telescopes [10] on La Palma, Canary Islands. This facility is used not only for scientific observations but also for technological development toward the future observatory CTA.

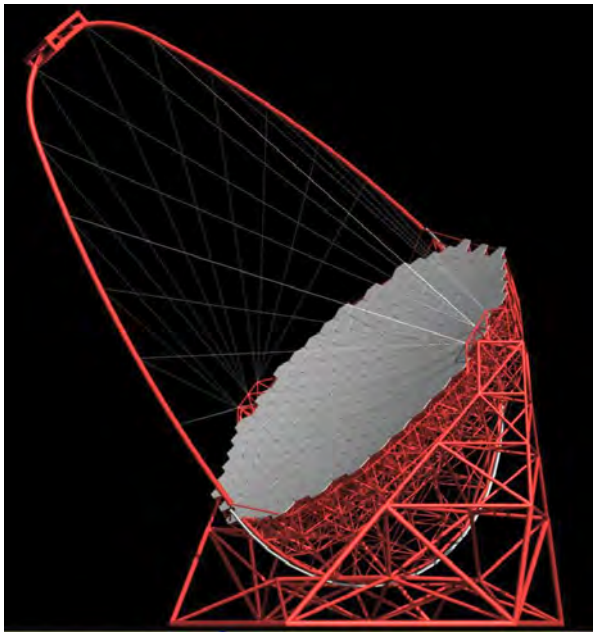

Fig. 2. Large Size Telescope (23m diameter) designed by Max–Planck-Institute for Physics. CTA Japan is contributing to the design and and construction of the imaging camera at the focal plane, ultrafast readout electronics, and high precision segmented mirrors.

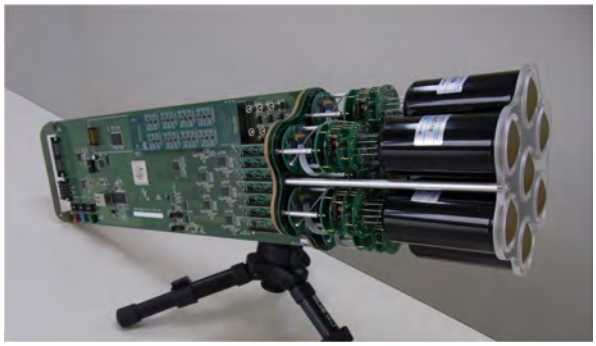

Fig. 3. Camera cluster for the Large Size Telescope (LST) developed by CTA-Japan. This cluster consists of seven high quantum efficiency photomultipliers (R11920-100), CW High Voltages, pre-amplifier, Slow Control Board, DRS4 Ultra fast waveform recording system and Trigger. The LST camera can be assembled with 265 of these clusters, cooling plates and camera housing.

Fig. 4. The high precision segmented mirrors for the Large Size Telescope (LST) developed by CTA-Japan in cooperation with Sanko Co.LTD. The mirror is made of a 60mm thick aluminum honeycomb sandwiched by 3mm thin glass on both sides. A surface protection coat consisting of the materials SiO2 and HfO2 is applied to enhance the reflectivity and to elongate the lifetime.

## Bibliography

[1] CTA Consortium website: `http://www.cta-observatory.jp/` and `http://www.cta-observatory.org/`.

[2] Science with the Cherenkov Telescope Array,

Fig. 5. The Large Size Telescope prototype (LST-1) under construction at Observatory de Roque de los Muchachos. The diameter of dish and mirror surface area are 23m and 400m$^2$.

Fig. 6. MAGIC Stereo System with two Cherenkov telescopes of 17m diameters, so far achieved the threshold energy of 25GeV. It locates near the mountain top of the Roque de los Muchachos on the Canary Island of La Palma. Two telescopes are located with the distance of 85 meters.

arXiv:1709.07997

[3] The Cherenkov Telescope Array potential for the study of young supernova remnants, Astropart. Phys. 62 (2015) 152-164.

[4] Introducing the CTA concept, The CTA Consortium, Astropart. Phys. 43 (2013) 3-18.

[5] Gamma-ray burst science in the era of the Cherenkov Telescope Array, S. Inoue et al., Astropart. Phys. 43 (2013) 252-275.

[6] Design Concepts for The Cherenkov Telescope Array, The CTA Consortium, Exper. Astron. 32 (2011) 193-316.

[7] Status of Very High Energy Gamma Ray Astronomy and Future Prospects, M. Teshima, The Astronomical Herald, 104 (2011) 333-342.

[8] Design Study of a CTA Large Size Telescope, Proc. of ICRC2012 at Beijing China, M. Teshima, arXiv:1111.2183.

[9] Introducing the CTA Concept, B. Acharya et al., Astroparticle Physics, 34 (2013) 3.

[10] MAGIC Collaboration website: `http://magic.mppmu.mpg.de/`.

### *MAGIC*

The MAGIC Collaboration has built in 2002 / 2003 a first large atmospheric imaging Cherenkov telescope, MAGIC-I, with a mirror surface of 236 sq.m. and equipped with photomultiplier tubes of optimal efficiency. In 2009, a second telescope of essentially the same characteristics was added; MAGIC-II was installed at a distance of 85m from MAGIC-I. With the accent of these instruments on large mirror surface and best light collection, cosmic gamma-rays at an energy threshold lower than any existing or planned terrestrial gamma-ray telescope have become accessible. So far achieved has been a threshold of 25 GeV. The Japanese group has joined the MAGIC collaboration since 2010, and contributed to the operation, observations and data analysis. The MAGIC telescopes are upgraded with new cameras, electronics and partially new mirrors in 2012, and are now operated with an unprecedented sensitivity by an international collaboration of 17 institutes from 8 countries.

The recent highlights from MAGIC are, 1) Observation of sub-TeV gamma rays from the IceCube170922A [1], [2] , 2) the successful observation of pulsed gamma ray signal from the Crab pulsar up to TeV regime [3], 3) the discoveries of the most distant blazers 3S 0218 + 35 with the redshift of 0.944 [4] and PKS 1441 + 25 with the redshift of 0.939 [5], 4) the observation of the very fast flare of 1min time scale from the blazar inside Perseus cluster, IC310 [6]. These results brought new questions on the pulsar emission mechanism, the EBL energy density, and gamma ray emission mechanism from the supermassive blackholes or vicinity of them. 5) In 2019 January, the MAGIC telescopes, for the first time, observed the TeV Gamma Ray Burst GRB 190114C [**?**]ith the redshift of 0.42 [7]. The observation shows about the 100 times higher flux of gamma rays than Crab Nebula. The highest-energy photon reaches above 1000GeV, and clearly, the new gamma-ray emission mechanism is required. The light curve shows the power-law decay $t^{-1.6}$.

## Bibliography

[1] First-time detection of VHE gamma rays by MAGIC from a direction consistent with the recent EHE neutrino event IceCube-170922A, ATel #10817.

[2] Multimessenger observations of a flaring blazar coincident with high-energy neutrino IceCube-170922A, Science 12 July 2018, Science.eaat1378.

[3] Phase-resolved energy spectra of the Crab pulsar in the range of 50-400 GeV measured with the MAGIC telescopes, the MAGIC Collaboration, Aleksić et al. A&A 540 (2012) A69.

[4] ATEL # 6349.

[5] Discovery of Very High Energy Gamma-Ray Emission from the distant FSRQ PKS 1441+25 with the MAGIC telescopes, ATEL # 7416.

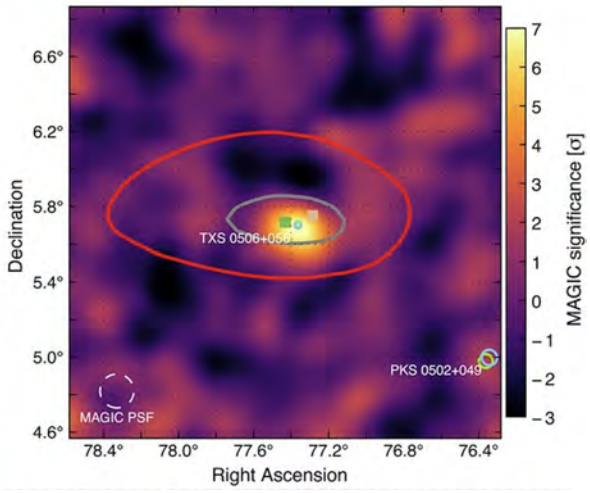


Fig. 7. Sky position of IceCube-170922A in the equatorial coordinate with contour of 50% and 90% confidence level overlaying the gamma-ray colour contour map observed by MAGIC (7 sigma in the peak).

Fig. 8. Akeno atmospheric Cherenkov telescope of 3 m diameter, located in the Akeno Observatory.

[6] Black hole lightning due to particle acceleration at sub-horizon scales, the MAGIC collaboration, Science 346 (2014) 1080-1084.

[7] The first detection of a GRB at sub-TeV energies; MAGIC detects the GRB190114C., ATEL # 12390.

### *Other Activities*

As a test bench for domestic R & D activities of future ground-based gamma-ray observatory projects, an old atmospheric Cherenkov telescope of 3 m diameter was repaired and then placed at the Akeno Observatory in November 2010. This telescope shown in Figure 8 (Akeno telescope, hereafter) is currently the only atmospheric Cherenkov telescope located in Japan [1]. We have developed an R & D imaging camera system with the Akeno telescope since 2009, the purpose of which is to make a battery-powered data acquisition system for a future mobile imaging atmospheric Cherenkov telescope array [2]. The system consists of 32 PMTs, of which detected Cherenkov light signals are read out by only four GHz-sampling analog memory ASICs.

After test observations of atmospheric Cherenkov light events in 2016, we performed observations of the Crab Nebula using this system in 2017. The Crab Nebula is the standard candle in the TeV gamma-ray energy region and utilized for checking performance of telescope systems. We could accumulate about 10 hr Crab data after two observation periods of about one week each. The data are under analysis for detecting the gamma-ray signal from the Crab and for estimating performance of the system.

## Bibliography

[1] M. Ohishi et al., Proc. of 33rd Internat. Cosmic Ray Conf. (Rio de Janeiro), 587 (2013).

[2] T. Yoshikoshi et al., Proc. of 34th Internat. Cosmic Ray Conf. (The Hague), 887 (2015).

# TA: Telescope Array Experiment

Spokespersons (S. Ogio[1], C.C.H. Jui[2])

1 : Graduate School of Science, Osaka City University
2 : Dept. of Physics and Astronomy, University of Utah

Collaborating Institutions:

Chiba Univ., Chiba, Japan; Chubu Univ., Kasugai, Japan; Earthquake Research Institute, Univ. of Tokyo, Tokyo, Japan; Ehime Univ., Matsuyama, Japan; Ewha W. Univ., Seoul, Korea; Hiroshima City Univ., Hiroshima, Japan; Hanyang Univ., Seoul, Korea; ICRR, Univ. of Tokyo, Kashiwa, Japan; INR, Moscow, Russia; Inst. of Phys, Czech Acad. of Sci., Prague, Czech; IPMU, Univ. of Tokyo, Kashiwa, Japan; Kanagawa Univ., Yokohama, Japan; KEK/ IPNS, Tsukuba, Japan; Kindai Univ., Higashi-Osaka, Japan; Kochi Univ., Kochi, Japan; Kyushu Univ., Fukuoka, Japan; Moscow M.V. Lomonosov State University; Moscow, Russia, Nat. Inst. of Rad. Sci., Chiba, Japan; Osaka Electro-Comm. Univ. Osaka, Japan Osaka City Univ., Osaka, Japan; RIKEN, Wako, Japan; Ritsumeikan Univ., Kusatsu, Japan; Rutgers Univ., Piscataway, NJ, USA; Saitama Univ., Saitama, Japan; Shinshu Univ., Nagano, Japan; SKKU, Suwon, Korea, Tokyo City Univ., Tokyo, Japan; Tokyo Inst. of Tech., Tokyo, Japan; Tokyo Univ. of Science, Noda, Japan; ULB, Brussels, Belgium; UNIST, Ulsan, Korea; Univ. of Utah, Salt Lake City, USA; Univ. of Yamanashi, Kofu, Japan; Waseda Univ., Tokyo, Japan; Yonsei Univ., Seoul, Korea

## Introduction

The Telescope Array (TA) is the largest Ultra-High Energy Cosmic Ray (UHECR) observatory in the northern hemisphere. The main aim of TA is to explore the origin and nature of UHECRs by measuring the energy spectrum, arrival direction distribution and mass composition. The TA collaboration consists of approximately 130 researchers from US, Russia, Korea, Belgium, Czech and Japan.

The TA detector consists of a surface array of 507 plastic scintillator detectors (SD) and three stations of fluorescence detectors (FD). It is located in the desert, approximately 200 km south from Salt Lake City in Utah in the U.S.A. The SDs were deployed on a square grid with 1.2-km spacing, and the SD array covers an area of $\sim$700 km$^2$. Each SD has two layers of 1.2-cm-thick scintillator with an area of 3 m$^2$. The full operation of SDs started in March 2008. The duty cycle is greater than 95%. The FDs view 3° - 31° or 33° above horizon. One northern FD station at the MD site uses refurbished HiRes telescopes. Two southern FD stations at the BR and LR sites were buit newly. All three FD stations started the observation in November 2007, and have duty cycles of approximately 10%.

The TA Low-Energy extension (TALE) enables detailed studies of the energy spectrum and composition from $\sim 10^{16}$ eV upwards. The main aim of TALE is to clarify the expected transition from galactic cosmic rays to extragalactic cosmic rays and the comparison of the data with Monte Carlo (MC) simulation that takes into account the results of the LHC experiments. The TALE detector is located north of the TA site (MD site). This FD station consists of refurbhised HiRes telescopes. The TALE FD views 31° - 59° in elevation angle. The TALE SD is described later.

We report the results from TA below.

## Energy Measurement

### TA energy spectrum

The preliminary result of cosmic-ray spectrum for nine years of the TA SD data is shown in Fig. 9 [1]. The systematic uncertainty of energy determination is 21%. TA confirmed the ankle at $10^{18.69\pm0.02}$ eV and the flux suppression above $10^{19.81\pm0.04}$ eV. The statistical significance of having the same spectral index above the ankle (no suppression) is $\sim 7\sigma$.

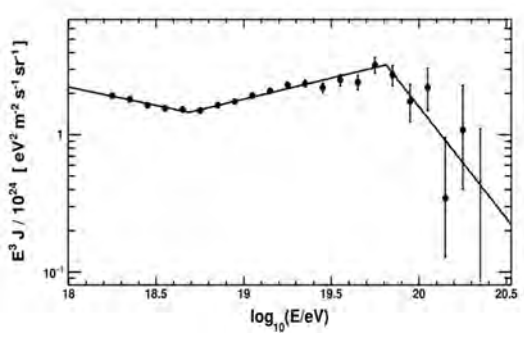


Fig. 9. The preliminary TA cosmic-ray flux multiplied by E$^3$ for TA SD nine-year data. The solid line shows the fit of the TA data to a broken power law.

### TALE energy spectrum

The energy spectrum using the TALE FD data between $\sim$2 PeV and 100 PeV is shown in Fig. 10 [2]. The events observed with the TALE FD are placed into three subsets: Cherenkov dominated events, fluoresence dominated events, and mixed signal events. We see two clear breaks at $10^{16.22\pm0.02}$ eV and $10^{17.04\pm0.03}$ eV. We possibly see the knee feature at around $10^{15.6}$ eV. It becomes of great importance to measure the composition precisely using hybrid events by adding the TALE SD array to understand this spectral feature. The TALE SD is described later.

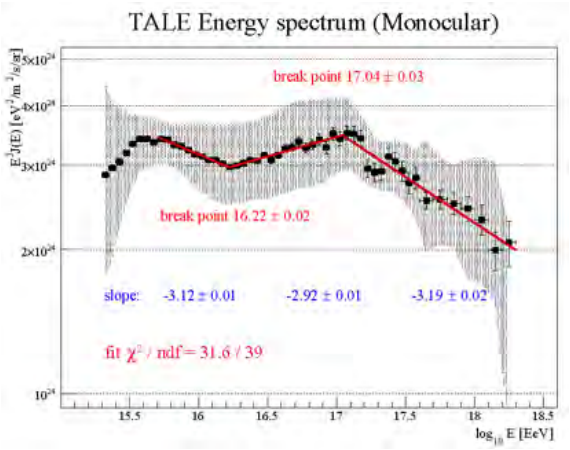


Fig. 10. a) TALE cosmic-ray energy spectrum. The gray band indicates the size of the systematic uncertainties.

### TA combined energy spectrum

Fig. 11 shows the TA combined spectrum (TA spectrum (Fig. 9) and the TALE spectrum (Fig. 10) together with the Pierre Auger Observatory (Auger) energy spectrum with energy shifts by +10.2% and the KASCADE-Grande energy spectrum. Good agreement between the TA combined (actually TALE) energy spectrum and the KASCDE-Grande energy spectrum is seen below $10^{18}$ eV. Significant discrepancy between the TA combined energy spectrum and the Auger combined energy spectrum is seen above around $10^{19.5}$ eV, whereas good agreement is seen below $10^{19.5}$ eV.

The TA and Auger collaborations formed a working group, and compared the TA and Auger spectra in the common declination ($\delta$) band (from -15.7° to +24.8°) as shown in Fig. 12a. The cutoff (or break) energies agree at 0.5$\sigma$ level. Based on this study, we compared TA energy spectra with $\delta > 25.8°$ and $\delta < 25.8°$and found the difference of the cutoff energies as shown in Fig. 12b. The chance probability of obtaining this difference is 3.5 $\sigma$ [3].

The TA collaboration performed the linearity check of SD with FD using hybrid events [4]. There was no evidence of nonlinearity. For energy estimation, we use MC energy table as the standard method. We compared it with the method of constant intensity cuts that is based on the idea that showers generated by primary cosmic rays with the same energy and composition would arrive at the detector with the same frequency due to the isotropy of the primary cosmic rays, assuming 100% detection efficiency. The results from both meth-

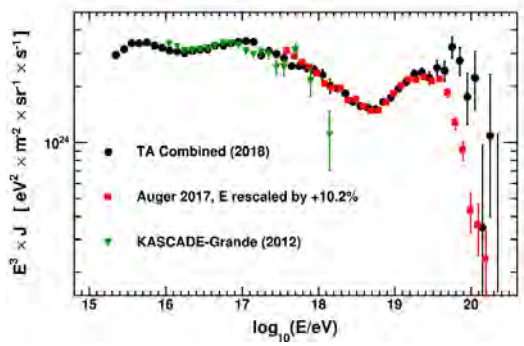


Fig. 11. The TA combined spectrum in black together with Auger combined energy spectra with energy shifts by +10.2% in red and KASCADE-Grande energy spectrum in green, respectively.

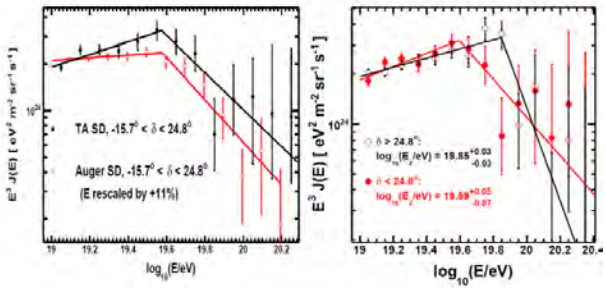


Fig. 12. a) The TA (black) and Auger (red) energy spectra of UHECR events in the common declination band after energy shift. b) The TA energy spectra for the declination angles below 24.8° in red and above 24.8° in black

ods are consistent. The TA energy estimation nonlinearity was finally evaluated as $-0.3 \pm 9\%$ per decade above $10^{19}$ eV. The Auger energy estimation nonnlineary was estimated to be $\pm 3\%$ per decade above $10^{19}$ eV [5].

## Mass Composition

### $X_{\rm max}$

The result of the depth of shower maximum $X_{\rm max}$ using the first 8.5 years of hybrid events using the surface detectors and the BR and LR FD telescopes was published [6]. Fig. 13 shows the evolution of the average $X_{\rm max}$ as a function of energy together with MC expectations for the BR and LR FD hybrid events, the MD FD hybrid events [7] and stereo FD only events [8]. All TA measurements are in agreement with each other. Here the BR/LR systematic errors are shown ($\pm 17.4$g/cm$^2$). The result is in agreement with light composition within systematic uncertainty.

The dependence of another parameter $\sigma(X_{\rm max})$, the width of $X_{\rm max}$, on energy is shown in Fig. 14. Below $10^{19}$ eV, the TA result is consistent with QGSJet II-04 proton model, whereas TA has insufficient exposure to make a careful measurement of the widths of $X_{\rm max}$ distributions above $10^{19}$ eV.

We checked the shape of $X_{\rm max}$ distributions, too. After allowing for systematic shfting of the data $X_{\rm max}$ and performing the likelihood test on the data and MC distributions, we find that we fail to reject QGSJet II-04 protons as being compatible with the data for all energy bins at the 95% confidence level as shown in Fig. 15. QGSJet II-04 helium, nitrogn and iron are rejected for $\log_{10}$(E) $< 19.0$, 19.2, and 19.4, respectively. For $\log_{10}$(E) $> 19.0$, TA has insufficient statistics to distinguish the difference between different composition.

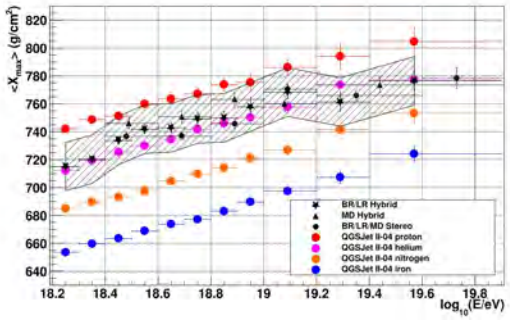


Fig. 13. The average reconstructed $X_{\rm max}$ as a function of energy. The black, red, magenta, orange and blue colors denote the data, pure proton, helium, nitrogen and iron QGSJet II-04 predictions, respectively. For data, stars, triangles and circles denote the results using the BR/LR hybrid, MD hybird and BR/LR/MD stereo events, respectively.

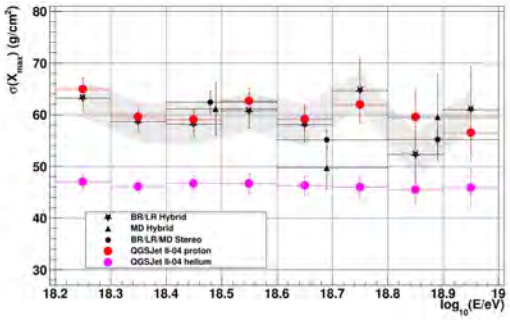


Fig. 14. The RMS of reconstructed $X_{\rm max}$ ($\sigma(X_{\rm max})$) as a function of energy. The black, red, magenta, orange and blue colors denote the data, pure proton, helium, nitrogen and iron QGSJet II-04 predictions, respectively. For data, stars, triangles and circles denote the results using the BR/LR hybrid, MD hybird and BR/LR/MD stereo events, respectively.

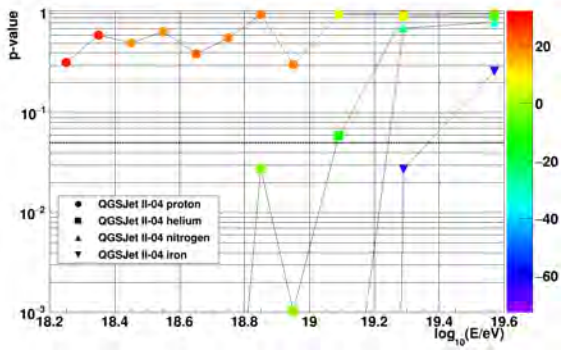


Fig. 15. Unbinned maximum likelihood test on observed and simulated QGSJet II-04 $X_{\rm max}$ distributions after systematic shifting of the data to find the best log likelihood.

### TA SD composition

The result on UHECR mass composition obtained with the TA SD is presented [9] using the boosted decision tree

multivariate analysis based on 14 observables sensitive to the properties of the shower front and the lateral distribution function. The multivariate classifier is trained with MC simulations with the QGSJET II-03 model. Within the errors, the average atomic mass of primary particles shows no significant energy dependence and corresponds to $< lnA >= 2.0 \pm 0.1$ (stat.) $\pm$ 0.44 (syst.). The obtained composition is qualitatively consistent with the TA hybrid results as shown in Fig. 16 while all the points lie higher than the pure proton composition..

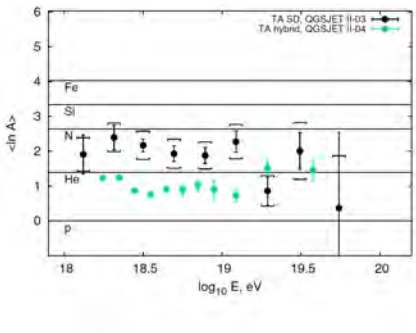


Fig. 16. The result of average atomic mass $< lnA >$ from the TA SD events in black in comparison with the TA hybrid results in green.

### TA muon studies

The number of muons in inclined air showers observed with water Cherenkov surface detectors at the Pierre Auger Observatory is approximately 1.8 times that of the proton prediction with QGSJET II-03 model at $10^{19}$ eV [10]. We studied muons in air showers using seven years of the TA SD data [11, 12]. Air shower events are classified using $\theta$, $\phi$ and $R$ parameters to search for the condition of high purity of muons. Here $\theta$ is the zenith angle of the shower axis, $\phi$ is the azimuthal angle of the location of a surface detector around the shower core on the ground, and $R$ is the distance of the location of the surface detector from the shower axis. The direction of zero degrees of $\phi$ is opposite to the cosmic-ray incident direction projected onto the ground. The counterclockwise direction is positive. The condition ( $30^\circ < \theta < 45^\circ$ and $150^\circ < |\phi| < 180^\circ$ (the older shower side in an inclined shower), 2000 m $< R <$ 4000 m) gives muon purity of $\sim$65% from the MC expectation at E $\sim 10^{19}$ eV. Typical ratios of charge densities of the data to those of the MC are $1.72 \pm 0.10$ (stat) $\pm$ 0.40 (syst) at 1910 m $< R <$ 2160 m and $3.14 \pm 0.36$ (stat) $\pm$ 0.72 (syst) at 2760 m $< R <$ 3120 m for QGSJET II-03 model together with other hadronic models as shown in Fig. 17. A similar excess is seen in comparison with other hadronic models.

### Search for the diffuse photons above $10^{18}$ eV

We present the search for photons using the first nine years of the TA SD data, employing multivariate analysis with the classifier based on the Boosted Decision Tree [13]. There are no photon candidates found in the data set for $10^{18.0}$, $10^{18.5}$, $10^{19.0}$, $10^{19.5}$ and $10^{20}$ eV, and the diffuse flux limits for photons are compared to the results of other experiments as shown in Fig. 18.

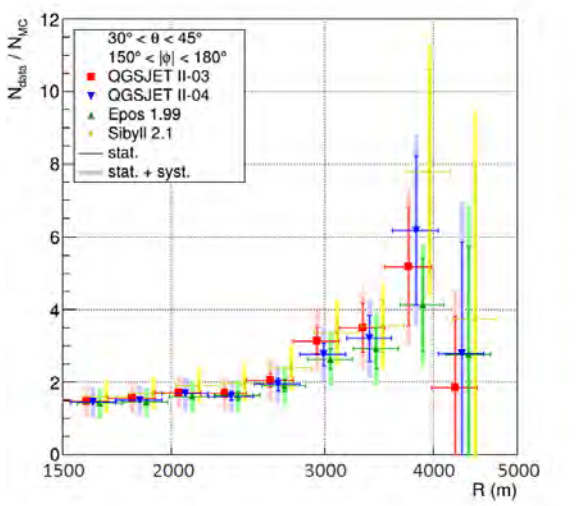


Fig. 17. The ratios of the average charge densities of the data to MC simulations as a function of core distance for $30^\circ < \theta < 45^\circ$, $150^\circ < |\phi| < 180^\circ$ and 1500 m $< R <$ 4500 m. The red, blue, green and yellow represent QGSJET II-03, QGSJET II-04, EPOS1.99 and SIBYLL2.1, respectively.

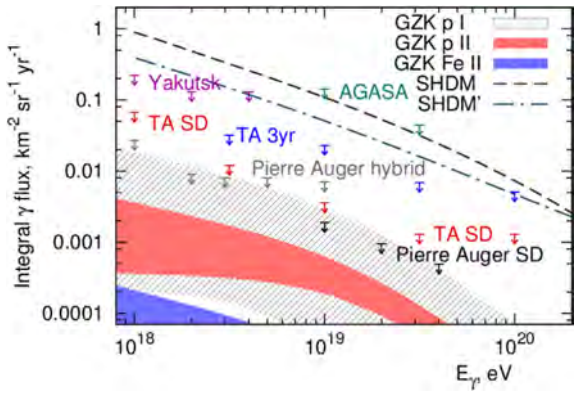


Fig. 18. The photon flux limit presented in [13] (TA SD, red arrows) compared with the results from AGASA (light blue), Pierre Auger Observatory SD (black) and hybrid data (gray), Yakutsk (magenta) and previously published TA SD result (TA 3yr, dark blue) and the predictions of some models.

## Arrival Directions of UHECRs

### TA hotspot for the highest-energy cosmic rays

We have searched for intermediate-scale anisotropy of 72 cosmic-ray events above $5.7 \times 10^{19}$ eV using the first five years of the TA SD data [14]. We reported a cluster of events that we call the hotspot, found by oversampling using circles 20° in radius. The hotspot has a Li-Ma pre-trial statistical significance of $5.1\sigma$. The probability of such a hotspot appearing by chance in an isotropic cosmic-ray sky is estimated to be $3.4\sigma$.

For the first ten years of the TA data, 157 events above $5.7 \times 10^{19}$ eV were observed. We scanned by circles with different radii and obtained the maximum Li-Ma pre-trial significance of $5.0\sigma$ at right ascension of 144.3° and declination of +40.3° with oversampling using circles with a radius of

25° [15]. The preliminary Li-Ma significance plot is shown in Fig. 19.

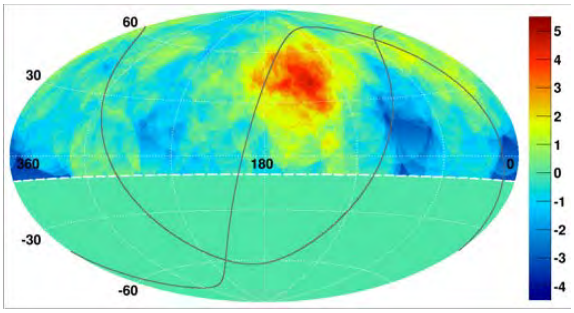


Fig. 19. Preliminary aitoff projection of Li-Ma significance map using cosmic-ray events above $5.7\times10^{19}$ eV for the first ten years of the TA SD data in equatorial coordinates. Our FoV is defined as the region above the dashed curve at decl. = -10°.

### Hot/cold spot

An energy dependent intermediate-scale anisotropy was studied using UHECRs above $10^{19.2}$ eV for seven years of the TA SD data [16]. The energy distributions inside oversampled circles are compared to that outside using the Poisson Likelihood Ratio test. The maximum pre-trial significance was obtained to be $6.17\sigma$ at right ascension of 139° and declination of 45°. The energy distribution within the circle at the center of maximum significance shows a deficit of events below $10^{19.75}$ eV and an excess above $10^{19.75}$ eV as shown in Fig. 20. The post-trial probability of this energy anisotropy, appearing by chance anywhere on isotropic sky, is found to be $9\times10^{-5}$ ($3.74\sigma$) by MC simulation.

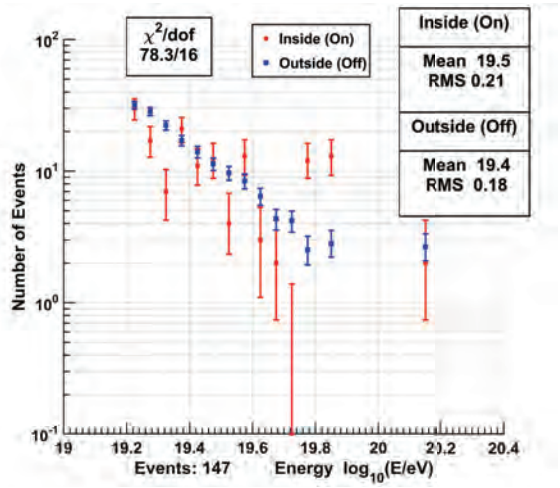


Fig. 20. The histogram of energies of events inside the spherical cap bin of radius 28.43° (red) at the maximum pre-trial significance. It's compared to the histogram of expected (normalized outside) energies (blue).

### Small-scale clusters above $10^{20}$ eV

We searched for small-scale clusters for the highest-energy cosmic rays observed with the Telescope Array and the Pierre Auger Observatory. Here we used $10^{20}$ eV as the energy threshold although we have not adjusted the energy scales of TA and Auger. Fig. 21 shows the arrival directions of the TA events and Auger events above $10^{20}$ eV [15]. The distance of arrival directions of two cosmic rays is required to be less than $\sqrt{2}$ degrees. We observed two doublets in the sample of nine years of the TA events and six years of the Auger events. The preliminary probability to have greater than and equal to two doublets at less than $\sqrt{2}$ degrees is 0.30% ($2.8\sigma$).

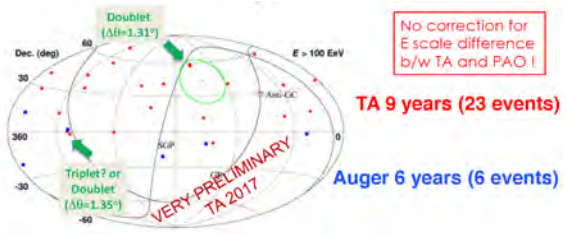


Fig. 21. The arrival directions of the TA events (red) and Auger events (blue) above $10^{20}$ eV in the equatorial coordinates.

### Search for correlation with starburst galaxies

Auger reported a correlation between the arrival directions of cosmic rays with energies above $3.9\times10^{19}$ eV and the flux pattern of 23 nearby starburst galaxies (SBGs) [17]. It was found that the starburst model fits the data better than the hypothesis of isotropy with a statistical significance of $4.0\sigma$, the highest value of the test statistic being for energies above $3.9\times10^{19}$ eV with SBG fraction of 9.7% and the search radius of 12.9°.

TA tested the Auger SBG hypothesis. Here we used the energy threshold of $4.3\times10^{19}$ eV when taking into account the energy-scale difference between two experiments. We found that the TA data is compatible with isotropy to within $1.1\sigma$ and with the Auger SBG hypothesis to within $1.4\sigma$.

## Interdisciplinary research

### TA SD burst events in coincdence with lightning

The TA SD observed several short-time bursts of air shower like events for the first five years. The expectation of chance coincidence is less than $10^{-4}$. We found evidence for correlations between these bursts of the TA SD events and powerful lightning data obtained with the National Lightning Detection Network in timing and position [20]. After installting a 3-D lightning mapping array and electric field change instrument at the TA SD site, detailed features were observed [21]. The observations provide a general description of downward-directed terestrial gamma flashes associated with downward negative lightning leaders. The result indicates that the showers consist primarily of downward-beamed gamma radiation, which is supported by GEANT simulation studies. We conclude that the showers are terrestrial gamma ray flashes, similar to those observed by satellites.

## TA extension

### TAx4

As mentioned above, TA found evidence for intermediate-scale anisotropy of arrival directions of cosmic rays with greater than $5.7\times10^{19}$ eV. With enhanced statistics, we expect

to observe the structure of the hotspot along with other possible excesses and point sources along with the correlations with extreme phenomena in the nearby universe. We proposed to quadruple the effective area of the TA SD aperture including the existing TA SD array (TAx4) by installing additional 500 counters of the current TA SD design on a square grid with wider, 2.08-km spacing between each [22, 23]. The new array would need two FD stations overlooking it to increase the number of hybrid events for the measurement of $X_{\rm max}$ and to confirm the energy scale. These FDs will be formed using additional refurbished HiRes telescopes.

The proposal of the SD part of TAx4 that was approved for the Japan Society for the Promotion of Science (JSPS) Grant-in-Aid for Scientific Research on Specially Promoted Research in Japan in 2015 as a five-year project. The TAx4 scintillator counters were assembled at MEISEI ELECTRIC CO., LTD in 2016 and at the Akeno Observtory in 2016, 2017 and 2018 as shown in Fig. 23. The assembled counters were sent to Utah, and the final assembly of the TAx4 SDs was partially performed at the Cosmic Ray Center in Delta city near the TA site. The SD deployment was performed in February and March of 2019. The FD part of TAx4 was approved by NSF in the USA in 2016. The TAx4 FD at the northern site was completed and started the stable operation in February of 2018. The TAx4 FD at the southern site is under construction in 2018. The layout of TAx4 is shown in Fig. 22 together with TALE.

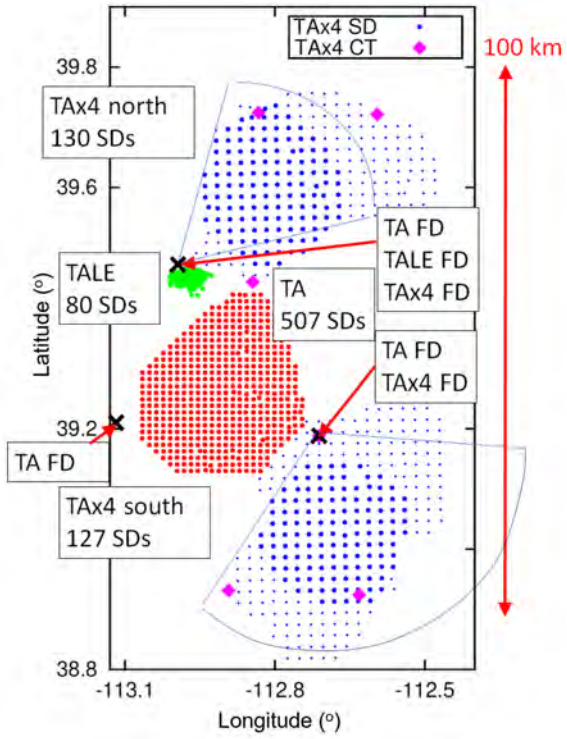


Fig. 22. The layout of the proposed TAx4. The array of 507 SDs (red filled circles on the left) is the current TA SD array. There are three TA FD stations (MD to the north, LR to the west, and BRM to the east of the TA SD array) with black cross symbols. The array of surface detectors (green) to the north of the TA SD array is the TALE SD array. Additional two sub-arrays of 500 surface detectors in total (blue) for TAx4 are located to the northeast and southeast of the TA SD array. The 257 large blue filled circles denote deployd SDs, whereas remaining blue dots denote SDs to be deployed. Additional two FD stations with refurbished HiRes telescopes for the TAx4 are located at the MD and BRM FD sites and view to the northeast and southeast as denoted each by the blue frame of the fan. Purple diamod symbols denote TAx4 communications towers.

## TALE

The layout of TALE is shown in Fig. 22. The TALE FD operation was commenced in the spring of 2013. We saw two clear breaks in the energy spectrum measured with the TALE FD as shown in Fig. 10. It is of importance to measure $X_{\rm max}$ precisely adding timing information of surface detectors near the shower core on the ground. The TALE SD array consists of 80 plastic scintillation counters, which are identical to those of the TA SD array. These counters have graded spacings, ranging from 400 m near the FD to 600 m further away. The 35 TALE SDs were firstly deployed in 2013. Therefore we proposed to complete the full TALE SD array. The proposal of adding remaining SDs in the TALE SD array was approved for the JSPS Grant-in-Aid for Scientific Research (S) in 2015 as a five-year project. The full TALE SDs were deployed in February of 2017. The TALE SD array is in stable operation [24]. Fig. 24 is an example of the footprint of a TALE SD event.

The observation of cosmic rays with energies down to $10^{15}$ eV, called the Non-Imaging CHErenkov (NICHE) array [25], was proposed. The plan is to install an array of simple Cherenkov counters of PMTs each three inches in diameter on the ground looking upwards within the TALE SD array. The part of the NICHE with 15 PMTs, called jNICHE, was constructed by the JSPS Grant-in-Aid for Young Scientists (A).

## R&D for future detectors

To collect much larger statistics at the highest energies, observatories of significantly larger aperture are needed to identify sources via anisotropy studies. Because of the prohibitive cost, it may be difficult to build a sufficiently large detector using existing technologies. Hence, it is important to develop new detectors. The TA site is used worldwidely for R&D of future detectors.

The JEM-EUSO is a new type of observatory that will utilize very large volumes of the earth's atmosphere as a detector of the highest-energy cosmic rays from the universe. K-EUSO [26] employs the technologies developed for the JEM-EUSO mission and will be mounted to the International Space Station (ISS) . K-EUSO is a wide-field (40°), fast, and large telescope, and observes brief UV flashes in the earth's atmosphere caused by the highest-energy cosmic rays. The advantage is its rather uniform and huge aperture in the whole sky. EUSO-TA, which is a EUSO prototype installed at the TA BRM FD site in 2013, has been tested occasionally. The first result from EUSO-TA for laser shots, star images, and UHECRs in association with those observed with the BRM FD was published in [27].

New types of fluorescence detector were proposed for large area and low-cost detection of UHECRs such as FAST with reflecting mirrors [28] and CRAFFT with fresnel

Fig. 23. Assembly of a plastic scintillator counter at the assembly hall of the Akeno Observatory

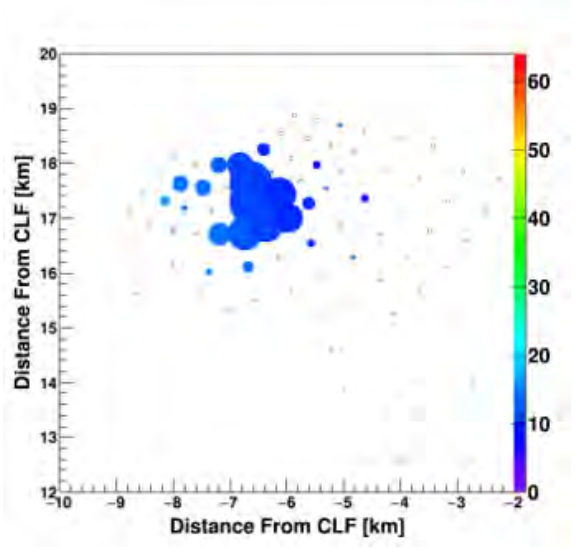


Fig. 24. An example of the footprint of a TALE SD event

lenses [29]. They were installed at the BRM FD site, and the observations of UHECRs are being performed.

## Summary

TA confirmed the ankle at $10^{18.7}$ eV and the flux suppression above $10^{19.8}$ eV. The statistical significance of having the same spectral index above the ankle (no suppression) is $\sim 7\sigma$.

We confirmed the breaks at $10^{16.2}$ eV and $10^{17.0}$ eV in the energy spectrum measured with the TALE FD.

The $X_{\rm max}$ measurement above $10^{18.2}$ eV is consistent with light composition. We need more statistics to clarify the feature above $10^{19}$ eV.

We obtained 143 cosmic-ray events above $5.7\times10^{19}$ eV in the nine years of the TA SD data. By scanning the sizes of circles for oversampling these events, we found maximum Li-Ma significance at $\sim 5\sigma$. Its significance appearing in an isotropic cosmic-ray sky is $\sim 3\sigma$. Evidence for some features of spectral anisotropy is seen.

In order to confirm the TA hotspot and understand its feature, we are constructing TAx4, which would quadruple the TA SD aperture and would add two FD stations. The assembly of the TAx4 SDs is under way. One of the TAx4 FDs at two sites was completed and started its operation in February, 2018.

The TALE SDs were fully deployed at the TALE site, and the data acquisition system is been checked. TA, TAx4, TALE, TAx4 and NICHE will provide important measurements of energy spectrum, composition, and arrival directions of UHECRs from the knee region up to the highest-energy region of over five to six decades in energy.

The TA BRM FD site is used for R&D of future detectors with larger aperture. The prototype (EUSO-TA) of JEM-EUSO has been tested occasionally since 2013. The first result from EUSO-TA was summarized in [27]. New types of fluorescence telescope consisting of a small number of PMTs that aim at a future large and low-cost detector of UHECRs such as FAST and CRAFFT are tested.

## Bibliography

[1] J.N. Matthews, “Highlights from the Telescope Array”, The 35th International Cosmic Ray Conference (ICRC2017), 2017/7/17 (invited).

[2] R.U. Abbasi *et al.* “Cosmic-Ray Energy Spectrum between 2 PeV and 2 EeV Observed with the TALE detector in monocular mode”, Astrophys. J. 865:74 (18pp), 2018, arXiv:1803.01288.

[3] R.U. Abbasi *et al.*, “Evidence for Declination Dependence of Ultrahigh Energy Cosmic Ray Spectrum in the Northern Hemisphere”, submitted to Astrophys. J., arXiv:1801.07820.

[4] D. Ivanov, “TA Spectrum”, Ultra-High-Energy-Cosmic-Ray Conference (UHER2018), 2018/10/08 (oral).

[5] D. Ivanov, “Auger-TA Energy Spectrum Working Group Report”, UHECR2018, 2018/10/08 (oral).

[6] R.U. Abbasi *et al.*, “Depth of Ultra HIgh Energy Cosmic Ray Induced Air Shower Maxima Measured by the Telescope Array Black Rock and Long Ridge FADC Fluorescence Detectors and Surace Array in Hybrid Mode”, Astrophys. J., 858:76 (27pp), 2018, arXiv:1801.09784.

[7] J. Lundquist, PoS ICRC2015 (2016) 441.

[8] D. Bergman and T. Stroman, PoS ICRC2017 (2018) 538.

[9] R.U. Abassi *et al.*, “Mass composition of ultra-high-energy cosmic rays with the Telescope Array Surface Detector Data”, Phys. Rev. D. 99, 022002, arXiv:1808.03680.

[10] A. Aab *et al.*, (Pierre Auger Collaboration), Phys. Rev. D 91 032003 (2015).

[11] R. Takeishi, ”Study of muons from ultra-high energy cosmic ray air showers measured with the Telescope Array experiment”, University of Tokyo (2016).

[12] R.U. Abbasi *et al.*, “Study of muons from ultra-high energy cosmic ray air showers measured with the Telescope Array experiment”, Phys. Rev. D 98, 022002 (2018).

[13] R.U Abbasi *et al.*, "Constraints on the diffuse photon flux with energies above $10^{18}$ eV using the surface detector of the Telescope Array experiment", Astroparticle Physics 110 (2019) 8-14, arXiv:1811.03920.

[14] R.U. Abbasi *et al.*, "INDICATIONS OF INTERMEDIATE-SCALE ANISOTROPY OF COSMIC RAYS WITH ENERGY GREATER THAN 57 EeV IN THE NORTHERN SKY MEASURED WITH THE SURFACE DETECTOR OF THE TELESCOPE ARRAY EXPERIMENT", Astrophys. J. Lett. 790:L21 (2014).

[15] K. Kawata, "TA Anisotropy Summary", UHECR2018, 2018/10/10 (oral).

[16] R.U. Abbasi. *et al.*, "Evidence of Intermediate-scale Energy Spectrum Anisotropy of Cosmic Rays E $\geq 10^{19.2}$ eV with the Telescope Array Surface Detector", Astrophys. J. 862:91 (6pp), 2018, arXiv:1802.05003.

[17] A. Aab *et al.*, Astrophysical Journal Letters, 853,:L29 (2018).

[18] R.U. Abbasi *et al.*, "Testing a Reported Correlation between Arrival Directions of Ultra-high-energy Cosmic Rays and a Flux Pattern from nearby Starburst Galaxies using Telescope Array Data", Astrophysical Journal Letters, 867:L27 (5pp), 2018.

[19] R.U. Abbasi *et al.*, "Search for Anisotropy in the Ultra High Energy Cosmic Ray Spectrum using the Telescope Array Surface Detector", submitted to Phys. Rev. Lett., arXiv:1707.04967.

[20] R.U. Abbasi *et al.* "The bursts of high energy events observed by the telescope array surface detector", Phys. Lett., A381 (2017) 2565-2572.

[21] R.U. Abbasi *et al.*, "Gamma Ray Showers Observed at Ground Level in Coincidence With Downward Lightning Leaders", J. Geophys. Res: Atmos., 123 (2018).

[22] H. Sagawa, "The plan of the Telescope Array Experiment for the Next Five Years", ICRC2013, 2013/7/2-7/9 (poster).

[23] E. Kido, "The TAx4 experiment", ICRC2017, Busan, Korea, 2017/7/15 (oral).

[24] S. Udo, "The Telescope Array Low-energy Extension", ICRC2017, Busan, Korea, 2017/7/15 (oral).

[25] D. Bergman, "j-NICHE: Prototype detectors of a non-imaging Cherenkov array at the Telescope Array site", ICRC2017, Busan, Korea, 2017/7/17 (oral).

[26] M. Casolino "KLYPVE-EUSO: Science and UHECR observational capabilities", ICRC2017, Busan, Korea (2017).

[27] G. Abdellaoui et al., JEM-EUSO Collaboration, "EUSO-TA - First results from a ground-based EUSO telescope", Astrop. Phys. 102 (2018) 98-111.

[28] T. Fujii, "First results from the full-scale prototype for the Fluorescence detector Array of Single-pixel Telescopes", ICRC2017, Busan, Korea, 2017/7/17 (oral).

[29] Y. Tameda, "The Cosmic Ray Air Fluorescence Fresnel lens Telescope (CRAFFT) for the next generation UHECR obsevatory", ICRC2017, Busan, Korea, 2017/7/18 (poster).

## Tibet AS$\gamma$ Project

[Spokesperson: M. Takita]
ICRR, The Univ. of Tokyo, Kashiwa, Chiba 277-8582

## 1. Experiment

The Tibet air shower experiment has been successfully operated at Yangbajing (90°31′ E, 30°06′ N; 4300 m above sea level) in Tibet, China since 1990. It has continuously made a wide field-of-view (approximately 2 steradian) observation of cosmic rays and gamma rays in the northern sky.

The Tibet I array was constructed in 1990 and it was gradually upgraded to the Tibet II by 1994 which consisted of 185 fast-timing (FT) scintillation counters placed on a 15 m square grid covering 36,900 $m^2$, and 36 density (D) counters around the FT-counter array. Each counter has a plastic scintillator plate of 0.5 $m^2$ in area and 3 cm in thickness. All the FT counters are equipped with a fast-timing 2-inch-in-diameter photomultiplier tube (FT-PMT), and 52 out of 185 FT counters are also equipped with a wide dynamic range 1.5-inch-in-diameter PMT (D-PMT) by which we measure up to 500 particles which saturates FT-PMT output, and all the D-counters have a D-PMT. A 0.5 cm thick lead plate is put on the top of each counter in order to increase the counter sensitivity by converting gamma rays into electron-positron pairs in an electromagnetic shower. The mode energy of the triggered events in Tibet II is 10 TeV.

In 1996, we added 77 FT counters with a 7.5 m lattice interval to a 5,200 $m^2$ area inside the northern part of the Tibet II array. We called this high-density array Tibet HD. The mode energy of the triggered events in Tibet HD is a few TeV.

In the late fall of 1999, the array was further upgraded by adding 235 FT-counters so as to enlarge the high-density area from 5,200 $m^2$ to 22,050 $m^2$, and we call this array and further upgraded one Tibet III. In 2002, all of the 36,900 $m^2$ area was covered by the high-density array by adding 200 FT-counters more. Finally we set up 56 FT-counters around the 36,900 $m^2$ high density array and equipped 8 D-counters with FT-PMT in 2003. At present, the Tibet air shower array consists of 761 FT-counters (249 of which have a D-PMT) and 28 D-counters as in Fig. 1.

The performance of the Tibet air shower array has been well examined by observing the Moon's shadow (approximately 0.5 degrees in diameter) in cosmic rays. The deficit

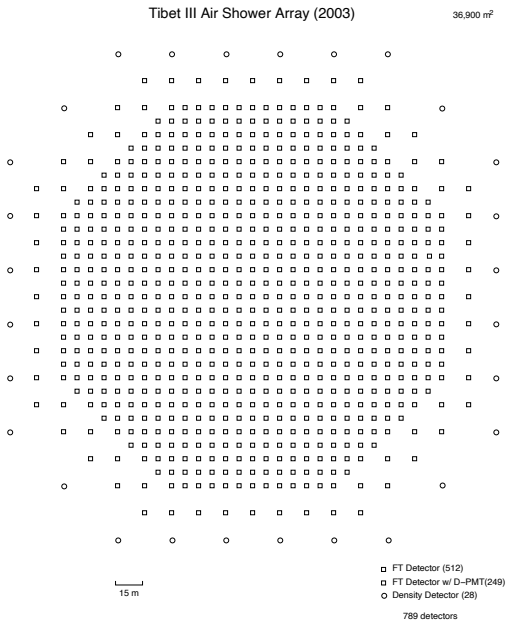


Fig. 1. Schematic view of Tibet III.

map of cosmic rays around the Moon demonstrates the angular resolution to be around 0.9° at a few TeV for the Tibet III array. The pointing error is estimated to be better than ∼0.01°, as shown in Fig. 2, by displacement of the shadow center from the apparent center in the north-south direction, as the east-west component of the geomagnetic field is very small at the experimental site. On the other hand, the shadow center displacement in the east-west direction due to the geomagnetic field enables us to spectroscopically estimate the energy scale uncertainty at ±12 % level, as shown in Fig. 3. Thus, the Tibet air shower experiment introduces a new method for energy scale calibration other than the conventional estimation by the difference between the measured cosmic-ray flux by an air shower experiment and the higher-energy extrapolation of cosmic-ray flux measured by direct measurements by balloon-borne or satellite experiments.

## 2. Physics Results

Our current research theme is classified into 4 categories:

(1) TeV celestial gamma-ray point/diffuse sources,

(2) Chemical composition and energy spectrum of primary cosmic rays in the knee energy region,

(3) Cosmic-ray anisotropy in the multi-TeV region with high precision,

(4) Global 3-dimensional structure of the solar and interplanetary magnetic fields by observing the Sun's shadow in cosmic

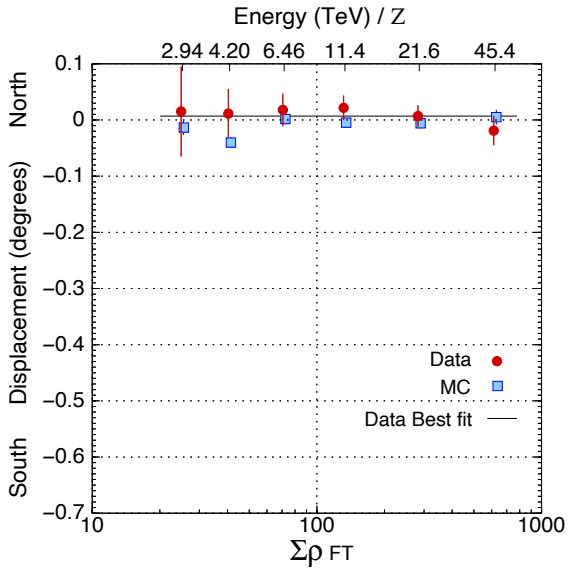


Fig. 2. From [1]. The Moon's shadow center displacement from the apparent position in the north-south direction as a function of energy, observed by Tibet III.

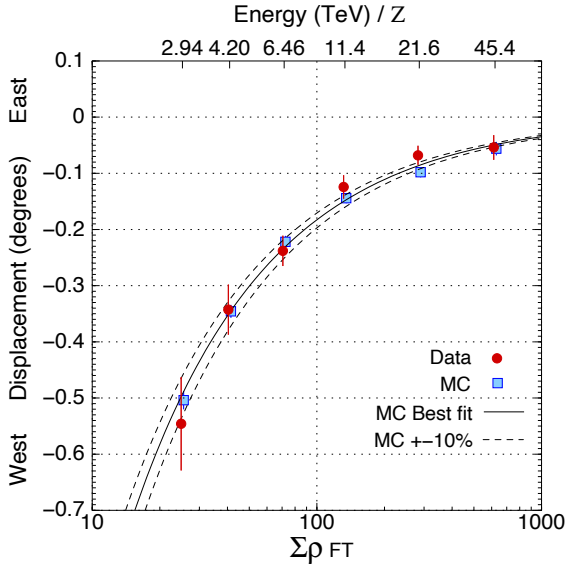


Fig. 3. From [1]. The Moon's shadow center displacement from the apparent position in the east-west direction as a function of energy, observed by Tibet III.

rays.

We will introduce a part of the results obtained in this fiscal year[2].

High-energy galactic cosmic rays arriving from the direction behind the Sun are shielded by the Sun and cast a shadow (Sun's shadow) in the galactic cosmic-ray intensity, which is affected by the solar magnetic field. Coronal mass ejections (CMEs) are large magnetized clouds of plasma ejected by solar eruptions going into the interplanetary space. A fast CME forms a strong shock wave and a magnetic sheath containing the turbulent magnetic field behind the shock front. CMEs sometimes have rope-like magnetic structures behind

the magnetic sheath. A CME spreading away from the Sun influences galactic cosmic rays in many manners. The famous phenomenon is the so-called "Forbush decrease," which is observed when an observation appratus is included in a region of suppressed galactic cosmic-ray density behind the shock caused by a CME. The CMEs may sometimes trigger major geomagnetic storms when they reach the Earth.

As the currently feasible measurements on board a satellite provide the one-dimensional distributions of the magnetic field in the CME along the satellite's orbit, there exist difficulties to precisely derive the three-dimensional magnetic structure of a CME. Galactic cosmic rays at TeV and sub-TeV energies with large Larmor radii can sense the remote CMEs and give useful additional information on their structure. Observations of these high-energy GCRs are also relevant to space weather, because these particles travel nearly at the speed of light, sense the CME, and escape into the upstream region of the shock. They can easily overtake the much slower CME, warning in advance of the Earth-directed CME (ECME) approaching the Earth. The solar modulation of galactic cosmic rays at sub-TeV energies has been already reported, but the influence of ECMEs has not been measured in the energy region exceeding 1 TeV. Therefore, using the Sun's shadow observed by Tibet-III, we studied the influence of ECMEs on the Sun's shadow observed in the 3 TeV galactic cosmic-ray intensity.

As regards the solar magnetic field model in the MC simulation, employed is the CSSS model. The CSSS model is a potential field model which reproduces the yearly variation of the Sun's shadow observed with Tibet-II at 10 TeV . The potential field models describe the coronal magnetic field based on the optical measurements of the photospheric magnetic field. We employ the photospheric field observed with the spectromagnetograph of the National Solar Observatory at Kitt Peak for each Carrington rotation (CR) period ($\sim$27.3 days) in the simulation. The CSSS model includes four free parameters, the radius $R_{\rm cp}$ ($= 1.7R_{\odot}$) of the sphere where the magnetic cusp structure in the helmet streamers appears, and the length scale $l_a$ of horizontal coronal electric currents, the radius $R_{\rm ss}$ of the spherical source surface (SS) where the supersonic solar wind starts blowing radially, and the order $n$ of the spherical harmonic series describing the observed photospheric field. We set $l_a$ to be one solar radius ($l_a = R_{\odot}$) and check two different cases with $R_{\rm ss}$ =2.5$R_{\odot}$ and $R_{\rm ss}$ = 10$R_{\odot}$. The former $R_{\rm ss}$ is a standard value used in the original study, while the latter gained support from some recent evidences. We set $n = 10$ which is sufficient to describe fine structures relevant to the orbital motion of high-energy particles with large Larmor radii. The radial component of the coronal magnetic field at $R_{\rm ss}$ is then stretched out forming the Parker's spiral interplanetary magnetic field (IMF). For the radial solar wind speed needed in the Parker's model, we use the solar wind speed synoptic chart estimated from the interplanetary scintillation measurement in each CR and averaged over the Carrington longitude. A dipole model is employed for the geomagnetic field.

Simulating primary galactic cosmic rays causing the Sun's shadow, we assume the energy spectra and the elemental compositions modeled by compiling various measurements between 0.3 TeV and 1000 TeV. The minimum energy of primary particles is set at 0.3 TeV, below the threshold energy for triggering our air shower detection. we randomly generate air shower events at the top of the atmosphere along the Sun's orbit using the CORSIKA code with the EPOS-LHC interaction model so that air shower cores are uniformly distributed within 300 m radius from the center of array. This area within 300 m from the center sufficiently covers detectors actually hit by air shower particles. We then distribute these simulated events among detectors configuring Tibet-III by the GEANT4 code and calculate the output of each detector, which can be analyzed for AS reconstruction and event selections in the same way as the experimental data. Then, an opposite charge is allocated to each primary particle at the top of the atmosphere and randomly throw it within 4° radios centered at the Sun, and we define it as the initial shooting direction. Subsequently, the orbital motion of each particle is bacctraced to the Sun in the assumed magnetic fields by the fourth-order Runge-Kutta method. Finally, its initial shooting direction is regarded as the direction contributing to the intensity deficit in the Sun's shadow, if a particle hits the photosphere. The final expected Sun's shadow equivalent to the observation is obtained, smearing initial shooting directions by the angular resolution event by event.

Air shower events observed from the direction of the Sun by Tibet-III in 2000-2009 are analyzed. The modal energy and the angular resolution of primary galactic cosmic rays recorded with the array are estimated to be 3 TeV and 0°.9, where we define the angular resolution as an angular radius containing 50% of air shower events. The number of on-source events ($N_{\rm on}$) is calculated as the number of events coming from a certain direction within a circular window centered at a certain point on the celestial sphere. The number of background events, namely, off-source events ($\langle N_{\rm off}\rangle$), on the other hand, is calculated as the number of events averaged over within each of the eight off-source windows which are located at the same zenith angle as the on-source window, but apart by $\pm$9°.6, $\pm$12°.8, $\pm$16°.0 and $\pm$19°.2 in the azimuthal direction. The window radius of 0°.9 (angular resolution for 3 TeV galactic cosmic rays) is adopted for calculating both $N_{\rm on}$ and $\langle N_{\rm off}\rangle$. We calculate $N_{\rm on}$ and $\langle N_{\rm off}\rangle$ on each gridpoint on 0°.1 $\times$ 0°.1 mesh of the geocentric solar ecliptic (GSE) longitude and latitude surrounding the optical center of the Sun. We then estimate the deficit relative to the number of background events as $D_{\rm obs} = (N_{\rm on} - \langle N_{\rm off}\rangle)/\langle N_{\rm off}\rangle$ at every grid. As for calibration purpose, the Moon's shadow in the equatorial coordinate system is calculated in a similar manner.

Figures 4 (a) and (b) show yearly maps of $D_{\rm obs}$ in the Sun's and the Moon's shadows, respectively, observed at 3 TeV in 2000-2009, except for 2006, which is excluded from Figure 4 (a) because of insufficient statistics. The Moon's shadow provides us with a good reference of the detector stabilities, because the Moon has no magnetic field and its diameter observed at the Earth is almost the same as that of the Sun. It is seen in Figure 1 (a) that the Sun's shadow is darker (with larger negative $D_{\rm obs}$) around 2008 when the solar activity was close to the minimum, while it becomes faint (with smaller negative $D_{\rm obs}$) around 2001 when the activity was close to the maximum. In contrast, the observed Moon's shadow shown in Figure 4 (b) is quite stable, ensuring the instrumental stability

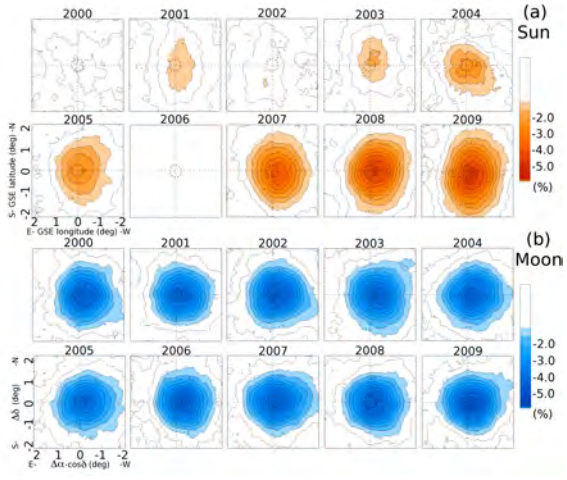


Fig. 4. From [2]. Year-to-year variation of (a) the Sun's shadow and (b) Moon's shadow observed by the Tibet-III array between 2000 and 2009. The upper panels show 2D contour maps of $D_{\rm obs}$ in the Sun's shadow in the GSE coordinate system, while the lower panels display $D_{\rm obs}$ in the Moon's shadow each as a function of right ascension and declination relative to the apparent center of the Moon.

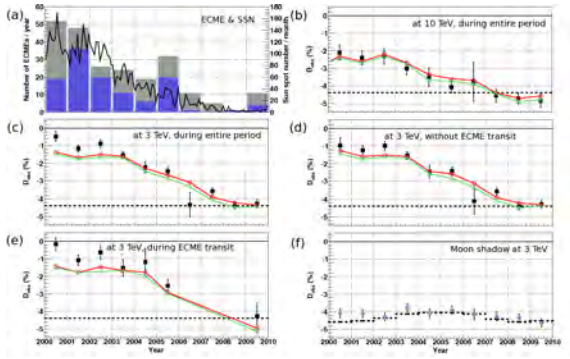


Fig. 5. From [2]. Temporal variations of $D_{\rm obs}$ in the Sun's shadow during ten years between 2000 and 2009. For reference, panel (a) shows the variations of the monthly mean sunspot number and the number of ECMEs recorded in each year plotted on the right and left vertical axes, respectively. The gray histogram in panel (a) shows all ECMEs listed in the catalog by [**?**], while the blue histogram displays only ECMEs each with the transit periods covered by the observation of the Sun's shadow by the Tibet-III array. The solid squares in each panel from (b) to (f) display (b) $D_{\rm obs}$ in the Sun's shadow observed at 10 TeV by the same detector configuration as the Tibet-II array [3], (c) $D_{\rm obs}$ in the Sun's shadow observed by the Tibet-III array at 3 TeV during an entire period, (d) $D_{\rm obs}$ of the Sun's shadow at 3 TeV observed during a period without ECMEs transit periods, (e) $D_{\rm obs}$ of the Sun's shadow at 3 TeV observed during the ECME transit periods that are excluded in (d), and (f) $D_{\rm obs}$ of the Moon's shadow at 3 TeV. The error bars indicate the statistical errors. The dashed lines in panels (b)-(e) and a dashed curve in (f) indicate $D_{\rm obs}$ expected from the apparent angular size of the Sun and the Moon. The red open circles and green open triangles in panels (b)-(e) display $D_{\rm obs}$ predicted by two different MC simulations using the CSSS models with $R_{\rm ss}$ = 2.5$R_\odot$ and $R_{\rm ss}$ = 10.0$R_\odot$, respectively.

during the same period.

Then, analyzed is the yearly variation of $D_{\rm obs}$, measured at the center of the yearly mean 2D map in Figure 4 (a). The solid curve in Figure 5 (a) displays the monthly mean sunspot number standing for the solar activities on the right vertical axis, while the solid squares in Figure 5 (b) show the yearly variation of $D_{\rm obs}$ observed by Tibet-II at the 10 TeV region. In Figure 5 (b), we notice that the magnitude $|D_{\rm obs}|$ shows a clear solar-cycle variation decreasing with increasing solar activity. The MC simulations suggest that galactic cosmic rays passing near the solar limb are scattered by the complex and violent coronal magnetic field during the solar maximum, and may appear from the direction of the optical solar disc reducing $|D_{\rm obs}|$. By the red open circles and green open triangles in Figure 5 (b), we show predictions by two different MC simulations employing the CSSS models with $R_{\rm ss}$ = 2.5$R_\odot$ and $R_{\rm ss}$ = 10.0$R_\odot$. We see that the yearly variation over the entire period [3] are reproduced by the models.

We show the yearly variation of $D_{\rm obs}$ observed at 3 TeV by Tibet-III by solid squares in Figure 5 (c) . We see the solar-cycle variation with a larger amplitude compared with that in Figure 5 (b) at 10 TeV, due to the larger magnetic deflection expected for lower energy galactic cosmic rays in the solar corona. This energy dependent feature of the solar-cycle variation is overall reproduced by the MC simulations using the CSSS models. It should be noted that $|D_{\rm obs}|$ in Figure 5 (c) is significantly smaller than those predicted by the MC simulations. The tendency is conspicuous in 2000-2002 around the solar maximum at the statistical significance of 4.6$\sigma$ and 5.4$\sigma$ for the CSSS models with $R_{\rm ss}$ = 2.5$R_\odot$ and $R_{\rm ss}$ = 10.0$R_\odot$, respectively. For 10 TeV galactic cosmic rays, however, we do not see the deviations from the MC simulations in Figure 5 (b).

We estmated the deviations quantitatively by the $\chi^2$ test in Figure 5 which are summarized in Table 1. The solid squares in Figure 5 (f) represent the yearly variation of $D_{\rm obs}$ in the Moon's shadow observed by Tibet-III array, while the dashed curve indicates the variation of $D_{\rm obs}$ expected from the distance variation between the Moon and the Earth. The systematic error of $D_{\rm obs}$ in Table 1 are estimated to be 0.178% from the deviation of $D_{\rm obs}$ from the dashed curve in this figure. In Table 1 we demonstrate that the deviation of $D_{\rm obs}$ from the MC simulation during the entire period in Figure 5 (c) is not acceptable.

We then check how the deviation is affected by the ECMEs that take place during the solar maximum period. For the purpose, the catalog of CMEs is adopted containing 228 ECMEs recorded in 2000-2009. The 3 TeV galacric cosmic rays take only $\sim$8 minutes to reach the Earth after passing near the Sun, while an ECME arrives at the Earth $2-4$ days after the solar eruption. As glactic cosmic rays reach the Earth in the direction of the Sun. they are affected by the ECME during a transit period between the arrival time at the Earth and the solar eruption time observed by the *Solar and Heliospheric Observatory* (*SOHO*)/Large Aperture Solar Coronagraph (LASCO). The influence of ECMEs is examined by analyzing $D_{\rm obs}$ observed during a period with/without these transit periods of ECMEs. Four days for the transit period are assumed, which is an average of all ECMEs covered by the SOHO/LASCO observation, with respect to ECMEs lacking in relevant eruption time information.

In Figure 5 (a), we show the yearly number of ECMEs. The gray histograms represent all the 228 ECMEs. The blue histograms indicate the 118 ECMEs with a transit period covered by the observation of $D_{\rm obs}$ by Tibet-III. W see that

Table 1. From [2]. Summary of the $\chi^2$ tests of the agreement between $D_{\rm obs}$ and predictions by MC simulations based on the statistical and systematic errors

| | During an Entire Period | | Without ECME Transit Periods | | During ECME Transit Periods | |
|---|---|---|---|---|---|---|
| Models | $\chi^2$/d.o.f. | Probability | $\chi^2$/d.o.f. | Probability | $\chi^2$/d.o.f. | Probability |
| 3 TeV CSSS $R_{\rm ss}$=2.5$R_\odot$ | 21.3(32.1)/10 | 0.019($3.9\times10^{-4}$) | 8.6(12.2)/10 | 0.57(0.27) | 19.2(23.9)/7 | 0.0076(0.0012) |
| 3 TeV CSSS $R_{\rm ss}$=10$R_\odot$ | 30.1(46.9)/10 | $8.2\times10^{-4}$($9.8\times10^{-7}$) | 14.3(21.0)/10 | 0.16(0.021) | 24.0(29.4)/7 | 0.0011($1.2\times10^{-4}$) |
| [a]10 TeV CSSS $R_{\rm ss}$=10$R_\odot$ | 8.3(10.3)/14 | 0.87(0.74) | 7.5(8.9)/14 | 0.91(0.84) | 20.1(21.1)/11 | 0.044(0.032) |

the number of ECMEs changes positively correlated with the sunspot numbers. Approximately, half of the analysis period is occupied by $20-35$ ECMEs per year in 2000-2002 around the solar maximum due to the correlation. On the contrary, more than 90% of the analysis period does not includes any ECME in 2007-2009 correspoinding to the solar minimum period. $D_{\rm obs}$ observed during periods without ECMEs transit periods is shown by solid squares in Figure 5 (d). In the meanwhile, the solid squares in Figure 5 (e) indicate $D_{\rm obs}$ during the ECME transit periods which are excluded in Figure 5 (d). We see that the deviation of $D_{\rm obs}$ from the MC simulations in 2000-2002 is significantly reduced in Figure 5 (d) than in Figure 5 (c), while it is increased in Figure 5 (e), as confirmed by the $\chi^2$ tests in Table 1. The $D_{\rm obs}$ at 10 TeV observed by the Tibet-II array during the ECME transit period seem to be somehow inconsistent with the MC simulation at the chance probability of 0.044.

Thus, the present result indicates the first observational evidence for the ECMEs which affect the Sun's shadow in cosmic rays in the 3 TeV energy region.

## 3. Other Activities

The emulsion-pouring facilities can meet the demands for making any kind of nuclear emulsion plates which are used for cosmic ray or accelerator experiments. The thermostatic emulsion-processing facilities are operated in order to develop nuclear emulsion plates or X-ray films. Using these facilities, it is also possible to make and develop emulsion pellicle in 600-micron thickness each. In this way, these facilities have been open to all the qualified scientists who want to carry out joint research programs successfully. Of recent, however, the shrinking demand for the facilities let us decide that we should suspend calls for joint research programs to utilize the emulsion-pouring facilities, starting from 2012.

## 4. Ongoing Plans

(1)Chemical composition of primary cosmic rays making the knee in the all-particle energy spectrum

We have measured the energy spectra of primary cosmic-ray protons, helium, all particles around the knee energy region. The main component responsible for making the knee structure in the all particle energy spectrum is heavier nuclei than helium. The next step is to identify the chemical component making the knee in the all particle energy spectrum. We have a plan to install an Yangbajing Air shower Core detector array (YAC) near the center of Tibet III to distinguish the chemical component making the knee. We completed construction of YAC2 (124 detectors over $\sim$500m$^2$ in area), as is shown in Fig. 6, and started data-taking in 2014. YAC2 aims at mainly studying the energy spectra of proton and helium components in the knee energy region.

Fig. 6. YAC2 set up at Yangbajing.

(2) Gamma-ray astronomy in the 100 TeV region

For the purpose of detecting high-energy cosmic gamma rays with an air shower array, a large underground muon detecter[4] is very effective to reduce cosmic-ray background.

We decided to add a large ($\sim$4,000 m$^2\times$1.5m deep) underground ($\sim$ 2.5 m soil+concrete overburden) water Cherenkov muon detector array (Tibet MD) under the present Tibet air shower array (Tibet AS). By Tibet AS + MD, we aim at background-free detection of celestial point-source gamma rays around 100 TeV with the world-best sensitivity and at locating the origins (PeVatrons) of cosmic rays accelerated up to the knee (PeV) energy region in the northern sky. The measurement of cut off energies in the energy spectra of such gamma rays in the 100 TeV region may contribute significantly to understanding of the cosmic- ray acceleration limit at SNRs. Search for extremely diffuse gamma-ray sources by Tibet AS + MD, for example, from the galactic plane or from the Cygnus region may be very intriguing as well. Above 100 TeV, the angular resolution of Tibet AS with 2-steradian wide field of view is 0.2$^\circ$ and the hadron rejection power of Tibet MD is 1/1000.

In addition to unknown point-like sources, we expect

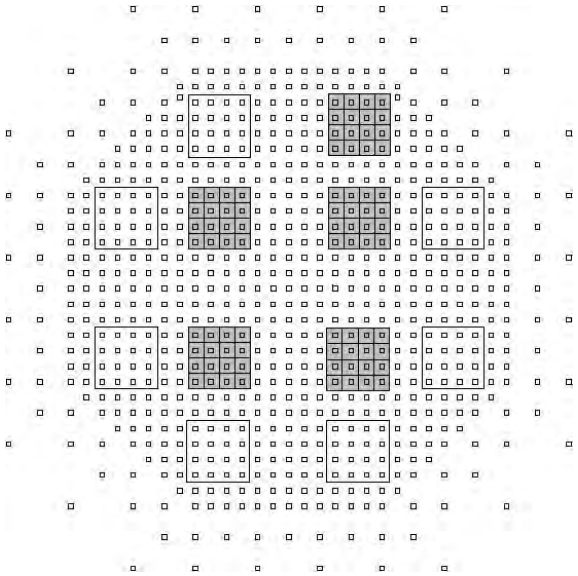

Fig. 7. The 5 shaded squares represent the constructed 5 MD pools.

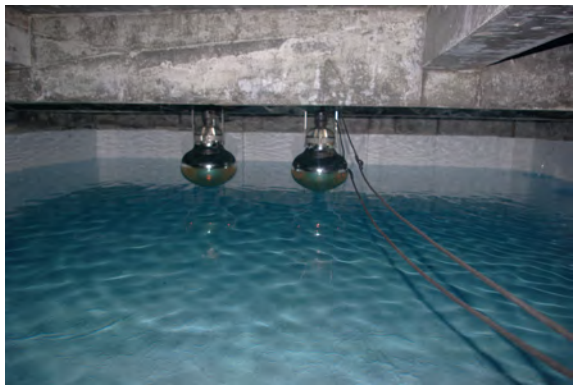

Fig. 8. PMTs mounted in a MD cell filled with water.

to detect established sources in the 100 TeV region: TeV J2032+4130, HESS J1837-069, Crab, MGRO J2019+37, MGRO J1908+06, Milagro candidate sources, Mrk421, Mrk501 are sufficiently detectable and Cas A, HESS J1834-087,LS I+63 303, IC443 and M87 are marginal.

Furthermore, our integral flux sensitivity to diffuse gamma rays will be very high. We hope that the diffuse gamma rays from the Cygnus region reported by the Milagro group and also diffuse gamma-rays from the galactic plane will be detected. Diffuse gamma-rays of extragalacitic origin may be an interesting target as well.

In 2007, a prototype 100-m$^2$ underground water Cherenkov muon detector was successfully constructed in Tibet to demonstrate the technical feasibility, cost estimate, validity of our Monte Carlo simulation. Data analyses demonstrate that our MC simulation reproduces real data quite reasonably.

In 2014, construction of the $\sim$4,000 m$^2$ MD, as is shown in Fig. 7, was successfully completed and data-taking started. We have accumulated approximately three-year data. One of the detector cell filled with water is demonstrated in Fig. 8.

Development of Monte Carlo simulation is under way for

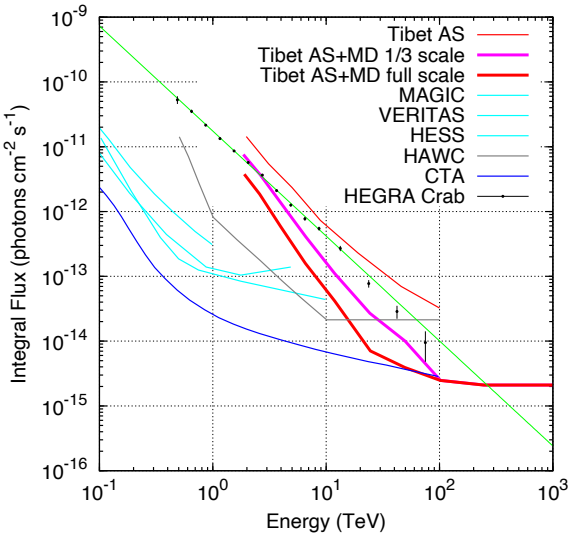


Fig. 9. Sensitivity to point-like gamma-ray sources with Tibet AS+MD (see,Tibet AS+MD 1/3 scale) by pink curve.

comparison with real data. Various analysis tools are also extensively being developed. According to the simulation, the sensitivity of the current configuration (Tibet AS + MD) is demonstrated in Fig. 9.

## Bibliography

### Papers in refereed journals

[1] "Multi-TeV Gamma-Ray Observation from the Crab Nebula Using the Tibet-III Air Shower Array Finely Tuned by the Cosmic-Ray Moon's Shadow", M. Amenomori *et al.*, Astrophysical Journal, **692** , 61-72 (2009).

[2] "Influence of Earth-Directed Coronal Mass Ejections on the Sun's Shadow O bserved by the Tibet-III Air Shower Array", M. Amenomori*et al.*, Astrophysical Journal, **860** :13-1-7 (2018).

[3] "Probe of the Solar Mangetic Field Using the "Cosmic-Ray Shadow" of the Sun", M. Amenomori*et al.*, Physical Review Letters, **111** 011101-1-5 (2013).

[4] "Exploration of a 100 TeV gamma-ray northern sky using the Tibet air-shower array combined with an underground water-Cherenkov muon-detector array", T.K. Sako *et al.*, Astroparticle Physics, **32** , 177-184 (2009).

The Tibet AS$\gamma$ Collaboration

M. Amenomori[1], X. J. Bi[2], D. Chen[3], T. L. Chen[4], W. Y. Chen[2], S. W. Cui[5], Danzengluobu[4], L. K. Ding[2], C. F. Feng[6], Zhaoyang Feng[2], Z. Y. Feng[7], Q. B. Gou[2], Y. Q. Guo[2], H. H. He[2], Z. T. He[5], K. Hibino[8], N. Hotta[9], Haibing Hu[4], H. B. Hu[2], J. Huang[2], H. Y. Jia[7], L. Jiang[2], F. Kajino[10], K. Kasahara[11], Y. Katayose[12], C. Kato[13], K. Kawata[14], M. Kozai[13,15], Labaciren[4], G. M. Le[16], A. F. Li[17,6,2], H. J. Li[4], W. J. Li[2,7], C. Liu[2], J. S. Liu[2],

M. Y. Liu[4], H. Lu[2], X. R. Meng[4], T. Miyazaki[13], K. Munakata[13], T. Nakajima[13], Y. Nakamura[13], H. Nanjo[1], M. Nishizawa[18], T. Niwa[13], M. Ohnishi[14], I. Ohta[19], S. Ozawa[11], X. L. Qian[6,2], X. B. Qu[20], T. Saito[21], T. Y. Saito[22], M. Sakata[10], T. K. Sako[23,14], J. Shao[2,6], M. Shibata[12], A. Shiomi[24], T. Shirai[8], H. Sugimoto[25], M. Takita[14], Y. H. Tan[2], N. Tateyama[8], S. Torii[11], H. Tsuchiya[26], S. Udo[8], H. Wang[2], H. R. Wu[2], L. Xue[6], Y. Yamamoto[10], K. Yamauchi[12], Z. Yang[2], A. F. Yuan[4], L. M. Zhai[3], H. M. Zhang[2], J. L. Zhang[2], X. Y. Zhang[6], Y. Zhang[2], Yi Zhang[2], Ying Zhang[2], Zhaxisangzhu[4], and X. X. Zhou[7]

[1]*Department of Physics, Hirosaki University, Hirosaki 036-8561, Japan*
[2]*Key Laboratory of Particle Astrophysics, Institute of High Energy Physics, Chinese Academy of Sciences, Beijing 100049, China*
[3]*National Astronomical Observatories, Chinese Academy of Sciences, Beijing 100012, China*
[4]*Department of Mathematics and Physics, Tibet University, Lhasa 850000, China*
[5]*Department of Physics, Hebei Normal University, Shijiazhuang 050016, China*
[6]*Department of Physics, Shandong University, Jinan 250100, China*
[7]*Institute of Modern Physics, SouthWest Jiaotong University, Chengdu 610031, China*
[8]*Faculty of Engineering, Kanagawa University, Yokohama 221-8686, Japan*
[9]*Faculty of Education, Utsunomiya University, Utsunomiya 321-8505, Japan*
[10]*Department of Physics, Konan University, Kobe 658-8501, Japan*
[11]*Research Institute for Science and Engineering, Waseda University, Tokyo 169-8555, Japan*
[12]*Faculty of Engineering, Yokohama National University, Yokohama 240-8501, Japan*
[13]*Department of Physics, Shinshu University, Matsumoto 390-8621, Japan*
[14]*Institute for Cosmic Ray Research, The University of Tokyo, Kashiwa 277-8582, Japan*
[15]*Institute of Space and Astronautical Science, Japan Aerospace Exploration Agency (ISAS/JAXA), Sagamihara 252-5210, Japan*
[16]*National Center for Space Weather, China Meteorological Administration, Beijing 100081, China*
[17]*School of Information Science and Engineering, Shandong Agriculture University, Taian 271018, China*
[18]*National Institute of Informatics, Tokyo 101-8430, Japan*
[19]*Sakushin Gakuin University, Utsunomiya 321-3295, Japan*
[20]*College of Science, China University of Petroleum, Qingdao 266555, China*
[21]*Tokyo Metropolitan College of Industrial Technology, Tokyo 116-8523, Japan*
[22]*Max-Planck-Institut für Physik, Munich D-80805, Germany*
[23]*Escuela de Ciencias Físicas y Nanotechnología, Yachay Tech, Imbabura 100115, Ecuador*
[24]*College of Industrial Technology, Nihon University, Narashino 275-8576, Japan*
[25]*Shonan Institute of Technology, Fujisawa 251-8511, Japan*
[26]*Japan Atomic Energy Agency, Tokai-mura 319-1195, Japan*

## ALPACA Project

[Spokesperson: M. Takita]
ICRR, The Univ. of Tokyo, Kashiwa, Chiba 277-8582

Cosmic rays are supposed to be accelerated up to the knee energy (PeV) region at supernova remnants (SNRs) in our galaxy. Therefore, we naturally expect gamma rays at 100 TeV energies, which originate in $\pi^0$ decays produced by the accelerated cosmic rays interacting with matter surrounding the SNRs. However, on-going experiments focus on measuring gamma rays in the 1 - 10 TeV region. The gamma-ray emission of electron origin might be highly suppressed above 10 TeV due to rapid decrease of inverse-Compton cross section by the Klein-Nishina effect as well as synchrotron radiation energy loss in the strong magnetic field around the SNRs. The detection and spectral measurement of gamma rays in the 100 TeV region from their celestial sources, together with multi-wavelength (radio, X-ray, gamma-ray) observations, will be an important experiment enabling us to discriminate between the two processes (cosmic-ray/electron origins), to locate the acceleration site (PeVatron which accelerate cosmic rays up to PeV energies) of cosmic rays and to verify the standard acceleration model of cosmic rays. Furthermore, diffuse gamma rays from the Fermi bubbles recently reported by the Fermi-LAT group and sub-PeV neutrino events[1] detected by IceCube suggests that the Fermi bubbles be a PeVatron candidate. Similarly, the energy spectrum of diffuse gamma rays from the extended region around the galactic center marginally measured by HESS up to approximately 10 TeV also strongly indicates existence of PeVatron[2], from which we expect to detect gamma rays at 100 TeV energies. Thus, a wide field-of-view gamma-ray imaging at 100 TeV energies in the southern sky, where the HESS sources, the Fermi bubbles and the galactic center are located within field of view, will be a key experiment.

## 1. Experiment

The ALPACA[3],[4] (Andes Large area PArticle detector for Cosmic ray physics and Astrophysics) is a cosmic-ray experiment with a large surface air shower array with a large underground muon detector array The experimental site (approximately 500 m$\times$500 m $\sim$250,000 m$^2$ in total area) is located on a flat high land called Chacaltaya Plateau (4,740 m above sea level, 16°23' S, 68°08' W ), as shown in Fig. 1, around Mount Chacaltaya, near La Paz, Bolivia. In some part in this area, our detectors will be set up.

We plan to set up a 5,400 m$^2$ underground (approximately one to a few meters) muon detector array (MD) and an 83,000 m$^2$ air shower array (AS), shown in Fig. 2. MD of

Fig. 1. From Ref.[3]. Experimental site for the ALPACA experiment, Chacaltaya Plateau ia (4,740 m above see level, 16°23' S, 68°08' W), near Mount Chacaltaya, in Bolivia.

water Cherenkov type is composed of eight pools with each pool (approximately 1 m deep) containing twelve 56 $m^2$ unit detectors. AS is made up of 401 1 $m^2$ plastic scintillation counters at 15 m spacing.

The AS field of view is roughly 2 steradian. The expected angular resolution of AS is approximately 1 degree at 5 TeV and 0.2 degrees around 100 TeV for gamma rays. For 100 TeV gamma rays, the AS energy resolution is estimated to be $\sim$20-25 %. The hadron rejection power of MD is more than 99.9 % at 100 TeV, while keeping most of gamma-ray events. Long-term detector stability, angular resolution, pointing accuracy and energy scale can be calibrated by the cosmic-ray shadow in the Moon as well as by some of the bright stable TeV gamma ray sources in the southern sky.

## 2. Covered Physics

Our reserch target is divided into four in ALPACA:

1. Measurement of high-energy (5 TeV – 1 PeV) cosmic gamma rays.

2. Measurement of cosmic ray energy spectra around the Knee energy region (100 TeV – 100 PeV)

3. Measurement of cosmic ray anisotropy $>$ 5 TeV at sidereal time frame.

4. Measurement of the Sun shadow in cosmic rays $>$ 5 TeV.

We aim at low-background detection of celestial gamma rays in the 100 TeV region with the world-best sensitivity (an order of magnitude better than any previous/existing experiments) and at locating the origins of cosmic rays accelerated up to the knee energy region in the southern sky. Presuming a Crab-like gamma-ray source extending up with power-law index -2.6 located in the southern sky, the ALPACA experiment is sensitive to the source with $\sim$15 % Crab intensity during one calendar year, as is demonstrated in Fig. 3.

The AS + MD in the southern hemisphere will be a unique/complementary experiment to on-going experiments

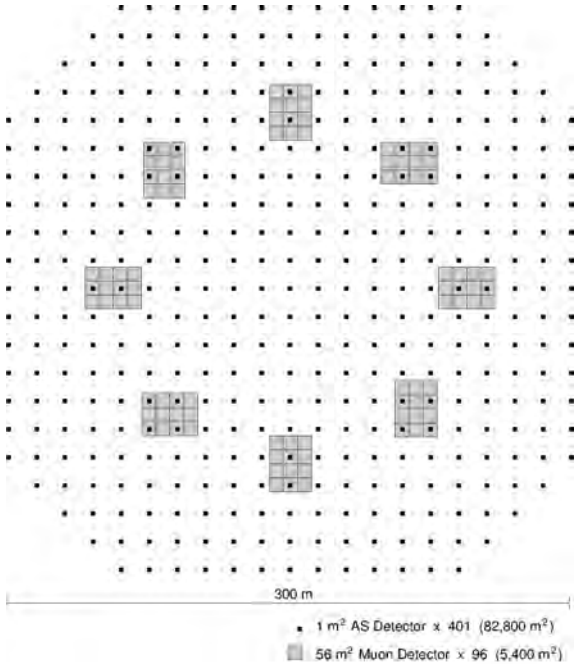


Fig. 2. From Ref.[3]. Schematic view of the ALPACA experiment. The small black squares indicate 401 1 $m^2$ plastic scintillarion detectors, forming an air shower array with 83,000 $m^2$ in area.The grey rectangles indicate eight underground muon detector pools, each of which contains twelve 56 $m^2$ muon detector units. The total area of the underground muon detector array is 5,400 $m^2$.

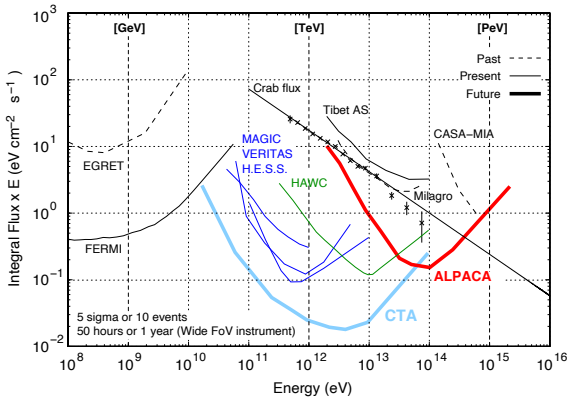


Fig. 3. Sensitivity of ALPACA to high-energy gamma-ray point source. Experimental data points are from HEGRA. The ALPACA sensitivity is evaluated from Ref.[6].

(FERMI, HESS, VERITAS, MAGIC, CALET, Tibet AS$\gamma$, HAWC) and future projects (LHAASO, CTA) in this field, which are either located in the northern hemisphere or aiming at gamma-ray astronomy below 10 TeV region, or having narrow field-of-view. Thus, the new energy window in the 100 TeV region observing gamma rays with wide field-of-view will be opened first in the southern sky by the ALPACA experiment. We expect to detect established more than a dozen of sources, i.e., young SNRs (SN1006, RX J1713.7-3946, RX J0852.0-4622), Pulsar Wind Nebulae, the galactic center, etc) in the 100 TeV region, some of which may be cosmic-ray PeVatron candidates. Furthermore, our wide field-of-view sensitivity to diffuse gamma rays allows us to study extremely diffuse gamma-ray sources which are difficult to

detect by IACTs. The diffuse gamma rays from the Fermi bubbles recently reported by the Fermi-LAT group may be clearly detected, if they extend up to the 100 TeV region. Similarly, detection of diffuse gamma rays above 100 TeV from extended region from the galactic center is promising, where the gamma-ray energy spectrum strongly suggests existence of PeVatron. Detection and spectral measurement of gamma rays in the 100 TeV region from these celestial sources, together with multi-wavelength (radio, X-ray, gamma-ray) observations, are key points enabling us to discriminate between the two processes (cosmic-ray/electron origins), to locate the acceleration site of cosmic rays and to examine the standard acceleration model of cosmic rays. In astronomical point of view, we pioneer the ultra-high energy (above 100 TeV) gamma-astronomy in the southern sky. Besides, gamma-ray emission from near-by extragalactic sources, e.g. M87, Cen A, gamma rays of dark matter origin, those from the Sun disk recently obseved by Fermi[7] may be interesting subjects.

We also aim at measuring energy spectra of proton, helium and iron components separately around the knee energy region with the new AS + MD. The standard cosmic-ray acceleration model at SNR predicts the knee energy of each nucleus component being proportional to Z (atomic number). We can discriminate proton and iron components by MD, as an iron nucleus produces approximately 2 times more muons than a proton with the same energy. Thus, the cosmic-ray acceleration scenario (SNR shock acceleration) will be verified by observing the linearly Z(atomic number)-dependent knee(=bent) positions of proton, helium, iron components around the knee energy region.

Precise cosmic-ray anisotropy measurement at sidereal time frame in the TeV energy region in the southern sky provides unique data for the community to understand the magnetic field structure in the heliosphere. The ALPACA experiment gives complementary data in the TeV region to those from IceCube above a few tens of TeV.

Furthermore, measurement of the Sun shadow in cosmic rays above the TeV energy region in the southern hemisphere also helps understand the modeling of the magnetic fields between the Sun and the Earth, complementary to the observations in the northern hemisphere.

## 3. ALPAQUITA

As a proto-type experiment, the ALPAQUITA[8] air shower array without MD, which is $\sim$25 % of the ALPACA air shower array in area will be constructed at the experimental site, Chacaltaya Plateau, in 2019. The containers including materials and equipments necessary to construct the ALPAQUITA array arrived at La Paz, Bolivia in early 2019.

## Bibliography

### Papers and references


[1] C. Lunardini et al., PRD, **92**, 021301-1-5 (2015).

[2] A. Abramoswski et al., Nature, **531**, 476 (2016).

[3] M. Takita for the ALPACA Collaboration, THE EUROPEAN PHYSICAL JOURNAL, **145**, 01002-1-3, (2017).

[4] T. Asaba et al, Proc. of ICRC2017, ID=827, Busan, Korea, July 12-20, (2017).

[5] F. Aharonian et al., ApJ, **614**, 897 (2004)

[6] T. K. Sako et al., Astroparticle Physics, **32**, 177 (2009).

[7] C. Y. Kenny et al., arXiv:1508.06276v1.

[8] T. Asaba et al, Proc. of ICRC2017, ID=437, Busan, Korea, July 12-20, (2017).


The ALPACA Collaboration as of April 2018


T. Asaba,[a] K. Hibino,[b] N. Hotta,[c] M. Kataoka,[a] Y. Katayose,[a] C. Kato,[d] K. Kawata,[e] H. Kojima,[fg] R. Mayta,[h] P. Miranda,[i] K. Munakata,[d] Y. Nakamura,[d] M. Nishizawa,[j] S. Ogio,[h] M. Ohnishi,[e] A. Oshima,[k] M. Raljevich,[i] H. Rivera,[i] T. Saito,[l] T. Sako,[e] T. K. Sako,[me] T. Sasaki,[a] S. Shibata,[k] A. Shiomi,[n] M. Subieta,[i] M. Suzuki,[a] N. Tajima,[o] M. Takita,[e] Y. Tameda,[p] K. Tanaka,[q] R. Ticona,[i] H. Tsuchiya,[r] Y. Tsunesada,[h] S. Udo[b] and M. Wakamatsu[a] (The ALPACA Collaboration)

[a]Faculty of Engineering, Yokohama National University, Japan
[b]Faculty of Engineering, Kanagawa University, Japan
[c]Faculty of Education, Utsunomiya University, Japan
[d]Department of Physics, Shinshu University, Japan
[e]Institute for Cosmic Ray Research, The University of Tokyo, Japan
[f]Faculty of Engineering, Aichi Institute of Technology, Japan
[g]Chubu Innovative Astronomical Observatory, Japan
[h]Graduate School of Science, Osaka City University, Japan
[i]Instituto de Investigaciones Físicas, Universidad Mayor de San Andrés, Bolivia
[j]National Institute of Informatics, Japan
[k]College of Engineering, Chubu University, Japan
[l]Tokyo Metropolitan College of Industrial Technology, Japan
[m]Escuela de Ciencias Físicas y Nanotechnología, Yachay Tech, Ecuador
[n]College of Industrial Technology, Nihon University, Japan
[o]RIKEN, Japan
[p]Faculty of Engineering, Osaka Electro-Communication University, Japan
[q]Graduate School of Information Sciences, Hiroshima City University, Japan
[r]Japan Atomic Energy Agency, Japan

## High Energy Astrophysics Group

[Spokesperson: K. Asano]
ICRR, The Univ. of Tokyo, Kashiwa, Chiba 277-8582

**Overview**

The high energy astrophysics group has been making theoretical and observational studies of violent astrophysical phenomena, in which nonthermal cosmic ray particles are being accelerated. Targets of the group's study include high energy astrophysical objects such as supernova remnants, pulsar, pulsar wind nebulae, black hole/neutron star mergers, jets from active galactic nuclei (AGNs), and gamma-ray bursts (GRBs). We especially study the formation of relativistic outflows, particle acceleration in jets, emission mechanisms of electromagnetic waves or neutrinos, and electromagnetic counterparts for compact binary mergers. Our research supports the multi-messenger astronomy, which probes astronomical phenomena through collaborating observations of electromagnetic waves, cosmic rays, neutrinos, and gravitational waves.

**Research Topic 1: Blazar Emission Model with Turbulence Particle Acceleration**

The double-peak structure of blazar spectra is well explained by leptonic models, in which gamma-ray emission is generated via inverse-Compton (IC) scattering. The synchrotron self-Compton (SSC) process upscatters synchrotron photons produced by the same electron population in jets. For flat spectrum radio quasars (FSRQs), external photons surrounding the disk dominate the seed photons for the IC scattering. In most models, the nonthermal electrons are assumed to be accelerated via shocks with the Fermi process. However, some blazar spectra imply that the electron power-law index is smaller than 2, the value from the simplest shock acceleration model. The change of the index at the spectral break is very large, which is inconsistent with the cooling break. An alternative acceleration mechanism candidate is the stochastic acceleration by turbulence.

We consider the case of so-called hard-sphere scattering as an interaction model between turbulences and electrons, in which the acceleration timescale is independent of the electron energy. We numerically simulate broadband emission from blazar jets with a one-zone time-dependent code, taking into account the turbulence acceleration. Our model spectra have reproduced the curved photon spectra of the five representative blazars from the radio to the high-energy gamma-ray bands well (see Figure 1).

The fast mode is most likely the dominant wave mode of the electron energy source in low-magnetized plasma. The energy of the turbulence is injected at a large scale as fast waves, and cascades to shorter scales following the Kolmogorov law. If the Larmor radius of electrons is significantly shorter than the wavelength, the pitch angle diffusion via gyroresonance is not responsible for particle scattering. In this case, the main mechanism of the energy exchange between electrons and waves is transit-time damping (TTD); electrons are accelerated when their velocity along the magnetic field equals the parallel component of the phase velocity. This non-gyroresonant scattering may provide a mechanism to realize the hard-sphere-like acceleration in blazars, as required by our models.

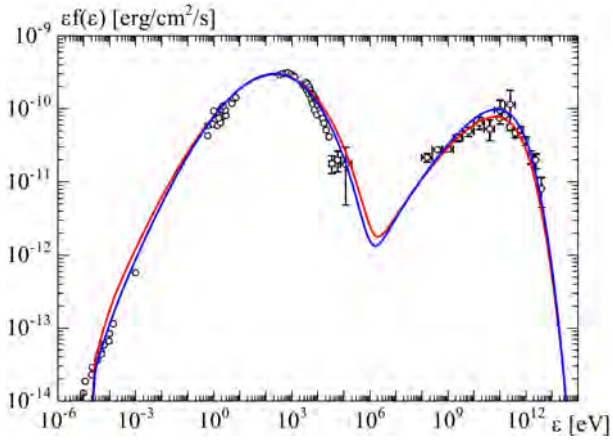


Fig. 1. Model photon spectra for Mrk 421.

**Research Topic 2: Pulsar Wind Nebulae with Particle Diffusion**

Pulsar wind nebulae (PWNe) are extended objects around a rotation-powered pulsar with a size of about a few pc, and their emission spectrum extends from radio to gamma-ray. The emission is due to synchrotron radiation and inverse Compton scattering by electrons and positrons accelerated at the termination shock generated by the interaction between the supernova remnant (SNR) and the pulsar wind. Based on this idea, Kennel & Coroniti (1984) established a 1-dimensional steady magnetohydrodynamical (MHD) model (hereafter the KC model) of PWNe. Although the KC model has been accepted as a standard model of PWNe, some problems in the KC model have been raised by morphology research with high angular resolution observations in X-ray. The X-ray photon spectrum becomes gradually softer as the radius increases. Such gradual softening is incompatible with the KC model, which predicts sudden softening at a certain radius. Our paper, Ishizaki et al. (2017), showed that the KC model has severe difficulty reproducing both the entire spectrum and the surface brightness profile simultaneously.

In the KC model, particles are simply advected with the spherical wind. Some authors have pointed out that the particle diffusion effect resolves the above discrepancy. We present a new PWN model that solves both advection and diffusion of nonthermal particles in a self-consistent way to satisfy the momentum and energy conservation laws. Assuming spherically symmetric steady outflow, we calculate the emission spectrum integrating over the entire nebula and the radial profile of the surface brightness. We find that the back reaction of the particle diffusion modifies the flow profile. The photon spectrum and the surface brightness profile are different from the model calculations without the back reaction of the particle diffusion.

Our model is applied to the two well-studied PWNe, 3C 58 and G21.5-0.9. By fitting the spectra of these PWNe, we determine the parameter sets and calculate the radial profiles

of X-ray surface brightness. For both the objects, obtained profiles of X-ray surface brightness and the photon index are well consistent with observations (see Figure 2).

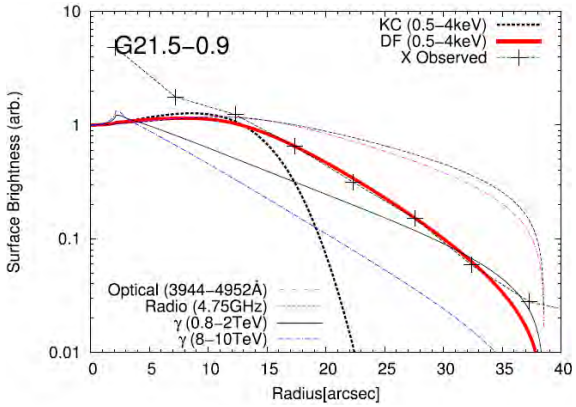


Fig. 2. Radial profiles of the surface brightness of X-rays, radio, optical and gamma-rays for G21.5–0.9. The red line represents the model with the diffusion effect, and the thin black solid line represents the X-ray profile of the KC model.

Our model suggests that particles that have escaped from the nebula significantly contribute to the gamma-ray flux. A gamma-ray halo larger than the radio nebula is predicted in our model.

**Research Topic 3: Hadronic Cascade in Gamma-Ray Bursts**

The high-energy ($> 100$ MeV) emission observed by the Fermi Large Area Telescope during the prompt phase of some luminous GRBs could arise from the hadronic cascade induced by the photomeson production. The cascade efficiency largely depends on the maximum proton energy. In previous studies, the maximum energy is assumed as the theoretically highest one. Although the maximum proton energy can reach such a high energy when considering the acceleration by a relativistic shock in the Bohm condition, such a condition may not be achieved in real shocks. In the case that the maximum proton energy falls below the threshold energy of the photomeson process to interact with the photons of energy of the spectral peak, the photomeson process may not be efficient to produce the observed high-energy flux in a GRB. On the other hand, the Bethe–Heitler (BH) pair production process of protons has a lower threshold energy. Thus, protons may still induce an electromagnetic cascade via this process, producing high-energy emission during the prompt emission phase.

We revisit the hadronic model for the prompt high-energy emission of GRBs with a smaller maximum proton energy. We show that with a relatively low maximum proton energy with a Lorentz factor of $10^5$ in the comoving frame, the cascade emission can still reproduce various types of high-energy spectra of GRBs as shown in Figure 3. The adopted parameters in the spectrum fittings are consistent with the constraints from the null detection of GRB-correlated neutrino events by the IceCube neutrino telescope. The cascade emission may also lead to a low-energy excess below a few keV and might be used as an indication of the baryon component in the GRB ejecta.

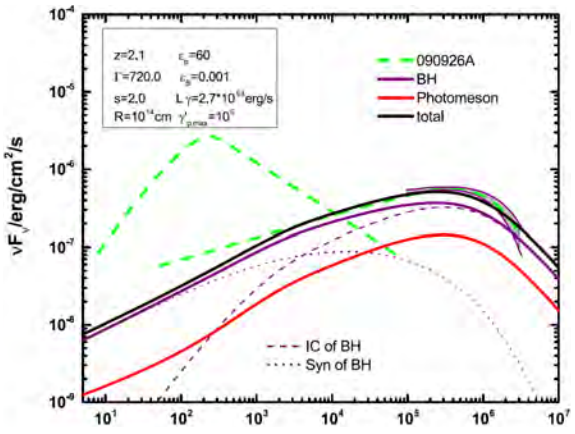


Fig. 3. Spectral fitting for GRB 090926A with a suppressed maximum proton energy. The photon energy unit is keV. The purple curves represent the emissions of cascaded electrons originating from the BH process, while the red curves represent that from the photomeson process. The red and purple dotted and dashed curves show the synchrotron and IC radiation of the electrons from the dominant process. The green dashed curves show the fitting of the burst's spectrum by the Fermi-LAT collaboration. The shaded region shows the uncertainty in the spectrum fitting at the high-energy end.

**Research Topic 4: Kilonova Emission**

A kilonova/macronova is the emission that has been expected to be associated with a neutron star-neutron star or black hole-neutron star merger as the consequence of the mass ejection from the system. The previous studies showed that lightcurves of kilonovae/macronovae depend on the mass, velocity, and element abundance of ejecta. Since those ejecta profiles reflect the merger process and the late time evolution of the merger remnant, detailed property of kilonova/macronova lightcurves, such as those brightness and color evolution, provide the physical information of the merged binary and the post-merger evolution of the system as complementary information to that inferred by the gravitational-wave data analysis.

Electromagnetic (EM) counterparts were observed simultaneously with the first gravitational wave event from a binary neutron star merger (GW170817) over the entire wavelength range, from gamma-ray to radio wavelengths. In particular, a counterpart in optical and infrared wavelengths is identified as the emission from a kilonova/macronova. A number of studies have shown that the optical and infrared EM counterparts found in GW170817 is consistent with kilonova/macronova models composed of multiple ejecta components with different lanthanide fraction. However, in most these studies, contribution from each ejecta component to the lightcurves is separately calculated and composited. In reality, the lightcurves are determined through the non-trivial radiation transfer of photons in both ejecta components.

We perform an axisymmetric radiative transfer simulation for kilonovae/macronovae taking the interplay of multiple ejecta components of non-spherical morphology into account. We show that the photon interplay of multiple ejecta components is important for the case that the post-merger ejecta

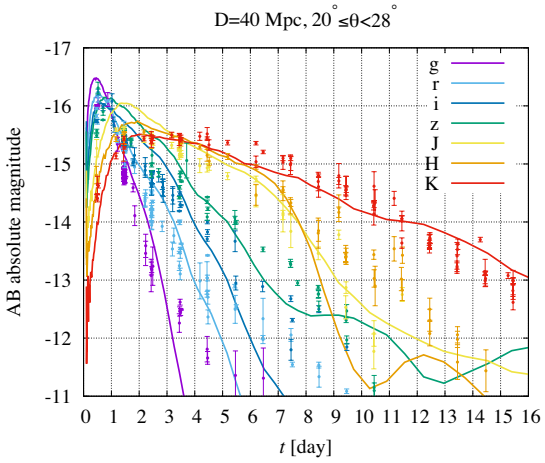


Fig. 4. Optical and infrared lightcurves of EM counterparts in GW170817 compared with the kilonova/macronova model observed from $20^\circ \leq \theta \leq 28^\circ$. We assume that GW170817 is at a distance of 40 Mpc. All the magnitudes are given in AB magnitudes.

is surrounded by a high-opacity dynamical ejecta, predicted by numerical-relativity simulations. In particular, we show that the optical and infrared lightcurves of EM counterparts in GW170817 can be reproduced by smaller ejecta masses than the previous studies by a factor of $\approx 1.5$–2. This implies that taking the interplay of multiple ejecta components into account is crucial for the ejecta mass estimation.

**Research Topic 5: CALET Project**

We have joined CALET, CALorimetric Electron Telescope, which is a mission for the Japanese Experiment Module-Exposed Facility (JEM-EF) on the International Space Station. The CALET mission aims at revealing unsolved problems in high energy phenomena of the Universe by carrying out accurate measurements of high energy spectra of electrons, gamma-rays and nuclei. HTV5 equipped with CALET was successfully launched by the H-IIB at 8:50:49 p.m. on August 19 2015 (JST) from the Tanegashima Space Center, and CALET is observing cosmic rays without apparent problems.

Major scientific objectives are to search nearby cosmic ray sources and dark matter signatures by carrying out accurate measurements of cosmic ray electrons in 1 GeV – 20 TeV and gamma-rays in 4 GeV – 10 TeV. Since proton background is very large, high proton rejection power is mandatory for high energy electron and gamma-ray measurements. CALET has an imaging and deep calorimeter with 30 radiation length for electromagnetic particles, which provides high proton rejection and excellent energy resolution.

First CALET results of a cosmic-ray electron and positron spectrum from 10 GeV to 3 TeV was published in 2017. Extended results on the cosmic-ray electron–positron spectrum from 11 GeV to 4.8 TeV, utilizing the data up to November 2017, are shown in Figure 5. In the energy region from 40 to 300 GeV, the power-law index is found to be $-3.12 \pm 0.02$, which is consistent with other experiments within errors. Our results agree with the AMS-02 results. However, the spectrum is considerably softer from 300 to 600 GeV than the spectra

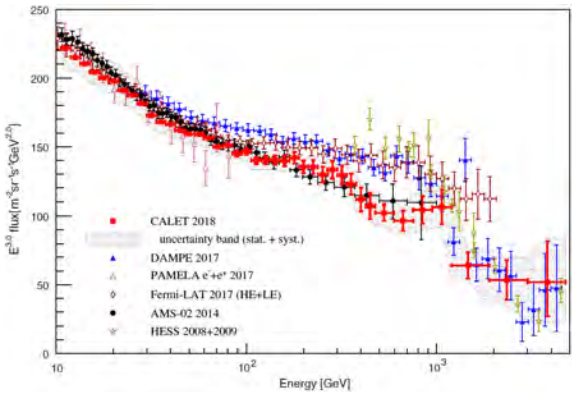


Fig. 5. Cosmic-ray all-electron spectrum measured by CALET from 10.6 GeV to 4.75 TeV, where the gray band indicates the quadratic sum of statistical and systematic errors (not including the uncertainty on the energy scale). Also plotted are direct measurements in space and from ground-based experiments.

measured by DAMPE and Fermi-LAT. The CALET results exhibit a lower flux than those of DAMPE and Fermi-LAT from 300 GeV up to near 1 TeV.

On the other hand, the flux in the 1.4 TeV bin of DAMPE spectrum, which might imply a peak structure, is not compatible with CALET results at a level of $4\sigma$ significance, including the systematic errors from both experiments.

## Bibliography

### Papers in refereed journals

1. Kai Wang, Ruo-Yu Liu, Zi-Gao Dai, Katsuaki Asano "Hadronic Origin of Prompt High-Energy Emission of Gamma-Ray Bursts Revisited: In the Case of a Limited Maximum Proton Energy", Astrophys. J., 857, 24(12pp) (2018).

2. O. Adriani, Y. Akaike, K. Asano, et al. "Extended Measurement of the Cosmic-Ray Electron and Positron Spectrum from 11 GeV to 4.8 TeV with the Calorimetric Electron Telescope on the International Space Station", Phys. Rev. Lett., 120, 261102(7pp) (2018).

3. Y. Asaoka, S. Ozawa, S. Torii, O. Adriani, Y. Akaike, K. Asano, et al. "On-Orbit Operations and Offline Data Processing of CALET onboard the ISS", Astropart. Phys., 100, 29-37 (2018).

4. Katsuaki Asano, Masaaki Hayashida "Blazar Spectra with Hard-Sphere-like Acceleration of Electrons", Astrophys. J., 861, 31(7pp) (2018).

5. O. Adriani, Y. Akaike, K. Asano, et al. "Search for GeV Gamma-Ray Counterparts of Gravitational Wave Events by CALET", Astrophys. J., 863, 160(9pp) (2018).

6. N. Cannady, Y. Asaoka, F. Satoh, et al. "Characteristics and Performance of the CALorimetric Electron Telescope (CALET) Calorimeter for Gamma-Ray Observations", Astrophys. J. Supp., 238, 5(16pp) (2018).

7. Kyohei Kawaguchi, Masaru Shibata, Masaomi Tanaka "Radiative Transfer Simulation for the Optical and Near-Infrared Electromagnetic Counterparts to GW170817", Astrophys. J. Lett., 865, L21(6pp) (2018).

8. Yutaro Tachibana, Makoto Arimoto, Katsuaki Asano, et al. "Late Engine Activity of GRB 161017A Revealed by Early Optical Observations", Pub. Astron. Soc. Jap., 70, 92(9pp) (2018).

9. G. Abdellaoui, et al. "EUSO–TA — First Results from a Ground-Based EUSO Telescope", Astropart. Phys., 102, 98-111 (2018).

10. Wataru Ishizaki, Katsuaki Asano, Kyohei Kawaguchi "Outflow and Emission Model of Pulsar Wind Nebulae with the Back Reaction of Particle Diffusion", Astrophys. J., 867, 141(12pp) (2018).

11. Tomoya Kinugawa, Yuichi Harikane, Katsuaki Asano "Long Gamma-Ray Burst Rate at Very High Redshift", Accepted for Astrophys. J., (2019).


**Textbook**


1. Nobuyuki Kawai, Katsuaki Asano "Gamma-Ray Burst", NIPPON HYORON SHA, Tokyo, (2019). ISBN: 978-4-535-60744-6


## Other Activities

### Ashra NTA

Combined detection of PeV $\nu$'s and $\gamma$'s from an accelerator provides indispensable identification of the location and the physics mechanism i.e. $p+\gamma \rightarrow \Delta^{+} \rightarrow \pi^{0}+p$, $\pi^{+}+n$; $p+$nucleus $\rightarrow \pi^{\pm,0}+X$, which can clearly reveal the long-standing unresolved origin(s) of cosmic rays. Recently several observations suggesting cosmic ray accelerators have been independently made [1, 2, 3]. Such a "multi-particle" paradigm [4] can be performed by Ashra NTA with the single unique detector system [5].

Since 2001, we have been developing the Earth-skimming tau $\nu$ (ES-$\nu_\tau$) air-shower technique [6], as a promising potential. which can enjoy a large target mass by detecting air-showers (ASs) produced by $\tau$ decays in the air. The $\tau$'s, produced by $\nu_\tau$'s that interact with the Earth matter, traverse, and emerge out of a mountain or the ground decaying and generating ASs. Adding to that, the advantages are perfect shielding of cosmic ray secondaries, precise arrival direction determination, and negligible background from atmospheric $\nu$'s [7]. The detectors of Ashra-1 and its extention plan NTA can precisely image AS Cherenkov (CE) and fluorescence (FL) light generated from ES-$\nu_\tau$ and $\gamma$ ASs in the huge effective volume of air around the mountain in the field of view (FOV) (Figure 6) [8].

The Ashra Phase 1 (Ashra-1) [9] light collector (LC) (Figure 7*left*) achieves the total resolution of $\sim 3$ arcmin covering $42^{\circ}$ (Figure 7*right*). The key feature is the use of electrostatic

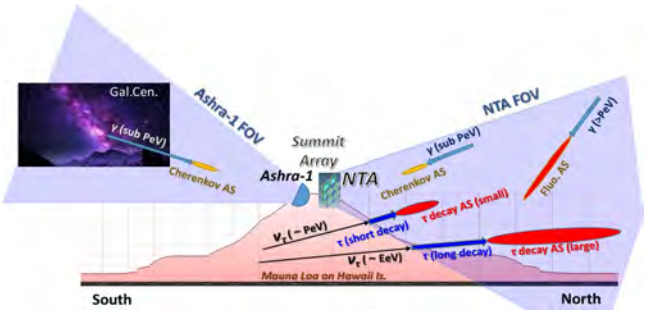


Fig. 6. Concept of imaging observation of PeV $\nu$'s, $\gamma$-rays, and nuclei with Ashra NTA summit array. For example, Ashra-1 and NTA detectors can simultaneously observe our galactic bulge in their FOV, checking the coincidence of $\nu$'s with $\gamma$-rays originating from the same objects or regions.

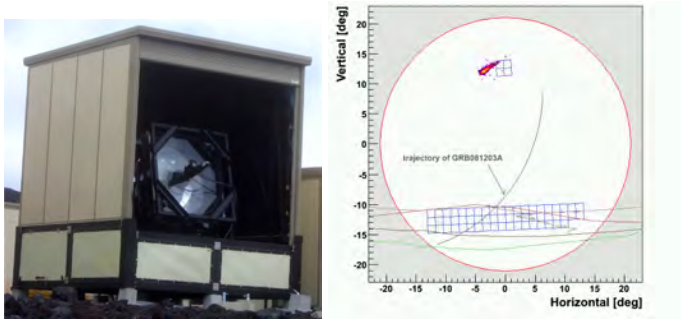


Fig. 7. *Left*: The Ashra-1 light collector (LC) facing Mauna Kea. *Right*: Boundary (large red circle) between the inside (open circle) and outside (hatched area) of the FOV of the LC and the layout of trigger pixel FOVs (blue boxes) for Cherenkov $\tau$ shower observation. Attached array of the trigger pixel FOVs (upper four blue boxes) to check the detection sensitivity with ordinary cosmic-ray air showers at a higher elevation. A simulated image of a cosmic-ray air shower readout along the trigger (points). The trajectory of GRB081203A counterpart (circular arc), the ridge lines of Mauna Kea (red) and Mauna Loa (green) mountains, the horizon, and Mauna Kea access road are shown.

rather than optical lenses to generate convergent beams with the 20 inch Photoelectric Lens Imaging tube (PLI) [10] (Figure 7) demagnifying to 1 inch at focal surface, enabling high resolution over a wide FOV [11]. The following trigger readout Photoelectric Image Pipeline (PIP) [12] can image and read out three independent phenomena on different time scales, i.e. AS CE emission (ns), AS FL ($\mu$s), and starlight (s), without sacrificing the S/N ratios. Figures 8 and 9 show the cosmic ray energy spectrum and the ES-$\nu_\tau$ limit from updated the Ashra-1 3rd observation period (Obs3) of 1863 hours [13]. The observed cosmic ray spectrum agrees reasonably well with the Monte Carlo simulation based on the cosmic ray flux observations in the knee region by the conventional air shower arrays as used in our first ES-$\nu_\tau$ search paper [14]. The estimation of the detection sensitivity of the Ashra-1 LC and the validity of the reconstruction procedure were well demonstrated.

Our results are the most stringent in the PeV–EeV region and complementary to other observational results for the sub-

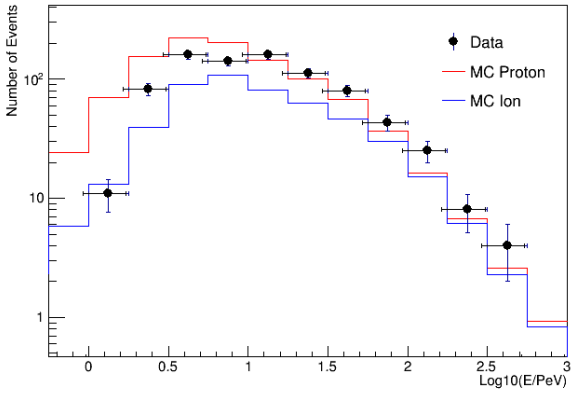


Fig. 8. Observed cosmic-ray flux spectrum (filled circles) with bars indicating statistical and systematic errors and the MC predictions for proton primary (red histogram) and iron primary (blue histogram) assumptions.

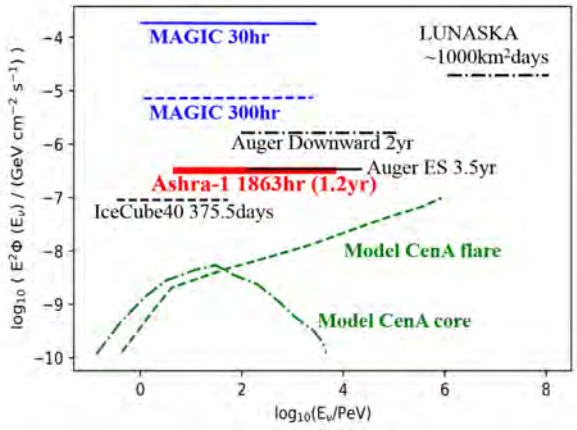


Fig. 9. Ashra 90% CL limit (thick continuous line (red)) on $\nu_\tau$ flux from sources in the PeV–EeV region (see the text). For comparison, MAGIC [15], IceCube [16], Auger [17], LUNASKA [18] limits as well as model predictions [19, 20] are shown. Plots adopted from [15].

PeV and over-EeV energy regions, and indicate the advanced sensitivity of the system.

By optimizing the layout of the NTA stations to enhance the sensitivity for ES-$\nu_\tau$'s around 1 PeV from the simulation studies [5, 7], four NTA stations will be served on Mauna Loa at 3000 - 3500 m asl (Summit Array), which watch the air volume surrounding the mountain including the surface. Mauna Loa is the world largest volcano suitable for detecting CE and FL light from $\tau$ ASs with both short and long decay lengths and $\gamma$ ASs as shown Figure 6. Figure 10 shows the neutrino flux sensitivity of NTA with only fluorescence mode, that including far-Cherenkov mode and other experiments, neutrino flux predictions, and existing flux constraints. The NTA neutrino sensitivity can be fairly competitive in PeV-EeV.

The combination between Ashra-1 and NTA detector units is planned to realize the comprehensive observation both with TeV-PeV $\gamma$-rays and PeV $\nu$'s. Six combined Ashra-1 LCs will be realigned for the FOV centers to be on the arc of the Galactic Center trajectory maximizing the stereoscopic observation efficiency. Each LC FOV will be overlapped with

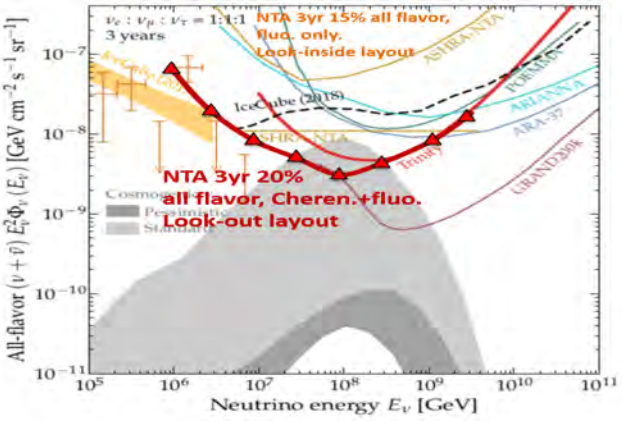


Fig. 10. Neutrino flux sensitivity of NTA with only fluorescence mode, that including far-Cherenkov mode and other experiments, neutrino flux predictions, and existing flux constraints. Figure adapted from [8].

the half of the adjacent ones. It results in total rate of the stereoscopic observation can be more than 70% of the trajectory in the sky. The estimated annual observable time of 1150 hours $\times\varepsilon_w$ during nights without moon in the south is more than 50 times better than HESS achieved i.e. 227 hours for Sgr A$^*$ in 10 years [2], assuming the weather efficiency $\varepsilon_w \sim 90\%$ according to the Ashra-1 operation.

Another fascinating is the detection of $\gamma$-rays with the large zenith-angle (LZA) ethod. The galactic bulge has the trajectory in the southern night sky with LZA more than 50 degrees, corresponding to the shower max distance larger than 9 km and the detection threshold energies higher than 16 TeV. Our situation studies check the cut-off energy in the $\gamma$-ray spectrum in the galactic bulge or central region. We confirm the LZA method is promising particularly for the PeV $\gamma$-ray detection. Once the northward NTA units detect $\nu$'s from the same $\gamma$-ray objects observed by Ashra-1 LCs, we can argue, more concretely than ever, the physics of the occurrence of $\gamma$-rays and $\nu$'s [8].

## Bibliography


[1] M. Aartsen *et al.*, PRL **113**, 101101 (2014).

[2] HESS Collab., Nature **531**, 476 (2016).

[3] IceCube Collab., Science **361**, 147 (2018).

[4] M. Sasaki, ICRR2000 Sat. Sympo., 109 (2000).

[5] M. Sasaki, G. Hou, arXiv:1408.6244 (2014).

[6] M. Sasaki, *et al.*, Astropart. Phys. **19**, 37 (2003).

[7] Y. Asaoka, M. Sasaki, Astropart. Phys. **41**, 7 (2013).

[8] M. Sasaki (Ashra-1/NTA), PoS (ICRC2019) 1003.

[9] M. Sasaki, Prog. Theo. Phys. Suppl. **151**, 192 (2003).

[10] Y. Asaoka, M. Sasaki, NIMA **647**, 34 (2011).

[11] M. Sasaki, *et al.*, NIMA **492**, 49 (2002).

[12] M. Sasaki *et al.*, NIMA **501**, 359 (2003).

[13] S. Ogawa (Ashra-1), PoS (ICRC2019) 970.

[14] Y. Aita, *et al.*, ApJL 736, L12 (2011).

[15] M. Ahnen, *et al.*, Astropart. Phys. 102, 77 (2018).

[16] R. Abbasi, *et al.*, ApJ, 732 (2011) 18.

[17] P. Abreu, *et al.*, ApJ Lett., 755 (2012) L4

[18] C. James, *et al.*, MNRAS, 410 (2011) 885.

[19] A. Cuoco, S. Hannestad, PRD, 78 (2008) 023007.

[20] M. Kachelriess, *et al.*, New J. Phys., 11, (2009) 065017.

## $\gamma I$ Group

$\gamma I$ Consortium
[Spokesperson : R.Enomoto]
Collaboration list:
ICRR, The University of Tokyo, Chiba, Japan; National Institute of Technology, Sendai College, Miyagi, Japan College of Science, Ibaraki University, Ibaraki, Japan; Faculty of Medical Engineering and Technology, Kitasato University, Kanagawa, Japan; Department of Radiological Sciences, Tokyo Metropolitan University, Tokyo, Japan; IPNS, High Energy Accelerator Research Organization, Ibaraki, Japan; National Cancer Center, East, Chiba, Japan;

### A portable radioactive detection system for outdoor measurement of concentration of radioactive caesium in a mushroom bed log at a low-level contaminated environment

Log cultivation of shiitake mushrooms has been declining in the Fukushima Prefecture and its surrounding areas due to the Fukushima Dai-ichi Nuclear Power Plant accident. Shiitake mushrooms by log cultivation can be rarely found in Kanto area nowadays. The Forestry Agency has set a maximum concentration limit for radioactive caesium of 50 Bq/kg for bed logs to cultivate safe shiitake mushrooms ($<$100 Bq/kg). The reason why the latter level is higher than the former is due to the high absorption feature by shiitake mushrooms[1]. In addition the difficulty is that this level of radioactivity is too small to be separated from the background by the natural radioactivity. In addition, broad area in East Japan is weakly polluted and its level is nearly that of natural background. The instruments to measure this level of radioactivity are available only for indoor measurement, however, they are too heavy to be portable with thick radiation shield[2]. Also they are expensive[2]. The demands to the detector to be used at the polluted area, i.e., cultivation area (outdoor), is high.

In this study, we developed a low-cost portable radioactive detection system without heavy radiation shield. The safe bed logs were selected using a screening test with the portable radioactive detection system even at a for levels of contamination ($\sim$0.1 Sv/h). The detail can be found in Kagaya et al[3].

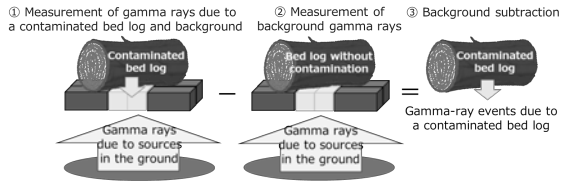


Fig. 11. Principles of measuring radioactive caesium concentrations in a bed log for the cultivation of shiitake mushrooms.

We developed the following method to measure low level radioactivity even in the polluted area as shown in Fig. 11. The inorganic scintillators made of CsI(Tl) are used to detect 662 keV $\gamma$-rays from $^{137}$Cs. The size of crystals is 5cm cube. 4 Crystals are used. The 2-inchi PMTs readout the light yields. The total procedure is consisted of two measurements. First, the polluted mushroom bed log is placed on the detector and the $\gamma$-ray's energy spectrum is taken. Second, the polluted log is replaced with un-polluted one which was bought from West Japan area. the 662-keV $\gamma$-ray peak is obtained from the difference of those two spectra. The reason why the log is placed above the crystals is that the 662-keV $\gamma$-rays rarely radiated from the sky direction compared with the other directions. Also the meaning to place un-polluted log is to compensate the effect of absorption by the wood itself of $\gamma$-ray from the direction of sky. All through two measurements, the detector is set at the same place in order to cancel the background radiations mainly from the ground, woods, and etc.

The photograph of the detector system is shown in Fig. 12. The electronic system is as same as the $\gamma$I Compton

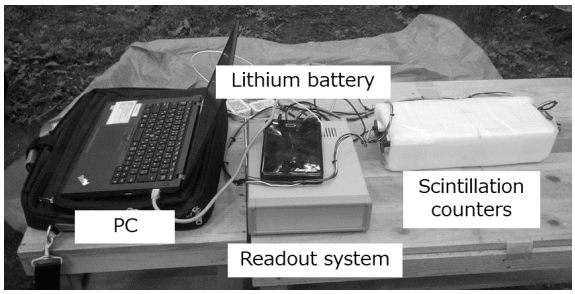


Fig. 12. A portable radioactive detection system.

Camera[4]. The total weight of the system is 5 kg. A single Li-ion battery pack can operate the system for 12 hours. Portability is, therefore, well guaranteed.

The obtained energy spectra are shown in Fig. 13. The solid histograms were obtained for the polluted bed log and the hatched ones were for the un-polluted bed log. The energy region only around 605, 662, and 795 keV show the differences, and the spectrum of the other region remains same.

After the outdoor measurements of 28 polluted bed logs, they were milled and measured by the Ge detector. The correlation between two data is shown in Fig. 3. The correlation coefficient is $0.83^{+0.08}_{-0.17}$. The total error including the systematic ones are considered to be 10 Bq/kg. The size difference of the measured and reference logs is one of those errors. We, therefore, concluded that our detector is suitable for screening the polluted bed log over 50 Bq/kg even at outside of 0.1$\mu$Sv/h

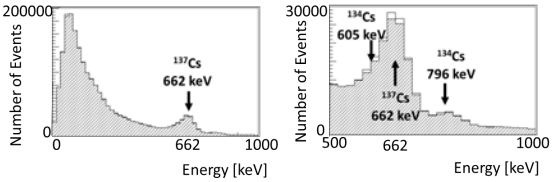


Fig. 13. An energy spectrum obtained from the measurement of a bed log outdoors. This energy spectrum was obtained from four scintillation counters and the exposure time was 20 minutes. The figure on the left side shows the energy spectrum from 0 to 1000 keV. The figure on the right side displays the enlarged, energy spectrum near the 662 keV peak. Areas with solid lines represent data obtained by measuring a contaminated bed log, whereas shaded areas represent data measured on a bed log without radioactive contamination.

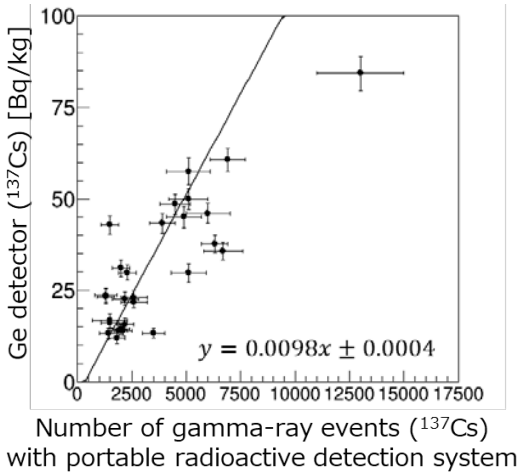


Fig. 14. Plotted gamma-ray events detected by a portable radioactive detection system and the concentrations of radioactive caesium measured by a Ge detector. Radioactive caesium concentrations were corrected using density and water content of the bed logs used for shiitake mushroom cultivation.

area. The prefectures of Tochigi, Ibaraki, and Miyagi corresponds to this level.

We developed a portable detector to measure the low-level radioactivity from the shiitake mushrooms bed log. The performance was proven by the comparison with the results of Ge detector. The screening of polluted bed log can be carried out even at the low-level polluted area such as prefectures surrounding Fukushima.

This detector only measures bed logs. The next target is to measure standing trees. The project is well going on using 32 keV $\gamma$-rays from $^{137}$Cs, i.e., $K\alpha$ of $^{133}$Ba. The advantage is that a thinner and lighter shield is applicable than in the case of 662-keV $\gamma$-rays.

## Bibliography

[1] http://www.rinya.maff.go.jp/j/press/tokuyou/120830.html

[2] For example, Gamma Spotter F, Furukawa Electric.

[3] M.Kagatya, H. Katagiri, R.Enomoto et al, RADIOISOTOPES, **68**, 305-315 (2019), doi: 10.3769/radioisotopes.68.305

[4] M.Kagaya, H.Katagiri, R.Enomoto et al, Nucl. Instrum. Meth. **A804**, 25-32 (2015).

# ASTROPHYSICS AND GRAVITY DIVISION

## Overview

Astrophysics and Gravity Division consists of Gravitational Wave Group, The Observational Cosmology Group, Primary Cosmic Ray Group and Theory Group.

The Gravitational Wave Group conducts experimental research of gravitational wave with researchers of gravitational wave experiment and theory in Japan. The main items are the construction of the large scale cryogenic interferometer(KAGRA) at Kamioka underground and the operation of CLIO. For this purpose, KAGRA observatory was established at the beginning of the fiscal year of 2016 to assist the construction of KAGRA gravitational wave telescope.

The Observational Cosmology Group studies the cosmic history based on deep multi-wavelength observations in collaboration with worldwide researchers. This group has started a new optical deep survey project with the wide-field imager of Hyper Suprime-Cam mounted on the Subaru telescope.

Theory Group conducts both theoretical study of the Universe and astroparticle physics.

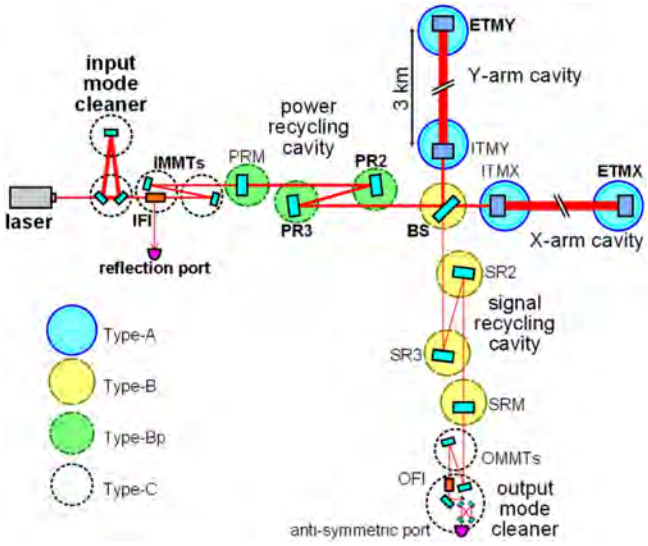


Fig. 1. Schematic view of the bKAGRA interferometer[4]. Type-A, Type-B, Type-Bp, and Type-C are the names of vibration isolation system for each mirror.

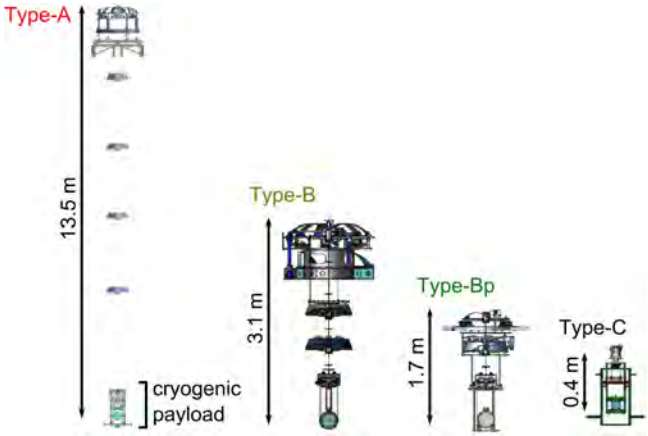


Fig. 2. KAGRA vibration isolation systems[4]. KAGRA equips four kinds of vibration isolation systems such as Type-A, Type-B, Type--Bp, and Type-C.

## Gravitational Wave Group

### *KAGRA Project Status*

[Spokesperson : Takashi UCHIYAMA]
ICRR, The Univ. of Tokyo, Hida, Gifu 506-1205

**Overview**

KAGRA, Large-scale Cryogenic Gravitational wave Telescope, aims at detecting gravitational waves and developing gravitational wave astronomy, which was established by the first detection of gravitational waves by LIGO. KAGRA employs a 3 km L-shaped laser interferometer with a cryogenic mirror system placed underground at Kamioka[1]. The KAGRA development is divided into two stages: the initial KAGRA (iKAGRA) and baseline KAGRA (bKAGRA). The iKAGRA interferometer is a simple Michelson interferometer with a 2-Watt laser, room-temperature mirrors, and a simple vibration isolation system. We completed the iKAGRA interferometer with a test run in April 2016[2]. Then we proceeded to bKAGRA.

Figure 1 and 2 show a schematic view of optical layout of the bKAGRA interferometer and the KAGRA vibration isolation systems. Table 1 shows design parameter of the bKAGRA interferometer[4]. The bKAGRA interferometer will employ a Resonant Sideband Extraction (RSE) interferometer with 180-Watt laser, cryogenic Sapphire mirrors, and several kinds of vibration isolation systems. The bKAGRA interferometer should attain the sensitivity high enough for the detection of gravitational waves with the help of the high power laser and RSE interferometer to reduce the quantum noise, the cryogenic Sapphire mirrors to reduce the thermal noise, and the vibration isolation systems to reduce the seismic noise. Figure 3 shows designed sensitivities of bKAGRA in case of Broadband RSE (BRSE) and of Detuned RSE (DRSE), where incoherent sum of the fundamental noise sources is assumed. Observation range for an in-spiral and merger of neutron-star binary reaches 135 Mpc in BRSE and 153 Mpc in DRSE with the same definition of the observation range as LIGO and Virgo.

Figure 4 shows the international collaborative observation scenario[3]. LIGO conducted Observation 1 (O1) from

Table 1. The design parameters of the bKAGRA interferometer[4].

| | | | |
|---|---|---|---|
| Arm cavity length | 3000 m | Test mass size | $\phi 22\,\mathrm{cm} \times 15\,\mathrm{cm}$ |
| Laser wave length | 1064 nm | Mass of test mass | 22.8 kg |
| Input power at PRM | 67W | Temperature of test mass | 22 K |
| Arm intra-cavity power | 340 kW | Beam radius at test mass | 3.5 cm |
| ITM transmittance | 0.4 % | PRC/SRC lengths | 66.6 m |
| PRM transmittance | 10 % | Detuning angle | 3.5 deg |
| SRM transmittance | 15 % | Homodyne angle | 135.1 deg |

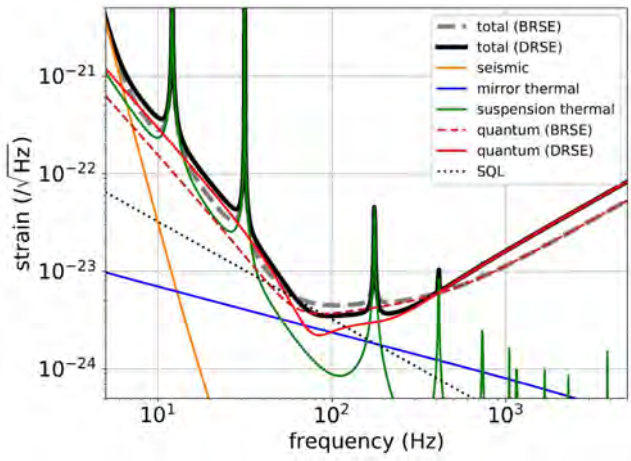


Fig. 3. The designed sensitivity of the bKAGRA interferometer[4]. "total", "seismic", "mirror thermal", "suspension thermal", "quantum", and "SQL" mean total sum of fundamental noise sources shown in this figure, seismic noise including gravity gradient noise, mirror thermal noise, suspension thermal noise, quantum noise, and standard quantum limit, respectively. The figure shows "total" and "quantum noise" in both Broadband RSE (BRSE) and Detuned RSE (DRSE) case. Observation range for an in-spiral and merger of neutron-star binary reaches 135 Mpc in BRSE and 153 Mpc in DRSE with the same definition of the observation range as LIGO and Virgo.

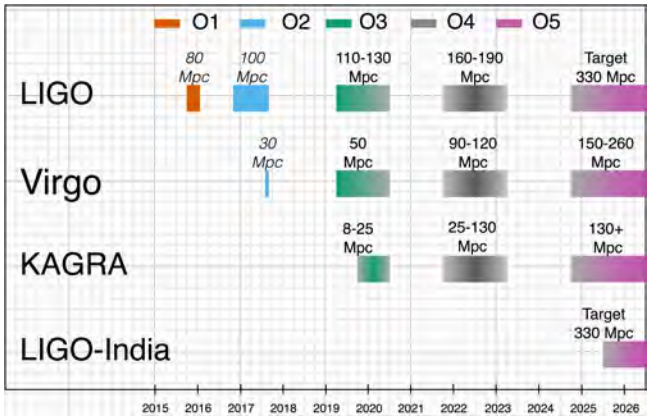


Fig. 4. International observation scenario[3]. Virgo was joined in Observation 2 (O2) from August 1st in 2017. LIGO and Virgo started Observation 3 (O3) from April 1st in 2019. O3 will continue by the end of April in 2020. KAGRA is aiming to join O3 in 2019.

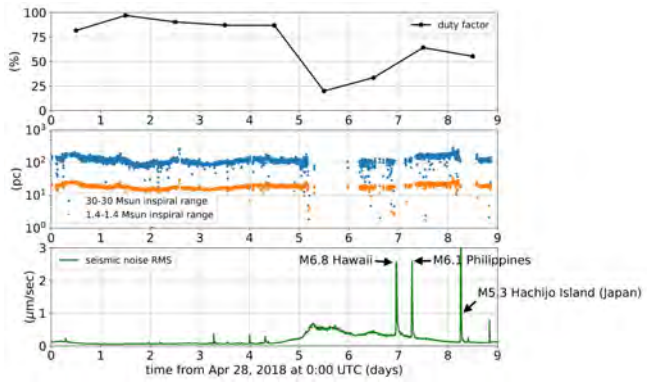


Fig. 5. Daily status of bKAGRA phase 1 operation[4]. The figure shows daily duty factor (Top panel), inspiral range (Middle panel), and seismic noise level (Bottom panel) during the operation. The operation was done from April 28 to May 6 in 2018.

September 12th, 2015 to January 19th, 2016 and Observation 2 (O2) from November 30th, 2016 to August 25th, 2017. Virgo joined O2 from August 1st, 2017. LIGO and Virgo started Observation 3 (O3) from April 1st, 2019 and O3 will continue by the end of April in 2020. KAGRA is aiming to join O3 in 2019.

In FY2018 we started with an operation of KAGRA interferometer as bKAGRA phase 1 which is 3 km Michelson interferometer with two sapphire mirrors suspended by the Type-A vibration isolation systems. One sapphire mirror was cooled at 18 K. The operation was done from April 28 to May 6 in 2018 and it was the first demonstration of operating km-class interferometer at cryogenic temperature. Figure 5 and Figure 6 shows a summary of daily status of the operation and a strain sensitivity comparing with noise sources[4], respectively. Duty factor in the first half of the operation reached 88.6%. The observation range for an in-spiral and merger of neutron-star binary and BH binary reached 17 pc and 100 pc, respectively. The longest continuous operation time was 11.1 hour.

After the bKAGRA phase 1 operation, we started construction of the bKAGRA interferometer with 40 W laser power. What we have installed were an infrared laser system with the maximum power of 40 W, two sets of arm length stabilization system using a green laser, calibration systems using photon radiation pressure, large beam baffles, transmission monitor systems, some optics consisting a signal recycling cavity and output optics, two input test masses called ITMX and ITMY in Figure 1, and so on. Physical Environmental Monitor (PEM) is a sensor network consisting several kinds of environmental sensors such as accelerometers,

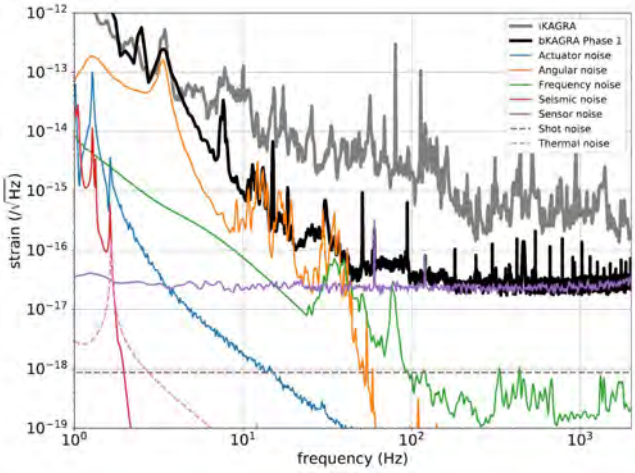


Fig. 6. Strain sensitivity of KAGRA in phase 1 operation[4].

seismometers, magnetometers, thermometers, acoustic sound monitors, power monitors and so on. Purpose of PEM is to check the detector health, noise sources, and data quality in cooperation with the detector characterization group. We placed many sensors in the KAGRA site and monitoring has already started.

We have tried lock acquisition of the X-arm cavity for the first time in parallel with the installation works mentioned above. The lock acquisition of the X-arm cavity was successfully achieved with helps of the arm length stabilization system. Then we carried out charcterization of the X-arm cavity. Table2 shows a summary of optical parameters of the X-arm cavity comparing with designed and measured values.

We also enhanced the international collaborations with the Einstein Telescope (ET) project, LIGO, Virgo, Korean and other Asian groups mainly based on the JSPS core-to-core program.

The rapidly progressing status of KAGAR were presented in many international conferences. Many papers about the progress of KAGRA were also published [1], [4], [5]. We also presented activities on our web-page.[6]

## Bibliography

[1] "KAGRA: 2.5 generation interferometric gravitational wave detector", KAGRA collaboration, Nature Astronomy, Vol. 3, January 2019, 35-40

[2] "Construction of KAGRA: an underground gravitational-wave observatory", KAGRA collaboration, Prog. Theor. Exp. Phys. 2018, 013F01 (2018)

[3] "Prospects for observing and localizing gravitational-wave transients with Advanced LIGO, Advanced Virgo and KAGRA", Abbott, B.P., Abbott, R., Abbott, T.D. et al. arXiv:1304.0670v9 [gr-qc]

[4] "First cryogenic test operation of underground km-scale gravitational-wave observatory KAGRA", KAGRA collaboration, Class. Quantum Grav. 36 165008 (2019)

[5] "An arm length stabilization system for KAGRA and future gravitational-wave detectors", KAGRA collaboration, to be published in Class. Quantum Grav. (2019)

[6] http://gwcenter.icrr.u-tokyo.ac.jp/en/

### Integrated DAQ/control system using real time computers

[Spokesperson : Osamu MIYAKAWA]

ICRR, The Univ. of Tokyo, Hida, Gifu 506-1205

The 2018 fiscal year, we started from 9 days short operation with a 3km simple Michelson configuration with a single end mirror in low temperature. By the short operation in May of 2018, basically we established the whole integrated control/data acquisition system for KAGRA.

***Stable operation with the real time control system*** The interferometer configuration was just a Michelson type and it was still much simpler than the same as the final one. However as a control system, it was almost the same as the final configuration. The difference was only that we had no input test masses. We had already prepared the control system for the two input test masses. So we did not increase the number of control computers in this FY, even the input test masses were installed after the short operation in the rest of this FY. On the other hand, we spent a lot of time to stabilized the whole control/data acquisition system. At this stage we had 25 real time control computers, 8 data acquisition computes, 10 servers as camera, script etc. and 15 workstations as user clients. Especially connecting such a many numbers of the real time control computers were the first experience for us. We had carefully performed many tests for this system in the independent test bench but the number of computers had been limited in the test. We experienced several serious issues caused by them number of computers working at a time.

The biggest issue was that we noticed some glitches happened in the signal. They happened when the control computers had a heavy load. Basically the control computers use a real time operating system. Some delay due to the heavy task causes a serious problem for control loops and it emerges as jumps or glitches on many signals. These glitches increased in proportional with the number of operated computers. Then we realized that this issue can be solved by replacing the slow computer to the faster one after some experiments at the test bench. We have just started replacing the slow computers which are being used in KAGRA. Once the new faster computer runs processes in the KAGRA system, it never happens glitches or some other serious problem. We keep replacing existing slow computers in the next year and we will finish it before the observation starts in the end of 2019.

***Guardian: automatic operation system*** One of the big topics of this fiscal year was that some automatic control system implemented drastically. It was called 'Guardian'. The Guardian is always looking at all important channels and puts proper commands according to a script that was written by human before. Almost of subsystems in KAGRA are controlled

Table 2. Optical parameters of the X-arm cavity[5].

| Parameter name | Designed | Measured |
|---|---|---|
| Cavity length | 3000 m | 29999.990(2) m |
| Finesse for 1064 nm | 1530 | 1410(30) |
| Roundtrip loss for 1064 nm | ¡ 100 ppm | 86(3) ppm |
| Finesse for 532 nm | 49.2 | 41.0(3) |

under this Guardian, and they are automatically operated as a whole gravitational wave detector. KAGRA is the huge plant which consists of a large number of subsystems. We need to connect the subsystems, and the KAGRA should work as a whole combined device as a gravitational wave detector.

***Stability of data acquisition system*** This system also has an important role as a data acquisition system. This data acquisition system consists of a collecting data server, data providing servers, and data writing servers. Actual chunk of data comes from the control computers and it was collected by the data collecting server. As increasing number of control computers, amount of data increased drastically in this year, and we noticed that the streaming data sometimes failed once or several times in a week. We had to replace some of the weakest servers to the faster one with more memories. We had prepared two paths for data acquisition as redundancy, so we did not miss data yet. We need to keep watching the stability of these data transfers until the actual observation starts.

In the FY of 2019, we plan to join an observation with LIGO and VIRGO. It is expected that this DAQ/control system performs stable automatic operations for commissioning work, noise hunting, and the observation.

### Data Analysis

[Spokesperson : Hideyuki Tagoshi]

ICRR, The Univ. of Tokyo, Kashiwa, Chiba, 277-8582

There are variety of data related activities in KAGRA. The main data server of KAGRA is located at ICRR Kashiwa. It has a 2.5PiB data storage. All KAGRA data taken at Kamioka are packed into one file for every 32 seconds, and are transferred continuously to the main data server at Kashiwa. Beside this, low latency data transfer is also done by packing only main interferometer data into one file for every 1 seconds. For low latency data transfer, the latency of about 3 seconds is achieved from Kamioka to Kashiwa (this time include the time necessary for calibration).

KAGRA detector is producing several hundreds thousands of channels of data which record signals from various sensors, signals to control instruments, signals to monitor environment of the detector. Those data are used to check the status of detector and to improve the sensitivity. It is important to introduce convenient tools to visualize the data in order to accelerate the installation and commissioning works. Web based visualization tools are now being developed. Some of tools developed by LIGO group are also installed. These tools are also useful when gravitational wave signals are detected. In order to have a confidence of detection of gravitational wave signals, it is important to investigate environmental channels whether there are any noise sources which might produce data which are similar to real gravitational wave signals. These visualization tools can be used to check various environmental channel data.

In order to detect gravitational wave signals, several pipelines have been developed in KAGRA. Among them, a pipeline to search for gravitational waves from compact binary coalescences (CBC) are developed in KAGRA Algorithmic Library (KAGALI). KAGALI is a common data analysis library written mainly in C. The CBC pipeline have been used to analyze KAGRA data during iKAGRA operation. Improvement of the CBC pipeline are now ongoing in order to treat multiple detectors and to introduce the spin parameters in the waveform. These tasks will be continued in 2019. The improvement of the parameter estimation pipeline for CBC signals based on the Markov Chain Monte Carlo method was continued from the last year. This work is lead by Hyung Won Lee (Inje Univ).

There are several efforts to introduce new data analysis methods in the analysis of gravitational wave data. Among them, the performance of Non-Harmonic Analysis (NHA) in visualizing the time-frequency behavior of the data was evaluated. NHA is a method to evaluate the spectrum of data by evaluating multiple instantaneous frequencies and amplitudes of data in a way which is different from discrete Fourier transform. We find that there are various advantage in NHA in visualizing CBC signals compared with the method of short time Fourier transform. We apply NHA to public data of LIGO-Virgo events, like GW150914, GW170817, and demonstrated the visualization of the signal on time-frequency plane. This work has been done in collaboration with the group of Shigeki Hirobayashi (Univ. Toyama).

Ref. Kenta Yanagisawa , Dongbao Jia, Shigeki Hirobayashi, Nami Uchikata , Tatsuya Narikawa, Koh Ueno, Hirotaka Takahashi, Hideyuki Tagoshi, PTEP 2019 (2019) no.6, 063F01.

## Observational Cosmology Group

[Spokesperson : Yoshiaki Ono]

ICRR, The Univ. of Tokyo, Kashiwa, Chiba 277-8582

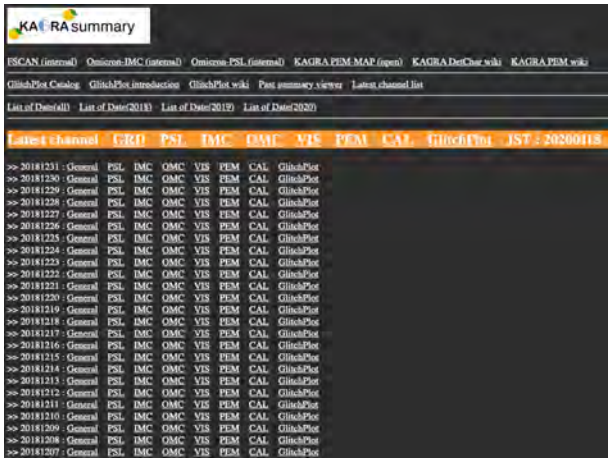


Fig. 7. Example of summary page

### *ALMA 26 arcmin$^2$ Survey of GOODS-S at One millimeter (ASAGAO): Average Morphology of High-$z$ Dusty Star-Forming Galaxies is an Exponential-Disk ($n \simeq 1$)* [1]

In collaboration with the members of The University of Tokyo, Kyoto University, Niels Bohr Institute, National Astronomical Observatory of Japan, Ehime University, Chinese Academy of Sciences, The Open University of Japan, RIKEN, Chulalongkorn University, National Astronomical Research Institute of Thailand, University of Edinburgh, European Southern Observatory, Academia Sinica, and Nagoya University.

We present morphological properties of dusty star-forming galaxies at $z = 1-3$ determined with the high-resolution (FWHM$\sim$0.″19) Atacama Large Milllimeter/submilimeter Array (ALMA) 1mm map of our ASAGAO survey covering a 26-arcmin$^2$ area in GOODS-S. In conjunction with the ALMA archival data, our sample consists of 45 ALMA sources with infrared luminosity ($L_{\rm IR}$) range of $\sim 10^{11} - 10^{13} L_\odot$. To obtain an average rest-frame far-infrared (FIR) profile, we perform individual measurements and careful stacking of the ALMA sources using the *uv*-visibility method that includes positional-uncertainty and smoothing-effect evaluations through Monte Carlo simulations. We find that our sample has an average FIR-wavelength Sérsic index and effective radius of $n_{\rm FIR} = 1.2 \pm 0.2$ and $R_{\rm e,FIR} = 1.0$–$1.3$ kpc (Figure 8), respectively, additionally with a point-source component at the center, indicative of the existence of AGN. The average FIR profile agrees with a morphology of an exponential-disk clearly distinguished from a de Vaucouleurs spheroidal profile (Sérsic index of 4). We also examine the rest-frame optical Sérsic index $n_{\rm opt}$ and effective radius $R_{\rm e,opt}$ with deep *Hubble Space Telescope* (HST) images. Interestingly, we obtain $n_{\rm opt} = 0.9 \pm 0.3$ ($\simeq n_{\rm FIR}$) and $R_{\rm e,opt} = 3.2 \pm 0.6$ kpc ($> R_{\rm e,FIR}$), suggesting that the dusty disk-like structure is embedded within a larger stellar disk. The rest-frame UV and FIR data of HST and ALMA provide us a radial profile of the total star-formation rate (SFR), where the infrared SFR dominates over the UV SFR at the center. Under the assumption of a constant SFR, a compact stellar distribution in $z \sim$1–2 compact quiescent galaxies (cQGs) is well reproduced, while a spheroidal stellar morphology of cQGs ($n_{\rm opt} = 4$) is not, suggestive of other important mechanism(s) such as dynamical dissipation.

## Bibliography

[1] Fujimoto, S., Ouchi, M., Kohno, K., Yamaguchi, Y., Hatsukade, B., Ueda, Y., Shibuya, T., Inoue, S., Oogi, T., Toft, S., Gómez-Guijarro, C., Wang, T., Espada, D., Nagao, T., Tanaka, I., Ao, Y., Umehata, H., Taniguchi, Y., Nakanishi, K., Rujopakarn, W., Ivison, R. J., Wang, W.-H., Lee, M. M., Tadaki, K., Tamura, Y., & Dunlop, J. S., 2018, The Astrophysical Journal, 861, 7

### *SILVERRUSH. V. Census of Ly$\alpha$, [OIII]$\lambda$5007, H$\alpha$, and [CII]158$\mu$m Line Emission with $\sim$ 1000 LAEs at $z = 4.9-7.0$ Revealed with Subaru/HSC* [2]

In collaboration with the members of The University of Tokyo, Kitami Institute of Technology, Osaka Sangyo University, The European Space Agency, California Institute of Technology, Ehime University, National Astronomical Observatory of Japan, University of California Santa Barbara, Carnegie Observatories, Universidad Nacional Autonoma de Mexico, Institut d'Astrophysique de Paris, Laboratoire d'Astrophysique de Marseille, and Niels Bohr Institute.

We investigate Ly$\alpha$, [OIII]$\lambda$5007, H$\alpha$, and [CII]158$\mu$m emission from 1124 galaxies at $z = 4.9$–$7.0$. Our sample is composed of 1092 Ly$\alpha$ emitters (LAEs) at $z = 4.9$, 5.7, 6.6, and 7.0 identified by Subaru/Hyper Suprime-Cam (HSC) narrowband surveys covered by *Spitzer* Large Area Survey with Subaru/HSC (SPLASH) and 34 galaxies at $z = 5.148 - 7.508$ with deep ALMA [CII]158$\mu$m data in the literature. Fluxes of strong rest-frame optical lines of [OIII] and H$\alpha$ (H$\beta$) are constrained by significant excesses found in the SPLASH 3.6 and 4.5$\mu$ photometry. At $z = 4.9$, we find that the rest-frame H$\alpha$ equivalent width and the Ly$\alpha$ escape fraction $f_{{\rm Ly}\alpha}$ positively correlate with the rest-frame Ly$\alpha$ equivalent width $EW^0_{{\rm Ly}\alpha}$. The $f_{{\rm Ly}\alpha} - EW^0_{{\rm Ly}\alpha}$ correlation is similarly found at $z \sim 0-2$, suggesting no evolution of the correlation over $z \simeq 0-5$. The typical ionizing photon production efficiency of LAEs is $\log \xi_{\rm ion}/[{\rm Hz\ erg^{-1}}] \simeq 25.5$, significantly (60%–100%) higher than those of LBGs at a given UV magnitude. At $z = 5.7-7.0$, there exists an interesting turnover trend that the [OIII]/H$\alpha$ flux ratio increases in $EW^0_{{\rm Ly}\alpha} \simeq$ 0–30 Å and then decreases out to $EW^0_{{\rm Ly}\alpha} \simeq 130$ Å (Figure 9). We also identify an anticorrelation between a ratio of [CII] luminosity to star formation rate ($L_{\rm [CII]}$/SFR) and $EW^0_{{\rm Ly}\alpha}$ at the $> 99\%$ confidence level. We carefully investigate physical origins of the correlations with stellar-synthesis and photoionization models, and find that a simple anticorrelation between $EW^0_{{\rm Ly}\alpha}$ and metallicity explains self-consistently all of the correlations of Ly$\alpha$, H$\alpha$, [OIII]/H$\alpha$, and [CII] identified in our study, indicating detections of metal-poor ($\sim 0.03 Z_\odot$) galaxies with $EW^0_{{\rm Ly}\alpha} \simeq 200$Å.

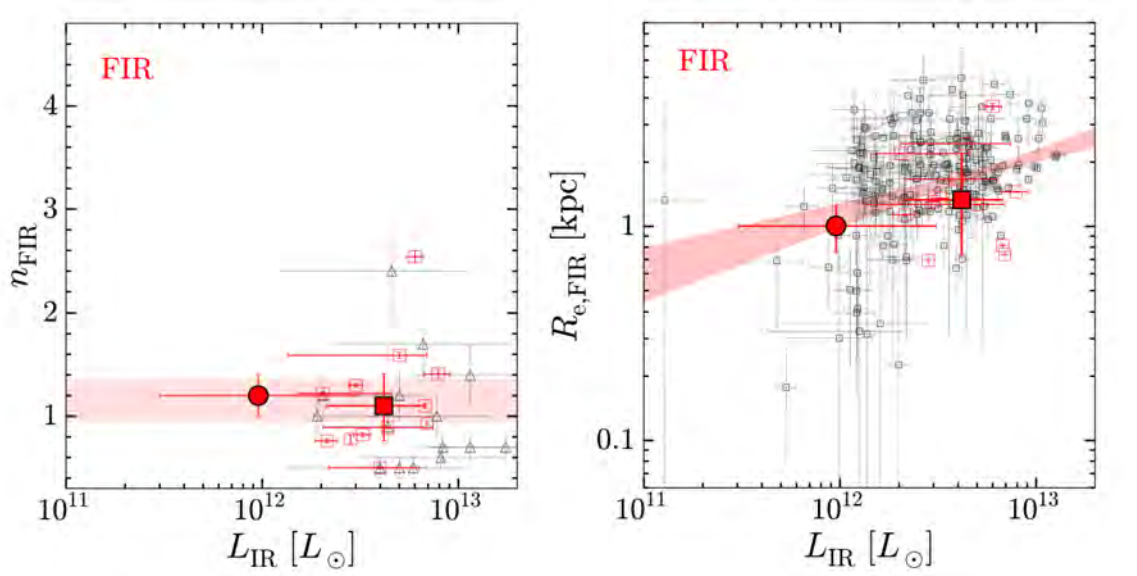


Fig. 8. Rest-frame FIR properties of $n_{\rm FIR}$ (left) and $R_{\rm e,FIR}$ (right) as a function of $L_{\rm IR}$. The red filled circle is obtained from the visibility-based stacking for the 33 ASAGAO sources at $z = 1$–3. The $L_{\rm IR}$ error bar represents the 16th–84th percentiles of the $L_{\rm IR}$ distribution for the ASAGAO sources, while the $n_{\rm FIR}$ and $R_{\rm e,FIR}$ error bars are evaluated by the bootstrap method and the MC simulations. The red open squares present the additional sample of the 12 individual bright ALMA sources at $z = 1$–3. The red filled square indicates the median value of the 12 individual ALMA sources, where the error bars denote the 16th–84th percentiles of the distribution. The black open triangles and squares are the previous ALMA results. In the right panel, the black open squares are estimated by fixing $n_{\rm FIR} = 1$, which we do not present in the left panel. The red shaded regions are the best estimates of the constant $n_{\rm FIR}$ (left) and the $R_{\rm e,FIR}$–$L_{\rm IR}$ relation (right). The constant $n_{\rm FIR}$ is estimated from the stacked ASAGAO and the median value of the 12 individual ALMA sources, while the best-fit $R_{\rm e,FIR}$–$L_{\rm IR}$ relation is obtained from the literature.

## Bibliography

[2] Harikane, Y., Ouchi, M., Shibuya, T., Kojima, T., Zhang, H., Itoh, R., Ono, Y., Higuchi, R., Inoue, A. K., Chevallard, J., Capak, P. L., Nagao, T., Onodera, M., Faisst, A. L., Martin, C. L., Bruzual, G. A., Charlot, S., Davidzon, I., Fujimoto, S., Hilmi, M., Ilbert, O., Lee, C.-H., Matsuoka, Y., Silverman, J. D., & Toft, S. 2018, The Astrophysical Journal, 859, 84

### *CHORUS II. Subaru/HSC Determination of the Ly$\alpha$ Luminosity Function at $z = 7.0$: Constraints on Cosmic Reionization Model Parameter* [3]

In collaboration with the members of The University of Tokyo, Osaka Sangyo University, Kitami Institute of Technology, National Astronomical Observatory of Japan, Ehime University, and The Open University of Japan.

We present the Ly$\alpha$ luminosity function (LF) derived from 34 LAEs at $z = 7.0$ on an area of sky of 3.1 deg$^2$, the largest sample of those in the literature to date obtained at a redshift $z \gtrsim 7$. The LAE sample is compiled from deep large-area narrowband observations with Subaru conducted by the Cosmic HydrOgen Reionization Unveiled with Subaru (CHORUS) project. The $z = 7.0$ Ly$\alpha$ LF of our project is consistent with those of the previous Dark Energy Camera and Subaru studies at the bright and faint ends, respectively, while having uncertainties that are significantly smaller than those of the previous study results. Exploiting the small errors of our measurements, we investigate the shape of the Ly$\alpha$ LF from the faint end to the bright end. We find that the shape of

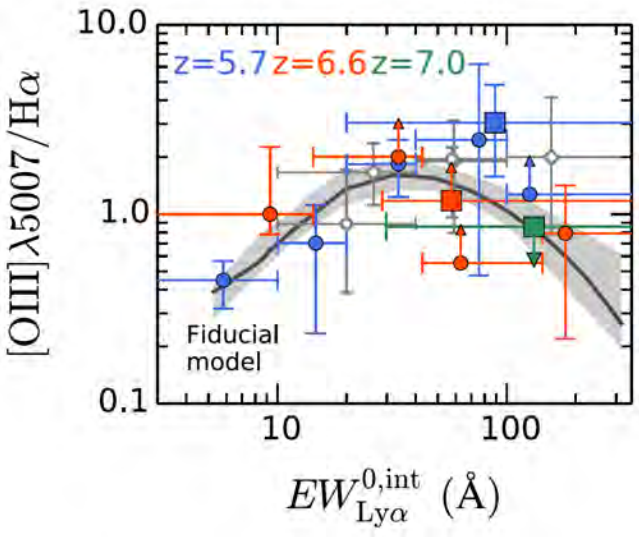


Fig. 9. [OIII]$\lambda$5007/H$\alpha$ flux ratios as a function of rest-frame Ly$\alpha$ EW. The blue, red, and green circles and squares are the [OIII]$\lambda$5007/H$\alpha$ flux ratios at $z = 5.7$, 6.6, and 7.0, respectively. The squares represent the results of the $EW_{\rm Ly\alpha} > 20$Å subsamples. The upward and downward arrows represent $2\sigma$ lower and upper limits, respectively. The open gray diamonds and circles are the ratios of $z = 2.5$ and 0.3 galaxies obtained in the literature. We plot the median and the $1\sigma$ scatters of the ratios in $EW^0_{\rm Ly\alpha}$ subsamples. We also plot the fitting result of the $(Z, \log U, {\rm Age})$–$EW^0_{\rm Ly\alpha}$ relations with the dark gray curve with the shaded region representing the $1\sigma$ uncertainty.

the $z = 7.0$ Ly$\alpha$ LF can be explained by the steep slope of $\alpha \simeq -2.5$ suggested at $z = 6.6$, and that there is no clear signature of a bright-end excess at $z \simeq 7$ claimed by the previous

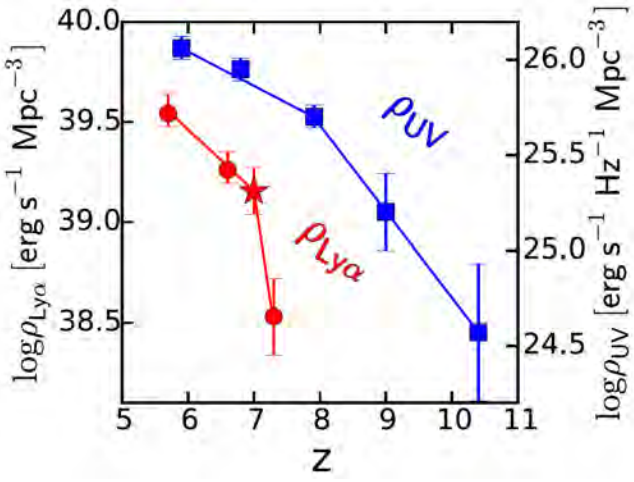


Fig. 10. Redshift evolution of the Ly$\alpha$ and UV LDs obtained with LAE and LBG samples. The red filled star represents the Ly$\alpha$ LDs at $z = 7.0$ from this study in the case of $\alpha = -2.5$. The red filled circles indicate the Ly$\alpha$ LDs at $z = 5.7$, 6.6, and 7.3 in the literature. The blue squares are the UV LDs for $z = 5.9,\ 6.8,\ 7.9,\ 9.0$, and 10.4 obtained in the literature. In this figure, we adopt the integration limits of $\log L_{Ly\alpha}[\mathrm{erg\ s^{-1}}] = 42.4$ and $M_{UV} = -17$ for the Ly$\alpha$ and UV LD estimates.

work, which was thought to be created by the ionized bubbles around bright LAEs, whose Ly$\alpha$ photons could easily escape from the partly neutral IGM at $z \simeq 7$. We estimate the Ly$\alpha$ luminosity densities (LDs) with Ly$\alpha$ LFs at $z \simeq 6-8$ given by our studies and the previous ones, and compare the evolution of the UV-continuum LD estimated with dropouts (Figure 10). The Ly$\alpha$ LD monotonically decreases from $z \sim 6$ to 8, and evolves stronger than the UV-continuum LD, which is indicative of the Ly$\alpha$ damping wing absorption of the IGM towards the heart of the reionization epoch.

## Bibliography

[3] Itoh, R., Ouchi, M., Zhang, H., Inoue, A. K., Mawatari, K., Shibuya, T., Harikane, Y., Ono, Y., Kusakabe, H., Shimasaku, K., Fujimoto, S., Iwata, I., Kajisawa, M., Kashikawa, N., Kawanomoto, S., Komiyama, Y., Lee, C.-H., Nagao, T., & Taniguchi, Y., 2018, The Astrophysical Journal, 867, 46

### ***Morphologies of*** $\sim 190,000$ ***Galaxies at*** $z = 0-10$ ***Revealed with HST Legacy Data. III. Continuum Profile and Size Evolution of Ly$\alpha$ Emitters*** [4]

In collaboration with the members of Kitami Institute of Technology, The University of Tokyo, and National Astronomical Observatory of Japan.

We present the redshift evolution of the radial surface brightness (SB) profile of the rest-frame UV and optical stellar continua for 9119 LAEs at $z \simeq 0-8$ and $0-2$, respectively. Using HST data and the LAE catalogs taken from the literature, we derive the structural quantities of the 9119 LAEs and of $\simeq 180,000$ photo-$z$ star-forming galaxies (SFGs) and Lyman break galaxies (LBGs) for comparison, by the well-tested profile fitting. From 936 well-fitted LAEs, we carefully define a homogeneous sample of LAEs falling in the same ranges of UV-continuum luminosity and Ly$\alpha$ equivalent width over $z \simeq 0-8$, and evaluate the redshift evolution. We find that the distribution of effective radius $r_e$ is represented by a log-normal function, and that the median Sérsic index is almost constant at $n \simeq 1-1.5$ for the LAEs over $z \simeq 0-7$, suggesting that typical LAEs have a stellar-disk morphology. The size–luminosity relation of the LAEs decreases monotonically towards high-$z$, following size–luminosity relations of SFGs and LBGs. The median $r_e$ values of the LAEs evolve significantly as $r_e \propto (1+z)^{-1.37}$, similar to those of the SFGs and LBGs in the same luminosity range (Figure 11), in contrast with the claims of no evolution made by previous studies, whose LAE samples are probably biased to faint sources at low-$z$. The $r_e$ distribution, star formation rate surface densities, and stellar-to-halo size ratios of the LAEs are comparable with those of the SFGs and LBGs, indicating that LAEs have stellar components similar to SFGs and LBGs with a Ly$\alpha$ emissivity controlled by the non-stellar physics such as the geometry, kinematics, and ionization states of the interstellar/circumgalactic medium.

## Bibliography

[4] Shibuya, T., Ouchi, M., Harikane, Y., & Nakajima, K., 2019, The Astrophysical Journal, 871, 164

### ***The onset of star formation 250 million years after the Big Bang*** [5]

In collaboration with the members of Osaka Sangyo University, National Astronomical Observatory of Japan, University College London, Université de Toulouse, Uppsala University, Johns Hopkins University, Nagoya University, Pontificia Universidad Católica de Chile, Millennium Institute of Astrophysics, Space Science Institute, The University of Tokyo, European Southern Observatory, Hokkaido University, Heidelberg University, Osaka University, The Open University of Japan, and RIKEN.

A fundamental quest of modern astronomy is to locate the earliest galaxies and study how they influenced the intergalactic medium a few hundred million years after the Big Bang. The abundance of star-forming galaxies is known to decline from redshifts of about 6 to 10, but a key question is the extent of star formation at even earlier times, corresponding to the period when the first galaxies might have emerged. Here we report spectroscopic observations of MACS1149-JD1, a gravitationally lensed galaxy observed when the Universe was less than four per cent of its present age. We detect an emission line of doubly ionized oxygen at a redshift of $9.1096 \pm 0.0006$, with an uncertainty of one standard deviation. This precisely determined redshift indicates that the red rest-frame optical color arises from a dominant stellar component that formed about 250 million years after the Big Bang, corresponding to a redshift of about 15. Our results indicate that it may be possible to detect such early episodes of star formation in similar galaxies with future telescopes. (Figure 12)

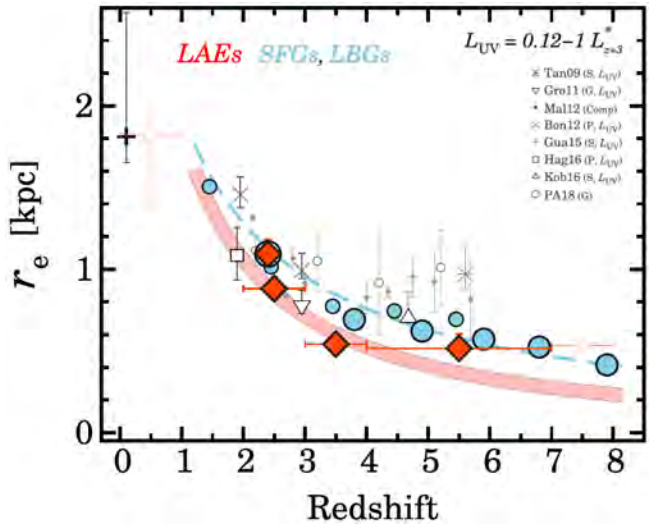


Fig. 11. Redshift evolution of $r_e$ in the $L_{UV}$ range of $0.12-1\ L^*_{z=3}$. The red filled diamonds with and without an open circle represent $r_e^{UV}$ and $r_e^{Opt}$ values measured for our LAEs, respectively. The red open diamond at $z\simeq0.5$ is $r_e^{Opt}$ for LAEs at $z\simeq0-1$ which is inferred from the extrapolation of the size–luminosity relation. The red open diamond at $z\simeq7.5$ represents $r_e^{UV}$ measured from the three LAEs at $z\simeq7-8$. The error bars of $r_e^{UV}$ at $z\simeq7-8$ are not reliably estimated because of the small statistics. The small and large cyan filled circles indicate the SFGs and LBGs, respectively. The magenta solid and cyan dashed lines present the best-fit $(1+z)^\beta$ functions for the LAEs and SFGs/LBGs, respectively. The best-fit $\beta$ value for $r_e^{UV}$ of the LAEs is $-1.37\pm0.65$, which is obtained from the three $r_e^{UV}$ data points at $z\simeq2-7$. The gray symbols present LAEs in the literature. The measurement technique is noted in the parenthesis of the legend (S: SExtractor; G: GALFIT; P: PHOT). For the previous studies with "$L_{UV}$" in the parenthesis of the legend, the median $r_e$ value is calculated in the range of $L_{UV}=0.12-1L^*_{z=3}$. The data points are slightly shifted along the $x$-axis for clarity. The error bars of some data points are smaller than the size of symbols.

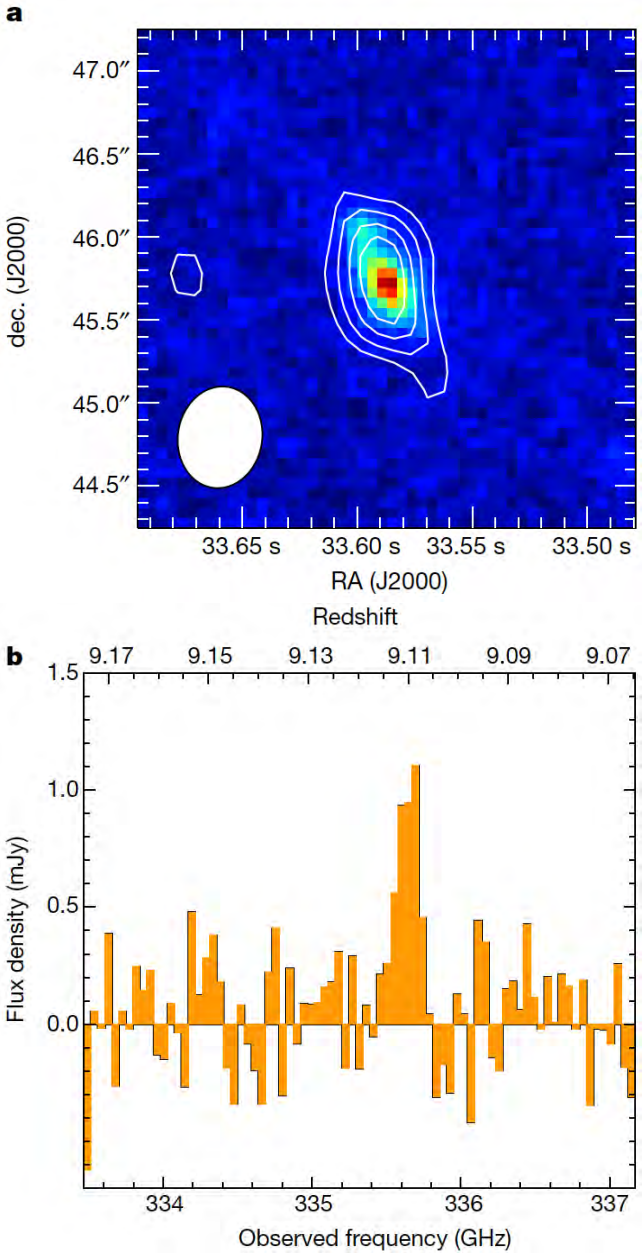


Fig. 12. ALMA [OIII] contours and spectrum of MACS1149-JD1. **a**) Magnification of an HST image (F160W), with the ALMA [OIII] contours overlaid. Contours are drawn at $-3\sigma$ (dashed line), $3\sigma$, $4\sigma$, $5\sigma$, and $6\sigma$, where $\sigma=17.5$ mJy km s$^{-1}$ per beam. The ellipse at the lower left corner indicates the synthesized beam size of ALMA. RA is the right ascension and dec. denotes the declination, both expressed in J2000 coordinates. **b**) The ALMA [OIII] 88$\mu$m spectrum in frequency space, obtained with a resolution of about 42 km s$^{-1}$.

## Bibliography

[5] Hashimoto, T.,; Laporte, N., Mawatari, K., Ellis, R. S., Inoue, A. K., Zackrisson, E., Roberts-Borsani, G., Zheng, W., Tamura, Y., Bauer, F. E., Fletcher, T., Harikane, Y., Hatsukade, B., Hayatsu, N. H., Matsuda, Y., Matsuo, H., Okamoto, T., Ouchi, M., Pelló, R., Rydberg, C.-E., Shimizu, I., Taniguchi, Y., Umehata, H., Yoshida, N., 2018, Nature, 557, 7705

# Theory Group

## Overview

The theory group is active in elementary particle physics focusing on particle phenomenology, and in astroparticle physics focusing on particle cosmology. In particle physics, the main topics are theoretical studies of dark matter, inflation and extensions of the standard model. In astroparticle physics, the main topics are theoretical studies of inflation, thermal history of the early universe, dark matter, baryogenesis and big-bang nucleosynthesis.

After the discovery of the Higgs boson, the LHC has shown no strong hints on new physics. In this situation, we need to reconsider many ideas of new physics models as well as conventional strategies to search for them. Accordingly, our studies on beyond the Standard Model physics becomes more and more diverse.

Since the LIGO detectors detected the first confirmed gravitational waves (GWs) from colliding black holes on September 14, 2015, new era of GW astronomy began. So far, more than 10 GW events were detected by LIGO. Among

them is the first detection of GW from binary neutron star. The discovery suggested strongly the existence of kilonova which can produce r-process elements. If they continue to find GW events from black holes and neutron stars, their origin becomes one of the most interesting topics.

The supersymmetric (SUSY) extension of the standard model (SM) in the particle physics is considered to be one of the most promising models beyond the standard model. It solves the naturalness problem for the Higgs boson mass term in the standard model, and it is also compatible with the grand unified theories (GUTs). Although no hints of the superparticles have been indicated from the LHC yet, the SUSY models are the most attractive candidates beyond the Standard Model. Our group has been studying phenomenological and cosmological aspects of the SUSY models.

Recent cosmological observations including the Planck data determine precisely the mean densities of matter and baryon in the Universe, and existence of non-baryonic dark matter is established. Weakly interacting massive particles (WIMPs) are considered to be good candidates of the dark matter. They act as the cold dark matter in the structure formation of the universe. Our group has been studying model building for dark matter and detectability in direct and indirect search experiments.

For understanding of the early universe, a role of the elementary particle physics is crucial. Recent progress in the particle physics such as grand unification theories and supersymmetry leads us to a more deeper insight into the fundamental aspects of the early universe. In the inflationary universe, the quantum fluctuations of the scalar field which drives the inflation become the density fluctuations and lead to formation of the structure observed in the present universe. On the other hand cosmology and astrophysics are used to test new theories in particle physics. Such particle cosmology is one of main subjects of our group.

Big Bang Nucleosynthesis (BBN) is one of the most important subjects in modern cosmology. Predicted abundances of the light elements are very sensitive to the cosmological scenario. On the other hand, physics beyond the standard model predicts the new particles which would have existed at the BBN epoch. Such particles may spoil the success of BBN, which leads to constraints on the new particles and the particle physics models.

The grand unified theories predict that our universe undergoes several vacuum phase transitions. In the course of phase transitions topological defects (monopoles, cosmic strings and domain walls) are generally produced depending on symmetries of the vacua. Our group has studied evolution of various topological defects.

## Particle Phenomenology

[Spokesperson : M. Ibe]
ICRR, The Univ. of Tokyo, Kashiwa, Chiba 277-8582

## Dark Matter Search

### • Foreground effect on the $J$-factor estimation of ultra-faint dwarf spheroidal galaxies [1]

In collaboration with the members of ICRR and Kavli IPMU

Dwarf spheroidal galaxies (dSphs) are promising targets for the gamma-ray dark matter (DM) search. In particular, DM annihilation signal is expected to be strong in some of the recently discovered nearby ultra-faint dSphs, which potentially give stringent constraints on the $\mathcal{O}(1)$ TeV WIMP DM. However, various non-negligible systematic uncertainties complicate the estimation of the astrophysical factors relevant for the DM search in these objects. Among them, the effects of foreground stars particularly attract attention because the contamination is unavoidable even for the future kinematical survey. In this article, we assess the effects of the foreground contamination on the astrophysical $J$-factor estimation by generating mock samples of stars in the four ultra-faint dSphs and using a model of future spectrographs. We investigate various data cuts to optimize the quality of the data and apply a likelihood analysis which takes member and foreground stellar distributions into account. We show that the foreground star contaminations in the signal region (the region of interest) and their statistical uncertainty can be estimated by interpolating the foreground star distribution in the control region where the foreground stars dominate the member stars. Such regions can be secured at future spectroscopic observations utilizing a multiple object spectrograph with a large field of view; e.g. the Prime Focus Spectrograph mounted on Subaru Telescope. The above estimation has several advantages: The data-driven estimation of the contamination makes the analysis of the astrophysical factor stable against the complicated foreground distribution. Besides, foreground contamination effect is considered in the likelihood analysis.

### • Dark halo structure in the Carina dwarf spheroidal galaxy: joint analysis of multiple stellar components [2]

In collaboration with the members of ICRR and NAOJ, INAF, ASI, Nicolaus Copernicus Astronomical Center, Sapienza Univ. of Roma, IAC, Dominion Astrophysical Observatory

Photometric and spectroscopic observations of the Carina dSph revealed that this galaxy contains two dominant stellar populations of different age and kinematics. The co-existence of multiple populations provides new constraints on the dark halo structure of the galaxy, because different populations should be in equilibrium in the same dark matter potential well. We develop non-spherical dynamical models including such multiple stellar components and attempt to constrain the properties of the non-spherical dark halo of Carina. We find that Carina probably has a larger and denser dark halo than found in previous works and a less cuspy inner dark matter density profile, even though the uncertainties of dark halo parameters are still large due to small volume of data sample. Using our fitting results, we evaluate astrophysical factors for dark matter annihilation and decay and find that Carina should be one of the most promising detectable targets among

classical dSph galaxies. We also calculate stellar velocity anisotropy profiles for both stellar populations and find that they are both radially anisotropic in the inner regions, while in the outer regions the older population becomes more tangentially biased than the intermediate one. This is consistent with the anisotropy predicted from tidal effects on the dynamical structure of a satellite galaxy and thereby can be considered as kinematic evidence for the tidal evolution of Carina.

• Effects of mass models on dynamical mass estimate: the case of ultra diffuse galaxy NGC1052-DF2 [3]

In collaboration with the members of ICRR, Kavli IPMU, The University of Tokyo

NGC1052-DF2 was recently discovered as the dark-matter deficient galaxy claimed by van Dokkum et al. (2018a, vD18). However, large uncertainties on its dynamical mass estimate have been pointed out, concerning the paucity of sample, statistical methods and distance measurements. In this work, we discuss the effects of the difference in modeling of the tracer profile of this galaxy on the dynamical mass estimate. To do this, we assume that the tracer densities are modeled with power-law and Sérsic profiles, and then we solve the spherical Jeans equation to estimate the dynamical mass. Applying these models to kinematic data of globular clusters in NGC1052-DF2, we compare 90 per cent upper limits of dynamical mass-to-light ratios estimated between from this analysis and from vD18. We find that the upper limit obtained by the power-law is virtually the same as the result from vD18, whilst this limit estimated by the Sérsic is significantly greater than that from vD18, thereby suggesting that NGC1052-DF2 can still be a dark-matter dominated system. Consequently, we propose that dynamical mass estimate of a galaxy is largely affected by not only small kinematic sample but the choice of tracer distributions, and thus the estimated mass still remains quite uncertain.

• Non-sphericity of ultralight axion dark matter haloes in the Galactic dwarf spheroidal galaxies [4]

In collaboration with the members of ICRR

Ultralight-axion (ULA) dark matter is one of the possible solutions to resolve small-scale problems, especially the core-cusp problem. This is because ULA dark matter can create a central soliton core in all dark matter haloes stemmed from the quantum pressure against gravity below the de Broglie wavelength, which becomes manifest on astrophysical scales with axion mass range $\sim 10^{-22}$ eV. In this work, we apply our non-spherical dynamical models to the kinematic data of eight classical dwarf spheroidals (dSphs) to obtain more reliable and realistic limits on ULA particle mass. This is motivated by the reasons that the light distributions of the dSphs are not spherical, nor are the shapes of dark matter haloes predicted by ULA dark matter simulations. Compared with the previous studies on ULA dark matter assuming spherical mass models, our result is less stringent than those constraints due to the uncertainties on non-sphericity. On the other hand, remarkably, we find that the dSphs would prefer to have a flattened dark matter halo rather than a spherical one, especially Draco favours a strongly elongated dark matter halo caused naively by the assumption of a soliton-core profile. Moreover, our consequent non-spherical core profiles are much more flattened than numerical predictions based on ULA dark matter, even though there are still uncertainties on the estimation of dark matter halo structure. To alleviate this discrepancy, further understanding of baryonic and/or ULA dark matter physics on small mass scales might be needed.

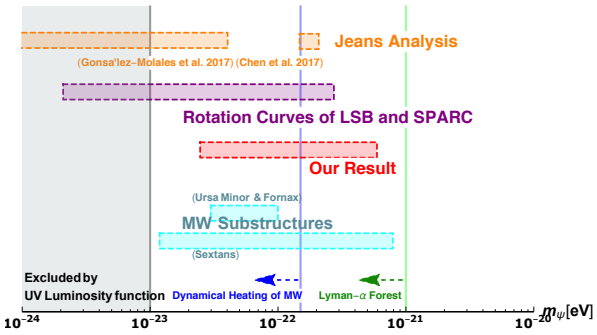


Fig. 13. *Constraints on the ULA mass from our study ($m_\psi = 1.05^{+4.98}_{-0.80} \times 10^{-22}$ eV, $2\sigma$ level) with red contour compared with the other mass bands favoured by several measurements such as previous Jeans analysis works (orange), presences of MW substructures (cyan), rotation curves of LSB and SPARC galaxies (purple). The lower mass regions less than blue and green line are disfavoured by dynamical heating of stellar streams in MW and Lyman-$\alpha$ forest ($m_\psi \gtrsim 10^{-21}$ eV, green) at around $2\sigma$ levels. The lower mass region $m_\psi \lesssim 10^{-23}$ eV is severely excluded by the UV Luminosity function of high-$z$ galaxies at more than $8\sigma$ level.*

## Bibliography

[1] K. Ichikawa, S. i. Horigome, M. N. Ishigaki, S. Matsumoto, M. Ibe, H. Sugai and K. Hayashi, Mon. Not. Roy. Astron. Soc. **479** (2018) no.1, 64 doi:10.1093/mnras/sty1387 [arXiv:1706.05481 [astro-ph.GA]].

[2] K. Hayashi, M. Fabrizio, E. L. Łokas, G. Bono, M. Monelli, M. Dall'Ora and P. B. Stetson, Mon. Not. Roy. Astron. Soc. **481** (2018) no.1, 250 doi:10.1093/mnras/sty2296 [arXiv:1804.01739 [astro-ph.GA]].

[3] K. Hayashi and S. Inoue, Mon. Not. Roy. Astron. Soc. **481** (2018) no.1, L59 doi:10.1093/mnrasl/sly162 [arXiv:1808.10116 [astro-ph.GA]].

[4] K. Hayashi and I. Obata, Mon. Not. Roy. Astron. Soc. **491** (2020) no.1, 615 doi:10.1093/mnras/stz2950 [arXiv:1902.03054 [astro-ph.CO]].

## Beyond Standard Model

• Composite Asymmetric Dark Matter with a Dark Photon Portal [1]

In collaboration with the members of ICRR and IBS Korea

Asymmetric dark matter (ADM) is an attractive framework relating the observed baryon asymmetry of the Universe to the dark matter density. A composite particle in a new strong dynamics is a promising candidate for ADM as the strong dynamics naturally explains the ADM mass in the GeV range. Its large annihilation cross section due to the strong dynamics leaves the asymmetric component to be dominant over the symmetric component. In such composite ADM scenarios, the dark sector has a relatively large entropy density in the early Universe. The large dark sector entropy results in the overclosure of the Universe or at best contradicts with the observations of the cosmic microwave background and the successful Big-Bang Nucleosynthesis. Thus, composite ADM models generically require some portal to transfer the entropy of the dark sector into the Standard Model sector. In this paper, we consider a dark photon portal with a mass in the sub-GeV range and kinetic mixing with the Standard Model photon. We investigate the viable parameter space of the dark photon in detail, which can find broad applications to dark photon portal models. We also provide a simple working example of composite ADM with a dark photon portal. Our model is compatible with thermal leptogenesis and $B-L$ symmetry. By taking into account the derived constraints, we show that the parameter space is largely tested by direct detection experiments.

• $B-L$ as a Gauged Peccei-Quinn Symmetry [2]

In collaboration with the members of ICRR and IPMU

The gauged Peccei-Quinn (PQ) mechanism provides a simple prescription to embed the global PQ symmetry into a gauged $U(1)$ symmetry. As it originates from the gauged PQ symmetry, the global PQ symmetry can be protected from explicit breaking by quantum gravitational effects once appropriate charge assignment is given. In this paper, we identify the gauged PQ symmetry with the $B-L$ symmetry, which is obviously attractive as the $B-L$ gauge symmetry is the most authentic extension of the Standard Model. As we will show, a natural $B-L$ charge assignment can be found in a model motivated by the seesaw mechanism in the $SU(5)$ Grand Unified Theory. As a notable feature of this model, it does not require extra $SU(5)$ singlet matter fields other than the right-handed neutrinos to cancel the self and the gravitational anomalies.

• The swampland conjecture and the Higgs expectation value [3]

In collaboration with the members of ICRR and University of Tokyo

The recently proposed de Sitter swampland conjecture excludes local extrema of a scalar potential with a positive energy density in a low energy effective theory. Under the conjecture, the observed dark energy cannot be explained by the cosmological constant. The local maximum of the Higgs potential at the symmetric point also contradicts with the conjecture. In order to make the Standard Model consistent with the conjecture, it has been proposed to introduce a quintessence field, $Q$, which couples to the cosmological constant and the local maximum of the Higgs potential. In this paper, we show that such a modified Higgs potential generically results in a $Q$-dependent Higgs vacuum expectation value (VEV). The $Q$-dependence of the Higgs VEV induces a long-range force, which is severely excluded by the tests of the equivalence principle. Besides, as the quintessence field is in motion, the Higgs VEV shows a time-dependence, which is also severely constrained by the measurements of the time-dependence of the proton-to-electron mass ratio. Those constraints require an additional fine-tuning which is justified neither by the swampland conjecture nor the anthropic principle. We further show that, even if such an unjustified fine-tuning condition is imposed at the tree level, radiative corrections upset it. Consequently, we argue that most of the habitable vacua in the string landscape are in tension with the phenomenological constraints.

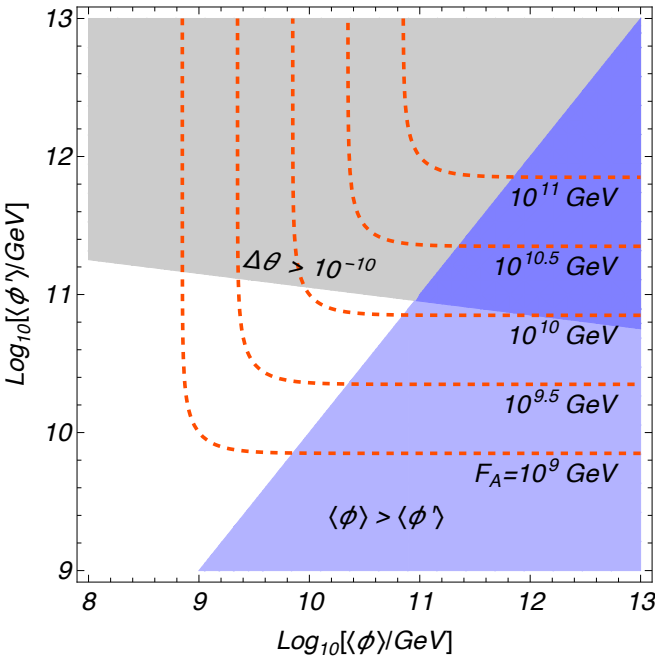


Fig. 14. *The constraint on the VEVs of $\phi$ and $\phi'$. The gray shaded region is excluded by $\Delta\theta < 10^{-10}$ for the non-SUSY model. The orange lines are the contours of the effective decay constant $F_A$. In the blue shaded region, $\langle\phi\rangle > \langle\phi'\rangle$.*

• Quintessence Axion Revisited in Light of Swampland Conjectures [4]

In collaboration with the members of ICRR and IPMU

We point out that the swampland conjectures, forbidding the presence of global symmetries and (meta-)stable de Sitter vacua within quantum gravity, pick up a dynamical axion for the electroweak SU(2) gauge theory as a natural candidate

for the quintessence field. The potential energy of the electroweak axion provides an attractive candidate for the dark energy. We discuss constraints from the weak gravity conjecture, from the conjecture of no global symmetry, and from observations, which can be satisfied elegantly in a supersymmetric extension of the standard model.

• Ultraviolet Completion of a Composite Asymmetric Dark Matter Model with a Dark Photon Portal [5]

In collaboration with the members of ICRR and IBS (Korea)

Composite asymmetric dark matter scenarios naturally explain why the dark matter mass density is comparable with the visible matter mass density. Such scenarios generically require some entropy transfer mechanism below the composite scale; otherwise, their late-time cosmology is incompatible with observations. A tiny kinetic mixing between a dark photon and the visible photon is a promising example of the low-energy portal. In this paper, we demonstrate that grand unifications in the dark and the visible sectors explain the origin of the tiny kinetic mixing. We particularly consider an ultraviolet completion of a simple composite asymmetric dark matter model, where asymmetric dark matter carries a $B-L$ charge. In this setup, the longevity of asymmetric dark matter is explained by the $B-L$ symmetry, while the dark matter asymmetry originates from the $B-L$ asymmetry generated by thermal leptogenesis. In our minimal setup, the Standard Model sector and the dark sector are unified into $SU(5)_{\rm GUT} \times SU(4)_{\rm DGUT}$ gauge theories, respectively. This model generates required $B-L$ portal operators while suppressing unwanted higher-dimensional operators that could wash out the generated $B-L$ asymmetry.

• Automatic Peccei-Quinn symmetry [6]

In collaboration with the members of ICRR, IPMU and IFT (Spain)

We present a dynamical (composite) axion model where the Peccei-Quinn (PQ) symmetry arises automatically as a consequence of chirality and gauge symmetry. The Standard Model is simply extended by a confining and chiral $SU(5)$ gauge symmetry. The PQ symmetry coincides with a $B-L$ symmetry of the exotic sector. The theory is protected by construction from quantum gravitational corrections stemming from operators with mass dimension lower than nine.

• Decay of I-ball/Oscillon in Classical Field Theory [7]

In collaboration with the members of ICRR

I-balls/oscillons are long-lived and spatially localized solutions of real scalar fields. They are produced in various contexts of the early universe in, such as, the inflaton evolution and the axion evolution. However, their decay process has long been unclear. In this paper, we derive an analytic formula of the decay rate of the I-balls/oscillons within the classical field theory. In our approach, we calculate the Poynting vector of the perturbation around the I-ball/oscillon profile by solving a relativistic field equation, with which the decay rate of the I-ball/oscillon is obtained. We also perform a classical lattice simulation and confirm the validity of our analytical formula of the decay rate numerically.

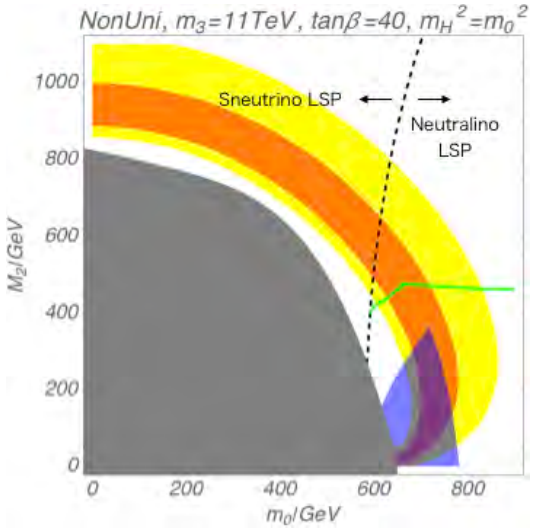


Fig. 15. *The summary plots for the collider constraints and the dark matter candidate. In the orange (yellow) region, $\Delta a_\mu$ is explained within 1 sigma $(2\sigma)$. The gray shaded region is excluded by the negative slepton masses. On the right (left) side of the black dashed line, the neutralino (the sneutrino) is the LSP. The blue shaded regions are excluded from the collider searches at 95% CL. On the green line, the observed current dark matter abundance $\Omega h^2 \simeq 0.12$ is achieved due to the bino-wino coannihilation.*

• Muon $g-2$ in Split-Family SUSY in light of LHC Run II [8]

In collaboration with the members of ICRR, IPMU, and Tohoku Univ.

The Split-Family supersymmetry is a model in which the sfermion masses of the first two generations are in $\mathcal{O}$(100-1000) GeV while that of the third one is in $\mathcal{O}(10)$TeV. With such a hierarchical spectrum, the deviation of the muon $g-2$ and the observed Higgs boson mass are explained simultaneously. In this paper, we revisit the Split-Family SUSY model in light of the updated LHC constraints. We also study the flavor changing neutral current problems in the model. As we will show, the problems do not lead to stringent constraints when the Cabibbo-Kobayashi-Maskawa matrix is the only source of the flavor mixing. We also study how large flavor mixing in the supersymmetry breaking parameters is allowed.

• More about Q-ball with elliptical orbit [9]

In collaboration with the members of ICRR and Seoul Natl. Univ.

Q-balls formed from the Affleck-Dine field have rich cosmological implications and have been extensively studied from both theoretical and simulational approaches. From the

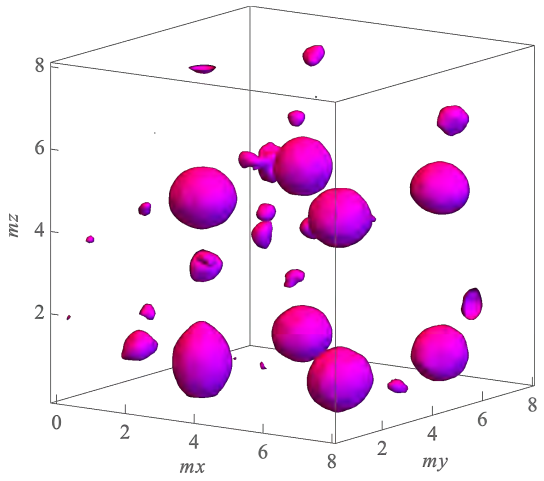


Fig. 16. *Formation of excited Q-balls in 3D lattice simulation at $t = t_f$. We plotted an isosurface of the energy density for the illustration. We set $\varepsilon_{\rm ini} = 0.2$.*

theoretical point of view, the exact solution of the Q-ball was obtained and it shows a circular orbit in the complex plane of the field value. In practice, however, it is reported that the Q-ball that appears after the Affleck-Dine mechanism has an *elliptical* orbit, which carries larger energy per unit $U(1)$ charge than the well-known solution with a circular orbit. We call them "elliptical" Q-balls. In this paper, we report the first detailed investigation of the properties of the elliptical Q-balls by 3D lattice simulation. The simulation results indicate that the elliptical Q-ball has an almost spherical spatial profile with no nodes, and we observed a highly elliptic orbit that cannot be described through small perturbations around the ground state Q-ball. Higher ellipticity leads to more excitation of the energy, whose relation is also derived as a dispersion relation. Finally, we derive two types of approximate solutions by extending the Gaussian approximation and considering the time-averaged equation of motion and we also show the consistency with the simulation results.

## Bibliography


[1] M. Ibe, A. Kamada, S. Kobayashi and W. Nakano, JHEP **1811** (2018) 203 doi:10.1007/JHEP11(2018)203 [arXiv:1805.06876 [hep-ph]].

[2] M. Ibe, M. Suzuki and T. T. Yanagida, JHEP **1808** (2018) 049 doi:10.1007/JHEP08(2018)049 [arXiv:1805.10029 [hep-ph]].

[3] K. Hamaguchi, M. Ibe and T. Moroi, JHEP **1812** (2018) 023 doi:10.1007/JHEP12(2018)023 [arXiv:1810.02095 [hep-th]].

[4] M. Yamazaki, arXiv:1910.08691 [hep-ph].

[5] M. Ibe, A. Kamada, S. Kobayashi, T. Kuwahara and W. Nakano, JHEP **1903** (2019) 173 doi:10.1007/JHEP03(2019)173 [arXiv:1811.10232 [hep-ph]].

[6] M. B. Gavela, M. Ibe, P. Quilez and T. T. Yanagida, Eur. Phys. J. C **79** (2019) no.6, 542 doi:10.1140/epjc/s10052-019-7046-3 [arXiv:1812.08174 [hep-ph]].

[7] M. Ibe, M. Kawasaki, W. Nakano and E. Sonomoto, JHEP **1904** (2019) 030 doi:10.1007/JHEP04(2019)030 [arXiv:1901.06130 [hep-ph]].

[8] M. Ibe, M. Suzuki, T. T. Yanagida and N. Yokozaki, Eur. Phys. J. C **79** (2019) no.8, 688 doi:10.1140/epjc/s10052-019-7186-5 [arXiv:1903.12433 [hep-ph]].

[9] F. Hasegawa, J. P. Hong and M. Suzuki, Phys. Lett. B **798** (2019) 135001 doi:10.1016/j.physletb.2019.135001 [arXiv:1903.07281 [hep-ph]].


# Particle Cosmology


[Spokesperson : M. Kawasaki]
ICRR, The Univ. of Tokyo, Kashiwa, Chiba 277-8582


## Inflation, CMB, Thermal History in the Early Universe

• Exploring compensated isocurvature perturbations with CMB spectral distortion anisotropies [1]

In collaboration with the members of Tokyo Institute of Technology, Utrecht Univ., and Università degli Studi di Padova

We develop a linear perturbation theory for the spectral $y$-distortions of the cosmic microwave background (CMB). The $y$-distortions generated during the recombination epoch are usually negligible because the energy transfer due to the Compton scattering is strongly suppressed at that time, but they can be significant if there is a considerable amount of compensated isocurvature perturbation (CIP), which is not tightly constrained from the present CMB observations. The linear $y$-distortions explicitly depend on the baryon density fluctuations, therefore $y$ anisotropies can completely resolve the degeneracy between the baryon isocurvature perturbations and the cold dark matter ones. This novel method is free from lensing contaminations that can affect the previous approach to the CIPs based on the nonlinear modulation of the CMB anisotropies. We compute the cross correlation functions of the $y$-distortions with the CMB temperature and the $E$ mode polarization anisotropies. They are sensitive to the correlated CIPs parameterized by $f' \equiv \mathscr{P}_{\mathrm{CIP}\zeta}/\mathscr{P}_{\zeta\zeta}$ with $\mathscr{P}_{\zeta\zeta}$ and $\mathscr{P}_{\mathrm{CIP}\zeta}$ being the auto correlation of the adiabatic perturbations and the cross correlation between them and the CIPs. We investigate how well the $y$ anisotropies will constrain $f'$ in future observations such as those provided by a PIXIE-like and a PRISM-like survey, LiteBIRD and a cosmic variance limited (CVL) survey, taking into account the degradation in constraining power due to the presence of Sunyaev Zel'dovich effect from galaxy clusters. For example, our forecasts show that it is possible to achieve an upper limit of $f' < 2 \times 10^5$ at 68LiteBIRD, and $f' < 2 \times 10^4$ with CVL observations.

• Big Bang Nucleosynthesis Constraint on Baryonic Isocurvature Perturbations [2]

In collaboration with the members of IPMU and UCLA

We study the effect of large baryonic isocurvature perturbations on the abundance of deuterium (D) synthesized in big bang nucleosynthesis (BBN). We found that large baryonic isocurvature perturbations existing at the BBN epoch ($T \sim 0.1\,\mathrm{MeV}$) change the D abundance by the second order effect, which, together with the recent precise D measurement, leads to a constraint on the amplitude of the power spectrum of the baryon isocurvature perturbations. The obtained constraint on the amplitude is $\lesssim 0.016\,(2\sigma)$ for scale $k^{-1} \gtrsim 0.0025\,\mathrm{pc}$. This gives the most stringent one for $0.1\,\mathrm{Mpc}^{-1} \lesssim k \lesssim 4\times10^{8}\,\mathrm{Mpc}^{-1}$. We apply the BBN constraint to the relaxation leptogenesis scenario, where large baryon isocurvature perturbations are produced in the last $N_{\mathrm{last}}$ $e$-fold of inflation, and we obtain a constraint on $N_{\mathrm{last}}$.

• Hunting for Statistical Anisotropy in Tensor Modes with B-mode Observations [3]

In collaboration with the members of Rikkyo University, Nagoya University, Kyoto University

We investigate a possibility of constraining statistical anisotropies of the primordial tensor perturbations by using future observations for the Cosmic Microwave Background (CMB) B-mode polarization. By parameterizing a statistically-anisotropic tensor power spectrum as $P_h(k) = P_h(k)\sum_n g_n \cos^n\theta_k$, where $\theta_k$ is an angle of the direction of $\hat{k} = k/k$ from a preferred direction, we find that it would be possible for future B-mode observations such as CMB-S4 to detect the tensor statistical anisotropy at the level of $g_n \sim \mathcal{O}(0.1)$.

• Circular polarization of the cosmic microwave background from vector and tensor perturbations [4]

In collaboration with the members of Johns Hopkins University

Circular polarization of the cosmic microwave background (CMB) can be induced by Faraday conversion of the primordial linearly polarized radiation as it propagates through a birefringent medium. Recent work has shown that the dominant source of birefringence from primordial density perturbations is the anisotropic background CMB. Here we extend prior work to allow for the additional birefringence that may arise from primordial vector and tensor perturbations. We derive the formulas for the power spectrum of the induced circular polarization and apply those to the standard cosmology. We find the root-variance of the induced circular polarization to be $\sqrt{<V^2>} \sim 3\times10^{-14}$ for scalar perturbations and $\sqrt{<V^2>} \sim 7\times10^{-18}(r/0.06)$ for tensor perturbations with a tensor-to-scalar ratio $r$.

• Chiral photons from chiral gravitational waves [5]

In collaboration with the members of Johns Hopkins University

We show that a parity-breaking uniform (averaged over all directions on the sky) circular polarization of amplitude $V_{00} \simeq 2.6\times10^{-17}\,\Delta\chi\,(r/0.06)$ can be induced by chiral gravitational-wave (GW) background with tensor-to-scalar ratio $r$ and chirality parameter $\Delta\chi$ (which is $\pm1$ for a maximally chiral background). We also show, however, that a uniform circular polarization can arise from a realization of a non-chiral GW background that spontaneously breaks parity. The magnitude of this polarization is drawn from a distribution of root-variance $\sqrt{<V_{00}^2>} \simeq 1.5\times10^{-18}\,(r/0.06)^{1/2}$ implying that the chirality parameter must be $\Delta\chi \gtrsim 0.12(r/0.06)^{-1/2}$ to establish that the GW background is chiral. Although these values are too small to be detected by any experiment in the foreseeable future, the calculation is a proof of principle that cosmological parity breaking in the form of a chiral gravitational-wave background can be imprinted in the chirality of the photons in the cosmic microwave background. It also illustrates how a seemingly parity-breaking cosmological signal can arise from parity-conserving physics.

## Bibliography


[1] T. Haga, K. Inomata, A. Ota and A. Ravenni, JCAP **1808** (2018) 036 doi:10.1088/1475-7516/2018/08/036 [arXiv:1805.08773 [astro-ph.CO]].

[2] K. Inomata, M. Kawasaki, A. Kusenko and L. Yang, JCAP **1812** (2018) 003 doi:10.1088/1475-7516/2018/12/003 [arXiv:1806.00123 [astro-ph.CO]].

[3] T. Hiramatsu, S. Yokoyama, T. Fujita and I. Obata, Phys. Rev. D **98** (2018) no.8, 083522 doi:10.1103/PhysRevD.98.083522 [arXiv:1808.08044 [astro-ph.CO]].

[4] K. Inomata and M. Kamionkowski, Phys. Rev. D **99** (2019) no.4, 043501 doi:10.1103/PhysRevD.99.043501 [arXiv:1811.04957 [astro-ph.CO]].

[5] K. Inomata and M. Kamionkowski, Phys. Rev. Lett. **123** (2019) no.3, 031305 doi:10.1103/PhysRevLett.123.031305 [arXiv:1811.04959 [astro-ph.CO]].


# Axions

• Optical Ring Cavity Search for Axion Dark Matter [1]

In collaboration with the members of Tokyo University (Hongo), Kyoto University

We propose a novel experiment to search for axion dark matter which differentiates the phase velocities of the left and right-handed polarized photons. Our optical cavity measures the difference of the resonant frequencies between two circular-polarizations of the laser beam. The design of our

cavity adopts double-pass configuration to realize a null experiment and give a high common mode rejection of environmental disturbances. We estimate the potential sensitivity to the axion-photon coupling constant $g_{a\gamma}$ for the axion mass $m \lesssim 10^{-10}$ eV. In a low mass range $m \lesssim 10^{-15}$ eV, we can achieve $g_{a\gamma} \lesssim 3 \times 10^{-16}$ GeV$^{-1}$ which is beyond the current bound by several orders of magnitude.

### • Long-term dynamics of cosmological axion strings [2]

In collaboration with the members of ICRR, University of Tokyo and Tokyo Institute of Technology

We present results of new field-theoretic simulation of cosmological axion strings, which are eight times longer than previous ones. We have upgraded our simulation of physical strings in Hiramatsu et al. (2011) in terms of the number of grids as well as the suite of analysis methods. These improvements enable us to monitor a variety of quantities characterizing the dynamics of the physical string network for the longest term ever. Our extended simulations have revealed that global strings do not evolve according to the scaling solution but its scaling parameter, or the number of long strings per horizon, increases logarithmically in time. In addition, we have also found that the scaling parameter shows nontrivial dependence on the breaking scale of the Peccei-Quinn symmetry.

### • Mixed Non-Gaussianity from Axion-Gauge Field Dynamics [3]

In collaboration with the members of Kyoto University, McGill University

We study scalar-tensor-tensor cross correlation $\langle \zeta hh \rangle$ generated by the dynamics of interacting axion and SU(2) gauge fields during inflation. We quantize the quadratic action and solve the linear equations by taking into account mixing terms in a non-perturbative manner. Combining that with the in-in formalism, we compute contributions from cubic interactions to the bispectrum $B_{\zeta hh}$. We find that the bispectrum is peaked at the folded configuration, which is a unique feature encoded by the scalar mixing and localized production of tensor modes. With our parameter choice, the amplitude of the bispectrum is $k^6 B_{\zeta hh} \sim 10^{-16}$. The unique shape dependence, together with the parity-violating nature, is thus a distinguishing feature to search for in the CMB observables.

### • Axion Dark Matter Search with Interferometric Gravitational Wave Detectors [4]

In collaboration with the members of ICRR, Tokyo University (Hongo), Kyoto University

Axion dark matter differentiates the phase velocities of the circular-polarized photons. In this Letter, a scheme to measure the phase difference by using a linear optical cavity is proposed. If the scheme is applied to the Fabry-Prot arm of Advanced LIGO-like (Cosmic-Explorer-like) gravitational wave detector, the potential sensitivity to the axion-photon coupling constant, $g_{a\gamma}$, reaches $g_{a\gamma} \simeq 8 \times 10^{-13}$ GeV$^{-1}$ ($4 \times 10^{-14}$ GeV$^{-1}$) at the axion mass $m \simeq 3 \times 10^{-13}$ eV ($2 \times 10^{-15}$ eV) and remains at around this sensitivity for 3 orders of magnitude in mass. Furthermore, its sensitivity has a sharp peak reaching $g_{a\gamma} \simeq 10^{-14}$ GeV$^{-1}$ ($8 \times 10^{-17}$ GeV$^{-1}$) at $m = 1.563 \times 10^{-10}$ eV ($1.563 \times 10^{-11}$ eV). This sensitivity can be achieved without loosing any sensitivity to gravitational waves.

## Bibliography


[1] I. Obata, T. Fujita and Y. Michimura, arXiv:1811.12051 [physics.ins-det].

[2] M. Kawasaki, T. Sekiguchi, M. Yamaguchi and J. Yokoyama, PTEP **2018** (2018) no.9, 091E01 doi:10.1093/ptep/pty098 [arXiv:1806.05566 [hep-ph]].

[3] T. Fujita, R. Namba and I. Obata, JCAP **1904** (2019) 044 doi:10.1088/1475-7516/2019/04/044 [arXiv:1811.12371 [astro-ph.CO]].

[4] K. Nagano, T. Fujita, Y. Michimura and I. Obata, Phys. Rev. Lett. **123** (2019) no.11, 111301 doi:10.1103/PhysRevLett.123.111301 [arXiv:1903.02017 [hep-ph]].


## Primodial Black Holes

### • Formation of primordial black holes in an axionlike curvaton model [1]

In collaboration with the members of ICRR

We performed the detailed analysis of the primordial black hole (PBH) formation mechanism in an axionlike curvaton model with a coupling to inflaton. The phase direction of the complex scalar works as a curvaton and produces enough PBHs to explain the black hole binaries ($\sim 30 M_\odot$) observed in the LIGO-Virgo Collaboration or PBHs as dark matter (DM) ($\sim 10^{-12} M_\odot$). We examine whether our model satisfies the current constraints on the PBH mass spectrum, the curvature perturbation and the secondarily produced gravitational waves. We also take into account ambiguity about the choice of the window functions and effect of the non-Gaussianity.

### • Primordial Black Holes from Affleck-Dine Mechanism [2]

In collaboration with the members of ICRR

The recent observations of the gravitational waves (GWs) by LIGO-Virgo collaboration infer the increasing possibility of the primordial black holes (PBHs). Recently it was pointed out that sufficient PBHs are produced by the Affleck-Dine mechanism where inhomogeneous baryogenesis takes place due to change of the Hubble induced mass during and after inflation and forms high baryon bubbles (HBBs). The produced HBBs have large density contrasts through the QCD phase transition or stable Q-ball formation, which leads to formation of the LIGO PBHs. Furthermore, in this model stringent constraints from CMB $\mu$-distortion and pulsar timing array

(PTA) experiments are completely absent. In this paper, we study the model in full details based on gravity and gauge mediated supersymmetry breaking scenarios and show that the model can explain the current GWs events evading observational constraints.

• Footprint of Two-Form Field: Statistical Anisotropy in Primordial Gravitational Waves [3]

In collaboration with the members of Kyoto University

We study the observational signatures of two-form field in the inflationary cosmology. In our setup a two-form field is kinetically coupled to a spectator scalar field and generates sizable gravitational waves and smaller curvature perturbation. We find that the sourced gravitational waves have a distinct signature: they are always statistically anisotropic and their spherical moments are non-zero for hexadecapole and tetrahexacontapole, while the quadrupole moment vanishes. Since their amplitude can reach $\mathcal{O}(10^{-3})$ in the tensor-to-scalar ratio, we expect this novel prediction will be tested in the next generation of the CMB experiments.

• Primordial Black Holes and the String Swampland [4]

In collaboration with the members of ICRR and UCLA(USA)

The "swampland conjectures" have been recently suggested as a set of criteria to assess if effective field theories (EFTs) are consistent with a quantum gravity embedding. Such criteria, which restrict the behavior of scalar fields in the theory, have strong implications for cosmology in the early universe. As we demonstrate, they will also have direct consequences for formation of primordial black holes (PBHs) and dark matter (DM).

• Gravitational waves induced by scalar perturbations as probes of the small-scale primordial spectrum [5]

In collaboration with the members of The Hong Kong University of Science and Technology

Compared to primordial perturbations on large scales, roughly larger than 1 megaparsec, those on smaller scales are not severely constrained. We revisit the issue of probing small-scale primordial perturbations using gravitational waves (GWs), based on the fact that, when large-amplitude primordial perturbations on small scales exist, GWs with relatively large amplitudes are induced at second order in scalar perturbations, and these induced GWs can be probed by both existing and planned gravitational-wave projects. We use accurate methods to calculate these induced GWs and take into account sensitivities of different experiments to induced GWs carefully, to report existing and expected limits on the small-scale primordial spectrum.

## Bibliography

[1] K. Ando, M. Kawasaki and H. Nakatsuka, Phys. Rev. D **98** (2018) no.8, 083508 doi:10.1103/PhysRevD.98.083508 [arXiv:1805.07757 [astro-ph.CO]].

[2] F. Hasegawa and M. Kawasaki, JCAP **1901** (2019) 027 doi:10.1088/1475-7516/2019/01/027 [arXiv:1807.00463 [astro-ph.CO]].

[3] I. Obata and T. Fujita, Phys. Rev. D **99** (2019) no.2, 023513 doi:10.1103/PhysRevD.99.023513 [arXiv:1808.00548 [astro-ph.CO]].

[4] M. Kawasaki and V. Takhistov, Phys. Rev. D **98** (2018) no.12, 123514 doi:10.1103/PhysRevD.98.123514 [arXiv:1810.02547 [hep-th]].

[5] K. Inomata and T. Nakama, Phys. Rev. D **99** (2019) no.4, 043511 doi:10.1103/PhysRevD.99.043511 [arXiv:1812.00674 [astro-ph.CO]].

# OBSERVATORIES and A RESEARCH CENTER

**Location of the Institute and the Observatories in Japan**


## Norikura Observatory

| | |
|---|---|
| Location: | Norikuradake, Nyukawa-cho, Takayama-shi, Gifu Prefecture 506-2100<br>N 36°06′, E 137°33′, 2770 m a.s.l. |
| Telephone (Fax): | +81-50-3730-3809 |
| Telephone (satellite): | +81-90-7721-5674 |
| Telephone (car): | +81-90-7408-6224 |

## Akeno Observatory

| | |
|---|---|
| Location: | 5259 Asao, Akeno-machi, Hokuto-shi, Yamanashi Prefecture 408-0201<br>N 35°47′, E 138°30′, 900 m a.s.l. |
| Telephone / Fax: | +81-551-25-2301 / +81-551-25-2303 |

## Kamioka Observatory

| | |
|---|---|
| Location: | 456 Higashi-mozumi, Kamioka-cho, Hida-shi, Gifu Prefecture 506-1205<br>N 36°25′26″, E 137°19′11″, 357.5 m a.s.l. |
| Telephone / Fax: | +81-578-85-2116 / +81-578-85-2121 |

## KAGRA Observatory

| | |
|---|---|
| Location: | 238 Higashi-mozumi, Kamioka-cho, Hida-shi, Gifu Prefecture 506-1205<br>N 36°25′26″, E 137°19′11″, 350 m a.s.l. |
| Telephone / Fax: | +81-578-85-2343 / +81-578-85-2346 |

## Research Center for Cosmic Neutrinos

| | |
|---|---|
| Location: | 5-1-5 Kashiwanoha, Kashiwa, Chiba Prefecture 277-8582 |
| Telephone / Fax: | +81-4-7136-3138 / +81-4-7136-3115 |

# NORIKURA OBSERVATORY

## Introduction

Norikura Observatory (36.10°N and 137.55°E) was founded in 1953 and attached to ICRR in 1976. It is located at 2770 m above sea level, and is the highest altitude manned laboratory in Japan (Fig. 1). Experimental facilities of the laboratory are made available to all the qualified scientists in the field of cosmic ray research and associated subjects. The AC electric power is generated by the dynamo and supplied throughout the observatory. The observatory can be accessed easily by car and public bus in summer (July-September). The 60th anniversary of Norikura Observatory was celebrated in 2013.

Fig. 1. Norikura Observatory

Norikura Observatory gave manned operation to the observations by the qualified scientists all the year until the year 2003. However, the feasibility of the automatic operation of Norikura Observatory during winter period has been tested since winter 2004 in order to study the possibilities to reduce maintenance and labor costs without causing serious inconveniences for the researches. A long-distance (∼40km) wireless LAN system (11M bps) was set up in 2003. Two new easy-to-handle and easy-to-maintain dynamos of 115 KVA each, as shown in Fig. 2 were installed in 2004 as well. The unmanned operation of Norikura Observatory has been mostly successful in winter, during which the battery backed-up solar panels and/or wind power generators kept supplying the electricity to the wireless LAN and on-going cosmic-ray experiments.

Present major scientific interests of the laboratory is focused on the modulation of high energy cosmic rays in the interplanetary space associated with the solar activity, the generation of energetic particles by the solar flares, and the particle acceleration mechanism in thunderclouds, all of which require long-term observation. These researches have been carried out by the group of user universities, where ICRR provides them with laboratory facility. A part of the facility has been open for the environmental study at high altitude such as aerosol-related mechanism in the atmosphere, observation of total ozone and UV solar radiation, for botanical study in the high-altitude environment, etc..


Fig. 2. A dynamo of 115KV.

## Cosmic Ray Physics

**Space weather observation**

Space weather observation is actively made by a 25 $m^2$ muon hodoscope at Norikura Observatory[1],[2],[3],[4],[5],[6],[7],[8],[9],[10]. Mt. Norikura muon hodoscope has started operation in May, 1998 and successfully observed a clear precursory signature of the interplanetary shock arrival at Earth. With its improved angular resolution of muon incident direction, the detector succeeded for the first time to observe a loss-cone signature which is an intensity deficit within a narrow cone around the interplanetary magnetic field (IMF). The observation of the loss-cone precursor gives us unique information for the space weather forecast and for understanding the interplanetary disturbances in near Earth space.

Following this successful observation, we installed a small muon hodoscope in Kuwait City, Kuwait as the fourth detector in our Global Muon Detector Network (GMDN) with other three multidirectional muon detectors in Nagoya (Japan), Hobart (Australia), and São Martinho (Brazil). The GMDN has started operation in March, 2006 monitoring the intensity of $\sim$ 50 GeV cosmic rays over an entire sky around Earth. The cosmic ray observations using muon detector are complementary to observations with neutron monitors monitoring a lower energy range below $\sim$ 10 GeV and the observations with GMDN have a great advantage particularly in precise measurement of the cosmic ray anisotropy, i.e. the dependence of intensity on incident direction in space, which gives us valuable information of the spatial distribution of the cosmic ray density in three dimensions. The Mt. Norikura muon hodoscope and GMDN have revealed the dynamic variations of the anisotropy which give us important information of the space weather. It has been already confirmed that the GMDN can measure the rapid variation of the anisotropy in the “cos-

mic ray burst" observed in June 2015 in 10 minute time resolution. The Kuwait muon hodoscope was enlarged three times in March 2016 and one minute data are now available from all of four detectors in the GMDN enabling us to analyze the anisotropy in 1 minute time resolution.

Recently, we also developed the method of the correction of the atmospheric temperature effect on muon count rate by using the GMDN data. This is a significant step, because it makes possible for the first time the analysis of the long-term variation of $\sim 50$ GeV cosmic ray density (i.e. isotropic intensity) which was possible so far only for cosmic ray below $\sim 10$ GeV using the neutron monitor data nearly free from the temperature effect. We have already published the long-term variation of the anisotropy observed by Nagoya muon detector.

**Solar neutron observation**

Observation of solar neutrons in solar cycle 24 has continued at Norikura Observatory of ICRR since fiscal 2007 to understand the acceleration mechanism of high energy (>100 MeV) ions associated with solar flares[11]. These neutrons are produced by the interaction between accelerated ions and the solar atmosphere. Neutrons are not reflected by the interplanetary magnetic field, and thought to be more informative than accelerated ions themselves to study the acceleration mechanism at the solar surface. Solar neutron events detected on the ground are rare, and about 10 events were reported before solar cycle 24. The group led by Institute for Space-Earth Environmental Research, Nagoya University has operated a world-wide network of 7 solar neutron telescopes in the world. The solar neutron telescope operated at Norikura Observatory has an area of 64 $m^2$, which is largest among the 7 stations. The solar neutron telescope at Norikura consists of plastic scintillation detector and proportional counters. The neutron is detected when a recoil proton is produced in the scintillator, and the energy of the recoil proton is measures. Proportional counters are used both to veto charged particles and measure the direction of recoil protons. The telescope is operated by solar power during the winter period when the Norikura observatory is closed.

Solar cycle 24 was its maximum in February 2014 and has decreased its activity since then. We searched for solar neutron signals from the world-wide network of the solar neutron telescopes between January 2010 and December 2014 when the large ($\geq$X1.0 class) solar flare occurred. No solar neutron event was detected by this search. We statistically studied the relation between upper limits of the neutron flux and the energy of soft X-rays during the solar flare. This comparison was also made for the successful detections of solar neutrons before solar cycle 24. The conclusion from this study is that the total energy obtained by neutrons during solar flare does not exceed 0.1 % of the total energy of soft X-rays.

**Relativistic electron acceleration in thunderstorm electric field and high-energy atmospheric phenomena at lightning**

The Gamma-Ray Observation of Winter THundercloud (GROWTH) collaboration is aiming at revealing high-energy atmospheric phenomena occurring at lightning and in thunderstorms[12],[13],[14],[15],[16]. The project started in 2006 and has detected bremsstrahlung gamma rays from relativistic electrons accelerated by strong electric fields in winter thunderstorms. This gamma-ray radiation events were named "long burst" by our group (as known as gamma-ray glow), which lasts for a minute time-scale corresponding with passage of a thundercloud above our detectors. Winter thunderstorms observed along the Japan sea are ideal targets for our observation campaigns thanks to its low altitude of the cloud base and frequent energetic lightning, while observations of summer thunderclouds at mountain tops are also important to measure the phenomena very close to or even inside thunderstorms. Our collaboration has used the Mount Norikura cosmic ray observatory to study the long bursts, and successfully recorded events.

The GROWTH collaboration newly launched multi-point mapping observation campaigns in 2015. The primary purpose is to study life cycle of the electron acceleration sites in thunderstorms comparing with weather-monitoring data. Another purpose of the project is to reveal mysterious "short burst" events, which have been sometimes detected in our past observations, associated with lightning discharges with its duration shorter than a second. Financially supported by the ICRR joint research programme, academic crowdfunding "academist", and JSPS/MEXT KAKENHI grant, we have developed portable and high-performance radiation detectors. In FY2016 and FY2017, the collaboration deployed radiation detectors at the Mt. Norikura cosmic ray observatory. So far, there is no detection of "long burst" nor "short burst" events from summer thunderclouds during the two years. However, we successfully used these summer campaigns as pilot observations toward the winter campaigns to check our operation and capability of the detectors. The Norikura observations are also educationally important as a training yard for Ph.D students in the team. In 2017 winter, our new mapping system at Kashiwazaki, Niigata, provided us a chance to solve the mystery of the short burst. This phenomena is revealed to be photonuclear reaction triggered by gamma rays from a lightning discharge. This discovery was selected, by the Physics World, as one of the top 10 breakthrough in the physics field in 2017. We are now trying to develop the "high-energy atmospheric physics" of lightning and thunderstorms, a new interdisciplinary field combining the gamma-ray and radio observations.

**Study of Secondary Cosmic Rays from Thundercloud at Mt. Norikura**

In order to study the relativistic electron acceleration mechanism by thundercloud-derived electric field and the relation between thunder and cosmic-ray air shower, we started an experiment in 2015, mainly using gamma-ray detectors at Norikura Observatory of Institute for Cosnic Ray Research, the University of Tokyo. This experiment consists of gamma-ray detectors, a lightning sensor, an electric field meter, a weather monitor, and an air shower array. Gamma-ray detectors using three crystals, NaI, CsI, and BGO respectively, cover the energy range over 3 orders of magnitude from 70 keV to 120 MeV as a whole.

*Observation period: 22 days from August 24 to September 14, 2015*
During this time, the thundercloud did not pass, and no gamma-ray burst derived from thundercloud was detected. However, the gamma ray detector was able to observe gamma rays derived from radon of less than 3 MeV as expected during rainfall. Also, gamma ray detectors using CsI and BGO for detecting gamma rays of 3 MeV or more did not observe an increase in gamma rays of 3 MeV or more. This means that gamma rays from radon can be distinguished from contributions from other gamma rays not derived from radon, and it can be expected that these detectors can operate normally even when they are installed at an altitude about 4000 m for a certain future project.

*Observation period: 30 days from July 19 to September 16, 2016 (excluding the summer season)*
No direct lightning strike event occurred during the observation period, but 6 atmospheric electric field fluctuations exceeding 30 kV/m, which seemed to be an influence of thunder cloud passage, were observed. In one of the events, it seems there was a lightning strike in the vicinity.

*Observation period: 41 days from July 31 to September 9, 2017*
Unfortunately, during this observation period there was no lightning strike nearby, but it was observed that the thundercloud passed several times. Currently, the data at the time of the thundercloud passing is being analyzed in detail (Fig. 3).

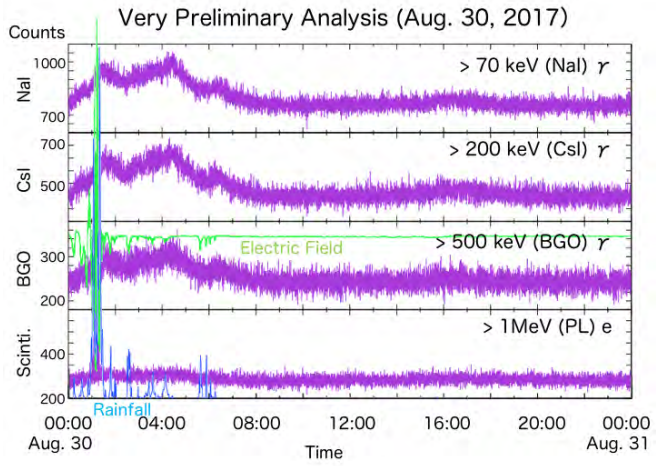


Fig. 3. Electric field (green), rainfall (blue), count value (purple) of each detector at the time of thundercloud passing.

**Study of gamma ray bursts from mountain-top thunderclouds**

We observed gamma ray bursts that arise in relation to thunderclouds at the Norikura Observatory of ICRR(2,770 m above sea level)[17],[18],[19],[20]. Measurement was carried out by placing PANDA64 detector outdoors of the observatory. The detector is made of 64-module plastic scintillators(total mass about 640 kg) developed for reactor operation monitoring. Our measurement has unprecedented features including high statistics, good energy response, direction sensitivity and neutron identification.

Long-duration persistent bursts were observed 12 times in 54 days from July to September 2014 and their energy spectrum extended up to 25 MeV in the largest burst. The duration of the bursts ranged from a few to ten minutes. Since these bursts were found in the energy range higher than 3 MeV, they were not attributed to the rain fallout of radon and its daughter nuclei.

According to the thundercloud information provided by the Japan Meteorological Agency, the bursts were observed when there was thunder activity near the observatory. The observation is qualitatively in good agreement with thundercloud radiation bursts previously observed in mountain areas or coastal areas of the Sea of Japan.

Monte Carlo simulation showed that the bremsstrahlung $\gamma$-rays by source electrons with monochromatic energy of 40–80 MeV falling downwards from altitude of 400–1000 m produced the observed total energy spectra of the bursts well. It is supposed that secondary cosmic ray electrons, which act as seed, were accelerated in electric field of thunderclouds and multiplied by relativistic runaway electron avalanche.

The estimated energy of the source electrons was higher than that of the bursts we previously observed at Ohi Power Station at sea level. Additionally, estimated electron flux at the estimated source height was remarkably lower than that of the Ohi site. These results give new restrictions to the model of electron acceleration and multiplication process in electric field of thunderclouds.

**Development of high energy proton irradiation technique for devices used in spaceship**

Space exploration is presently interesting in business field. Ion beam irradiation verification for devices to be mounted on spaceships is required to simulate cosmic rays expected in the universe to estimate lifetime of these devices[21],[22],[23],[24].

Flux estimation technique of primary ion beam in wide range from an accelerator is needed In this kind of cosmic ray simulation field. The desired flux of the ion beam for this kind of field is between $10^2$ and $10^6$ protons·cm$^{-2}$ ·s$^{-1}$ in typical proton cases. Plastic scintillators can be used in lower intense region to count direct primary ions, while ionization chambers can be used in higher intense region to count ionization caused by primary ions. But there have been no definite modalities available to measure throughout this whole intensity region.

One of the candidate techniques is to measure secondary $\gamma$-ray intensity emitted through a beam transport, which has nearly a maximum energy of the primary ion beam around 100 MeV for this kind of simulation field. This technique has a feature that detector components do not occupy the beam path and the presence of the detector do not influence the main simulation field at all.

NaI(Tl) scintillator system for high energetic $\gamma$-ray measurement which had been used in previous thunder lightning $\gamma$-ray measurement was used. This system has a 5-inch NaI(Tl) scintillator with NT100GPS pulse hight analysis system of Laboratory Equipment. Ion beam accelerator exper-

iments using 100 MeV proton beam were carried out at the Wakasa Wan Energy Research Center (WERC). Background measurements were carried out at Norikura Observatory of ICRR in summer, where one can expect high energetic $\gamma$-ray, which has the similar energy region compared to the accelerator field of this study. EFM100 atmospheric electric field monitor system of Boltek was added at Norikura to measure accidental high energetic $\gamma$-rays caused by thunder lightning.

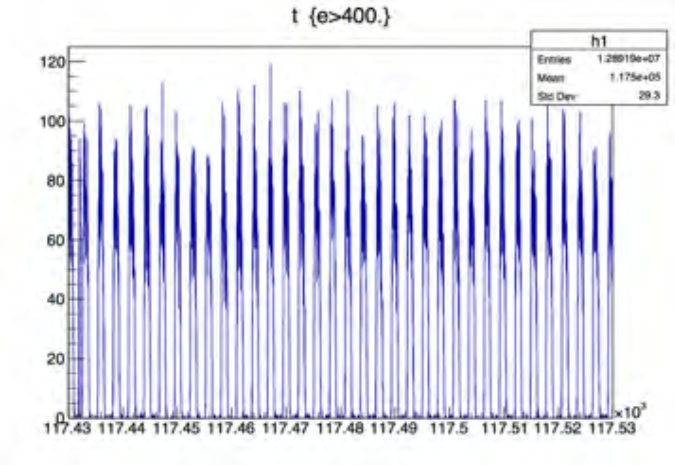


Fig. 4. Time structure of $\gamma$-ray above 3 MeV at WERC 100 MeV proton beam delivery. Vertical axis shows $\gamma$ intensity ( events/ms ) while horizontal shows time after beginning of the operation ( s ).

As shown in Fig.4 of a time structure of $\gamma$-ray during 100 MeV proton beam delivery duration obtained at WERC, the result clearly shows that this measurement system can distinguish the beam ON/Off, while this system is still in verification for a quantitative discussion. The dead time of the system should be defined.

In the meantime, thunder lightning events were searched using data obtained at Norikura. No events have been distinguished. The whole data at Norikura show a stable condition of the whole system for a couple of months.

With the help of this study, the trial to carry out cosmic ray simulation at the ion beam accelerator facility ( WERC ) has been successfully carried out. One will keep trying to estimate the quantitative property of the system in ion beam environment.

**Development of high energy proton irradiation technique for devices used in spaceship**

Aircraft crew are exposed to elevated levels of cosmic rays at aviation since the dose rate of cosmic rays increases with altitude. The occupational doses of aircraft crew have generally been evaluated by model calculation. It is necessary to verify the calculation with measurements to maintain accuracy and credibility of dose assessment. The purposes of this study were to construct a compact and inexpensive cosmic-ray neutron monitoring system which was based on a rem-counter at Norikura Observatory (2770 m above sea level), and to examine the feasibility of it. The monitoring system was installed in the Norikura Observatory in 2014. It consisted of an extended-energy neutron rem counter with wide energy range from 25 meV to 5 GeV, a custom-made data logger connected to LAN, and a battery power unit. The measured data was received in National Institute of Radiological Science in Chiba-city via the ICRR network. This monitoring system succeeded in continuous monitoring more than ten months twice during 2014 to 2016. The averaged counting rate was about 1 count per minute, which was equivalent to neutron ambient dose equivalent rate of about 15 nSv/h by the preliminary evaluation. It is a future problem to reveal the cause of the reduction in counting rate seen over from November to April.

**Evaluation of Response to the Gamma-ray of the Emulsion Telescope (2007, 2013)**

GRAINE project (Gamma-Ray Astro-Imager with Nuclear Emulsion) has been developing the observation of cosmic $\gamma$-ray in the energy range 10 MeV–100 GeV with precise ($0.08^\circ$ at 1–2 GeV), polarization-sensitive, large-aperture-area ($\sim$10 m$^2$) balloon-borne telescope using nuclear emulsion film[25],[26],[27],[28],[29],[30],[31]. Under the development of the telescope, we performed test observation at Norikura Observatory (2770 m a.s.l.) in 2007 and 2013 using prototype emulsion telescope in order to confirm detection performance using atmospheric $\gamma$-ray.

2007 test was the first trial of the detection to the $\gamma$-ray spread wide incoming angle. We established configuration of the telescope and its analysis scheme. Based on this experience, we finalized the design of the first balloon-borne emulsion telescope and performed 1st balloon experiment (GRAINE 2011) at the Taiki Aerospace Research Field of JAXA in June 2011.

In 2013 test, we introduced self-produced nuclear emulsion gel film with higher volume occupancy of silver bromide crystals with respect to conventional ordinary gel in order to improve track finding efficiency as well as signal-to-noise ratio. We obtained high ($> 97\%$) track finding efficiency in a single film and confirmed $\gamma$-ray detection capability at 100 MeV energy region (Figure 5).
Based on this experience, we performed 2nd balloon experiment (obs/Norikura/GRAINE 2015) in Japan-Australia JAXA collaborative balloon experiment at the Alice Springs balloon-launching station in May 2015.

## Environmental Study

**Aerosol sampling at Mt. Norikura**

Aerosol in the atmosphere has been sampled since 2013 at the Norikura observing site using air-samplers to investigate the production of cosmogenic nuclide $^7$Be in a free troposphere above 2 km in the altitude. The aerosol size distribution of $^7$Be was measured for the aerosols sampled by an Andersen sampler enable to separate aerosols to nine classes from 0.43 $\mu$m to 11 $\mu$m. The 81.7% of $^7$Be was covered with the aerosol sizes less than 1.1 $\mu$m and the $^7$Be with the aerosol sizes above 1.1 $\mu$m decrease with an exponential function. The $^7$Be concentration at Mt. Norikura was approximately 9.4 times greater than that at the ground level in Yamagata-city (Fig.6.). Its ratio is almost consistent to a simulated ratio 8.8 of $^7$Be productions due to secondary cosmic rays in the atmosphere by EXPACS. This experimental result is useful for an estimation of altitude distribution of cosmogenic nuclide.

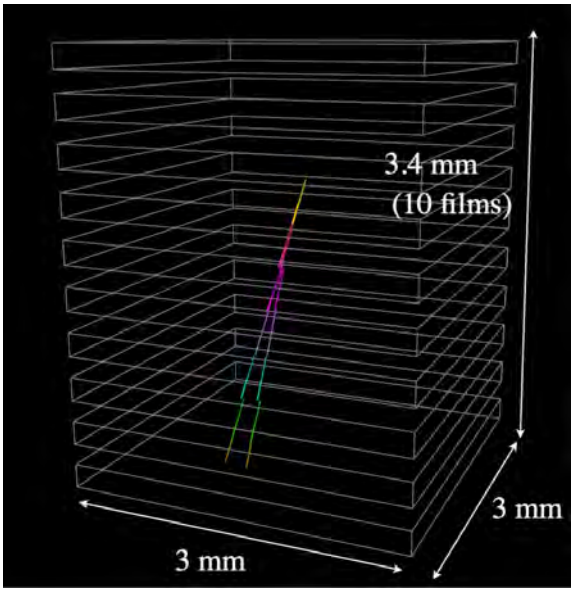


Fig. 5. 3-D view of $\gamma \to e^+ + e^-$ detected in the chamber employed in the obseration test at Norikura Observatory. The reconstructed energy of this event was 160 MeV.

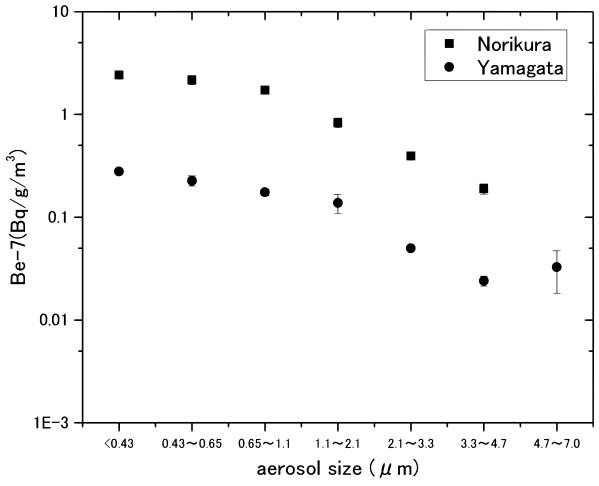


Fig. 6. $^7$Be concentration as a function of aerosol size

## Adaptation of alpine plants to severe environmental conditions

Trees in the alpine regions experience harsh conditions including strong winds, low temperatures, desiccation, and heavy snow. Thus, plants growing in such regions are predicted to have adaptations to these environmental stressors. Through the inter-university research of ICRR, we obtained an opportunity to intensively study plant responses to environmental factors. We identified several characteristics unique to alpine plants, some of which contradict conventional knowledges[32],[33],[34].

1. Adaptation of leaf cuticles in sub-alpine fir (Abies mariessii) at the alpine tree-line

Leaf browning and death are frequently observed in evergreen conifers at the alpine tree-line. These are thought to due to increased transpiration caused by a thinner cuticle and/or mechanical damage to the cuticle by wind-blown snow and ice particles. However, in the sub-alpine fir (Abies mariessii) at Mt. Norikura, mechanical damage was not observed, and the cuticle was rather thick, which may be an adaptation against overwintering at the alpine regions.

2. Embolism of sub-alpine fir (Abies mariessii) at the alpine tree-line

Trees at high altitudes experience severe embolism (loss of xylem conductivity for water) during winters, which is attributed to the entrapment of air in xylem conduits during frost-drought. However, in the sub-alpine fir (Abies mariessii) at Mt. Norikura, air-filled conduits were not observed even in severely-embolized (complete loss of conductivity) shoots. Rather, the pits (valves of partitions inter-conduits) closed before the severe frost-drought in mid-winter, thereby resulting in severe-embolism (complete loss of conductivity). Thus, by pit (valve) cloure, shoots could maintain water in the xylem throughout the winter, which is thought to be an adaptation against lethal filling of air in the conduits during severe frost-drought.

3. Photosynthesis of Haimatsu (Pinus pumila)

At wind-exposed sites on Mt. Norikura, photosynthesis in Haimatsu was suppressed by lower mesophyll $CO_2$ conductance, and not by stomatal closure.

## Investigation of alpine plants on Mt. Norikura

We studied mainly the following three researches on Mt. Norikura after 2012[35],[36],[37],[38],[39],[40],[41],[42],[43],[44],[45],[46],[47],[48],[49].

1) Long-term monitoring and community assembly of alpine plants

We made 40 plots for long-term monitoring of alpine vegetation because climate change possibly affects distributions of alpine plants. We also examined the community assembly process of alpine plants at the 40 plots from the view points of habitat filtering and limiting similarity. Habitat filtering and limiting similarity relate environmental conditions and interspecific competition, respectively. It is suggested that habitat filtering is more important than limiting similarity for the community assembly of alpine plants.

2) Soil respiration rates along an altitudinal gradient

This study investigated seasonal changes of soil respiration rates from forest soil along an altitudinal gradient (1600 m to 2800 m above sea level). The soil respiration rate positively correlated with soil temperatures and forest biomass. It is suggested that forest productivity is an important factor for soil respiration rates.

3) Genetic differentiation of Solidago virgaurea complex

Plant species distributed along wide altitudinal or latitudinal gradients show phenotypic variation due to their heterogeneous habitats. This study investigated whether phenotypic variation in populations of the Solidago virgaurea complex along an altitudinal gradient is caused by genetic differentiation. Population genetic analyses with microsatellite markers were used to infer the genetic structure and levels of gene flow between populations. However, the population genetic

analysis suggested an extremely low level of genetic differentiation of neutral genes among the nine populations. This study suggests that genome regions responsible for adaptive traits may differ among the populations despite the existence of gene flow and that phenotypic variation of the S. virgaurea complex along the altitudinal gradient is maintained by strong selection pressure.

## Bibliography


[1] “ Solar neutron events in association with large solar flares in November 2003”, Watanabe, K. *et al.*, Adv. Space Res., **38**, 425–430, 2006.

[2] K. Munakata, M. Kozai, P. Evenson, T. Kuwabara, C. Kato, M. Tokumaru, M. Rockenbach, A. Dal Lago, R. R. S. Mendonca, C. R. Braga, N. J. Schuch, H. K. Al Jassar, M. M. Sharma, M. L. Duldig, J. E. Humble, I. Sabbah, and J. Kota, “Cosmic Ray Short Burst Observed with the Global Muon Detector Network (GMDN) on June 22, 2015”, Astrophys. J., 862:170 (9pp), 2018 (August 1).

[3] R. R. S. Mendonca, C. R. Braga, E. Echer, A. Dal Lago, M. Rockenbach, N. J. Schuch,, K. Munakata, “Deriving the solar activity cycle modulation on cosmic ray intensity observed by Nagoya muon detector from October 1970 until December 2012”, Proc. IAU Sympo., 328, 1-4 (IAU-16-IAUS328-0453), 2016 (October 20).

[4] R. R. S. Mendonca, C. R. Braga, E. Echer, A. Dal Lago, K. Munakata, T. Kuwabara, M. Kozai, C. Kato, M. Rockenbach, N. J. Schuch, H. K. Al Jassar, M. M. Sharma, M. Tokumaru, M. L. Duldig, J. E. Humble, P. Evenson, I. Sabbah, “Temperature effect in secondary cosmic rays (muons) observed at ground: analysis of the global muon detector network data”, Astrophys. J., 830:88 (25pp), 2016 (October 20). Cited by 2.

[5] M. Kozai, K. Munakata, C. Kato, T. Kuwabara, M. Rockenbach, A. Dal Lago, N. J. Schuch, C. R. Braga, R. R. S. Mendon, H. K. Al Jassar, M. M. Sharma, M. L. Duldig, J. E. Humble, P. Evenson, I. Sabbah, and M. Tokumaru, “Average spatial distribution of cosmic rays behind the interplanetary shock– Global Muon Detector Network observations”, Astrophys. J., 825:100 (19pp), 2016 (July 10). Cited by 7.

[6] D. Ruffolo1, A. Saiz, P.-S. Mangeard, N. Kamyan, P. Muangha, T. Nutaro, S. Sumran, C. Chaiwattana, N. Gasiprong, C. Channok, C. Wuttiya, M. Rujiwarodom, P. Tooprakai, B. Asavapibhop, J. W. Bieber, J. Clem, P. Evenson, and K. Munakata, “Monitoring short-term cosmic-ray spectral variations using neutron monitor time-delay measurements”, Astrophys. J., 817:38 (12pp), 2016 (January 20). Cited by 8.

[7] M. Kozai, K. Munakata, C. Kato, T. Kuwabara, J. W. Bieber, P. Evenson, M. Rockenbach, A. Dal Lago, N. J. Schuch, M. Tokumaru, M. L. Duldig, J. E. Humble, I. Sabbah, H. K. Al Jassar, M. M. Sharma, J. Kota, “The spatial density gradient of galactic cosmic rays and its solar cycle variation observed with the Global Muon Detector Network”, Earth, Planets and Space, 66, 151-158, 2014 (November 14). Cited by 12.

[8] K. Munakata, M. Kozai, C. Kato, J. Kota, “Long term variation of the solar diurnal anisotropy of galactic cosmic rays observed with the Nagoya multi-directional muon detector”, Astrophys. J., 791:22, 1-16, 2014 (August 10). Cited by 19.

[9] M. Rockenbach, A. Dal Lago, N. J. Schuch, K. Munakata, T. Kuwabara, A. G. Oliveira, E. Echer, C. R. Braga, R. R. S. Mendonca, C. Kato, M. Kozai, M. Tokumaru, J. W. Bieber, P. Evenson, M. L. Duldig, J. E. Humble, H. K. Al Jassar, M. M. Sharma, I. Sabbah, “Global muon detector network use d for space weather applications”, Space Sci. Rev., 182, 1-18, 2014 (May 9). Cited by 18.

[10] K. Munakata, “For space weather applications”, Space Sci. Rev., 182, 1-18, 2014 (May 9).

[11] D. Lopez et al., Estimates of the neutron emission during solar flares in the rising and maximum period of solar cycle 24, Astroparticle Physics, 76 (2016) 19-28.

[12] Enoto, T. and Wada, Y. and Furuta, Y. and Nakazawa, K. and Yuasa, T. and Okuda, K. and Makishima, K. and Sato, M. and Sato, Y. and Nakano, T. and Umemoto, D. and Tsuchiya, H, ”Photonuclear reactions triggered by lightning discharge”, Nature 551, (2017) 481-484.

[13] Dwyer, J. R. and Smith, D. M. and Cummer, S. A., ”High-Energy Atmospheric Physics: Terrestrial Gamma-Ray Flashes and Related Phenomena”, 173 (2012) 133-196.

[14] Tsuchiya, H. and Enoto, T. and Torii, T. and Nakazawa, K. and Yuasa, T. and Torii, S. and Fukuyama, T. and Yamaguchi, T. and Kato, H. and Okano, M. and Takita, M. and Makishima, K., ”Observation of an Energetic Radiation Burst from Mountain-Top Thunderclouds”, Physical Review Letters, 102, (2009) 255003.

[15] Wada, Y. and Bowers, G. S. and Enoto, T. and Kamogawa, M. and Nakamura, Y. and Morimoto, T. and Smith, D. M. and Furuta, Y. and Nakazawa, K. and Yuasa, T. and Matsuki, A. and Kubo, M. and Tamagawa, T. and Makishima, K. and Tsuchiya, H., ”Termination of Electron Acceleration in Thundercloud by Intracloud/Intercloud Discharge”, Geophysical Research Journal 45, (2018) 5700-5707.

[16] Tsuchiya, H. and Enoto, T. and Yamada, S. and Yuasa, T. and Kawaharada, M. and Kitaguchi, T. and Kokubun, M. and Kato, H. and Okano, M. and Nakamura, S. and Makishima, K., ”Detection of High-Energy Gamma Rays from Winter Thunderclouds”, Physical Review Letters, 99, (2007) 165002.

[17] Yo Kato, “Observational study of thundercloud radiation bursts using a segmented organic scintillator installed at a mounaintop”, Ph.D. thesis, The University of Tokyo, September, 2015.

[18] Y. Kato, “Thundercloud-related radiation bursts observed at a coastal area and a mountaintop using segmented organic scintillators”, Thunderstorms and Elementary Particle Acceleration (TEPA-2015), 5-9 October 2015, Yerevan, Armenia.

[19] Y. Kato, “Development of Plastic Anti-neutrino Detector Array (PANDA)”, Applied Antineutrino Physics(AAP) 2015, 7-8 December 2015, Virginia Tech Research Center, United States.

[20] Y. Kato “Observation of thundercloud radiation bursts using segmented plastic scintillators”, European Geosciences Union General Assembly (EGU), 8-13 April 2018, Austria Center Vienna, Austria.

[21] T. Torii *et al*., ”Gradual increase of energetic radiation associated with thunderstorm activity at the top of Mt. Fuji”, Geophys. Res. Lett 36(13) , 2009.

[22] T. Kuritai *et al*., ”The Status of the synchrotron of the Wakasa Wan Energy Research Center”, Proc. 12th Annual Meeting of the Particle Accelerator Societ of Japan, 288, 2015.

[23] K. Kume, T. Torii, M. Takita and T. Hasegawa, ”Development of a beam fluence measurement technique at atmosphere”, Igaku Butsuri, Vol.36 Suppl.3 178, 2016 ( in Japanese ).

[24] K. Kume, T. Hasegawa, S. Hatori, M. Takita and H. Tsuji, ”Space engineering application of therapeutic broad beam for cosmic rai simulation”, Igaku Butsuri, Vol.37 Suppl. 112, 2017 ( in Japanese ).

[25] Satoru Takahashi,Ph.D Thesis (2011) Nagoya University, http://hdl.handle.net/2237/14900.

[26] Hiroaki Kawahara, Master Thesis (2015), Nagoya University.

[27] “GRAINE project: gamma-ray observation with a balloon-borne emulsion telescope”, Hiroki Rokujo on behalf of GRAINE Collaboration, Proceeding of Science KMI2013 (2014) 042.

[28] “GRAINE project: The first balloon-borne, emulsion gamma-ray telescope experiment”, S. Takahashi, S. Aoki, K. Kamada, S. Mizutani, R. Nakagawa, K. Ozaki and H. Rokujo, PTEP 2015 (2015) no.4, 043H01.

[29] “Gamma-Ray Astro-Imager with Nuclear Emulsion, GRAINE (in Japanese)”, Satoru Takahashi, Shigeki Aoki for GRAINE collaboration, Journal of the SPSTJ, Vol,78(2015) No.4, pp.228-234.

[30] “GRAINE 2015, a balloon-borne emulsion $\gamma$-ray telescope experiment in Australia”, Satoru Takahashi et al. (GRAINE collaboration), PTEP 2016 (2016) no.7, 073F01.

[31] “GRAINE project, prospects for scientific balloon-borne experiments”, Satoru Takahashi, Shigeki Aoki for GRAINE collaboration, Advances in Space Research, Articles in press.

[32] Nakamoto A., Ikeda T., Maruta E. (2013) Needle browning and death in the flagged crown of Abies mariesii in the timberline ecotone of the alpine region in central Japan. Trees 27:815-825.

[33] Maruta E., Yazaki K.(submitted) Mechanism of embolism as induced by pit closure during winter in subalpine fir (Abies mariesii)on Mt. Norikura.

[34] Nagano S., Nakano T., Hikosaka K., Maruta E. (2013) Pinus pumila photosynthesis is suppressed by water stress in a wind-exposed mountain site. Arctic, Antarctic, and Alpine Research 45:229-237.

[35] Takahashi, K., Hirosawa, T. and Morishima, R. (2012) How the timberline formed: altitudinal changes in stand structure and dynamics around the timberline in central Japan. Annals of Botany 109: 1165-1174.

[36] Takahashi, K. and Okuhara, I. (2013) Forecasting the effects of global warming on radial growth of subalpine trees at the upper and lower distribution limits 3n central Japan. Climatic Change 117: 278-287.

[37] Takahashi, K. and Obata, Y. (2014) Growth, allometry and shade tolerance of understory saplings of four subalpine conifers in central Japan. Journal of Plant Research127: 329-338.

[38] Takahashi, K. (2014) Effects of wind and thermal conditions on timberline formation in central Japan: a lattice model. Ecological Research 29:121-131.

[39] Takahashi, K. and Koike, S. (2014) Altitudinal differences in bud burst and onset and cessation of cambial activity of four subalpine tree species. Landscape and Ecological Engineering 10:349-354.

[40] Takahashi, K. and Murayama, Y. (2014) Effects of topographic and edaphic conditions on alpine plant species distribution along a slope gradient on Mount Norikura, central Japan. Ecological Research 29: 823-833.

[41] Singh, D., Takahashi, K., Park, J. and Adams, J. M. (2016) Similarities and contrasts in the archaeal community of two Japanese mountains: Mt Norikura compared to Mt Fuji. Microbial Ecology 71: 428-441.

[42] Takahashi, K. and Furuhata, K. (2016) Shoot growth and seasonal changes of non-structural carbohydrate concentrations at the upper and lower distribution limits of three conifers. Landscape and Ecological Engineering 12: 239-245.

[43] Takahashi, K. and Tanaka, S. (2016) Relative importance of habitat filtering and limiting similarity on species assemblages of alpine and subalpine plant communities. Journal of Plant Research 129: 1041-1049.

[44] Takahashi, K. and Matsuki, S. (2017) Morphological variations of the Solidago virgaurea L. complex along an elevational gradient on Mt. Norikura, central Japan. Plant Species Biology 32: 238-246.

[45] Kerfahi, D., Tateno, R., Takahashi, K., Cho, H., Kim, H. and Adams, J. M. (2017) Development of soil bacterial communities on volcanic ash microcosms in a range of climates. Microbial Ecology 73: 775-790.

[46] Sakurai, A. and Takahashi, K. (2017) Flowering phenology and reproduction of the Solidago virgaurea L. complex along an elevational gradient on Mt. Norikura, central Japan. Plant Species Biology 32: 270-278.

[47] Dong, K., Moroenyane, I., Tripathi, B., Kerfahi, D., Takahashi, K., Yamamoto, N., An, C., Cho, H., and Adams, J. (2017) Soil nematodes show a mid-elevation diversity maximum and elevational zonation on Mt. Norikura, Japan. Scientific Reports 7: 3028.

[48] Hirano, M., Sakaguchi, S. and Takahashi, K. (2017) Phenotypic differentiation of the Solidago virgaurea complex along an elevational gradient: Insights from a common garden experiment and population genetics. Ecology and Evolution 7: 6949-6962.

[49] Takahashi, K., Otsubo, S. and Kobayashi, H. (2017) Comparison of photosynthetic traits of codominating subalpine conifers Abies veitchii and A. mariesii in central Japan. Landscape and Ecological Engineering 14: 91-97.

# AKENO OBSERVATORY

## Introduction

The Akeno Observatory is situated in Akeno of Hokuto-city, 20 km northwest of Kofu and 130 km west of metropolitan Tokyo. The location is at the longitude of 138.5°E and the latitude of 35.8°N. The altitude is ∼900 m above sea level. It was established in 1977 as a research center for air shower studies in the very high energy region, and it has been administered by the ICRR as a facility of joint-university-use.

The 40th anniversary of the Akeno Observatory was held in 2017.

## Akeno Air Shower Experiments

The Akeno Air Shower Experiment started in 1979 with an array covering 1 km$^2$ area (the 1 km$^2$ array, see Fig.1). The array was enlarged to 20 km$^2$ in 1984 and was gradually expanded to Akeno Giant Air Shower Array (AGASA) of approximately 100 km$^2$ area by 1990. The AGASA was built

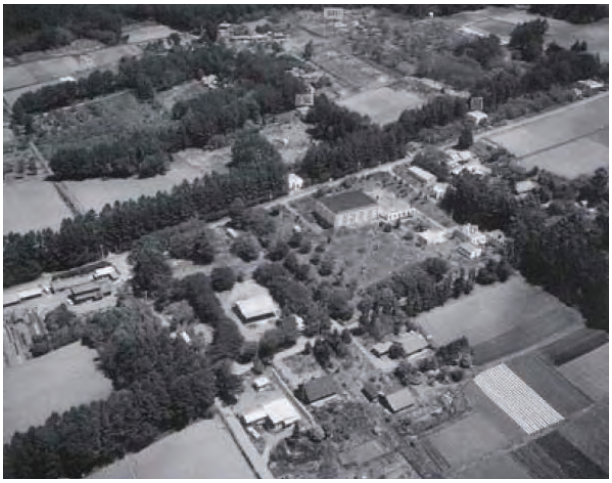

Fig. 1. Aerial View of Akeno Observatory and 1 km$^2$ Array Area

to detect Ultra-High Energy Cosmic Rays (UHECRs) in the energy range of $10^{20}$ eV.

One of the distinctive features of Akeno experiments is that the measurements were made over five decades of energies well covering $10^{15}$ eV - $10^{20}$ eV by using both the surface detector for electromagnetic component, and the shielded detector for muon component (Fig.2). The wide energy coverage was accomplished by the arrays of scintillation detectors of various inter-detector spacings from 3 m to 1 km and with different triggering conditions. This feature of Akeno air shower measurement is well demonstrated in Fig.3, in which the spectra from Akeno 1 km$^2$ array for $10^{14.5}$ eV - $10^{18.8}$ eV [2] and AGASA for $10^{18.5}$ eV - $10^{20.3}$ eV [3] are plotted.

*2 M. Nagano et al., J. Phys. **G10**, 1295 (1984); M. Nagano et al., J. Phys. **G18**, 423 (1992).

*3 M. Takeda et al., Astropart. Phys. **19**, 447 (2003).

Fig. 2. One of the muon detector housings with concrete shielding.

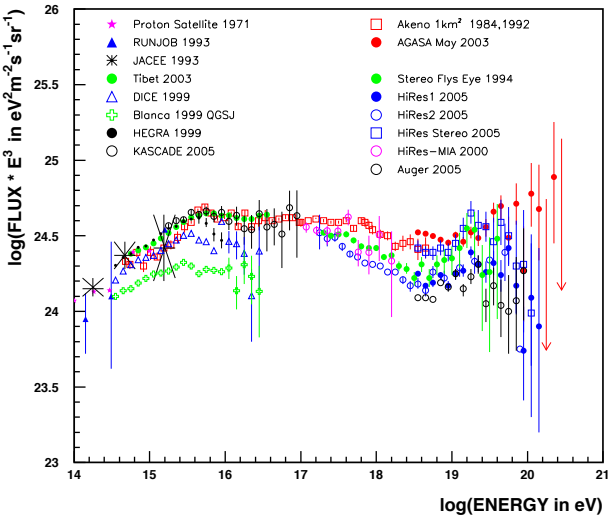


Fig. 3. Akeno energy spectrum measurements for $10^{15}$ eV - $10^{20}$ eV.

## AGASA

The AGASA was composed of 111 surface detectors, each with plastic scintillator of 2.2 m$^2$ area and 5 cm thickness. The counters were deployed with ∼1 km spacing covering the ground area of about 100 km$^2$ in the suburban area of Akeno, outside of the observatory campus. The AGASA served as the largest air shower array in the world since its commissioning in 1990 until it stopped data taking in January 2004, when the construction of the succeeding experiment, Telescope Array (TA), started in Utah. The AGASA was dismantled in 2007 together with other Akeno air shower arrays.

An exposure of 5.8 × $10^{16}$ m$^2$ s sr above $10^{19}$ eV was accumulated by AGASA in 13 years of operation. Extensive air showers with zenith angles smaller than 45° and with core

locations inside the array area were used for the analysis. The AGASA reported an extension of the energy spectrum beyond the predicted Greisen-Zatsepin-Kuzmin (GZK) cutoff in 1998 [4] and a total of eleven UHECR events were observed above $10^{20}$ eV by 2003.

## Measurement of UHECRs

Since the AGASA measurement in 1998, High Resolution Fly's Eye (HiRes) [5], Pierre Auger Observatory (PAO) [6], and Telescope Array (TA) [7] measured the energy spectra of UHECRs with higher statistics.

The HiRes observed the UHECR using the fluorescence telescope. The PAO and the TA measure the energy spectra using the surface array consisting of either water tanks (PAO) or plastic scintillators (TA), but the energy scale of the array is determined by the fluorescence telescope using a subset of events observed by the fluorescence telescope and surface array at the same time. The adoption of the energy scale by the fluorescence telescopes is based on its small dependence on the air shower simulation.

The energy spectra above $10^{18}$ eV by AGASA and other experiments are compiled and compared by the working group represented by UHECR experiments in the UHECR2012 symposium held in 2012 [8]. The result is plotted in Fig.4 with the energy scale of each experiment adjusted to a reference energy, which is set halfway between PAO and TA/HiRes. Following factors were applied for the energy scale; $\times$1.10 for PAO, $\times$0.91 for TA and HiRes, $\times$0.65 for AGASA and $\times$0.56 for Yakutsk.

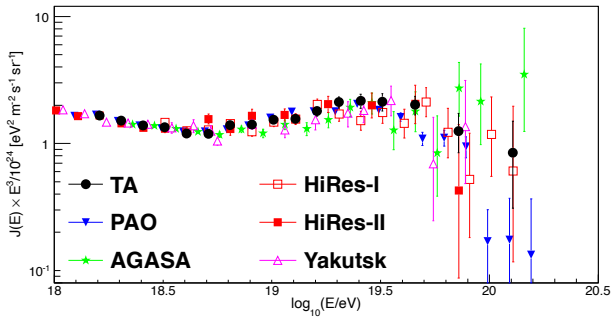


Fig. 4. Compilation of UHECR energy spectra (UHECR2012). The energy scale of each experiment is adjusted as described in the text.

As seen in Fig.4, the overall agreement between experiments is good, and a "dip" structure was seen around $10^{18.7}$ eV by all experiments. The HiRes, PAO and TA confirmed a strong flux suppression above approximately $10^{19.7}$ eV. Although the AGASA spectrum does not demonstrate the cutoff structure, the number of events above $10^{20}$ eV became only two after the energy rescaling, making the claim of the extended spectrum statistically insignificant. The estimate of systematic uncertainty of the energy measurement is approximately 20% for all the experiments, and rescalings for the TA/HiRes and PAO are within this limit. Rescaling of the surface array energy for AGASA and Yaktsuk indicates that there exist larger systematic uncertainties than originally estimated by running the air shower simulation. This difference of energy scale obtained by the surface array and by the fluorescence telescope remains as a basic question in the understanding of the air shower phenomena.

## Recent Research Activities

The study of UHECRs by AGASA in Akeno was succeeded by the TA experiment in Utah, USA since 2008. After the cessation of AGASA, the Akeno Observatory has been used for small scale cosmic ray experiments, astrophysical observations and as a test and maintenance facility of TA by the ICRR and university researchers. Fig.5 shows a recent photograph of the main site of the Akeno Observatory.

Fig. 5. The main site of the Akeno Observatory. There are the movable tent for a small atmospheric Cherenkov telescope, the large experimental hall, the research building and the lodging facility from the left.

### *Observation by the multi-color imager for transients, survey and monstrous explosions (MITSuME) by N. Kawai (Tokyo Institute of Technology) et al.*

One of the three MITSuME robotic telescopes was installed in the Akeno Observatory in 2003 (Fig. 6). The telescope has an aperture of 50 cm, an FOV of 28' $\times$ 28' and is equipped with a tricolor CCD camera capable of $g'R_CI_C$-bands photometry (g':400$\sim$550 nm, Rc:570$\sim$730 nm, Ic:730$\sim$ 850 nm). It is operated remotely from the Tokyo Tech at the Ookayama Campus. Upon receiving a GRB alert from Swift or Fermi satellite, it directs the telescope toward the GRB direction within two minutes, and makes a prompt observation of the GRB and its afterglow.

The follow-up observation of GRBs was continued by the MITSuME telescope. In this fiscal year the values of limiting magnitude of 53 GRBs were observed. The objects were identified for four GRBs, and light variations were observed for three objects during observation.

As the part of OISTER (Optical and Infrared Synergetic Telescopes for Education and Research) program by universities, the MITSuME telescope performed the follow-up observations of three events of supernova explosion afterglow, two

*4 M. Takeda et al., Phys. Rev. Lett. **81**, 1163 (1998).
*5 R.U. Abbasi et al., Phys. Rev. Lett. **100**, 101101 (2008).
*6 J. Abraham et al., Phys. Lett. **B685**, 239 (2010).
*7 T. Abu-Zayyad et al., Astrophys. J. **768**, L1 (2013).
*8 http://indico.cern.ch/conferenceDisplay.py?confId=152124

X-ray binaries detected by MAXI (Monitor of All-sky X-ray Image) and Swift, and two dwarf novae.

In order to perform follow-up visible-light observations of gravitational objects, the MITSuME participated in J-GEM (Japanese collaboration for Gravitational-wave ElectroMagnetic follow-up) and GROWTH(Global Relay of Observatories Watching Transients Happen) to establish worldwide observation network focusing on the electromagnetic identification of gravitational wave sources as one of scientific themes. In this fiscal year, the system of summarizing observational information and results for J-GEM was developed. And the observation of a transient source with the MiTSuME telescope related to the GROWTH project was reported.

Fig. 6. The dome in which the MITSuME telescope was installed in Akeno.

### *Observation of galactic cosmic rays by large area muon telescope by A. Oshima (Chubu University) et al.*

Four layers of proportional counter telescopes, each with 25 $m^2$ area, were installed in three muon houses in Akeno and have been continuously measuring the cosmic ray muons since 2003. Fig. 2 shows one of the muon houses. The mode energy of the primary cosmic rays is approximately 2.5 GeV corresponding to 2m thick concrete ceiling of the muon house at the latitude of the Akeno Observatory. The measurement in Akeno is combined with a simultaneous measurement by the GRAPES-3 experiment at Ooty in India, and this telescope aims at measuring the modulation effects and anisotropy of galactic cosmic rays in the region of about 100 GeV and detecting trasient phenomena of cosmic rays. It is expected to understand cosmic-ray flow in the universe magnetic field and to obtain a clue to the solution of cosmic-ray propagation. And it is challenging to establish the method of a new space weather observation by simultaneous multi-directional observations with high statistical precision. In JFY 2018, the maintenance of three muon houses were performed for data servers and proportional counters, and the observations with all three houses resumed.

### *Research and development for a small atmospheric Cherenkov telescope at the Akeno Observatory by T. Yoshikoshi (ICRR) et al.*

An alt-azimuth telescope with an aperture of three meters (Fig. 7) was setup in the Akeno Observatory for various prototype tests with atmospheric Cherenkov observations of gamma rays on the ground [9]. This telescope is the only telescope to observe atmospherice Cherenkov light emitted from air showers induced by TeV gamma rays in Japan. In JFY2016, an atmospheric cherenkov light event was firstly observed with this telescope.

One of the R&D performed at the Akeno Observatory is the development of low-power-consumption data acquisition system with 32 photomultipliers. It is planned to observe the Crab Pulsar using the part of this system.

In JFY2018, it succeeded in reading out data continuously at 100-$\mu$sec sample interval which is sufficiently shorter than the period of the Crab Pulsar. Around the end of JFY2018, the final tuning of the timing calibration was being performed. It is planed to introduce the main system into the telescope to detect optical pulse signal by observing the Crab Pulsar.

Fig. 7. The Cherenkov telescope at the tour of the 40th anniversary of the Akeno Observatory in 2017.

### *Research and development for the Telescope Array observation in Utah by the TA collaboration and others*

All the TA fluorescence imaging cameras were assembled in the Akeno Observatory by the TA collaboration team. The detectors were tested in Akeno and shipped to the Utah observation site for the installation. All the unit mirrors of the TA fluorescence telescope were tested in Akeno and the atmospheric monitoring lidar of TA using YAG laser was developed in Akeno. In JFY 2015, the R&D of the surface detectors were performed in the large experimental hall of the Akeno Observatory for the TAx4 project that aims at quadrupling the TA surface detector array in Utah. In August in 2016, 2017 and 2018 the TAx4 scintillator counters were assembled in the Akeno Observatory. They were sent to the Cosmic Ray Center in Delta City in Utah, USA, where the TAx4 surface detectors were finally assembled.

The tests using facilities in the Akeno Observatory by other subjects were also performed.

*[9] M. Ohishi et al., 33rd ICRC, (Rio deJaneiro), 587 (2013).

# KAMIOKA OBSERVATORY

Kamioka observatory is located at 1000 m underground (2700 m water equivalent) in the Kamioka Mine, Gifu prefecture, about 200 km west of Tokyo. The observatory was established in 1995 in order to operate Super-Kamiokande experiment (SK). The underground laboratories are located under Mt.Ikeno-yama and accessible to the experimental site through a 1.7 km horizontal tunnel. The observatory also has surface research buildings and a dormitory located at the distance of 15 minutes drive from the entrance of the underground laboratories.

The Super-Kamiokande experiment had discovered neutrino oscillations through the observations of atmospheric and solar neutrinos (see the section for Neutrino and Astroparticle Division). The atmospheric neutrino oscillation was confirmed by the long baseline neutrino oscillation experiment, K2K, using accelerator neutrino beam, which was conducted between 1999 and 2004. A new long baseline neutrino oscillation experiment (the T2K experiment) using a high intensity beam, 50 times of the K2K neutrino beam, by the J-PARC proton accelerator has started in 2009. In 2011, the experiment has observed 6 $\nu_e$ appearance events indicating non-zero $\theta_{13}$ which was as yet determined the last neutrino oscillation parameter. Anti-neutrino beam data was taken from 2014 to 2016 in order to search for CP violation. Based on the whole data taken until 2016, T2K presented the first CP violation search result in August 2016.

The low cosmic ray flux and low seismic noise environment in the underground site enables us to conduct various researches. There is a 100 m long laser interferometer, which is a proto-type of the 3 km gravitational wave antenna (KAGRA). Using the low radioactive background environment in the Kamioka Mine, a dark matter experiment, called XMASS is operated in Lab-C. The XMASS group constructed a 800kg liquid xenon detector and started data taking from 2010. The detector has been improved and searches for dark matter interactions and rare phenomena in luquid xenon have been conducted in the last few years. The R&D study of a tracking type detector for dark matter detection led by the Kobe University group (the NEWAGE experiment) has also been performed in Lab-B. A double beta decay experiment using $^{48}$Ca (the CANDLES experiment) led by the Osaka University group has been running in Lab-D. The study to improve the neutrino detection sensitivity by adding gadolinium to Super-Kamiokande (called SK-Gd project) has been performed at Lab-E. A 200 ton test tank dedicated for the R&D study of the SK-Gd project was constructed and a feasibility study has been performed. In order to support those experiments and also related R&D works, the Observatory is equipped with low background Germanium detector in Lab-1 and Lab-A, ICP-MS and so on to measure extremely low radioactive backgrounds. Lab-G area was newly excavated in 2015 and the SK-Gd equipments which include a Gd dissolving system, a pre-treatment system and a Gd-water circulation system were installed in 2016.

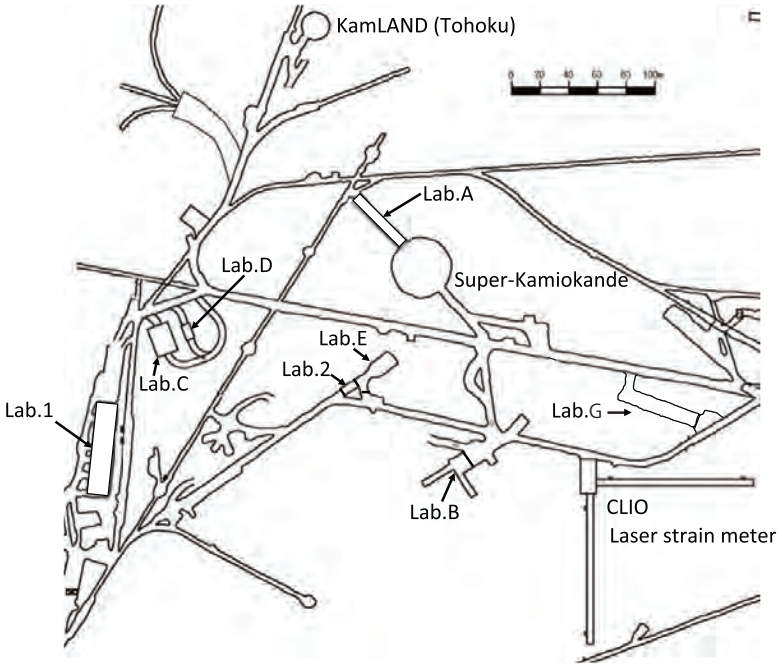


Fig. 1. Kamioka Underground Observatory.

# KAGRA OBSERVATORY

KAGRA observatory is located in the Ikenoyama-mountain on the border between Gifu and Toyama prefecture, about 35 km south of Toyama city in Japan. The observatory was established in 2016 in order to operate Large -scale Cryogenic Gravitational Wave Telescope (nicknamed “KAGRA”). KAGRA itself has a L-shape tunnel facility, and it is located more than 200m under Mt.Ikeno-yama. The corner station of the L-shape tunnel is accessible through a 500-m horizontal access tunnel from Atotsu area. The observatory has its own surface research buildings and rental space in the community center of Hida city located about 5km away from the Atotsu entrance of KAGRA.

KAGRA aims to observe several gravitational waves (GWs) per a year with its designed sensitivity as one of observatories of the world GW detection network including Advanced-LIGO, Advanced-Virgo and planned LIGO-India. KAGRA project (formerly named LCGT) was partially approved in 2010 as one of Leading-edge Research Infrastructure Program, and also supported by Program for Promoting Large-scale Science Projects, Subsidy for Facilities Expense and Grants-in-Aid for Scientific Research from Ministry of Education, Culture, Sports, Science and Technology (MEXT).

In KAGRA project, Institute for Cosmic Ray Research plays a role of a host promoting institute, and National Astronomical Observatory in Japan (NAOJ) and High Energy Accelerator Research Organization (KEK) are the main support organizations, then more than 297 researchers in 85 institutes and universities in the world are collaborating for construction and data analysis of KAGRA.

The tunnel excavation started in May 2012, and finished in March 2014. After that, the basic laboratory environment was prepared until September 2015. A Michelson interferometer with 3km arm (iKAGRA) was demonstrated in March 2016, and the first engineering run was performed until May 2016. At present (April 2019), all the interferometer components had been installed to complete the KAGRA Observatory that adopts a power recycled Fabry-Perot Michelson type interferometer with the resonant sideband extraction and the interferometer is under commissioning. We plan to start the joint observation with LIGO and Virgo within 2019.

Fig. 1. Surface Research Building.

Fig. 2. Atotsu Entrance of KAGRA.

# RESEARCH CENTER FOR COSMIC NEUTRINOS

The Research Center for Cosmic Neutrinos (RCCN) was established in April 1999. The main mission of this center is to promote researches related to neutrinos based on data from various observations and experiments, and we have provided the occasion to discuss theoretical ideas and experimental results on neutrino physics. Members of this center have been involved in the Super-Kamiokande and T2K experiments, and contributing precise measurements of neutrino oscillations. Also, we have been involved in Hyper-Kamiokande project, and worked on the calculation of the atmospheric neutrino flux to have better predictions of the neutrino flux.

RCCN, together with the computer committee, oversees the operation of the central computer system in ICRR (Fig 1). The computer facility has high performance to analyze huge amount of data, and has been operated without any serious trouble since it was upgraded in 2014. Since 2004, RCCN has been accepted inter-university programs related to activities in the low-background underground facility also (Fig 2). In FY2018, we accepted 9 programs related to these facilities.

RCCN has been organizing domestic neutrino-related workshop since it was established. On March 23, 2019, we hosted one neutrino workshop on “Supernova relic neutrino”. Twenty-one physicists participated in this meeting. We have also contributed holding public lectures. Since JFY2009, ICRR and the Kavli Institute for the Physics and Mathematics of the Universe (Kavli-IPMU) have co-sponsored two public lectures each year. The public lecture held in Spring is co-organized by RCCN and the Public Relation Office of ICRR. The Spring public lecture in FY2018 was held on April 14, 2018. Two scientists lectured on the supernova neutrino and theoretical study using LHC accelerator data.

Fig. 1. Photo of the central computer facility in ICRR upgraded in 2014.

Fig. 2. Photo of the low-background underground facility in ICRR.

# APPENDICES

# A. ICRR Workshops and Ceremonies

## The first meeting of the Hyper-Kamiokande Experiment Financial Forum

Date: Jan. 11, 2019
Place: Kojima Hall, Hongo Campus, The University of Tokyo

**Outline:** Hyper-Kamiokande (HK) is a new world-leading international scientific research project aiming to start its operation in the second half of the 2020s. In October 2017, the Next-Generation Neutrino Science Organization (NNSO) was established in the University of Tokyo by the Institute for Cosmic Ray Research (ICRR), the Kavli Institute for the Physics and Mathematics of the Universe (Kavli IPMU), and the School of Science to cooperate in pioneering the future of neutrino physics programs through the development of neutrino research techniques and detector technologies. Professor Takaaki Kajita, the director of NNSO, invited foreign agency representatives and researchers from 14 countries (Armenia, Brazil, Canada, France, Italy, South Korea, Poland, Russia, Spain, Sweden, Switzerland, UK, USA and Japan) and about 50 people gathered to hold discussions. The forum was established to offer a place for agencies to find out the details of the Hyper-Kamiokande project including its goals, timelines and the organizational structure, and to share information on interests and constraints of each country and region. We discussed to identify the necessary tasks to further solidify the international collaboration.

**Participants:** 50 participants.

Fig. 1. About 50 participants attended the first meeting of HKFF.

# Inauguration Ceremony of the First Large Size Telescope of Cherenkov Telescope Array

Date: Oct. 10, 2018

Place: IAC ' s observatory of Roque de los Muchachos on the island of La Palma, Spain

**Outline:** The Cherenkov Telescope Array (CTA) is the next-generation observatory for gamma-ray astronomy, and is the project more than 1,400 researchers and engineers from 31 countries have joined. The first of four Large Size Telescopes (CTA-LST1) was completed, and its inauguration ceremony was held on 10th of October, 2018, on the island of La Palma, Spain. More than 200 guests from around the world gathered on the northern array site of CTA to celebrate its debut.

Professor Takaaki Kajita, Director of ICRR, stated a celebration and CTA is expected to play an essential role not only in the gamma-ray astronomy but in the multi-messenger astronomy, in his remarks. Professor Masahiro Teshima, LST work package leader, appreciated the related countries ' governments who extended the strong financial support up to this point, and rewarded the researchers and the engineers involved for their effort, and asked for continuous support to complete the construction of both CTA ' s northern and southern hemisphere arrays.

The ceremony was followed by congratulatory speeches from Professor Masashi Haneda, Executive Vice President of the University of Tokyo, Mr. Pestana Anselmo, Presidente del Cabildo de La Palma, and Mr. Pedro Duque, Ministro de Ciencia in Spain.

The ceremony was closed with ribbon-cutting.

**Participants:** 187 participants.

Fig. 2. CTA-LST1 on the top of the island of La Palma.

Fig. 3. Ribbon-Cutting Ceremony.

# Symposium and Celebration to Commemorate the 10th anniversary of Telescope Array

Date: Dec. 19, 2018
Place: Media Hall, Kashiwa Campus of the University of Tokyo.

**Outline:** The symposium and the celebration to commemorate the 10th anniversary of Telescope Array was held on 19th of December 2018, at Kashiwa Campus of the University of Tokyo, and the approximately 90 people involved attended in these events.

Telescope Array is an international collaborative project, and about 130 researchers from 6 countries have been working on. The 507 surface detectors (SDs) and the 3 fluorescence detectors (FDs) have been deployed in 700 square kilometers in the dessert of Utah, USA, to study the origin and the nature of Ultra-High Energy Cosmic Rays. Currently TA extension named “TA×4” has been ongoing to quadruple the TA effective area, and about 250 SDs were deployed in February and March of 2019.

Professor Takaaki Kajita, Director of ICRR, greeted the attendee and expressed his appreciation of the kind support and cooperation for those who are involved in this experiment in his opening remarks. Dr. Norio Matsuki, Executive Vice President of the University of Tokyo, stated the importance of the role expected to ICRR and the University of Tokyo to contribute to academia and even to the humanity. The ceremony was followed by the congratulatory addresses from Hiroyuki Sakuragi, Executive Director and Vice President of Osaka City University which is the affiliation of Professor and Co-spokesperson of TA experiment Shoichi Ogio, and Professor Charles Jui, Co-spokesperson of TA experiment in the University of Utah.

In this ceremony, the letters of gratitude were presented by Prof. Kajita to the nine companies for their contribution to TA project.

**Participants:** 91 participants.


Fig. 4. Prof. Kajita’s opening remarks.

Fig. 5. Celebration for the 10th anniversary of TA experiment.

# B. ICRR Seminars

1. April 20, 2018: Dr. Takashi Sako (ICRR), " Forward Particle Measurements at Colliders and Air Shower Development"
2. May 25, 2018: Dr. Koji Noda (ICRR), " Gamma-ray Burst Physics with MAGIC and CTA LST"
3. June 19, 2018: Dr. Ken Mawatari (ICRR), " Challenge to the Most Distant Evolved Galaxies: Hint on Star-formation Activity during the First 500 Million Years of the Cosmic History"
4. July 24, 2018: Dr. Manel Martínez (IFAE-BIST, Visiting Prof. of ICRR), " On Bounds on a Possible Energy Dependence of the Speed of Light in Vacuum"
5. July 27, 2018: Dr. Kyohei Kawaguchi (ICRR), " Modelling Gravitational Waveforms and Electromagnetic Signals from Neutron Star Binary Mergers"
6. October 3, 2018: Dr. Susumu Inoue (RIKEN), " The Dawning of Electroweak Astronomy: Interpreting Electromagnetic+neutrino Observations of Blazars"
7. November 2, 2018: Dr. Jonathan R. Gair (The University of Edinburgh), " Gravitational-wave standard siren measurements of the Hubble constant"
8. November 8, 2018: Dr. Kenny C. Y. Ng (Weizmann Institute of Science), " The Surprising Solar Gamma-ray Emission from Cosmic-Ray Interactions"
9. November 26, 2018: Dr. A. Nepomuk Otte (Georgia Institute of Technology), " An instrument to detect cosmogenic neutrinos with the Earth skimming technique"
10. December 3, 2018: Dr. Angela Olinto (The University of Chicago), " Space Probes of the Highest Energy Particles: POEMMA & EUSO-SPB"
11. December 27, 2018: Dr. Toshihiro Fujii (Kyoto University), " A personal decadal survey in ultrahigh-energy cosmic-ray observatories"
12. January 10, 2019: Dr. Kimihiro Okumura (ICRR), " Updated results from the T2K experiment with $3.13\times10^{21}$ protons on target"
13. January 25, 2019: Dr. Kohei Hayashi (ICRR), " Milky Way dwarf spheroidal galaxies as a probe of dark matter properties"
14. February 20, 2019: Dr. Olaf Reimer (University of Innsbruck), " Diffuse Galactic Gamma-Ray Emission before CTA"
15. February 25, 2019: Dr. Kumiko Kotera (Institut d'astrophysique de Paris), " Hunting the highest energy astroparticles with GRAND"
16. February 27, 2019: Dr. Shigeyuki Sako (Institute of Astronomy, U. Tokyo), " The Tomo-e Gozen project"
17. March 11, 2019: Dr. Jishnu Suresh (ICRR), " Efficient technique to probe Stochastic Gravitational Wave Background Anisotropy with ground-based detectors"
18. March 25, 2019: Dr. Felix Riehn (Lab. Inst. Fisica Experim. Particulas), " Interactions of ultra-high energy cosmic rays"

# C. List of Publications

## (a) Papers Published in Journals

1. "Search for Neutrinos in Super-Kamiokande Associated with the GW170817 Neutron-star Merger", The Super-Kamiokande Collaboration, Astrophys. J. Lett. **857**, L4, 2018.
2. "Direct dark matter search by annual modulation with 2.7 years of XMASS-I data", XMASS Collaboration, Physical Review D **97**, 102006 (2018).

3. ”Search for Boosted Dark Matter Interacting With Electrons in Super-Kamiokande”, The Super-Kamiokande Collaboration, Phys. Rev. Lett. **120**, 221301 (2018).

4. ”Improved search for two-neutrino double electron capture on $^{124}$Xe and $^{126}$Xe using particle identification in XMASS-I”, XMASS Collaboration, Prog. Theor. Exp. Phys. **2018** (2018) 053D03.

5. ”Physics Potentials with the Second Hyper-Kamiokande Detector in Korea”, Hyper-Kamiokande proto-collaboration, Prog. Theo. Exp. Phys. **2018**, 063C01 (2018).

6. ”Measurement of the tau neutrino cross section in atmospheric neutrino oscillations with Super-Kamiokande”, Z. Li et al. (Super-Kamiokande Collaboration), Phys. Rev. D **98**, 052006.

7. ”Search for dark matter in the form of hidden photons and axion-like particles in the XMASS detector”, XMASS Collaboration, Phys. Lett. B**787** (2018) 153-158.

8. ”A direct dark matter search in XMASS-I”, XMASS Collaboration, Phys. Lett. B **789** (2019) 45-53.

9. ”A measurement of the scintillation decay time constant of nuclear recoils in liquid xenon with the XMASS-I detector”, XMASS Collaboration, JINST **13** (2018) P12032.

10. ”Development of low radioactivity photomultiplier tubes for the XMASS-I detector”, XMASS Collaboration, Nuclear Inst. and Methods in Physics Research, A **922** (2019) 171-176.

11. ”Search for WIMP-$^{129}$Xe inelastic scattering with particle identification in XMASS-I”, XMASS Collaboration, Astroparticle Physics **110**(2019), 1-7.

12. ”Development of new radon monitoring systems in the Kamioka mine”, G. Pronost, M. Ikeda, T. Nakamura, H. Sekiya, S. Tasaka, Progress of Theoretical and Experimental Physics, Volume **2018**, Issue 9, 1 September 2018, 093H01.

13. ”Gamma Ray Spectrum from Thermal Neutron Capture on Gadolinium-157”, K. Hagiwara, T. Yano et al., Progress of Theoretical and Experimental Physics, **2019** - 023D01.

14. ”Atmospheric neutrino oscillation analysis with external constraints in Super-Kamiokande I-IV ”, The Super-Kamiokande Collaboration, Phys. Rev. D **97**, 072001 (2018).

15. ”Search for CP Violation in Neutrino and Antineutrino Oscillations by the T2K Experiment with $2.2\times10^{21}$ Protons on Target”, T2K Collaboration, Phys.Rev.Lett. **121** (2018) no.17, 171802.

16. ”Characterization of nuclear effects in muon-neutrino scattering on hydrocarbon with a measurement of final-state kinematics and correlations in charged-current pionless interactions at T2K”, T2K Collaboration, Phys.Rev. D**98** (2018) no.3, 032003.

17. ”Measurement of inclusive double-differential $\nu_\mu$ charged-current cross section with improved acceptance in the T2K off-axis near detector”, T2K Collaboration, Phys.Rev. D**98** (2018) 012004.

18. ”First measurement of the $\nu_\mu$ charged-current cross section on a water target without pions in the final state”, T2K Collaboration, Phys.Rev. D**97** (2018) no.1, 012001.

19. ”Deep observations of the globular cluster M15 with the MAGIC telescopes”, V.A.Achari et al (MAGIC Collaboration), Mon.Not.Roy.Astron.Soc.**484** (2019) no.2, 2876-2885.

20. ”A Fast Very High Energy $\gamma$-ray Flare from BL Lacertae during a Period of Multiwavelength activity in June 2015”, V.A.Achari et al (MAGIC Collaboration), Astron.Astrophys. **623** (2019) A175.

21. ”Development of three silicon photomultiplier detector modules for the MAGIC telescopes for a performance comparison to PMTs”, A.Hahn, A. Dettlaff, D. Fink, D. Mazin, M. Razmik, M.Teshima, Nucl.Instrum.Meth. A**912** (2018) 259-263.

22. ”Discovery of TeV gamma ray emission from the neighbourhood of the supernova remnant G24.7+0.6 by MAGIC”, V.A.Achari et al (MAGIC Collaboration), Mon.Not.Roy.Astron.Soc. **483** (2019) no.4, 4578-4585.

23. ”Periastron Observations of TeV Gamma-Ray Emission from a Binary System with a 50-year Period”, A.E Abeysekara et al. (VERITAS and MAGIC Collaborations), Astrophys.J.Lett. **867** (2018) no.1, L19.

24. ”Constraining very-high-energy and optical emission from FRB 121102 with the MAGIC telescopes”, V.A.Achari et al (MAGIC Collaboration), Mon.Not.Roy.Astron.Soc. **481** (2018) 2479-2486.

25. ”Extreme HBL behavior of Markarian 501 during 2012”, M.L.Ahnen et al (MAGIC, FACT and VERITAS collaborations), Astron.Astrophys. **620** (2018) A181.

26. ”Multimessenger observations of a flaring blazar coincident with high-energy neutrino IceCube-170922A”, IceCube, Fermi, MAGIC,,, collaborations, Science **361** (2018) no.6398, eaat1378.

27. ”The blazar TXS 0506+056 associated with a high-energy neutrino: insights into extragalactic jets and cosmic ray acceleration”, S.Ansoldi et al (MAGIC Collaboration), Astrophys.J. **863** (2018) L10.

28. ”The broad-band properties of the intermediate synchrotron peaked BL Lac S2 0109+22 from radio to VHE gamma-ray”, S.Ansoldi et al (MAGIC Collaboration), Mon.Not.Roy.Astron.Soc. **480** (2018) no.1, 879-892.

29. ”Multi-wavelength characterization of the blazar S5 0716+714 during an unprecedented outburst phase”, M.L.Ahnen et al (MAGIC, MWL, Fermi Collaborations), Astron.Astrophys. **619** (2018) A45.

30. ”Constraining Dark Matter lifetime with a deep gamma-ray survey of the Perseus Galaxy Cluster with MAGIC”, V.A.Achari et al (MAGIC Collaboration), Phys.Dark Univ. **22** (2018) 38-47.

31. ”Detection of persistent VHE gamma-ray emission from PKS 1510-089 by the MAGIC telescopes during low states between 2012 and 2017”, V.A.Achari et al (MAGIC and Fermi Collaboration), Astron.Astrophys.**619** (2018) A159.

32. ”Gamma-ray flaring activity of NGC1275 in 2016-2017 measured by MAGIC”, S.Ansoldi et al (MAGIC Collaboration), Astron.Astrophys. **617** (2018) A91.

33. ”A technique for estimating the absolute gain of a photomultiplier tube”, M. Takahashi et al , Nucl.Instrum.Meth. A**894** (2018) 1-7.

34. ”Detection of the blazar S4 0954+65 at very-high-energy with the MAGIC telescopes during an exceptionally high optical state”, M.L.Ahnen et al (MAGIC Collaborations), Astron.Astrophys. **617** (2018) A30.

35. ”Indirect dark matter searches in the dwarf satellite galaxy Ursa Major II with the MAGIC Telescopes”, M.L.Ahnen et al (MAGIC Collaborations), JCAP 1803 (**2018**) no.03, 009.

36. ”Hadronic Origin of Prompt High-energy Emission of Gamma-ray Bursts Revisited: in the Case of a Limited Maximum Proton Energy”, Kai Wang, Ruo-Yu Liu, Zi-Gao Dai, and Katsuaki Asano, ApJ, **857**:24(2018)12pp.

37. ”Extended Measurement of Cosmic-ray Electron and Positron Spectrum from 11 GeV to 4.8 TeV with the Calorimetric Electron Telescope on the International Space Station”, O. Adriani, Y. Akaike, K. Asano, et al. (CALET Collaboration), Phys. Rev. Lett. **120**, 261102.

38. ”On-Orbit Operations and Offline Data Processing of CALET onboard the ISS”, Y. Asaoka, S. Ozawa, S. Torii et al., Aph **100**, 29-37.

39. ”Blazar Spectra with Hard-sphere-like Acceleration of Electrons”, Katsuaki Asano, Masaaki Hayashida, ApJ **861** 31(2018).

40. ”Radiative Transfer Simulation for the Optical and Near-infrared Electromagnetic Counterparts to GW170817”, Kyohei Kawaguchi, Masaru Shibata, Masaomi Tanaka, ApJL **865** L21(2018).

41. ”Search for GeV Gamma-ray Counterparts of Gravitational Wave Events by CALET”, O. Adriani, Y. Akaike, K. Asano, et al., ApJ **863** 160(2018).

42. ”Late Engine Activity of GRB 161017A Revealed by Early Optical Observations”, Yutaro Tachibana, Makoto Arimoto, Katsuaki Asano et al., PASJ (2018) **70** (5), 92 (1-9).

43. ”EUSO-TA — First Results from a Ground-Based EUSO Telescope”, G. Abdellaoui, et al., Aph **102**, 98-111.

44. ”Characteristics and Performance of the CALorimetric Electron Telescope (CALET) Calorimeter for Gamma-Ray Observations”, N. Cannady, Y. Asaoka, F. Satoh, et al., ApJS, **238**, 5(16pp).

45. ”Outflow and Emission Model of Pulsar Wind Nebulae with the Back-reaction of Particle Diffusion”, Wataru Ishizaki, Katsuaki Asano, and Kyohei Kawaguchi,, ApJ **867** 141(2018).

46. ”Depth of Ultra High Energy Cosmic Ray Induced Air Shower Maxima Measured by the Telescope Array Black Rock and Long Ridge FADC Fluorescence Detectors and Surface Array in Hybrid Mode”, R.U. Abbasi et al. (The Telescope Array Collaboration), The Astrophysical Journal, **858**:76 (27pp).

47. ”Gamma Ray Showers Observed at Ground Level in Coincidence With Downward Lightning Leaders”, R.U. Abassi et al. (Telescope Array Collaboration), Journal of Geophysical Research: Atmospheres, **123** (2018).

48. ”Study of muons from ultrahigh energy cosmic ray air showers measured with the Telescope Array experiment”, R.U. Abbasi et al. (Telescope Array Collaboration), PHYSICAL REVIEW D **98**, 022002 (2018).

49. ”Evidence of Intermediate-scale Energy Spectrum Anisotropy of Cosmic Rays $E \geq 10^{19.2}$ eV with the Telescope Array Surface Detector”, R.U. Abbasi et al. (the Telescope Array Collaboration), Astrophys. J. **862**:91 (2018).

50. ”The Cosmic Ray Energy Spectrum between 2 PeV and 2 EeV Observed with the TALE Detector in Monocular Mode”, R.U. Abbasi et al. (Telescope Array Collaboration), The Astrophysical Journal, **865**:74 (18pp).

51. ”Testing a Reported Correlation between Arrival Directions of Ultra-high-energy Cosmic Rays and a Flux Pattern from nearby Starburst Galaxies using Telescope Array Data”, R.U. Abbasi et al. (Telescope Array Collaboration), The Astrophysical Journal Letters, **867**:L27 (5pp),2018.

52. ”Mass composition of ultra-high-energy cosmic rays with the Telescope Array Surface Detector Data”, R.U. Abbasi et al. (Telescope Array Collaboration), Physical Review D **99**, 022002 (2019).

53. ”Constraints on the diffuse photon flux with energies above $10^{18}$ eV using the surface detector of the Telescope Array experiment”, R.U.Abbasi et al. (Telescope Array Collaboration), Astroparticle Physics **110**(2019) 8-14.

54. ”Measurement of inclusive forward neutron production cross section in proton-proton collisions at $\sqrt{s} = 13$ TeV with the LHCf Arm2 detector”, The LHCf collaboration, JHEP11(**2018**)073.

55. ”Influence of Earth-directed Coronal Mass Ejections on the Sun’s Shadow Observed by the Tibet-III Air Shower Array”, M. Amenomori et al. (The Tibet AS$\gamma$ Collaboration), The Astrophysical Journal, **860**, 13 (2018).

56. ”Development of an all-sky gamma-ray Compton camera based on scintillators for high-dose environments”, Hideaki Katagiri et al., JOURNAL OF NUCLEAR SCIENCE AND TECHNOLOGY 2018, VOL. **55**, NO. 10, 1172-1179 .

57. ”Remote measurement of urinary radioactivity in $^{18}$F-FDG PET patients using Compton camera for accuracy evaluation of standardized uptake value”, Takara Watanabe et al., Biomed. Phys. Eng. Express, **4**, 065029 (2018).

58. ”On the stability of a superspinar”, Ken-ichi Nakao, Pankaj S. Joshi, Jun-Qi Guo, Prashant Kocherlakota, Hideyuki Tagoshi, Tomohiro Harada, Mandar Patil, Andrzej Krolak, Phys.Lett. B**780** (2018) 410-413.

59. ”Time-frequency-based non-harmonic analysis to reduce line-noise impact for LIGO observation system ”, D.Jia, K. Yanagisawa, M. Hasegawa, S. Hirobayashi, H. Tagoshi, T. Narikawa, N. Uchikata, H. Takahashi, Astronomy and Computing, **25**, (2018) 238-246.

60. ”Multiwindow Nonharmonic Analysis Method for Gravitational Waves”, Dongbao Jia, Kenta Yanagisawa, Yuta Ono, Kanna Hirobayashi, Masaya Hasegawa, Shigeki Hirobayashi, Hideyuki Tagoshi, Tatsuya Narikawa, Nami Uchikata, Hirotaka Takahashi, IEEE Access., **6**, 48645 (2018).

61. ”Detectability of the 21cm-signal during the epoch of reionization with 21cm-Lyman- $\alpha$ emitter cross-correlation. I. ”, Kenji Kubota, et al, MNRAS, **479**(2018), 2, p.2754-2766.

62. ”SILVERRUSH. V. Census of Ly$\alpha$, [O iii] $\lambda$5007, H$\alpha$, and [C ii] 158 $\mu$m Line Emission with $\sim$1000 LAEs at $z = 4.9 - 7.0$ Revealed with Subaru/HSC”, Yuichi Harikane, et al., Astrophys.J, **859**:84(21pp).

63. ”SPLASH-SXDF Multi-wavelength Photometric Catalog”, Vihang Mehta, et al, ApJ Supplement Series,**235**:36(18pp).

64. ”SILVERRUSH. VI. A simulation of Ly$\alpha$ emitters in the reionization epoch and a comparison with Subaru Hyper Suprime-Cam survey early data”, Akio K. Inoue et al., PASJ, (2018) **70** (3), 55 (1-30).

65. ”A Candidate $z \sim 10$ Galaxy Strongly Lensed into a Spatially Resolved Arc”, Brett Salmon et al., ApJL **864**:L22(6pp).

66. ”ALMA 26 Arcmin$^2$ Survey of GOODS-S at One-millimeter (ASAGAO): Average Morphology of High-$z$ Dusty Star-Forming Galaxies is an Exponential-Disk ($n \simeq 1$)”, Seiji Fujimoto et al., ApJ **861**:7(12pp).

67. ”Subaru High-z Exploration of Low-Luminosity Quasars (SHELLQs) III. Star formation properties of the host galaxies at $z \gtrsim 6$ studied with ALMA”, Takuma Izumi et al., PASJ, (2018) **70** (3), 36 (1-21).

68. ”Large Scale Environment of a $z = 6.61$ Luminous Quasar Probed by Ly$\alpha$ Emitters and Lyman Break Galaxies”, Kazuaki Ota et al., ApJ **856**:109(27pp).

69. "Subaru High-$z$ Exploration of Low-Luminosity Quasars (SHELLQs). IV. Discovery of 41 Quasars and Luminous Galaxies at 5.7 $\leqslant$z$\leqslant$ 6.9", Y. Matsuoka et al., ApJ S, **237**:5(17pp).

70. "RELICS: Strong Lensing analysis of the galaxy clusters Abell S295, Abell 697, MACS J0025.4-1222, and MACS J0159.8-0849", Nathália Cibirka et al., ApJ **863**:145.

71. "The onset of star formation 250 million years after the Big Bang", Takuya Hashimoto et al., Nature **557**, 392-395 (2018).

72. "CHORUS II. Subaru/HSC Determination of the Ly$\alpha$ Luminosity Function at z=7.0: Constraints on Cosmic Reionization Model Parameter", Ryohei Itoh et al., Astrophys.J. **867** (2018) no.1, 46.

73. "The distribution and physical properties of high-redshift [OIII] emitters in a cosmological hydrodynamics simulation", Kana Moriwaki et al., MNRAS **481**, L84-L88(2018).

74. "Detection of the Far-infrared [O III] and Dust Emission in a Galaxy at Redshift 8.312: Early Metal Enrichment in the Heart of the Reionization Era", Yoichi Tamura et al., ApJ **874** 27(2019).

75. "Alma Twenty-six Arcmin$^2$ Survey Of Goods-s At One-millimeter (asagao): Source Catalog And Number Counts", Hatsukade, Bunyo et al., PASJ(2018) **70** (6), 105 (1-20).

76. "Morphologies of $\sim$190,000 Galaxies at $z = 0 - 10$ Revealed with HST Legacy Data. III. Continuum Profile and Size Evolution of Ly$\alpha$ Emitters", Shibuya, Takatoshi; et al., ApJ **871** 164(2019).

77. "RELICS: High-Resolution Constraints on the Inner Mass Distribution of the z=0.83 Merging Cluster RXJ0152.7-1357 from strong lensing", Ana Acebron et al., ApJ **874** 132(2019).

78. "Subaru High-$z$ Exploration of Low-Luminosity Quasars (SHELLQs). V. Quasar Luminosity Function and Contribution to Cosmic Reionization at $z$=6", Yoshiki Matsuoka, et al., ApJ **869** 150(2018).

79. "The infrared-luminous progenitors of high-$z$ quasars", Michele Ginolfi, et al, MNRAS **483**,1, 1256-1264 .

80. "Near-Infrared Survey and Photometric Redshifts in the Extended GOODS-North field", Li-Ting Hsu, et al, ApJ **871** 233(2019).

81. "Environmental impacts on molecular gas in protocluster galaxies at $z \sim 2$", Ken-ichi Tadaki, et al., PASJ.

82. "Discovery of the First Low-Luminosity Quasar at $z > 7$", Yoshiki Matsuoka, et al, ApJL **872** L2(2019).

83. "Enhancement of H I absorption associated with the $z = 3.1$ large-scale proto-cluster and characteristic structures with AGNs sculptured over Gpc scale in the SSA22 field", T. Hayashino, et al, MNRAS **484**,5868-5887 (2019).

84. "Foreground effect on the J-factor estimation of ultra-faint dwarf spheroidal galaxies ", Koji Ichikawa, Shun-ichi Horigome, Miho N. Ishigaki, Shigeki Matsumoto, Masahiro Ibe, Hajime Sugai, Kohei Hayashi, MNRAS **479** (2018) no.1, 64-74 .

85. "Domain wall and isocurvature perturbation problems in a supersymmetric axion model", Masahiro Kawasaki and Eisuke Sonomoto, Phys. Rev. D **97**, 083507.

86. "Cogenesis of LIGO Primordial Black Holes and Dark Matter", Fuminori Hasegawa and Masahiro Kawasaki,, Phys. Rev. D **98**, 043514.

87. "Primordial black holes for the LIGO events in the axion-like curvaton model", Kenta Ando, Keisuke Inomata, Masahiro Kawasaki, Kyohei Mukaida and Tsutomu T. Yanagida,, Phys. Rev. D **97**, 123512 (2018).

88. "Oscillons from Pure Natural Inflation", Jeong-Pyong Hong, Masahiro Kawasaki and Masahito Yamazaki, Phys. Rev. D **98**, 043531.

89. "Cosmologically allowed regions for the axion decay constant $F_a$", Masahiro Kawasaki, Eisuke Sonomoto, Tsutomu T. Yanagida, Phys.Lett.B, **782**(2018)181-184.

90. "QCD axion dark matter from long-lived domain walls during matter domination", Keisuke Harigaya and Masahiro Kawasaki, Phys.Lett.B, **782**(2018)1-5.

91. "Primordial black holes and uncertainties on choice of window function", Kenta Ando, Keisuke Inomata and Masahiro Kawasaki,, Phys. Rev.D **97**,103528 (2018).

92. ”Decay Rate of Electroweak Vacuum in the Standard Model and Beyond”, S. Chigusa, T. Moroi and Y. Shoji, Phys. Rev. D **97**, 116012.

93. ”Inflaton fragmentation in E-models of cosmological $\alpha$-attractors”, Fuminori Hasegawa, Jeong-Pyong Hong, Phys.Rev. D**97** (2018) , 083514.

94. ”Gauged Peccei-Quinn Symmetry - A Case of Simultaneous Breaking of SUSY and PQ Symmetry”, Hajime Fukuda, Masahiro Ibe, Motoo Suzuki, Tsutomu T. Yanagida,, JHEP(2018) **2018**: 128.

95. ”Composite Asymmetric Dark Matter with a Dark Photon Portal”, Masahiro Ibe, Ayuki Kamada, Shin Kobayashi, Wakutaka Nakano, JHEP(2018) **2018**: 203.

96. ”Formation of primordial black holes as dark matter or LIGO black hole binaries in an axion-like curvaton model”, Kenta Ando, Masahiro Kawasaki, Hiromasa Nakatsuka, Phys. Rev. D **98**, 083508.

97. ”$B-L$ as a Gauged Peccei-Quinn Symmetry”, Masahiro Ibe, Motoo Suzuki, Tsutomu T. Yanagida, JHEP(2018) **2018**: 49.

98. ”Big Bang Nucleosynthesis Constraint on Baryonic Isocurvature Perturbations”, Keisuke Inomata, Masahiro Kawasaki, Alexander Kusenko, Louis Yang, JCAP12(**2018**)003.

99. ”Primordial Black Holes from Affleck-Dine Mechanism”, Fuminori Hasegawa and Masahiro Kawasaki, JCAP01(**2019**)027.

100. ”Long-term dynamics of cosmological axion strings”, Masahiro Kawasaki, Toyokazu Sekiguchi, Masahide Yamaguchi and Jun’ichi Yokoyama, PTEP **2018**, 091E01(2018).

101. ”The swampland conjecture and the Higgs expectation value”, Koichi Hamaguchi, Masahiro Ibe, Takeo Moroi,, JHEP(2018) **2018**: 23.

102. ”Primordial Black Holes and the String Swampland”, Masahiro Kawasaki and Volodymyr Takhistov, Phys. Rev. D **98**, 123514 (2018).

103. ”Exploring compensated isocurvature perturbations with CMB spectral distortion anisotropies”, Taku Haga, Keisuke Inomata, Atsuhisa Ota, Andrea Ravenni, JCAP 1808 (**2018**) no.08, 036.

104. ”Circular polarization of the cosmic microwave background from vector and tensor perturbations”, Keisuke Inomata, Marc Kamionkowski, Phys.Rev. D**99** (2019) no.4, 043501.

105. ”Gravitational waves induced by scalar perturbations as probes of the small-scale primordial spectrum”, Keisuke Inomata, Tomohiro Nakama, Phys.Rev. D**99** (2019) no.4, 043511.

106. ”Dark halo structure in the Carina dwarf spheroidal galaxy: joint analysis of multiple stellar components”, Kohei Hayashi, Michele Fabrizio, Ewa L. Lokas, Giuseppe Bono, Matteo Monelli, Massimo Dall’Ora and Peter B. Stetson, MNRAS **481**,1, 50-261.

107. ”Effects of mass models on dynamical mass estimate: the case of ultradiffuse galaxy NGC 1052-DF2”, Kohei Hayashi and Shigeki Inoue, MNRAS**481**,L59-L63.

108. ”Hunting for Statistical Anisotropy in Tensor Modes with B-mode Observations”, T.Hiramatsu, S.Yokoyama, T.Fujita, I.Obata, Physical Review D**98**, 083522.

109. ”Footprint of Two-Form Field: Statistical Anisotropy in Primordial Gravitational Waves”, I.Obata, T.Fujita, Physical Review D**99**, 023513.

110. ”Optical Ring Cavity Search for Axion Dark Matter”, I.Obata, T.Fujita, Y.Michimura, Physical Review Letter **121**, 161301.

111. ”Ultraviolet Completion of a Composite Asymmetric Dark Matter Model with a Dark Photon Portal ”, Masahiro Ibe, Ayuki Kamada, Shin Kobayashi, Wakutaka Nakano, JHEP 1903 (**2019**) 173 .

## (b) Conference Papers (Proceedings)

1. ”Development of three silicon photomultiplier detector modules for the MAGIC telescopes for a performance comparison to PMTs”, Hahn, A.; Dettlaff, A.; Fink, D.; Mazin, D.; Mirzoyan, R.; Teshima, M., 8th International Conference on New Developments in Photodetection (NDIP), JUL, 2017.

2. ”VHE observations of binary systems performed with the MAGIC telescopes”, Lopez-Oramas, Alicia; Blanch, Oscar; de Ona Wilhelmi, Emma; Fernandez-Barral, Alba; Hadasch, Daniela; Moretti, Elena; Munar-Adrover, Pere; Maria Paredes, Josep; Ribo, Marc; Torres, Diego F.; Bordas, Pol; Brun, Francois; Casares, Jorge; Zanin, Roberta, 6th Conference on High Energy Phenomena in Relativistic Outflows (HEPRO), SEP 11-15, 2017.

3. ”Simulation of the Large Size Telescope drive system”, Piel, Quentin; Brunetti, Laurent; Eder, Josef; Fiasson, Armand; Guizzo, Gian Paolo; Monteiro, Inocencio; Noda, Koji; Schweizer, Thomas, Conference on High Energy, Optical, and Infrared Detectors for Astronomy VIII, JUN 10-13, 2018.

4. ”The e-ASTROGAM gamma-ray space observatory for the multimessenger astronomy of the 2030s”, Tatischeff, V.; Hayashida, M.et al., Conference on Space Telescopes and Instrumentation - Ultraviolet to Gamma Ray, JUN 10-15, 2018.

5. ”Energy Spectrum of Ultra-High-Energy Cosmic Rays Measured by The Telescope Array”, Yoshiki Tsunesada et al., The 35th International Cosmic Ray Conference (ICRC2017), BEXCO, BUSAN, KOREA, 12-20 JUL 2017.

6. ”Telescope Array anisotropy summary”, Sergey Troitsky on behalf of the Telescope Array collaboration, The 35th International Cosmic Ray Conference (ICRC2017), BEXCO, BUSAN, KOREA, 12-20 JUL 2017.

7. ”Auger at the Telescope Array: toward a direct cross-calibration of surface-detector stations ”, Sean Quinn on behalf of the Pierre Auger collaboration and on behalf of the Telescope Array collaboration, The 35th International Cosmic Ray Conference (ICRC2017), BEXCO, BUSAN, KOREA, 12-20 JUL 2017.

8. ”Declination Dependence of the Telescope Array Surface Detector Spectrum”, Dmitri Ivanov, The 35th International Cosmic Ray Conference (ICRC2017), BEXCO, BUSAN, KOREA, 12-20 JUL 2017.

9. ”The Cosmic Ray Spectrum above 0.1 EeV measured by the Telescope Array and TALE Fluorescence Detectors”, JiHee Kim on behalf of the Telescope Array collaboration, The 35th International Cosmic Ray Conference (ICRC2017), BEXCO, BUSAN, KOREA, 12-20 JUL 2017.

10. ”Interpretation of the energy spectrum observed with the Telescope Array detectors”, Eiji Kido on behalf of the Telescope Array collaboration, The 35th International Cosmic Ray Conference (ICRC2017), BEXCO, BUSAN, KOREA, 12-20 JUL 2017.

11. ”Study of muons from ultra-high energy cosmic ray air showers measured with the Telescope Array experiment”, Ryuji Takeishi on behalf of the Telescope Array collaboration, The 35th International Cosmic Ray Conference (ICRC2017), BEXCO, BUSAN, KOREA, 12-20 JUL 2017.

12. ”Anisotropy search in Energy distribution in Northern hemisphere using Telescope Array Surface Detector data”, Toshiyuki Nonaka on behalf of the Telescope Array collaboration, The 35th International Cosmic Ray Conference (ICRC2017), BEXCO, BUSAN, KOREA, 12-20 JUL 2017.

13. ”A systematic uncertainty on the energy scale of the Telescope Array fluorescence detectors”, Toshihiro Fujii on behalf of the Telescope Array collaboration, The 35th International Cosmic Ray Conference (ICRC2017), BEXCO, BUSAN, KOREA, 12-20 JUL 2017.

14. ”Hybrid Measurement of the Energy Spectrum and Composition of Ultra-High Energy Cosmic Rays by the Telescope Array”, Daisuke Ikeda on behalf of the Telescope Array collaboration, The 35th International Cosmic Ray Conference (ICRC2017), BEXCO, BUSAN, KOREA, 12-20 JUL 2017.

15. ”Telescope Array measurement of UHECR composition from stereoscopic fluorescence detection”, Douglas Bergman and T. Stroman, The 35th International Cosmic Ray Conference (ICRC2017), BEXCO, BUSAN, KOREA, 12-20 JUL 2017.

16. ”Telescope Array Composition Summary”, William Hanlon on behalf of the Telescope Array collaboration, The 35th International Cosmic Ray Conference (ICRC2017), BEXCO, BUSAN, KOREA, 12-20 JUL 2017.

17. ”Report of the Telescope Array- Pierre Auger Observatory Working Group on Energy Spectrum ”, Dmitri Ivanov on behalf of the Pierre Auger collaboration and on behalf of the Telescope Array collaboration, The 35th International Cosmic Ray Conference (ICRC2017), BEXCO, BUSAN, KOREA, 12-20 JUL 2017.

18. ”Testing the agreement between the Xmax distributions measured by the Pierre Auger and Telescope Array Observations”, Vitor de Souza on behalf of the Pierre Auger collaboration and on behalf of the Telescope Array collaboration, The 35th International Cosmic Ray Conference (ICRC2017), BEXCO, BUSAN, KOREA, 12-20 JUL 2017.

19. ”Telescope Array search for EeV photons and neutrinos”, Grigory Rubtsov on behalf of the Telescope Array collaboration, The 35th International Cosmic Ray Conference (ICRC2017), BEXCO, BUSAN, KOREA, 12-20 JUL 2017.

20. ”Composition Studies with the Telescope Array surface detector”, Yana Zhezher on behalf of the Telescope Array collaboration, The 35th International Cosmic Ray Conference (ICRC2017), BEXCO, BUSAN, KOREA, 12-20 JUL 2017.

21. ”All-sky search for correlations in the arrival directions of astrophysical neutrino candidates and ultrahigh-energy cosmic rays”, I.Al Samarai on behalf of IceCube Collaboration, on behalf of the Pierre Collaboration and on behalf of the Telescope Array collaboration, The 35th International Cosmic Ray Conference (ICRC2017), BEXCO, BUSAN, KOREA, 12-20 JUL 2017.

22. ”Highlights from the Telescope Array”, John N. Matthew on behalf of the Telescope Array collaboration, The 35th International Cosmic Ray Conference (ICRC2017), BEXCO, BUSAN, KOREA, 12-20 JUL 2017.

23. ”The TA$\times$4 experiment”, Eiji Kido on behalf of the Telescope Array collaboration, The 35th International Cosmic Ray Conference (ICRC2017), BEXCO, BUSAN, KOREA, 12-20 JUL 2017.

24. ”The Telescope Array Low-energy Extension”, S. Udo on behalf of the Telescope Array collaboration, The 35th International Cosmic Ray Conference (ICRC2017), BEXCO, BUSAN, KOREA, 12-20 JUL 2017.

25. ”TA fluorescence detector calibration by UV LED with an unmanned aerial vehicle”, Y. Tameda on behalf of the Telescope Array collaboration, The 35th International Cosmic Ray Conference (ICRC2017), BEXCO, BUSAN, KOREA, 12-20 JUL 2017.

26. ”Telescope Array Lightning Location System”, T. Okuda on behalf of the Telescope Array collaboration, The 35th International Cosmic Ray Conference (ICRC2017), BEXCO, BUSAN, KOREA, 12-20 JUL 2017.

27. ”Evidence of Intermediate-Scale Energy Spectrum Anisotropy in the Northern Hemisphere from Telescope Array”, P.J.Lundquist on behalf of the Telescope Array collaboration, The 35th International Cosmic Ray Conference (ICRC2017), BEXCO, BUSAN, KOREA, 12-20 JUL 2017.

28. ”Cosmic Rays Energy Spectrum from PeV to EeV energies measured by the TALE detector”, T. AbuZayyad on behalf of the Telescope Array collaboration, The 35th International Cosmic Ray Conference (ICRC2017), BEXCO, BUSAN, KOREA, 12-20 JUL 2017.

29. ”Multi-Messenger Signatures of PeV-ZeV Cosmic Ray Sources”, Meszaros, Peter; Murase, Kohta; Asano, Katsuaki; Senno, Nicholas; Xiao, Di, 2nd Conference on Cosmic Ray Origin - Beyond the Standard Models (CRBTSM), SEP 18-24, 2016.

30. ”Development status of the simultaneous two-color near-infrared multi-object spectrograph SWIMS for the TAO 6.5m telescope”, Konishi, Masahiro; Motohara, Kentaro; Takahashi, Hidenori; Kato, Natsuko; Terao, Yasunori; Ohashi, Hirofumi; Kono, Yukihiro; Kushibiki, Kosuke; Kodama, Tadayuki; Hayashi, Masao; Tanaka, Ichi; Tadaki, Ken-ichi; Toshikawa, Jun; Koyama, Yusei; Shimakawa, Rhythm; Suzuki, Tomoko; Tateuchi, Ken; Kitagawa, Yutaro; Kobayakawa, Yutaka; Todo, Soya; Aoki, Tsutomu; Doi, Mamoru; Hatsukade, Bunyo; Kamizuka, Takafumi; Kohno, Kotaro; Minezaki, Takeo; Miyata, Takashi; Morokuma, Tomoki; Sako, Shigeyuki; Soyano, Takao; Tanabc, Toshihiko; Tanaka, Masuo; Tarusawa, Ken’ichi; Tamura, Yoichi; Koshida, Shintaro; Ohsawa, Ryou; Uchiyama, Masahito; Mori, Tomohiro; Yamaguchi, Jumpei; Yoshida, Yutaka; Yoshii, Yuzuru, Conference on Ground-Based and Airborne Instrumentation for Astronomy VII, JUN 10-14, 2018.

31. ”Interplanetary Coronal Mass Ejection and the Sun’s Shadow Observed by the Tibet Air Shower Array,” M. Amenomori et al., The 35th International Cosmic Ray Conference (ICRC2017), BEXCO, BUSAN, KOREA, 12-20 JUL 2017.

32. ”Solar magnetic field strength and the ”Sun’s Shadow” ,” M. Amenomori et al., The 35th International Cosmic Ray Conference (ICRC2017), BEXCO, BUSAN, KOREA, 12-20 JUL 2017.

33. ”Measurement of high energy cosmic rays by the new Tibet hybrid experiment,” M. Amenomori et al., The 35th International Cosmic Ray Conference (ICRC2017), BEXCO, BUSAN, KOREA, 12-20 JUL 2017.

34. ”The Tibet AS+MD Project; status report 2017,” M. Amenomori et al., The 35th International Cosmic Ray Conference (ICRC2017), BEXCO, BUSAN, KOREA, 12-20 JUL 2017.

35. ”The overview of the ALPACA Experiment,” A. Asaba et al., The 35th International Cosmic Ray Conference (ICRC2017), BEXCO, BUSAN, KOREA, 12-20 JUL 2017.

36. ”ALPAQUITA Array in the ALPACA Project,” A. Asaba et al., The 35th International Cosmic Ray Conference (ICRC2017), BEXCO, BUSAN, KOREA, 12-20 JUL 2017.

# D. Doctoral Theses

1. Primordial black hole formation in Affleck-Dine baryogenesis,
   Fuminori HASEGAWA,
   Ph.D Thesis, Mar. 2019

2. Dark Matter search with high-energy gamma-ray observations,
   Nagisa HIROSHIMA,
   Ph.D Thesis, Mar. 2019

3. Realistic Construction of Axion Model with Gauged Peccei-Quinn Symmetry,
   Motoo SUZUKI,
   Ph.D Thesis, Mar. 2019

4. Subaru Census of Early Galaxies in the Hierarchical Structure Formation of the Universe,
   Yuichi HARIKANE,
   Ph.D Thesis, Mar. 2019

5. Demographics of the Cold Universe with ALMA: From Inter-Stellar and Circum-Galactic to Cosmic Structures,
   Seiji FUJIMOTO,
   Ph.D Thesis, Mar. 2019

6. New parameter estimation method being free from the bias depending on sky region for Gravitational wave from compact binary coalescence,
   Kenji ONO,
   Ph.D Thesis, Mar. 2019

7. Theoretical Study on the Radial Profile of Pulsar Wind Nebulae,
   Wataru ISHIZAKI,
   Ph.D Thesis, Mar. 2019

8. Search for Neutrinos associated with Gamma-ray Bursts in Super-Kamiokande,
   Asato ORII,
   Ph.D Thesis, Mar. 2019

9. Study of Emissions of Gamma ray Bursts above 10GeV with the Standard and Newly Recovered Data of the Fermi-LAT,
   Mitsunari TAKAHASHI,
   Ph.D Thesis, Sep. 2018

10. Srerile neutrino oscillation studies with the T2K far detector Super-Kamiokande,
    Ka Ming TSUI,
    Ph.D Thesis, Dec. 2018

11. Development of input optics for the gravitational wave detector KAGRA,
    Masayuki NAKANO,
    Ph.D Thesis, Dec. 2018

# E. Public Relations

## (a) ICRR News

ICRR News is a quarterly publication written in Japanese about scientific and educational activities at ICRR. It includes:

1. reports on scientific activities of ICRR staff members and those conducted at one or more of its facilities,

2. reports of international conferences on topics relevant to ICRR’s research activities,

3. reports on topics discussed at ICRR's Committees,
4. list of publications published by ICRR [ICRR-Report],
5. list of seminars held at ICRR,
6. announcements, and
7. other items of relevance.

Below lists the main topics in the issues published in FY 2018:

**No.102** (2018 Summer)

- Features: Super-Kamiokande's refurbishment work
- Features: Observation of Ultra-High Energy Cosmic Ray using air fluorescence detectors
- Reports: 18th ICRR × IPMU Public Lecture
- Press Release: ALMA finds Oxygen 13.28 Billion Light-Years Away
- Event: Sicence Cafe "Cafe KAGRA"
- Staff Reassignment
- ICRR Seminar

**No.103** (2018 Autumn)

- Features: Telescope Array Experiment; studying Ultra-High Energy Comic Rays to confirm their source, and reveal ultra-high energy phenomena
- Reports: Open Campus 2018
- Reports: Inauguration for CTA LST-1
- Reports: 19th ICRR × IPMU Public Lecture
- Topics: Workshop of cloud chamber at Matsudo International Science Art Festival
- Awards
- Topics: Release of second version of Super-Kamiokande Jigsaw Puzzle
- Topics: Reprodction of first version of Super-Kamiokande Jigsaw Puzzle
- Staff Reassignment
- ICRR Seminar

**No.104** (2019 Winter & Spring)

- Features: Focus on the riddles of the large-scale structures and galaxy formation of the universe 13 billion years ago
- Reports: Construction of TA extension (TA×4) started in mid winter
- Topics: Super-Kamiokande restarted its operation after 6 months' upgrade work
- Topics: The first Meeting of Hyper-Kamiokande Experiment Financial Forum
- Topics: CTA LST-1 Records its First Light
- Topics: Final Agreements Signed for CTA's Southern Hemisphere Site in Chile
- Topics: Award

- Topics: ICRR acknowledged as International Joint Usage/Research Center and start calling Applications
- Topics: CTA LST-1 awarded El Suplemento Premios Tecnologia Siglo XXI (21 Century Technology Award)
- Information: Staff Reassignment
- Information: ICRR Seminar

## (b) Public Lectures

- "Public Lecuture," Apr. 15, 2018, Kyushu University, Takaaki Kajita (ICRR, The University of Tokyo).
- "Public Lecuture," Apr. 27, 2018, Matsumoto University, Takaaki Kajita (ICRR, The University of Tokyo).
- "Public Lecuture," May. 2, 2018, Chubu University, Takaaki Kajita (ICRR, The University of Tokyo).
- "Public Lecuture," May. 13, 2018, Higashimatsuyama-City, Saitama, Takaaki Kajita (ICRR, The University of Tokyo).
- "Public Lecture in 20th International Symposium on Very High Energy Cosmic Ray Interations," May. 23, 2018, Nagoya University, Takaaki Kajita (ICRR, The University of Tokyo).
- "Public Lecuture," Jun. 23, 2018, Toho University, Takaaki Kajita (ICRR, The University of Tokyo).
- "Public Lecuture," Jul. 21, 2018, Kochi-City, Kochi, Takaaki Kajita (ICRR, The University of Tokyo).
- "Shinao Kizaki Kaki Daigaku," Aug. 2, 2018, Omachi-City, Nagano, Takaaki Kajita (ICRR, The University of Tokyo).
- "Public Lecture in JPS Autumn Meeting 2018," Sep. 16, 2018, Matumoto-City, Nagano, Takaaki Kajita (ICRR, The University of Tokyo).
- "Public Lecuture," Sep. 2. 2018, Toyama-City, Toyama, Takaaki Kajita (ICRR, The University of Tokyo).
- "Kaisei Festival," Sep. 22, 2018, Arakawa-Ku, Tokyo, Takaaki Kajita (ICRR, The University of Tokyo).
- "Public Lecture," Sep. 29, 2018, Yasuda Auditorium, The University of Tokyo, Tokyo, Takaaki Kajita (ICRR, The University of Tokyo).
- "Public Lecture," Oct. 21, 2018, Izumo Science Center, Shimane, Takaaki Kajita (ICRR, The University of Tokyo).
- "Public Lecuture," Nov. 3, 2018, Koshigaya-City, Saitama, Takaaki Kajita (ICRR, The University of Tokyo).
- "Public Lecture," Nov. 21, 2018, Mitaka-City, Tokyo, Takaaki Kajita (ICRR, The University of Tokyo).
- "Nagoya University Lecture," Nov. 23, 2018, Nagoya University, Takaaki Kajita (ICRR, The University of Tokyo).
- "Fukui Science Festa," Feb. 11, 2019, Fukui-City, Fukui, Takaaki Kajita (ICRR, The University of Tokyo).
- "Saturday Program," Feb. 23, 2019, Tokai Junior and Junior High School, Takaaki Kajita (ICRR, The University of Tokyo).
- "Global Peace Dialogue in Okinawa," Mar. 8, 2019, Okinawa Convention Center, Okinawa, Takaaki Kajita (ICRR, The University of Tokyo).
- "The 18th ICRR $\times$ IPMU Public Lecture," Apr. 14, 2018, Kashiwa-City, Chiba, Masayuki Nakahata (Kamioka Observatory, ICRR, The University of Tokyo).
- "Public Lecture for the America-Japan Society in Toyama," Jun. 27, 2018, ANA Crowne Plaza, Toyama-City, Toyama, Masayuki Nakahata (Kamioka Observatory, ICRR, The University of Tokyo).
- "Open College in Hida 2018," Jul. 14, 2018, Hida Earth Wisdom Center, Masato Shiozawa (Kamioka Observatory, ICRR, The University of Tokyo).
- "Geo Space Adventure," Jul. 14, 2018, Kamioka Observatory, Gifu, Kamioka Observatory, ICRR, The University of Tokyo.
- "Yume-no-Tamago-Juku," Aug. 6, 2018, Hida-City, Gifu, Jun Kameda (Kamioka Observatory, ICRR, The University of Tokyo).

- ”Hirameki Tokimeki Science,” Aug. 9, 2018, Kamioka Observatory, Gifu, Masayuki Nakahata, Yoshinari Hayato (Kamioka Observatory, ICRR, The University of Tokyo).
- ”Public Lecture,” Aug. 26, 2018, Toyama International Conference Center, Toyama, Masayuki Nakahata (Kamioka Observatory, ICRR, The University of Tokyo).
- ”Hyogo Prefectural Kakogawa Higashi High School,” Aug. 29, 2018, Kashiwa Campus, Chiba, Masaki Yamashita (Kamioka Observatory, ICRR, The University of Tokyo).
- ”VACUUM2018,” Sep. 5, 2018, Pacifico Yokohama, Kanagawa, Masayuki Nakahata (Kamioka Observatory, ICRR, The University of Tokyo).
- ”Science Café in Gifu,” Oct. 13, 2018, Gifu Shinbun sha, Gifu, Masayuki Nakahata (Kamioka Observatory, ICRR, The University of Tokyo).
- ”Public Lecture for Elementary School attached to University of Toyama,” Nov. 12, 2018, Toyama-City, Toyama, Motoyasu Ikeda (Kamioka Observatory, ICRR, The University of Tokyo).
- ”NHK Culture Center,” Dec. 9, 2018, NHK Culture Center Yokohama Landmark, Kanagawa, Masayuki Nakahata (Kamioka Observatory, ICRR, The University of Tokyo).
- ”Public Lecture,” Jan. 12, 2019, Hida-city, Gifu, Masato Shiozawa (Kamioka Observatory, ICRR, The University of Tokyo).
- ”Public Lecture for Kamioka Junior High School,” Feb. 22, 2019, Kamioka Junior High School, Hida-City, Gifu, Motoyasu Ikeda (Kamioka Observatory, ICRR, The University of Tokyo).
- ”Akita High School,” Aug. 2, 2018, ICRR, The University of Tokyo, Chiba, Takayuki Saito, Yuki Iwamura, Yoshiki Ohtani (ICRR, The University of Tokyo).
- ”Science Café,” Mar. 21, 2019, Tamarokuto Science Center, Tokyo, Takayuki Saito (ICRR, The University of Tokyo).
- ”Miyagi Prefecture Sendaidaiichi High School,” Jul. 5, 2018, ICRR, The University of Tokyo, Chiba, Toshiyuki Nonaka (ICRR, The University of Tokyo).
- ”The 19th ICRR $\times$ IPMU Public Lecture,” Nov. 11, 2018, Yasuda Auditorium, The University of Tokyo, Takashi Sako (ICRR, The University of Tokyo).
- ”Musashi High school,” Nov. 7, 2018, Musashi High School, Tokyo, Yoshiaki Ono (ICRR, The University of Tokyo).
- ”Science Café, ” Dec. 8, 2018, Tamarokuto Science Center, Tokyo, Ken Mawatari (ICRR, The University of Tokyo).
- ”Public Lecture,” Jun. 20, 2018, Chiyoda-Ku, Tokyo, Shinji Miyoki (KAGRA Observatory, ICRR, The University of Tokyo).
- ”The University of Tokyo’s EMP Club Network,” Jun. 22, 2018, KAGRA Observatory, Gifu, Shinji Miyoki (KAGRA Observatory, ICRR, The University of Tokyo).
- ”Yoshiki High School,” Jul. 12, 2018, Hida-City, Gifu, Shinji Miyoki (KAGRA Observatory, ICRR, The University of Tokyo).
- ”Public Lecture,” Jul. 14, 2018, Gifu-City, Gifu, Osamu Miyakawa (KAGRA Observatory, ICRR, The University of Tokyo).
- ”Public Lecture,” Jul. 21, 2018, Sanuki-City, Kagawa, Osamu Miyakawa (KAGRA Observatory, ICRR, The University of Tokyo).
- ”Hida-Kamioka High School,” Jul. 25, 2018, Hida-City, Gifu, Takaaki Yokozawa (KAGRA Observatory, ICRR, The University of Tokyo).
- ”Toyama High School,” Jul. 26, 2018, KAGRA Observatory, Gifu, Takahiro Yamamoto (KAGRA Observatory, ICRR, The University of Tokyo).
- ”Momoyama High School,” Jul. 27, 2018, KAGRA Observatory, Gifu, Chihiro Kosakai (KAGRA Collaborator)(Gravitational Wave Project Office, NAOJ).

- ”Nanao High School,” Aug. 2, 2018, KAGRA Observatory, Gifu, Takafumi Ushiba (KAGRA Observatory, ICRR, The University of Tokyo).
- ”Suwa Seiryo High School, Matsumoto Fukashi High School,” Aug. 3, 2018, KAGRA Observatory, Gifu, Naoko Ohishi (KAGRA Collaborator)(Gravitational Wave Project Office, NAOJ).
- ”Seisho High School,” Aug. 3, 2018, KAGRA Observatory, Gifu, Yoichi Aso (KAGRA Collaborator)(Gravitational Wave Project Office, NAOJ).
- ”Public Lecture,” Aug. 5, 2018, Kiso Observatory, Tokyo University, Osamu Miyakawa (KAGRA Observatory, ICRR, The University of Tokyo).
- Yoshiki High School,” Aug. 6-7, 2018, Takayama-city, Gifu, Kohei Yamamoto, Ryohei Kozu (KAGRA Observatory, ICRR, The University of Tokyo).
- ”Sapporo Nishi High School,” Aug. 7, 2018, KAGRA Observatory, Gifu, Kazuhiro Yamamoto (Visiting Associate Professor, KAGRA Observatory, ICRR, The University of Tokyo).
- ”Science Café, Café KAGRA,” Aug. 11, 2018, Hida-City, Gifu, Masatake Ohashi (KAGRA Observatory, ICRR, The University of Tokyo).
- ”Senior High School Attached to Kyoto University of Education,” Aug. 23, 2018, KAGRA Observatory, Gifu, Shinji Miyoki (KAGRA Observatory, ICRR, The University of Tokyo).
- ”Dutch Vacuum Society,” Sep. 4, 2018, KAGRA Observatory, Gifu, Yoichi Aso (KAGRA Collaborator)(Gravitational Wave Project Office, NAOJ).
- ”Public Lecture,” Sep. 6, 2018, Pacifico Yokohama, Kanagawa, Yoshio Saito (KAGRA Observatory, ICRR, The University of Tokyo).
- ”Faculty of Science, Toho University,” Sep. 7, 2018, KAGRA Observatory, Gifu, Yoshihisa Obayashi (KAGRA Observatory, ICRR, The University of Tokyo).
- ”KAGRA Tour for Donators to KAGRA Project,” Sep. 8, 2018, KAGRA Observatory, Gifu, KAGRA Observatory, ICRR, The University of Tokyo.
- ”Faculty of Science, Toyama University,” Sep. 14, 2018, KAGRA Observatory, Gifu, Kazuhiro Yamamoto (Visiting Associate Professor, KAGRA Observatory, ICRR, The University of Tokyo).
- ”Public Lecture,” Oct. 6, 2018, Saitama Prefectual Kawagoe High School, Saitama, Hideyuki Tagoshi (KAGRA Observatory, ICRR, The University of Tokyo).
- ”High Energy Accelerator Research Organization,” Oct. 9, 2018, KAGRA Observatory, Gifu, Osamu Miyakawa (KAGRA Observatory, ICRR, The University of Tokyo).
- ”Japan Stainless Steel Association,” Oct. 12, 2018, KAGRA Observatory, Gifu, Yoshio Saito (KAGRA Observatory, ICRR, The University of Tokyo).
- ”Public Lecture,” Oct. 27, 2018, The Nagasaki Institute of Applied Science, Nagasaki, Masatake Ohashi (KAGRA Observatory, ICRR, The University of Tokyo).
- ”Public Lecture,” Nov. 1, 2018, Hachikoku Elementary School, Saitama, Hideyuki Tagoshi (KAGRA Observatory, ICRR, The University of Tokyo).
- ”Public Lecture,” Nov. 1, 2018, Rihga Royal Hotel Tokyo, Shinji Miyoki (KAGRA Observatory, ICRR, The University of Tokyo).
- ”KAGRA Tour,” Nov. 17, 2018, KAGRA Observatory, Gifu, KAGRA Observatory, ICRR, The University of Tokyo.
- ”Japan Environmental Education Forum,” Dec. 13, 2018, KAGRA Observatory, Gifu, Yoshio Saito (KAGRA Observatory, ICRR, The University of Tokyo).
- ”Asahi Culture Center Yokohama,” Jan. 19, 2019, ASAHI Culture center, Yokohama school, Shinji Miyoki (KAGRA Observatory, ICRR, The University of Tokyo).
- ”Yume-no-Tamago-Juku,” Mar. 24, 2019, Hida-City, Gifu, Hirotaka Yuzurihara (KAGRA Observatory, ICRR, The University of Tokyo).

- ”NHK Culture Center Shinjuku,” Aug. 25, 2018, Shinjuku-ku, Tokyo, Masahiro Kawasaki (ICRR, The University of Tokyo).

## (c) Visitors

Kashiwa Campus (Total: 35 groups, 2,336 people)

- Junior High and High schools: 5 groups
- Universities and Graduate schools: 4 groups
- Researchers: 0 group
- Inspections: 6 groups
- Press: 19 groups
- Others: 1 group

KAMIOKA Observatory (Total: 322 groups, 2,769 people)

- Junior High and High schools: 25 groups
- Universities and Graduate schools: 25 groups
- Researchers: 71 groups
- Inspections: 47 groups
- Press: 56 groups
- Others: 98 groups

KAGRA Observatory (Total: 130 groups, 1,622 people)

- Elementary Junior High and High schools: 15 groups
- Universities and Graduate schools: 18 groups
- Researchers: 12 groups
- Inspections: 24 groups
- Press: 14 groups
- Others: 47 groups

# F. Inter-University Research Activities

## Numbers of Researchers

| | Number of Applications | Number of Adoptions | Number of Researchers |
|---|---|---|---|
| Facility Usage | | | |
| Kamioka Observatory | 40 | 40 | 1,107 |
| Akeno Observatory | 4 | 4 | 175 |
| Norikura Observatory | 8 | 8 | 95 |
| Low-Level Radioisotope Measurement Facility | 4 | 4 | 29 |
| Cryogenic Laser Interferometer in Kashiwa | 15 | 15 | 508 |
| Laboratorial Facility in Kashiwa | 3 | 3 | 31 |
| Computer Facility in Kashiwa | 16 | 16 | 388 |
| Conference Facility in Kashiwa | 7 | 7 | 225 |
| Over Sea Facilities | 26 | 26 | 392 |
| Annual Sums | 123 | 123 | 2,950 |

| | | | |
|---|---|---|---|
| Joint Research | | | |
| Neutrino and Astroparticle Research | 41 | 41 | 1,118 |
| High Energy Cosmic Ray Research | 54 | 54 | 1,181 |
| Astrophysics and Gravity Research | 20 | 20 | 597 |
| Research Center for Cosmic neutrinos | 8 | 8 | 54 |
| Annual Sums | 123 | 123 | 2,950 |

## Research Project Titles

1. Astroparticle physics using the Super-Kamiokande detector
2. Study of atmospheric neutrino flux and neutrino oscillations
3. Study of simulation for atmospheric neutrino
4. Studying the Neutrino Mass Hierarchy With Atmospheric Neutrinos
5. Study of flavor identification of atmospheric and beam neutrinos
6. Study of solar neutrino energy spectrum
7. Precise measurement of Day/Night effect for $^8B$ solar neutrinos
8. Study for Supernova monitor
9. Study of Supernova Relic Neutrinos
10. Search for proton decay via $e^+\pi^0$ mode
11. Study of proton decay p $\rightarrow \nu K^+$
12. Study in upward-going muons and high energy neutrinos
13. Sidereal daily variation of $\sim$10TeV galactic cosmic ray intensity observed by the Super-Kamiokande
14. Tokai to Kamioka Long Baseline Experiment T2K
15. Neutrino interaction study using accelerator data
16. Study to improve sensitivity of neutrino oscillation measurement in T2K expriment
17. Joint Oscillation Analysis With the T2K and Super-Kamiokande Experiments

18. Energy calibration for Super-Kamiokande
19. Research and development of computer simulation of Super-Kamiokande detector
20. Development of low concentration radon detection system
21. R&D of Megaton scale water Cherenkov Detector Hyper-Kamiokande
22. Development of the Large Aperture Photodetector for a next-generation neutrino detector
23. Development of software for the next generation neutrino detector
24. A Search for Dark Matter using Liquid Xenon Detector
25. Detector structure study for future direct dark matter search experiment
26. Study on neutrino physics using liquid xenon
27. Radon emanation measurement from material using dark matter search experiment(2).
28. A study on scattering processes of scintillation photons in liquid xenon
29. Study on surface background removal in the dark matter search
30. Research and development for XENONnT and search for dark matter
31. Simulation study and data analysis for dark matter search in XENONnT
32. RI measurement of the PMT by HPGe detector
33. Study of double beta decay of $^{48}Ca$
34. Direction-sensitive dark matter search
35. Study for lowering backgrounds of radioisotopes in large volume detectors
36. Studies on the background evaluation using laser spectroscopy analysis
37. Development of a radioactivity assay system for underground experiments
38. Dark Matter Search with double-phase Argon detector
39. Integration of crustal activity observation around the Atotsugawa fault
40. Strain, tilt, seismic measurement in Kamioka-mine
41. Searches for neutrinoless double beta decay and dark matter with high-pressure Xenon gas detector
42. Multi-Color Imager for Transients, Survey and Monstrous Explosions
43. Observation of Galactic Cosmic Ray Intensities using Large Area Muon Telescopes
44. Observation of solar neutrons in solar cycle 24
45. Space weather observation using muon hodoscope at Mt. Norikura
46. Observation of cosmogenic nuclides concentrations at Mt. Norikura
47. Study of secondary cosmic rays from Thundercloud at Mt. Norikura
48. Development of high energy proton irradiation technique for devices used in spaceship
49. Investigation of alpine plants on Mt. Norikura
50. Effect of forest fragmentation on the belowground microorganisms
51. Symbiosis betweem Pinus pumila and Nucifraga caryocatactes on Mt.Norikura
52. CTA Project
53. CTA-Japan Physics Research

54. Development of Focal Plane Instrumemnts for the CTA Large Sized Telescope
55. Development of the readout system for the CTA large sized telescopes
56. Installation and commissioning of the first Large Size Telescope of CTA in La Palma, Canary Islands, Spain
57. Development and commissioning of the onsite data analysis for CTA North in La Palma, Spain
58. Development of camera for CTA small-sized telescopes
59. CTA Monte Carlo Simulation
60. Localization of very high energy gamma-ray emission region in an active galactic nuclei
61. The study on simultaneous observations of gamma ray bursts by CTA and LEAP
62. Early phase observations with CTA Large Sized Telescopes
63. Study of High Energy Gamma-ray Objects with the MAGIC telescope
64. R&D for a Small Atmospheric Cherenkov Telescope in Akeno Observatory
65. Study of Extremely-high Energy Cosmic Rays by Telescope Array
66. Observing ultrahigh-energy cosmic rays with new fluorescence detectors at Telescope Array site
67. Timing and position calibration of surface detectors of TA$\times$4 and TALE experiment
68. Research and development of the surface detectors for the TALE experiment
69. Study of radio detection of highest energy cosmic rays
70. Research and development of a Fresnel lens air fluorescence telescope for the next generation UHECR observation
71. The observation of abnormal shower event with lightning by TA surface particle detector
72. Development of solar power system and detector protection system for the new-type fluorescent detector
73. Calibration of fluorescence detector responce and optical system with standard light source mounted on UAV
74. Development and analysis of night cloud observation by CCD camera for automatic observation of air fluorescence detector
75. Observation of airshower fluorescence light at the TA FD site by using an Imaging UV telescope
76. Development of new surface detector for observation of ultra high energy cosmic ray at Telescope Array site
77. Development of an advanced Compton camera using SOI pixel semiconductor
78. Design study of a Compton camera for study of cosmic rays
79. Experimental Study of High-energy Cosmic Rays in the Tibet AS$\gamma$ experiment
80. Study of High Energetic Radiation from Thundercloud in the Altiplano
81. Sidereal daily variation of $\sim$10TeV galactic cosmic ray intensity observed by the Tibet air shower array
82. Study of the composition of cosmic-rays at the Knee
83. A study on variation of interplanetary magnetic field with the cosmic-ray shadow by the sun
84. Air shower observation for high-energy gamma ray and cosmic ray detections at the Chacaltaya Cosmic Ray Observatory
85. Study on High Energy Cosmic Ray Sources by Observation in Spac with CALET
86. Observation with Ahsra
87. Integration of the optical fiber trigger system for Ashra
88. Cosmic-ray chemical composition study using air shower muons

89. Study of solar magnetic fields using the cosmic-ray Sun's shadow observed at the southern hemishpere
90. Cosmic ray interactions in the knee and the highest energy regions
91. Study of Fast Moving Dark Matters and Meteoroids using High Sensitivity CMOS Camera System
92. Comparative study of astrophysical particle acceleration processes
93. The extreme Universe viewed in very-high-energy gamma rays 2018
94. Development of a new code for cosmic-ray air shower simulation
95. YMAP symposium 2018 (Basic Part)
96. Research of Large-scale Gravitational wave Telescope (Ⅷ)
97. Development of High Performance Cryogenic Mirror Control System
98. Research on cryogenic payload for KAGRA
99. Construction of KAGRA data transfer and storage system (4)
100. R&D for the intensity stabilization of the laser system in KAGRA
101. Technical development for effects on high optical power for bKAGRA mode cleaner Ⅱ
102. Precise geophysical observation at the Kamioka underground site and modeling of crustal activities
103. Development of precision profiler for mirrors of LCGT interferometer 8
104. Development of optical cavity for ultranarrow stable lasers
105. Installation of the output mode-cleaner for KAGRA
106. Study of Gravitational-wave by cryogenic laser interferometer CLIO in KAMIOKA Mine(Ⅱ)
107. Study for improving a curing time of silicate bonding by controlling gas environment
108. Development of ultra-low loss coating for the KAGRA sapphire mirror-3
109. Numerical Simulation of Electro-Magnetic Wave Propagation in Gravitational wave Detector VI
110. Control and automatic operation for KAGRA
111. Data analysis of KAGRA detector (IV)
112. Development of a high performance sapphire mirror suspension
113. Development of KAGRA detector characterization
114. Cosmic Reionization and Galaxy Formation Probed with Large Optical Near-Infrared Telescope
115. Evolution of the universe and particle physics
116. Detection of time variations for cosmogenic nucleid Be-7
117. Evaluation of the erupted radioactivities into the environment
118. Frontier of the planetary material science
119. Time profile of radioactive Cs concentration and its aerosol size distribution in local area
120. Continuous Measuerment of Underground Laboratory Environment
121. Precise calculation of the atmospheric neutrino flux
122. Energy Determination of the LPM showers
123. Neutrino Workshop
124. CRC workshop for future plans in cosmic ray research

# G. List of Committee Members

**(a) Board of Councillors**

| | |
|---|---|
| KAJITA, Takaaki | ICRR, The University of Tokyo |
| NAKAHATA, Masayuki | ICRR, The University of Tokyo |
| SAGAWA, Hiroyuki | ICRR, The University of Tokyo |
| OHASHI, Masatake | ICRR, The University of Tokyo |
| TAKEDA, Hiroyuki | Graduate School of Science, The University of Tokyo |
| KOSEKI, Toshihiko | The University of Tokyo |
| TOKUSHUKU, Katsuo | Institute of Particle and Nuclear Studies, KEK |
| AOKI, Shinya | Yukawa Institute for Theoretical Physics, Kyoto University |
| TSUNETA, Saku | National Astronomical Observatory of Japan |
| TORII, Shoji | Faculty of Science and Engineering, Waseda University |
| ITOW, Yoshitaka | Institute for Space-Earth Environmental Research, Nagoya University |
| TANAKA, Takahiro | Yukawa Institute for Theoretical Physics, Kyoto University |
| MITSUDA, Kazuhisa | Institute of Space and Astronautical Science |
| ASAI, Shoji | International Center for Elementary Particle Physics, The University of Tokyo |
| KUSANO, Kanya | Institute for Space-Earth Environmental Research, Nagoya University |

**(b) Advisory Committee**

| | |
|---|---|
| KAJITA, Takaaki | ICRR, The University of Tokyo |
| KITANO, Ryuichiro | KEK Theory Center |
| SUZUKI, Hideyuki | Tokyo University of Science |
| KUZE, Masahiro | School of Science, Tokyo Institute of Technology |
| AOI, Nori | Research Center for Nuclear Physics, Osaka University |
| YOKOYAMA, Masashi | Graduate School of Science, The University of Tokyo |
| YOSHIDA, Atsumasa | Aoyama Gakuin University |
| NISHIJIMA, Kyoshi | Tokai University |
| OGIO, Shoichi | Graduate School of Science, Osaka City University |
| MORI, Masaki | Ritsumeikan University |
| KANDA, Nobuyuki | Graduate School of Science, Osaka City University |
| KAWASAKI, Masahiro | ICRR, The University of Tokyo |
| NAKAHATA, Masayuki | ICRR, The University of Tokyo |
| SHIOZAWA, Masato | ICRR, The University of Tokyo |
| TESHIMA, Masahiro | ICRR, The University of Tokyo |
| OHASHI, Masatake | ICRR, The University of Tokyo |
| SAGAWA, Hiroyuki | ICRR, The University of Tokyo |
| TAKITA, Masato | ICRR, The University of Tokyo |

**(c) Inter-University Research Advisory Committee**

| | |
|---|---|
| MUNAKATA, Kazuoki | Shinshu University |
| ITOW, Yoshitaka | Institute for Space-Earth Environmental Research, Nagoya University |
| OGIO, Shoichi | Graduate School of Science, Osaka City University |
| TAJIMA, Hiroyasu | Institute for Space-Earth Environmental Research, Nagoya University |
| HIBINO, Kinya | Kanagawa University |
| KUBO, Hidetoshi | Kyoto University |
| SATO, Shuichi | Hosei University |
| TOKANAI, Fuyuki | Yamagata University |
| TAKEUCHI, Yasuo | Graduate School of Science, Kobe University |
| NAKAHATA, Masayuki | ICRR, The University of Tokyo |
| TAKITA, Masato | ICRR, The University of Tokyo |
| UCHIYAMA, Takashi | ICRR, The University of Tokyo |
| YOSHIKOSHI, Takanori | ICRR, The University of Tokyo |
| SAKO, Takashi | ICRR, The University of Tokyo |

# H. List of Personnel

| | | | |
|---|---|---|---|
| **Director** | KAJITA, Takaaki, | | |
| **Vice-Director** | KAWASAKI, Masahiro, | NAKAHATA, Masayuki, | |
| **Kamioka Observatory (Neutrino and Astroparticle Division)** | | | |
| Scientific Staff | ABE, Ko, | BRONNER, Christophe, | HAYATO, Yoshinari, |
| | HIRAIDE, Katsuki, | ICHIMURA, Koichi, | IKEDA, Motoyasu, |
| | KAMEDA, Jun, | KATAOKA, Yosuke, | KATO, Yo, |
| | KISHIMOTO, Yasuhiro, | KOBAYASHI, Kazuyoshi, | MARTI MAGRO, Lluis, |
| | MIURA, Makoto, | MORIYAMA, Shigetaka, | NAKAHATA, Masayuki, |
| | NAKAJIMA, Yasuhiro, | NAKAYAMA, Shoei, | SEKIYA, Hiroyuki, |
| | SHIOZAWA, Masato, | TAKEDA, Atsushi, | TANAKA, Hidekazu, |
| | YAMASHITA, Masaki, | YANO, Takatomi, | |
| Administrative Staff | SHIMIZU, Akihiko, | | |
| Public Relations Staff | TAKENAGA, Yumiko, | | |
| Technical Staff | HIGASHI, Tetsuji, | NOZAWA, Noriyuki, | ONOUE, Tatsuya, |
| Research Fellow | KOBAYASHI, Masatoshi, | McCAULEY, Neil Kevin, | MINAKATA, Hisakazu, |
| | NAKANO, Yuki, | SATO, Kazufumi, | TASAKA, Shigeki, |
| | YANG, Byeongsu, | | |
| Secretary | DOI, Kyoko, | FUJIMURA, Yuko, | KAMIKAWATO, Rie, |
| **Research Center for Cosmic Neutrinos (Neutrino and Astroparticle Division)** | | | |
| Scientific Staff | KAJITA, Takaaki, | MASUDA, Kimiaki, | NISHIMURA, Yasuhiro, |
| | OKUMURA, Kimihiro, | TOKANAI, Fuyuki, | |
| Technical Staff | SHINOHARA, Masanobu, | | |
| Research Fellow | ZIEMBICKI, Marcin, | | |
| Secretary | KITSUGI, Atsuko, | MASHIMA, Chieko, | |
| **High Energy Cosmic Ray Division** | | | |
| Scientific Staff | ASANO, Katsuaki, | ENOMOTO, Ryoji, | HADASCH, Daniela, |
| | KAWATA, Kazumasa, | KIDO, Eiji, | KUBO, Hidetoshi, |
| | MARTINEZ, Manel, | MAZIN, Daniel Mihajlovic, | NODA, Koji, |
| | NONAKA, Toshiyuki, | OHISHI, Michiko, | OHNISHI, Munehiro, |
| | SAITO, Takayuki, | SAKO, Takashi, | SASAKI, Makoto, |
| | TAKEDA, Masahiro, | TAKITA, Masato, | TESHIMA, Masahiro, |
| | YAMAMOTO, Tokonatsu, | YOSHIDA, Tatsuo, | YOSHIKOSHI, Takanori, |
| Technical Staff | AOKI, Toshifumi, | INOME, Yusuke, | SEKINO, Koichi, |
| Research Fellow | FUJII, Toshihiro, | NAKAMURA, Yoshiaki, | SAKO, Takashi, |
| Secretary | IDOMURA, Takako, | SHIRAGA, Ryoko, | SUGAHARA, Midori, |
| **Akeno Observatory (High Energy Cosmic Ray Division)** | | | |
| Scientific Staff | SAGAWA, Hiroyuki, | | |
| Technical Staff | KOBAYASHI, Ryoichi, | | |
| **Norikura Observatory (High Energy Cosmic Ray Division)** | | | |
| Technical Staff | AWAI, Kyosuke, | HAYAKAWA, Hideaki, | IMANISHI, Hidenori, |
| | OKAZAKI, Nao, | SHIMODAIRA, Hideaki, | TOMURA, Tomonobu, |
| | USHIMARU, Tsukasa, | | |

**Astrophysics and Gravity Division**

| | | | |
|---|---|---|---|
| Scientific Staff | IBE, Masahiro, | KAWASAKI, Masahiro, | ONO, Yoshiaki, |
| | OUCHI, Masami, | | |
| Research Fellow | HAYASHI, Kohei, | NAGAI, Ryo, | OBATA, Ippei, |
| | TOSHIKAWA, Jun, | | |

**KAGRA Observatory (Astrophysics and Gravity Division)**

| | | | |
|---|---|---|---|
| Scientific Staff | BALLMER, Stefan Werner, | HIROSE, Eiichi, | KAWAGUCHI, Kyohei, |
| | KIMURA, Nobuhiro, | KOKEYAMA, Keiko, | MIO, Norikatsu, |
| | MIYAKAWA, Osamu, | MIYOKI, Shinji, | OHASHI, Masatake, |
| | SAITO, Yoshio, | TAGOSHI, Hideyuki, | TOMARU, Takayuki, |
| | TROZZO, Lucia, | UCHIYAMA, Takashi, | USHIBA, Takafumi, |
| | YAMAMOTO, Kazuhiro, | YOSHII, Yuzuru, | |
| Administrative Staff | OKINAKA, Mihoko, | TAKAYAMA, Kyoichi, | |
| Technical Staff | FURUTA, Kiyoshi, | KAMIIZUMI, Masahiro, | NAKADA, Kazuo, |
| | OBAYASHI, Yoshihisa, | OHOKA, Hideyuki, | SHIMODE, Katsuhiko, |
| | TAKAHASHI, Masahiro, | TAMORI, Yukio, | |
| Research Fellow | LEE, Hyung Won, | NARIKAWA, Tatsuya, | OSHINO, Shoichi |
| | PENA ARELLANO, Fabian, | SURESH, Jishnu, | SUZUKI, Toshikazu, |
| | YAMAMOTO, Takahiro, | YOKOZAWA, Takaaki, | YUZURIHARA, Hirotaka, |
| Secretary | CHIDA, Ai, | HARA, Yayoi, | IWAMATSU, Miho, |
| | KIKUCHI, Rie, | MAEDA, Yukari, | |

**Graduate Students**

| | | | |
|---|---|---|---|
| Doctor | AKUTSU, Ryosuke, | FUJIMOTO, Seiji, | FUKAMI, Satoshi, |
| | HARIKANE, Yuichi, | HASEGAWA, Fuminori, | HASEGAWA, Kunihiko, |
| | HIROSHIMA, Nagisa, | INADA, Tomohiro, | INOMATA, Keisuke, |
| | ISHIZAKI, Wataru, | IWAMURA, Yuki, | KOJIMA, Takashi, |
| | MIYAMOTO, Takahiro, | MIYO, Koseki, | MUKAE, Shiro, |
| | NAGANO, Koji, | NAKANO, Masayuki, | NAKANO, Wakutaka, |
| | ONO, Kenji, | ORII, Asato, | SHIN, Heungsu, |
| | SONODA, Yutaro, | SUGAHARA, Yuma, | SUZUKI, Motoo, |
| | TANAKA, Hiroki, | TO, Sho, | TSUI, Kaming, |
| | ZHANG, Haibin, | | |
| Master | ANDO, Kenta, | ARAI, Koya, | ARAI, Yuya, |
| | CHEN, Yu-chin, | FUKUNAGA, Masashi, | HIGUCHI, Ryo, |
| | HILMI, Miftahul, | HSIEH, Bin-Hua, | IIDA, Kento, |
| | IMAIZUMI, Shuichi, | ITO, Ryohei, | KAKUMA, Ryota, |
| | KATO, Sei, | KATO, Nobuyuki, | KIKUCHIHARA, Shotaro, |
| | KIRII, Shin, | KOBAYASHI, Shin, | KOBAYASHI, Yukiho, |
| | KOZU, Ryohei, | KUMON, Taku, | MOCHIZUKI, Toshiki, |
| | MURAI, Kai, | NAKATSUKA, Hiromasa, | OGAKI, Wataru, |
| | OHTANI,Yoshiki, | OKADA, Takeshi, | OKAMOTO, Kohei, |
| | OTANI, Francis, | PEDERSEN, Juan William, | SAKURAI, Shunsuke, |
| | SATO, Yuta, | SHIMODATE, Karin, | SONOMOTO, Eisuke, |
| | SUZUKI, Takumi, | TAKENAKA, Akira, | TANAKA, Kenta, |
| | TANAKA, Taiki, | WANG, Ru, | XIA, Junjie, |
| | YADA, Kohei, | YAMADA, Tomohiro, | YAMAMOTO, Kohei, |

**Administrative Division**

| | | | |
|---|---|---|---|
| Administrative Staff | AKAIDA, Yohei, | AKIYAMA, Makiko, | BOLENS, Yukari, |
| | FUKUHARA, Nana, | HIRAGA, Takuya, | KOBAYASHI, Toyoki, |
| | KONDO, Hitomi, | MARUMORI, Yasuko, | NAKAJIMA, Kazumi, |
| | NAMATAME, Kaneo, | OHURA, Kiichi, | OKANO, Yuka, |
| | SAITO, Akiko, | SATO, Yu, | TAKAMICHI, Ryo, |
| | YAMAGUCHI, Akiko, | | |
| Research Administrator | SATO, Ritsuko, | | |
| Public Relations Staff | FUKUDA, Hironobu, | ITO, Yoriko, | NAKAMURA, Makio, |


INSTITUTE FOR COSMIC RAY RESEARCH
THE UNIVERSITY OF TOKYO

Address 5-1-5, Kashiwanoha, Kashiwa-shi, Chiba, 277-8582 Japan
TEL +81-4-7136-3102
FAX +81-4-7136-3115
URL www.icrr.u-tokyo.ac.jp


ICRR
Institute for Cosmic Ray Research
University of Tokyo